

***COST IC0802 - Propagation tools and data for  
integrated Telecommunication, Navigation and Earth  
Observation systems***



***Assessment of FSO Propagation  
Models by means of System  
Test-Beds and Measurements***

***Final Report of WG3 of COST IC0802  
Channel modelling for free-space optical systems and  
airborne terminals***

**Chairs of WG3**  
Erich Leitgeb  
Gorazd Kandus  
Zabih Ghassemlooy

**December 2012**  
**Final update: May 2013**

## CONTENT

<b>0. Content and list of authors .....</b>	<b>page 0-1</b>
<b>1. Introduction (EL, ZG+, GK, SSM).....</b>	<b>page 1-1</b>
<b>2. Main important weather parameters for analysing the FSO-channel (OF+, CC+, ZG+, VK+, EL, HLM).....</b>	<b>page 2-1</b>
<b>3. Fog measurements on FSO in Nice (France Telecom) and Graz (SSM+, EL).....</b>	<b>page 3-1</b>
<b>4. Weather parameter and fog measurements in Milano (CC, RN) .....</b>	<b>page 4-1</b>
<b>5. Weather parameter and fog measurements in Prague (VK, MG, OF).....</b>	<b>page 5-1</b>
<b>6. Weather parameter and fog measurements in Miletovka (OF+, OW) .....</b>	<b>page 6-1</b>
<b>7. Weather parameter and fog measurements on FSO in Budapest (LC, IF).....</b>	<b>page 7-1</b>
<b>8. Weather parameter and fog measurements in Rome (FM+) .....</b>	<b>page 8-1</b>
<b>9. Channel Measurement and Markov Modelling of an Urban Free-Space Optical Link (in Canadian Conditions) (SH+).....</b>	<b>page 9-1</b>
<b>10. FSO link propagation measurements and channel model under fog conditions developed at Northumbria University (ZG, SR, WP, JPS, HLM).....</b>	<b>page 10-1</b>
<b>11. FSO link performance under atmospheric turbulence (ZG, WP, SR, IF, LC, SZ).....</b>	<b>page 11-1</b>
<b>12. Combination of FSO and RF as Hybrid Solutions (including applications) (IF, GK, LC, ZG, EL+, VK+) ).....</b>	<b>page 12-1</b>
<b>13. The weather influence and its mitigation (ZG, SSM, SR, WP, TJ, GK).....</b>	<b>page 13-1</b>
<b>14. Diversity, Networking and Redundancy (WP, SR, ZG, SSM, EL+, GK, FO, HLM, IF).....</b>	<b>page 14-1</b>
<b>15. Conclusions (JPS, EL, GK, ZG).....</b>	<b>page 15-1</b>
<b>Appendix A: Visibility and weather statistics on FSO in Ankara and Istanbul (FO, FI, EL).....</b>	<b>page A-1</b>
<b>Appendix B: Co-operations and Interaction of WG3 (EL, GK) .....</b>	<b>page B-1</b>

## AUTHORS LIST

The authors of chapters are visible within the structure / headers as following abbreviations (see below):

Prof. Erich Leitgeb.....EL  
Prof. Zabih Ghassemlooy .....ZG  
Prof. Gorazd Kandus .....GK  
Dr. Sajid Sheikh Muhammad.....SSM  
Dr. Vaclav Kvicera.....VK  
Dr. Martin Grabner.....MG  
Prof. Steve Hranilovic.....SH  
Prof. Ondrej Fiser.....OF  
Prof. Carlo Capsoni.....CC  
Dr. Roberto Nebuloni.....RN  
Prof. Istvan Frigyes.....IF  
Prof. Janos Bito.....JB  
Dr. Laszlo Csurgai .....LC  
Prof. Faruk Ozek.....FO  
Dr. Filiz Icat.....FI  
Dr. Frank Marzano.....FM  
Dr. Tomaz Javornik.....TJ  
Dr. Stanislav Zvánovec.....SZ  
Prof. Otakar Wilfert.....OW  
Dr. Hoa Le-Minh.....HLM  
Dr. Wasiu Popoola.....WP  
Dr. Sujan Rajbhandari.....SR  
Dr. Joaquin Perez Soler.....JPS

+..... means that Co-authors will also be within the research groups of the named author

# 1 INTRODUCTION

(Erich Leitgeb, Zabih Ghassemlooy, Gorazd Kandus, Sajid Sheikh Muhammad)

The Working Group 3 (WG3) of the COST action IC0802 is focussed on the channel modelling for free-space optical communication systems and airborne terminals. The activities of the group also include fog measurements, simulations and channel modelling with interaction between the SGMP (for measurements and experiments). Integration of WG3 organisations of COST action IC0802 (including non-COST countries) was accomplished in the first year of the project.

Further co-operation was initiated with ITU-R and EU-projects (mainly BONE and OMEGA) in the free space optics field and airborne terminals in WG3. BONE and the COST IC0802 have carried out joint activities and planned further co-operations. The results and findings of personal exchanges (including Short Term Scientific Missions) within the WG3 have been implemented in cooperation with SGMP to validate the channel models with measurements and experiments.

Joint publications (conferences and journals), organizing special sessions on Optical Wireless Communications at international conferences and workshops are important outcomes of WG3, including dissemination of the knowledge of IC 0802. In this report it is important to mention that in each year of the running COST action the participants had at minimum around 5 joint Journal papers and around 15 reviewed joint conference contributions. Of course each organisation within WG3 had each year around 10 to 20 individual publications within the FSO-field.

The networking (covering other WG's, mainly the SGMP) has been fruitful for the investigation of new Simulation-Tools and Models and also for further co-operations and contributions to ITU-R in Free Space Optics (including further work in international projects), which are of central importance in WG3.

An important task of COST actions is the dissemination of the project achievements. So it has been decided at the meeting in Graz (June 14, 2011, connected to the IC0802 workshop and the ConTEL 2011) to prepare an end-of-project document titled "FSO Propagation Models analysed by real experiments and measurements" as a final report of the WG3 activities. The details and first structure were also discussed at the meeting in Prague, September 2011. After discussion with a possible publisher in October 2011, it was decided to prepare only a Final Report for WG3 of IC0802, not a book.

The first 2 thirds of the chapters are showing our measurements within different experiments and test-beds of our WG3 participants. The structure clearly represents (as mentioned often within this report), that FSO is much younger than RF-technology. So we have to make still a lot of data-analysis before improving old channel models and before generating new ones. The authors of these chapters describe the set-up of their sites (very often very special for each location), the measurements and the analysis and of course their influence on the channel-models. In the following chapters the authors refer to special applications, special modulation and coding schemes, combinations of RF- and FSO. All these techniques are shown to improve FSO-systems for the Next Generation Networks.

## 1.1 FSO-channel compared to the RF-channel

Before starting with the main advantages and differences of Free Space Optics (FSO) and RF-channels it must be mentioned that FSO is a much younger technology compared to RF. When in 1960 the LASER were investigated people had the idea to transmit high data rates through the atmosphere by light for long distances, but then they found out about the problem of fog and clouds for light transmission. Of course in relevance to the high carrier frequencies in optics we have the high usable bandwidth, that is a big advantage compared to RF, but the high frequency also means short wavelengths (some  $\mu\text{m}$ ), and that means the same size like the small particles within the fog and clouds. So it is not a surprise that Optical Wireless is mainly influenced by fog and clouds. It is the same relation like in RF between RF-wavelengths and the size of rain particles. In both cases the Mie-scattering is the main attenuator for the different technologies.

Now it is clear, why in 1960 the scientists (in the optical field) searched for better fibers (as medium) to use light transmission instead of using the atmosphere with the non-predictable weather conditions. But of course work also started in Optical Wireless (a few ambitious scientists still hoped for solving the problems by using high power laser sources and so on). Additional for Intersatellite Links FSO is a perfect solution, because we have no fog and clouds higher than the troposphere. So the main limiter and attenuator do not exist between the satellites.

It must also be mentioned that scientists starting on real channel modelling for FSO the last 10 years, before they only made some measurements on attenuations or they developed FSO-systems. So the channel-modelling in FSO is much younger than in RF. RF started with scientists like Hertz and Marconi 120 years ago and a lot of scientists studied the propagation of RF since this time. At first of course they started experiments and measurements and later they analysed. Now they have a lot of valid models for RF, but still they are evaluating them by newer results.

In FSO we are 70 years behind, the LASER were developed in 1960. First single scientists started to work on FSO 30 years ago, and we know the first scientists in our WG3 started with FSO 15 or 20 years ago. Since the last 10 years this technology is becoming more important and much more scientists working in this field. That is also one reason, why we have still only a few models, which we can use for FSO. Additional we have different models for different atmospheric influences. As example in the FSO-field we have models for the attenuation (from fog, clouds, rain etc.) and we have additional models for atmospheric turbulences. The different models are necessary, because the atmospheric turbulences (the so called scintillations) have completely different influences on the transmitted light, they are disturbing the wave-front and they also cause beam-wandering or beam-spreading).

Before we are looking into details, we want to show the reader that channel-modelling is always an important technology and method to improve the transmission technologies and to counter-act to atmospheric influences. But to compare between RF and FSO, we have to clarify that FSO scientists have to make a lot of further experiments and investigations, before they can have a general valid channel model. For that reason the WG3 has done much more measurements and experiments compared to the RF WG's. Our report consists mainly on experiments (including FSO-test-beds) and analysing data to validate and improve existing channel models before generating new models.

## 1.2 Principles and Properties of Free Space Optics

FSO-links through the troposphere are mainly influenced by weather conditions. Therefore, some important characteristics of the atmosphere have to be discussed before describing the optical wireless systems in more detail. The lowest part of the atmosphere up to 10 km above the Earth's surface is called the troposphere or the weather sphere. It has a varying refraction index, which is dependent on the height above the Earth's surface. Normally the refraction index decrease with the height, but at weather inversion situations there is a different relationship. Atmospheric conditions degrade laser communications through the atmosphere in two ways. First, the atmosphere acts as a variable attenuator between the transmitting and receiving terminals. Second, a free space laser link is subjected to scintillations. Attenuation is caused by the weather conditions along the transmission path. Generally, there is low atmospheric attenuation during clear days and high attenuation during foggy days. Rain does not influence optical transmissions heavily, because raindrops have the size of a few millimeters and are large compared to laser wavelengths (1.5 microns) and thus cause minimal scattering of the laser energy. Furthermore, water has minimal absorption at a 1550 nm laser wavelength. Therefore, it is not surprising that the optical transmission is not heavily impacted by rain (only about 3 dB/km). Similarly it is not astonishing that optical transmission is impacted dramatically by heavy fog (30 dB/km), because the fog aerosols have a comparable size as the used wavelengths.

### 1.3 Different Types of FSO-systems

Different FSO-systems for various applications have been developed by research groups and industry. In order to describe the different technologies implemented in available systems, we simplify the concepts to some important elements. Such a simplified scheme for a typical FSO unit for data transmission is shown in Figure 1. On the basis of this concept, three types of system design can be distinguished, each as a compromise regarding reliable operation and installation costs for certain applications and distances. For the first type of systems, available standard components are combined to build cost-effective solutions. Generally, the value of the beam divergence is high (up to 60 mrad) and allows an easy alignment for the user without the need for a telescope. All elements including the optics do not require as high precision as compared to the other two approaches, allowing higher tolerances at fabrication, and allowing the use of simple mounts at installation. Suitable distances for high availability operation are limited up to 300 meters because of the wide beam angle (and depending on local climate).

Systems of the second type take advantage of a collimated beam as much as possible without active alignment, which leads to a beam divergence of about 2 to 6 mrad. To achieve the same intensity at the receiver in longer distance, the concept requires precise optical components being carefully adjusted, and telescopes or adjustment procedures are needed for the installation (Figure 2 b). These first two types of FSO systems are mainly used for short range terrestrial applications and especially for Last-mile access. For increasing the intensity at the receiver and to overcome atmospheric turbulences (scintillation) caused by variation of the refraction index, more than one transmitter- and / or receiver-units are used in one housing.

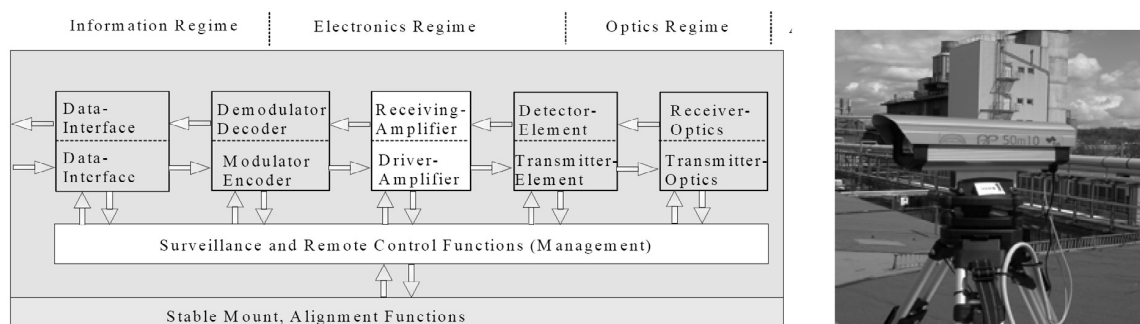


Figure 1. a) Simplified scheme of the elements of an FSO unit, b) a type 1 system for ranges of several 100m.

The third category contains the sophisticated solutions, including strategies to extend the distance for reliable operation as much as possible. The beam divergence reaches values less than 1 mrad leading to low geometrical losses, concentrating all incoming light on a small area around the receiver. To compensate building sway and deviation, automatic tracking of

the beam is implemented, adaptive optics may help to compensate atmospheric fluctuations or allow higher optical output over a large area. Using Free Space Optics-systems from all three categories, various communication links or networks can be realized, including terrestrial FSO (between buildings, hospitals, campus), horizontal and slant paths, air-borne and space communications (between aircraft, unmanned aerial vehicles (UAV), high altitude platforms (HAP) and satellites). By connecting FSO-links and networks to the “Backbone” realized with optical fibers, the FSO-networks and -links can be seen as parts of a global all optical network around the world (figure 2 a).

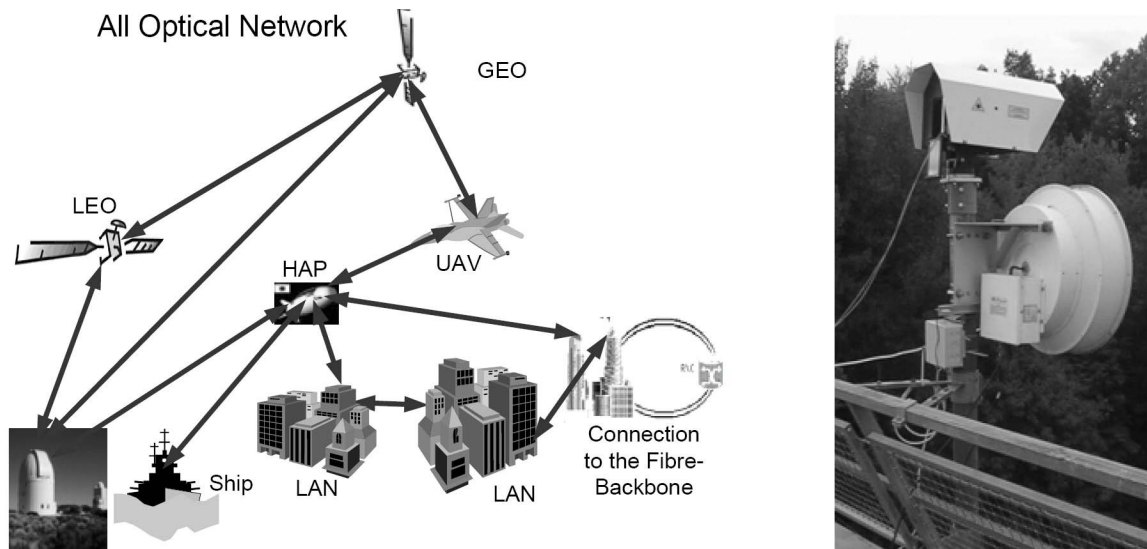


Figure 2. a) FSO as part of an “All Optical Network”, b) a type 2 system (multi beam) for ranges up to 2000 m.

## 2 MAIN IMPORTANT WEATHER PARAMETERS FOR ANALYSING THE FSO-CHANNEL

(Ondrej Fiser, Vladimir Brazda, Zuzana Chladova, Jaroslav Svoboda, Petr Pesice)

### 2.1 Overview

This part is dealing with the description of the most relevant atmospheric phenomena and its parameters being important from the FSO signal propagation point of view. All parameters can be used as input values for the FSO link attenuation estimation. Models predicting atmospheric attenuation help to design system parameters of FSO link taking into consideration atmospheric status.

These phenomena are: fog, cloud, rain, snow, atmospheric turbulence, wind turbulence and water vapour.

### 2.2 Fog, Cloud and Rain Attenuation Based on Scattering Theory

This scattering theory was formulated by Van de Hulst [Van de Hulst, 1957]. For this theory a scattering function must be defined.

Let us consider one isolated droplet particle. Between scattered and incident intensity of light radiance it is valid:

$$\mathbf{E}^s = \mathbf{E}^i \cdot f(D) \cdot r^{-1} \cdot e^{(jk_0 r)} \quad (2.3-1)$$

where:

$\mathbf{E}^s$  is the light radiance of a scattered wave

$\mathbf{E}^i$  is the light radiance of a wave impressing on the fog droplet

$f(D)$  is the forward scattering function [m]

$k_0$  is the wave number

$D$  is the drop or droplet diameter [m]

Following the Van de Hulst derivation a resulting formula for attenuation in homogenous volume filled in by fog droplets is obtained (usual unit is dB/km even if it is concerning a local part of volume; it is called “specific attenuation”):

$$\alpha = 8.686 \cdot 10^3 \cdot \lambda \cdot \text{Im} \int f(D) \cdot N(D) dD \text{ [dB/km]}, \quad (2.2-2)$$

where  $\lambda$  denotes the vacuum wavelength of the optical wave and  $N$  is drop size distribution (DSD) representing the probability density of equivolumetric drop or droplet diameter  $D$  being in the unity volume. The product  $N(D) dD$  gives the number of drops of the diameter between  $D$  and  $D+dD$  per unity volume.

To evaluate the scattering function the Mie scattering technique should be used for the FSO propagation through fog or cloud. Scattering theory for spherical dielectric particles (e.g. droplets) was developed and published by Gustav Mie in 1908 [Mie, 1908]:

$$f_f = \frac{-j \lambda^3}{\pi^3 D^2} \left[ \sum_{n=1}^{\infty} (2n+1)(a_n + b_n) \right]^* \quad (2.2-3)$$

where  $\lambda$  denotes the vacuum wavelength of the optical wave and  $D$  the diameter of the spherical drops, \* is symbol for the conjugate imaginary numbers. The coefficients  $a_n$  and  $b_n$  according to Mie depend on the complex relative refractivity  $\epsilon_r = \epsilon / \epsilon_0$  of the material (rain, fog or rain water in our case) and on the diameter  $D$  of the scattering sphere.

$a_n, b_n$  are the Mie's coefficient being dependent on the complex refractivity index of the droplet water and on the diameter  $D$  of the scattering drop or droplet. Its evaluation need not to be very complicated, see [Fiser, 1993]. The question of numbers of series terms to evaluate approximately the infinity series (3) emerged an unexpected serious problem. In the case of rain and microwaves it is sufficient to be limited in not more than 10 terms of series. But in the case of light (FSO links) and fog droplets hundreds terms must be used.

### 2.2.1 Classical Drop Size Regions for Light Scattering Approach

The radius to wavelength regions for well known backward scattering (used in meteorological radar areas) we have taken picture from [Wolff, 1997]. It is dependence of efficiency factor  $Q$  defined as ratio of scattering cross-section  $\sigma$  (proportional to scattering energy backwards to the transmitter) of a particle and geometric cross-section of a particle to the size parameter  $x$ , which is given as

$$x = \frac{\pi D}{\lambda}, \quad (2.2-4)$$

where  $D$  is diameter of a particle and  $\lambda$  is a used wavelength.

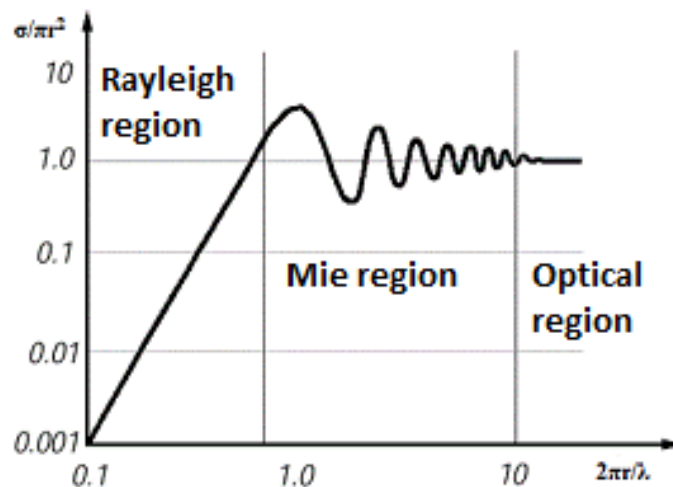


Figure 2.2-1: The backward efficiency factor,  $r$  (particle radius) =  $D/2$  [Wolff, 1997]

Fig. 2.2-1 is divided into 3 regions. Two of them (Rayleigh and Optical regions) are very simply evaluable.

Scattering cross section  $\sigma$  is equal to the geometric one in the Optical region ( $x > 10$ ). Enumeration of scattering cross section in region where the size of particle is similar to the wavelength is much more complicated (Mie region). So called Mie solution [Mie, 1908] based on analytical infinite series solves the calculation for the full range of size parameter  $x$ . As it is often confused it should be stressed that Mie region is not Mie scattering - Mie scattering represents the exact scattering solution on perfect sphere for any size parameter  $x$ .

The forward light scattering corresponds to the FSO signal attenuation issues. The dependence of the efficiency factor  $Q$  for forward scattering on the size parameter “ $x$ ” (see Fig. 2.2-2) is (according to our analysis) very similar to the backscatter one (cf. Fig. 2.2-1). Extinction efficiency factor  $Q=Q_{\text{sca}}+Q_{\text{abs}}$  while  $Q_{\text{sca}}$  is expressing the scattering on a drop or droplet and  $Q_{\text{abs}}$  is describing the absorption of the light energy inside the water particle. One can see (Fig. 2) that the scattering is dominant when considering the optical waves.

The Rayleigh region is also found for  $x < 1$ . Optical region is found for  $x > 100$  (it differs from the backward scattering case) and the efficiency factor  $Q$  convergates to the value of 2. This means that the scattering cross-section is doubled in comparison with the geometric one. This fact is also known as the “extinction paradox.”

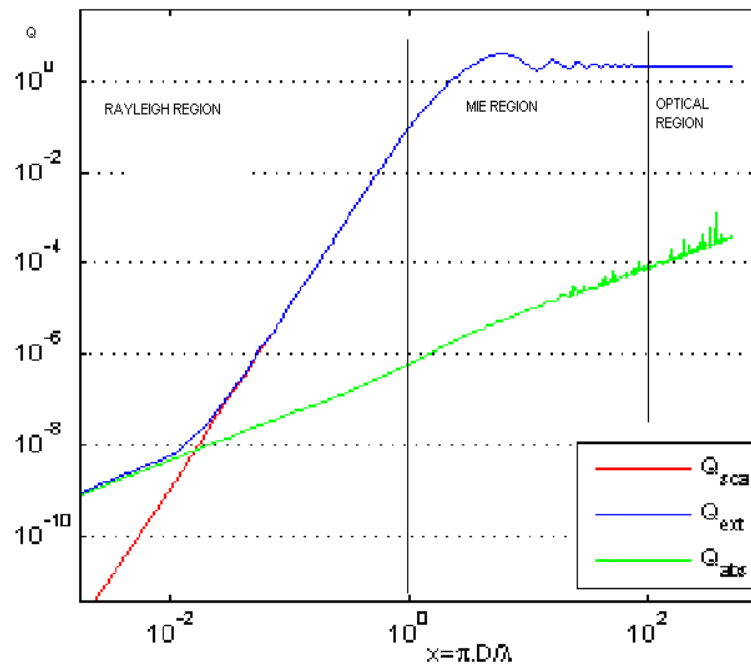


Figure 2.2-2: Course of efficiency factor  $Q(x)$  for forward scattering

Important regions for forward scattering of the light are shown in Table 2.2-1 (under the expression “regions” we can understand possibility of approximate attenuation solutions). One can see that the light attenuation in rain is definitely solvable in the optical region, fog and cloud are in the Mie region. For comparison, we added last column for radio frequency of 120 GHz. We see that rain attenuation for radiowaves is to be solved in Mie region. On the other hand, radiowave attenuation in fog and clouds can be evaluated through simple Rayleigh scattering.

Table 2.2-1. Regions for attenuation computations in rain, fog and clouds for various wavelengths. Yellow colour is the Optical region, white colour represents the Mie region and red colour corresponds to the Rayleigh region.

$\lambda$ [nm]	550	830	1190	1550	250000
<b>D[mm]</b>					
<b>rain</b>	120 GHz				
0,1	571	379	264	203	1,26
0,5	2856	1893	1320	1013	6,28
1	5712	3785	2640	2027	12,57
4	22848	15140	10560	8107	50,27
7	39984	26495	18480	14188	87,96
<b>Fog or cloud</b>					
0,002	11,42	7,57	5,28	4,05	0,03
0,01	57,12	37,85	26,40	20,27	0,13
0,02	114	75,70	52,80	40,54	0,25
0,06	343	227	158	122	0,75

### 2.3 Parameters representing fog and clouds

Fog and clouds are formed by small spherical water particles of a diameter 2 to 60  $\mu\text{m}$ . These particles are lossy dielectrics. The fog (or cloud) particles are causing the FSO signal attenuation due to the absorption as well as due to the signal scattering. To describe absorption and scattering, so called scattering functions are used (see part 2.1.1). As the fog and cloud particles are spherical ones, Mie scattering can be applied [Mie, 1908]. In the case of optical signal and fog droplets nor Rayleigh, nor Optical approach is applicable (see part 2.1.2).

Basically the fog attenuation is computable from scattering and absorption on droplets while knowledge of fog or cloud “**drop size distribution**” is required. Practically, we compute fog attenuation from macroscopic parameters which are “**visibility**” or “**liquid water content**” (LWC). A quite exact relation between visibility and LWC is used, however, this relation can differ in different locations [Fisak et al., 2006].

The DSD in the case of fog can be, for instance, approximated by the Khrghian-Mazin DSD model

$$N(D) = X D^2 e^{-YD} \quad (2.3-1)$$

where X and Y are parameters which can be related to any two DSD moments based on DSD knowledge (measurement, literature). The n-th DSD moment is defined as

$$M_n = \int_0^{\infty} D^n N(D) dD \quad (2.3-2)$$

As the fog droplet size distribution sometimes is not known we approximated a typical fog DSD from following equation (it is based on figures in [Pruppacher, Klett 1980], see also Fig. 2.1-1):

$$N(D) = 500 D^{-3} [\text{cm}^{-3} \mu\text{m}^{-1}] \quad (2.3-3)$$

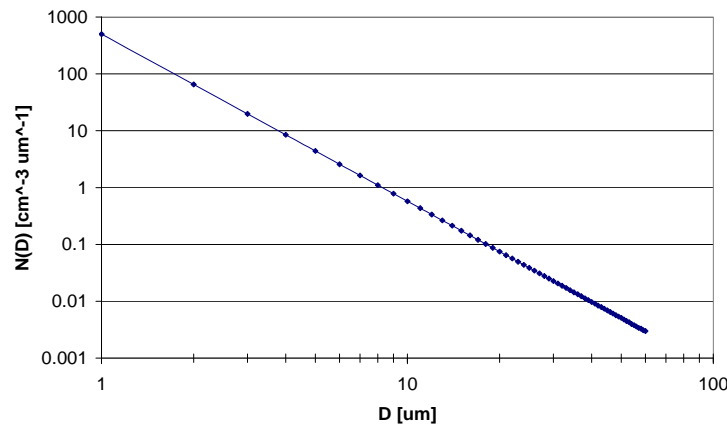


Figure 2.3-1: Approximation of typical fog DSD

To evaluate attenuation of fog or cloud droplets a refractivity index of water is needed. As the refractivity index is wavelength of pertinent signal dependent, we must carefully look for right formulas.

Next table shows the refractivity index for most used FSO link wavelengths:

Table 2.3-1. Refractivity index

Wavelength [nm]	Refractivity index	
	Real part	Imaginary part
830	1,325	2,04 E-07
850	1,325	2,96 E-07
1550	1,311	1,34 E-04

### 2.3.1 Visibility- important and usual fog parameter

The meteorological visibility by day, and meteorological visibility at night are defined as the greatest distance at which a black object of suitable dimensions (located on the ground) can be seen and recognized when observed against the horizon sky during daylight, or could be seen and recognized during the night, if the general illumination were raised to the normal daylight level [Meulen, 1992].

In the FSO link practice, we understand visibility as the meteorological optical range (MOR), is that the length of path in the atmosphere required to reduce the luminous flux in a collimated beam from an incandescent lamp, at a colour temperature of 2700 K, to 5 percent of its original value, the luminous flux being evaluated by means of the photometric luminosity function of the International Commission on Illumination (exact definition taken from [Meulen, 1992]).

The most common devices that are used to measure visibility are the series of optical sensors PWD (Present Weather Detector) from the Finnish company Vaisala [VAISALA, 2011]. The visibility can be determined also through the liquid water content (LWC) or subjectively (not preferred).

Present weather detectors (PWD) determine visibility (meteorological optical range) through the optical signal attenuation and/or bi-static reflection (from atmospheric particles).

Also methods determining **visibility from camera pictures** have been developed. One of the options is an analysis of panoramic picture capturing various objects with known distance. This technique is based on edge detection of the objects [Bäumer et al., 2008]. Another similar system was published in [Colvero et al., 2005]. Determination of visibility in this paper is based on Beer-Lambert-Boguer's law resulting in following formula:

$$V = \frac{\ln(0.02)}{\ln\left(\frac{C}{C_0}\right)} \cdot x \quad 2.3-4)$$

where  $C$  is a contrast of ideal black and white target at the distance  $x$ . The contrast is measured by digital CCD camera.  $C_0$  is an intrinsic contrast measured at maximum visibility conditions close to the target. This system is cheap and can determine average visibility between two given points – optical transmitter and receiver, which solves problem with inhomogeneity of fog.

## 2.4 Rain

Rain consists of water drops of a diameter 0.2 to 7 mm. Smaller drops are of the spherical shape, the drops of diameter above 1mm are spherical, the greatest ones are oblate spheroids. The FSO signal attenuation is caused by the rain drop absorption as well as by the signal scattering. The rain drops are in the “Optical region” from the FSO signal scattering point of view (cf. part 2.1.2).

Rain attenuation of the FSO signal can be computed from the same formula of Van de Hulst as it is shown in chapter 2.1.1 describing the fog and cloud attenuation (equation 2). The same refractivity index as for fog and cloud droplets is needed (see Tab. 2). As the rain drops are not of the exact spherical shape, the Mie method to derive scattering functions can be used as an approximation only. The more exact techniques like Fredholm integral method, point matching, perturbation method (and others) should be preferred.

The scattering properties of rain drops (and FSO link attenuation through this) are dependent on wavelength (slightly) and polarization of incident wave, shape of drops (see Fig. 4) and on the rain drop's size. Since the rain drop's shape is not the spherical one (except by approximation used by simple models), its size is expressed in equivolumetric radiuses, see [Pruppacher, Pitter, 1971].

It is also known that rain drops greater than 7 mm are not very stable and split themselves.

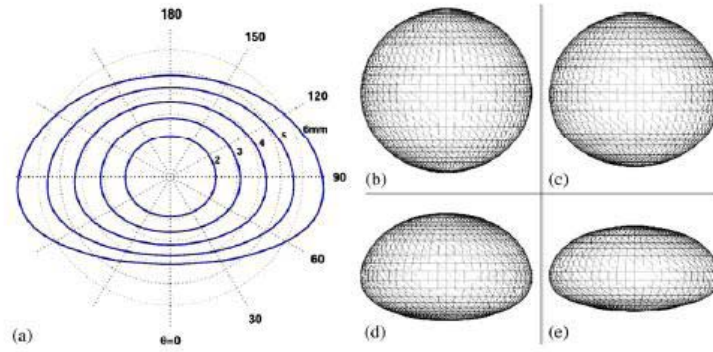


Figure 2.4-1: Shape of rain drops. Small ones are more spherical

### 2.4.1 DSD

Rain drop size distribution plays an important role to determine radio wave propagation through rain volume and also an important role in Free Space Optics (FSO) signal propagation modelling.

For the computation of rain attenuation as well as of the rain depolarization the value of the product  $\{\text{Im } f(D) N(D)\}$  is important. This product is integrated with respect to the equivolumetric diameter  $\{D\}$ ;  $f(D)$  is the complex scattering function and  $N(D)$  is the pertinent value of the rain drop spectrum (DSD), see part 2.2.

To describe DSD of rain mathematically, the Gamma DSD model should be preferred to the exponential one because of huge role of small rain drops. Therefore we do not recommend utilisation of the well known Marshall-Palmer DSD. Also the two main rain types (convective and stratiform) should be distinguished.

The equation (2.4-1) expresses the Gamma model of rain drop size distribution function (DSD)

$$N(D) = N_0 D^\mu \exp(-\lambda D) \quad (2.4-1)$$

where

$D$  [mm] is the rain drop diameter

$N(D)$  [ $\text{m}^{-3} \text{mm}^{-1-\mu}$ ] is the number of drops per unit volume per drop diameter interval ( $D$  to  $D+dD$ )

$N_0$  [ $\text{m}^{-3} \text{mm}^{-1-\mu}$ ] is the intercept parameter of DSD

$\lambda$  [ $\text{mm}^{-1}$ ] is the slope parameter (not wave length in this case)

$\mu$  [-] is shape of the DSD

Examples of numerical values of parameters of Gamma DSD are in Tab. 2.4-1 [Iguchi, 1999].

Table 2.4-1. Examples of numerical values of the Gamma DSD model parameters where  $R$  is the rain rate in [mm/h]. These example is for tropical region.

Gamma	No	$\lambda$	$\mu$
Rain type	mm-3- $\mu$ m-3	mm-1	-
Convective	$6.29E5 \cdot R^{-0.416}$	$8.35R^{-0.185}$	3
Stratiform	$2.57E4 \cdot R^{0.012}$	$5.5R^{-0.129}$	3

It must be stressed that it is very convenient to characterise the DSD in the dependence on macroscopic parameter - rain rate  $R$ . It was done in example in Tab 3.

Fig. 2.4-2 shows a specific attenuation computed by equation (2.2-2) for a wide spectrum of wavelengths with rain rate as a parameter. The two vertical lines define a spectrum used in free space optics – 550 nm to 1550 nm. It is obvious that attenuation practically doesn't depend on a wavelength in this spectrum. It depends only on a rain rate.

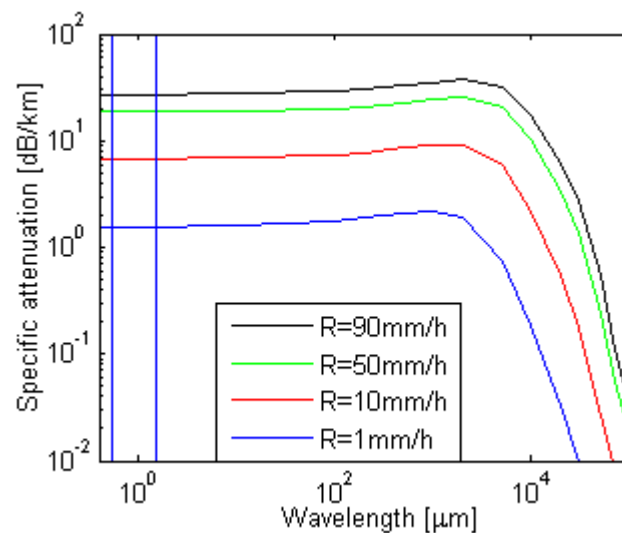


Figure 2.4-2: Frequency dependence of specific attenuation due to rain computed by (2) with highlighted spectrum lines of 550nm and 1550nm.

For practical FSO attenuation through rain the Carbonneau formula is used [Carbonneau, Wisley, 1998]:

$$\alpha_{1,rain} = 1,076 \cdot R^{0.67} \left[ \frac{dB}{km} \right] \quad (2.4-10)$$

In Fig. 2.4-3 we compare this formula with other formula we derived from the Mie scattering approach, where blue points represent averaged scatterplot derived from our three years measurement (FSO experimental link on the Milesovka observatory, IAP, Czech Republic). It is obvious that rain attenuation is low on 1550 nm wavelength.

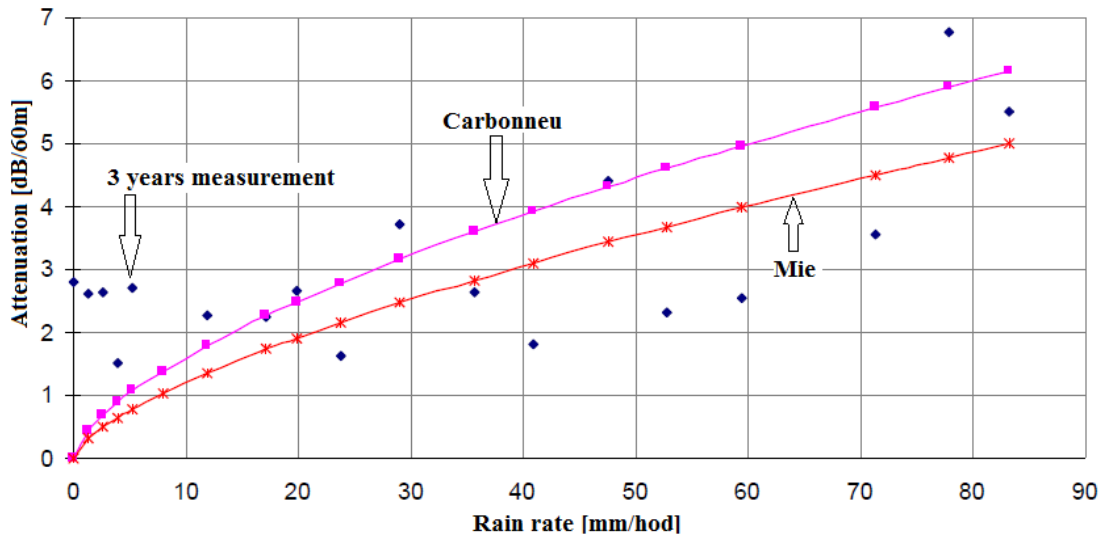


Figure 2.4-3: FSO link rain attenuation after Mie and Carbonneau theory and averaged scatterplot points (blue) derived from three years measurement.

To prove the weakness of the dependence rain attenuation-wavelength we computed the differences between specific rain attenuation values on 1550 nm and 850 nm. The results are obvious from Fig. 2.4-4. One can see that the difference is negligible.

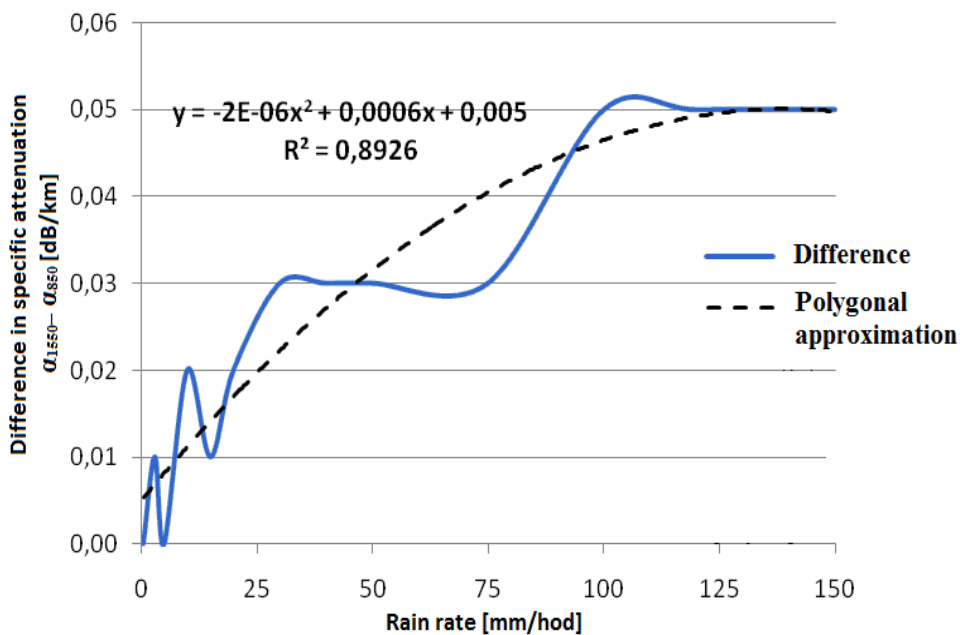


Figure 2.4-4: Computed differences between specific rain attenuation values on 1550 nm and 850 nm

### 2.4.2 Rain rate –what is it?

Rain rate is related with the DSD through next equation:

$$R = \frac{\pi}{6} \int_0^{\infty} N(D)D^3v(D)dD \text{ (mm h}^{-1}\text{)}, \tag{2.4-11}$$

where  $v(D)$  is the terminal fall rain drop velocity

To understand the rain rate it is advantageous to be familiar with the quantity “Rain amount.” Rain amount  $H$  is columnar height of rain water having been caught by a sampling container of constant cross section for certain time period (in meteorology, it is 24, 12 or 6 hours usually). Rain amount is widely measured by meteorologists. For propagation purposes it cannot be used directly. Approximate models are used to convert 6-hours statistics into rain rate statistics, for example see Rice-Holmberg model [Rice, Holmberg, 1973].

Rain rate is measured by meteorologists as well as by propagation people. It is desired to agree with meteorologists the method of data format as meteorologists tends to round rain rate data into longer integration periods (for propagation purposes one minute integration periods is a standard, 10 sec would be slightly better).

Rain rate  $R$  is derived from the measurement of the time response of rain amount  $H(t)$ . It is defined by the following equation:

$$R = dH/dt \quad 2.4-12)$$

This rain rate can be called "instantaneous rain rate." The rain intensity that has the integration time  $x$  minutes i.e.  $R_x$ , is also called “the (average)  $x$  - minute rain intensity.” It is defined by the following equation:

$$R_x \approx 60 \cdot \Delta H / x \quad 2.4-13)$$

where  $R_x$  is the rain intensity (mm/h),  $\Delta H$  (or  $dH$ ) is the rainfall amount increment (mm) and  $x$  is the integration time (e.g. one minute) which can be replaced by  $\Delta t$ . In propagation, the standard integration time ( $x$ ) is one minute usually.

In this equation, the  $\Delta H$  (or  $dH$ ) is the rainfall amount increment (mm) within the time interval of  $x$  minutes. One must understand: the longer integration time  $x$  the higher inaccuracy of derived “instantaneous” rain intensities (intensities of very short integration time). Strictly said, we can speak about average rain intensity in the  $x$  time interval only.

*Remark: In the Tipping-bucket rain gauge case  $\Delta H$  is fixed to 0.1 (or 0.2) mm depending on the mechanical construction of rain gauge.*

## 2.5 Snow Attenuation on FSO links

Snow is a precipitation in the form of crystalline water ice, consisting of snowflakes. Snowflakes come in a variety of sizes and shapes. A non-aggregated snowflake often exhibits six-fold radial symmetry. Complex shapes emerge as the flake moves through differing temperature and humidity regimes, such that individual snowflakes are nearly unique in structure. Types which fall in the form of a ball due to melting and refreezing, rather than a flake, are known as hail, ice pellets or snow grains.

Additional attenuation of atmospheric transmission media can be caused by snow. Absorption as well as scattering is influencing the attenuation like in the rain case. Snow attenuation  $\alpha_{\text{snow}}$  (in dB/km) is a function of snowfall rate and it is usually given by the relation

$$\alpha_{\text{snow}} = a S^b, \quad (2.5-1)$$

where  $S$  is the snowfall rate (in mm/h), and coefficients  $a$  and  $b$  are functions of wavelength, given by the following relations

$$\text{Wet snow} \quad a = 0.0001023 \cdot \lambda_{mm} + 3.7855466 \quad b = 0.72$$

$$\text{Dry snow} \quad a = 0.0000542 \cdot \lambda_{mm} + 5.4958776 \quad b = 1.38$$

## 2.6 Wind

Wind is generally the flow of gases on a large scale. On Earth, wind consists of the bulk movement of air. In meteorology, winds are often referred to according to their strength, and the direction from which the wind is blowing. Wind occurs on a range of scales, from thunderstorm flows lasting tens of minutes, to local breezes generated by heating of land surfaces and lasting a few hours, to global winds resulting from the difference in absorption of solar energy between the climate zones on Earth. The two main causes of large-scale atmospheric circulation are the differential heating between the equator and the poles, and the rotation of the planet (Coriolis effect).

We selected next wind parameters which could influence the FSO attenuation [Stull, 1991]. The selected characteristics of wind are listed in Table 4. Here  $u$ ,  $v$  and  $w$  are  $x$ -,  $z$ - and  $y$ - axis components of the wind speed vector  $v$  and  $g$  is the horizontal wind speed:

$$g = \sqrt{(u^2 + v^2)} \quad (2.6-1)$$

Table 2.6-1. Selected wind parameters

Wind parameter	Symbol
mean horizontal wind speed [m/s]	E(g)
intensity of turbulence (2D)	I(2D)
vertical turbulent heat flow	$W_z$
turbulent energy	$E_T$
Std. dev. $u$	D(u)
Std. dev. $v$	D(v)
Std. dev. $w$	D(w)
Std. dev. T (sonic temperature)	D(T)
Std. dev. of absolute value of 2D wind speed „g“	D(g)
mean 3D wind speed	E(v)
intensity of turbulence (3D)	I(3D)

Examples of formulas for chosen wind parameters are the following ones:

$$\text{Intensity of turbulence (2D)} \quad I(2D) = \frac{\sqrt{\frac{1}{N} \sum (g - \bar{g})^2}}{\bar{g}} \quad (2.6-2)$$

$$\text{Vertical turbulent heat flow} \quad W_z = \frac{1}{N} \sum ((w - \bar{w}) * (T - \bar{T})) \quad (2.6-3)$$

$$\text{Turbulent energy} \quad E_T = 0.5 * \frac{1}{N} \sum ((u - \bar{u})^2 + (v - \bar{v})^2 + (w - \bar{w})^2) \quad (2.6-4)$$

$$I(3D) = \frac{\sqrt{((u - \bar{u})^2 + ((v - \bar{v})^2 + (w - \bar{w})^2)}}{\sqrt{N} \sqrt{(\bar{u})^2 + (\bar{v})^2 + (\bar{w})^2}} \quad (2.6-5)$$

Intensity of turbulence (3D)

Intensity of 3D turbulence after equation (2.6-5) is our definition.

For wind behaviour illustration, here are figures 2.6-1 - 4 showing long term (5 month) diurnal variation of wind speed and wind turbulence. It is obvious that the wind speed is lowest at noon while maxima are reached close to midnight. The intensity of turbulence is maximal at noon, minimum was observed at midnight.

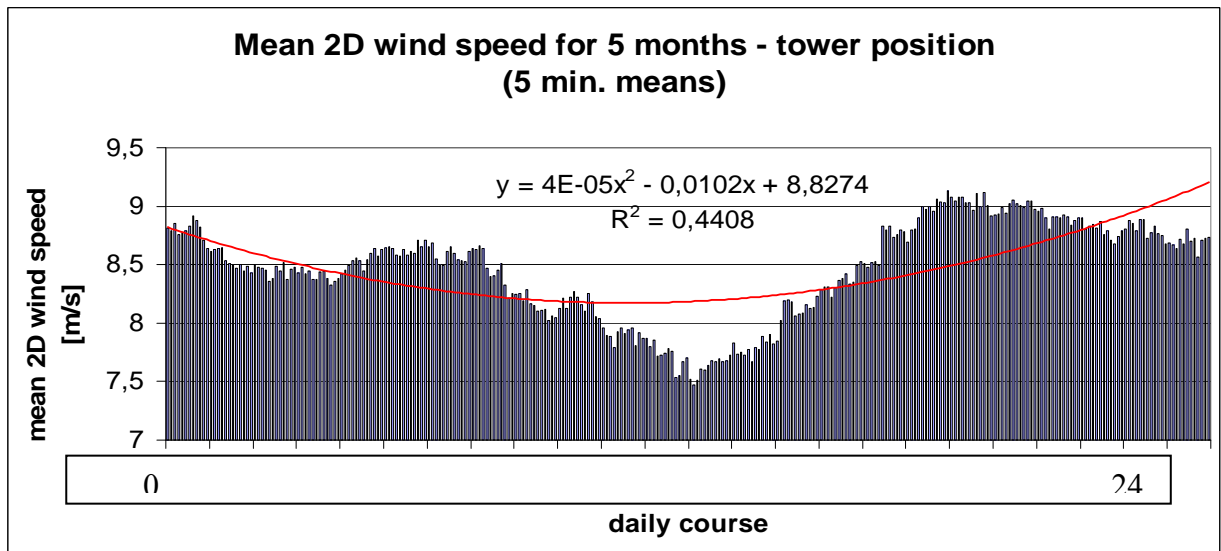


Figure 2.6-1: Daily course of mean 2D wind speed for 5 months at the tower position. 5 min. means were used.

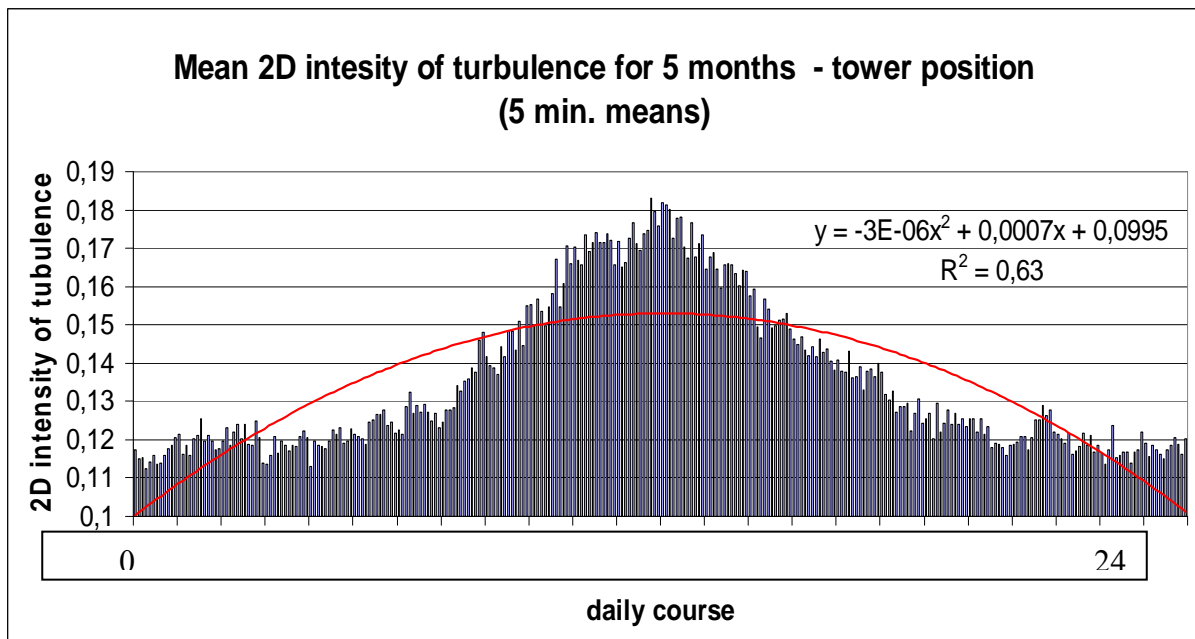


Figure 2.6-2: Daily course of mean 2D intensity of turbulence for 5 months at the tower position.

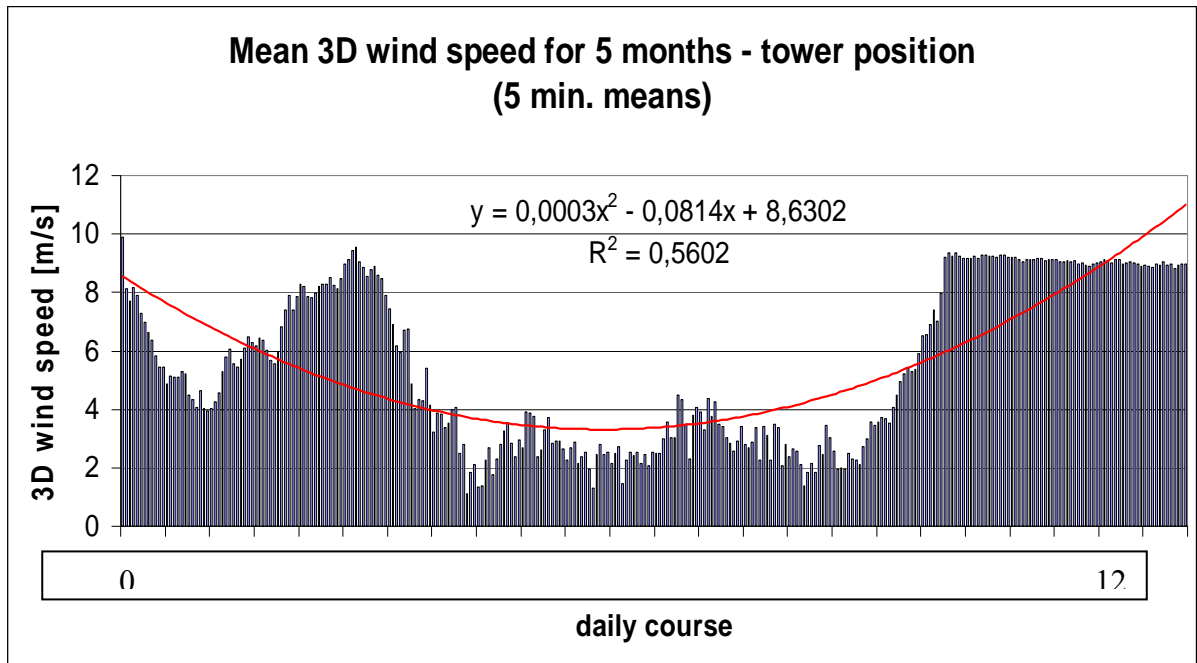


Figure 2.6-3: Daily course of mean 3D wind speed for 5 months at the tower position.

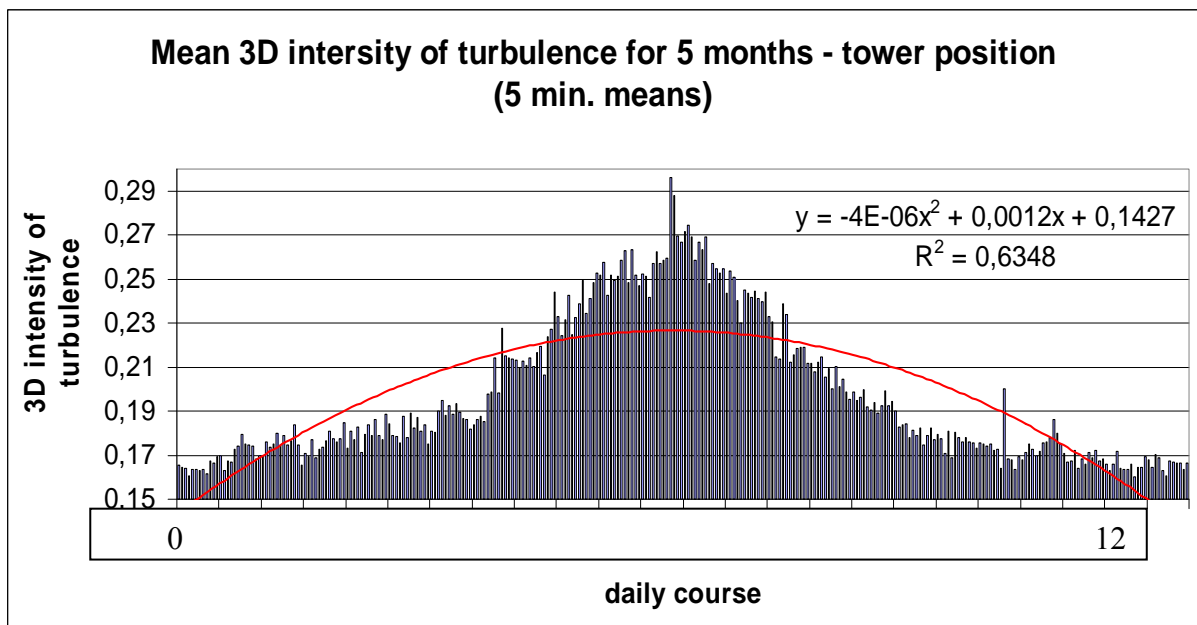


Figure 2.6-4: Daily course of mean 3D intensity of turbulence for 5 months at the tower position.

Also orographical phenomena play role in the case of wind parameters values, especially the vertical component of the wind speed vector is dependent on the vicinity.

## 2.7 Atmospheric turbulence

Atmospheric turbulence is caused by the air refractivity index inhomogeneity. This inhomogeneity is causing the redistribution of the FSO signal energy. Attenuation due to the atmospheric turbulence  $\alpha_{\text{turb}}$  can be estimated from the Rytov formula:

$$\alpha_{\text{turb}} = 2 \cdot \sqrt{23.17 \cdot k^{7/6} \cdot C_n^2 \cdot L^{11/6}} \quad (2.7-1)$$

where  $k$  is the wave number,  $C_n$  is the structure parameter of refractive index, and  $L$  represents the distance between transmitter and receiver.

Structure index  $C_n^2$  is defined through next equation

$$E(n_1 - n_2)^2 = C_n^2 r^{\frac{2}{3}} \quad (2.7-2)$$

where  $r$  is distance between measurement points of refractive index of values,  $n_1$  and  $n_2$  are refractive indexes of atmosphere in these two points and operator  $E$  represents the mean value. The averaging is performed owing the chosen time period, its length is a question, we use one minute. The formulas for the air refractivity index are in the Annex 1.

## 2.8 Summary

This chapter describes most important atmospheric parameters from the FSO link attenuation point of view. The fog is the worst phenomenon which attenuates the optical signal of the order of hundreds dB per km. Rain is causing lower attenuation of the order of tens dB per km. On the other hand, wind as well as atmospheric turbulences play lower role in the attenuation. The attenuation due to water vapour is quite negligible and is not described in this chapter.

## 2.9 References

[Bäumer et al., 2008] Bäumer D., Versick S., Vogel B. “Determination of the visibility using a digital panorama camera”, *Atmospheric Environment*, Vol. 42, Iss. 11, pp. 2593-2602, April 2008

[Carbonneau, Wisley, 1998] Carbonneau T. and D. Wisley, “Opportunities and challenges for optical wireless; the competitive advantage of free space telecommunications links in today’s crowded market place”, in *SPIE Conference on Optical Wireless Communications*, 1998, pp. 119–128.

[Colvero et al., 2005] Colvero C.P., Cordeiro M.C.R., von der Weid J.P., New Proposal for Real Time Measurements of Visibility and Signal Levels in Free Space Optical Systems, *Microwave and Optoelectronics*, SBMO/IEEE MTT-S International Conference, pp. 344 – 347, 2005.

[Fisak et al., 2006] Fisak, J., D. Rezacova, J. Mattanen. “Calculated and measured values of liquid water content in clean and polluted environments.” *Studia Geophysica et Geodaetica*. 2006, Vol. 50, No. 1, pp. 121-130. ISSN 0039-3169. DOI: 10.1007/s11200-006-0006-z.

[Fiser, 1993] Fiser, O. “A simple generator of forward scattering functions on spherical dielectrics.” *Radioengineering*. April 1993, vol. 2, No. 1, pp. 21-22. 1993.

[Iguchi, 1999], Iguchi T., personal communication.

[Kim et al. 2000] Kim I. I., Mc Arthur B. and Korevaar E., "Comparison of laser beam propagation at 785 nm and 1550 nm in fog and haze for optical wireless communications," Proc. of SPIE, vol. 4214, pp. 26-37, Boston, 2000

[Meulen, 1992] J.P. van der Meulen, 'Visibility measuring instruments: Differences between scatterometers and transmissometers'. Papers Presented at the WMO Technical conference on Instruments and Methods of Observation (TECO-92) (Vienna, Austria, 11-15 May 1992), Instruments and Observing Methods Report , No. 49, WMO/TD-No. 462, Geneva.

[Mie, 1908] G. Mie, „Beiträge zur Optik trüber Medien, speziell kolloidaler Metallösungen.“ Annalen der Physik, Vierte Folge, 25(3), pp. 377-445, 1908.

[Pruppacher, Klett 1980] H. Pruppacher, J.D. Klett "Microphysics of Clouds and Precipitation" Boston, D.Reidel Publishing Company, Boston,1980", (picture 2.16)

[Pruppacher, Pitter, 1971] Pruppacher H.R., Pitter R.L. "A semi-empirical determination of the shape of cloud and rain drops," J. Atmos. Sci., vol. 28, pp. 86-94, 1971

[Rice, Holmberg, 1973] Rice, P., Holmberg, N. "Cumulative Time Statistics of Surface-Point Rainfall Rates," Communications, IEEE Transactions on, vol.21, no.10, pp. 1131- 1136, Oct 1973

[Stull, 1991] Stull, R.B. "An Introduction to Boundary Layer Meteorology", Kluwer Academic Publisher, 1991

[Van de Hulst, 1957] Van de Hulst, "Light Scattering by Small particles." New York, J.Wiley pub, 1957.

[Wolff, 1997] Wolff, Ch. "Radartutorial.eu: Rayleigh- versus Mie- Scattering." Available on WWW: <<http://www.radartutorial.eu/18.explanations/ex22.en.html>>. 1997

## Annex 1: Formulas to compute air refractivity index $n$ in visible and infrared region

In this study, we have used next formulas to compute the air refractivity index from

Stone Jr, J. A. Zimmerman, J. H. "Index of Refraction of Air", The National Institute of Standards and Technology (NIST), USA, February 16, 2001

### Part 1

$$n = n_{tp} - 10^{-10}[(292.75)/(t + 273.15)] \times [3.7345 - 0.0401S] \times p_v$$

$$n_{tp} = 1 + p(n_s - 1)X/D$$

$$X = [1 + 10^{-8}(E - Ft)p]/(1 + Gt)$$

$$n_s = 1 + 10^{-8}[A + B/(130 - S) + C/(38.9 - S)]$$

$$S = 1/\lambda^2$$

where  $n$  is the air refractivity index,  $\lambda$  is the wavelength in micrometers and  $p$  is the air pressure in Pascal.

For  $p_v$  see Part 2:

### Part 2

$$p_v = (RH/100) \times p_{sv}(t)$$

$$p_{sv}(t) = 10^6 (2C/X)^4$$

$$X = -B + \sqrt{B^2 - 4AC}$$

$$A = \Omega^2 + K_1\Omega + K_2$$

$$B = K_3\Omega^2 + K_4\Omega + K_5$$

$$C = K_6\Omega^2 + K_7\Omega + K_8$$

$$\Omega = T + K_9/(T - K_{10})$$

$$T = t + 273.15$$

where  $p_v$  is the water vapour partial pressure in Pascal,  $t$  is the air temperature in °C, RH is the air relative humidity in percents.

Table of constants to compute the air refractivity index in optical and infrared region

<b>ON PART 1:</b>	<b>ON PART 2:</b>
A=8342.54	K1= 1.16705214528E3
B=2406147	K2= -7.24213167032E5
C=15998	K3= -1.70738469401E1
D=96095.43	K4= 1.20208247025E4
E=0.601	K5= -3.23255503223E6
F=0.00972	K6= 1.49151086135E1
G=0.003661	K7= -4.82326573616E3
	K8= 4.05113405421E5
	K9=-2.38555575678E-1
	K10=6.50175348448E2

### **3 FOG MEASUREMENTS ON FSO IN NICE AND GRAZ (STARTED IN COST 270 AND SATNEX)**

(Sajid Sheikh Muhammad, Kiran Fatima, Erich Leitgeb)

#### **3.1 Overview**

Currently, worldwide a lot of distributors offer optical free space links and in international research co-operations Optical Wireless systems are investigated, developed and evaluated for manufacturers, telephone companies and providers. Optical links are projected and calculated in regard to range, bandwidth, traffic and weather (link budget, margin). The main emphasis of the research work is to increase the channel capacity, reliability and availability of Optical Free Space Links as important part of the “next generation” future network. With the current optical backhauls providing as high a data rate as 40 Gbps, the end user is also looking for and demanding higher bandwidths to their personal computers or laptops. FSO is the technology to provide the end users with the data rates they can be satisfied with, at present, touching up to 1 Gbps [1]. Free Space Optics, thus forms, a core component of the evolving optical broadband network and will prove to be a technology of high importance in the coming years, particularly in combination with RF-links in hybrid systems.

#### **3.2 Availability Measurement**

The first commercial system which we have installed uses multiple transmitter and receiver optics technology at 850 nm wavelength and transmits up to 155 Mbit/s over a comparatively long link distance of 2.7 km, which allowed us to study several kinds of weather influence. The system was used for different measurements, including a one-year trial with an SDH fiber optic network analyzer and a hybrid 40 GHz / FSO combination for wireless Ethernet connection. Figure 3.2-1 shows the resulting data on link availability of all measurements combined, covering 4 years of data ranging from 2000 to 2004.

The seasonal variation of availability, as well as the differences from one year to another can be seen clearly. The availability, first averaged over one month for several years and then averaged over the year, was 93.58 %, with a minimum of 79.52 % in December 2000 and a maximum of 100 % for some months in spring and summer. The reason for a broken link is increased attenuation in the atmosphere, mainly caused by haze and fog. For a better understanding, some parameters of the link power budget need to be considered.

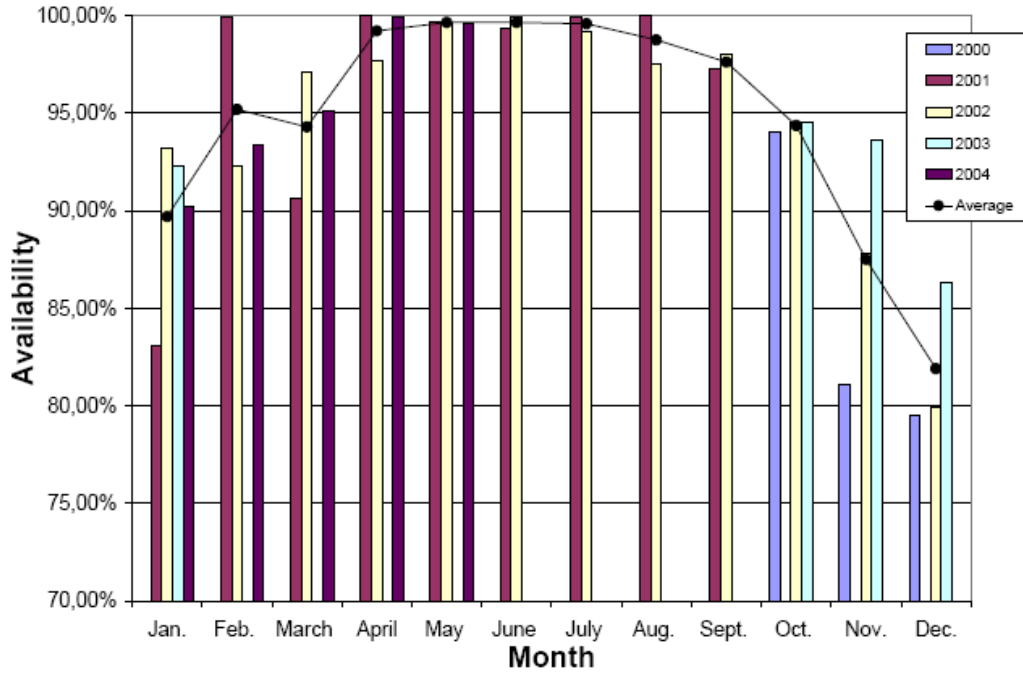


Figure 3.2-1: Availability of a 2.7 km link over four years.

Fig

The system properties can be expressed by the (virtual) system power figure  $P_{SYS}$  [1],

$$P_{SYS} = P_{TX} + G_{TX} + A_{RX} - \sum a_{SYS} \tag{3.2-1}$$

In this expression  $P_{TX}$  represents the total average optical output power in dBm,  $G_{TX}$  represents the geometrical transmitter gain in dB,  $A_{RX}$  represents the receiver area in dB (m) and  $\sum a_{SYS}$  summarizes all system losses like absorption and reflection at lenses or misalignment.

The geometrical transmitter gain can be derived from beam divergence full angle  $\alpha$  by

$$G_{TX}(dB) = 10 \log \left( \frac{4\pi}{2\pi \left( 1 - \cos \frac{\alpha}{2} \right)} \right) \tag{3.2-2}$$

For circular receiver optics the receiver area is calculated by

$$A_{RX} = 20 \log (R_{OPTIC}) \quad 3.2-3.$$

Neglecting atmospheric attenuation the received average optical power  $P_{RX}$  after the link path distance  $d_L$  (m) is [1]

$$P_{RX} = P_{SYS} - D_L = P_{SYS} - 20 \log (2d_L) \quad 3.2-4.$$

The margin  $M_{SYS}$  (in dB) for an installed system to compensate all atmospheric path losses is then

$$M_{SYS} = P_{SYS} - P_{RS} - D_L \quad 3.2-5.$$

where  $P_{RS}$  is the receiver sensitivity limit for correct operation. Finally the specific link margin  $M_{SPEC}$  (in dB/km) dependent on link path distance  $d_L$  (in m) is given by [1]

$$M_{SPEC}(d_L) = \frac{1000m}{d_L} \cdot M_{SYS} = \frac{1000m}{d_L} \cdot [P_{SYS} - P_{RS} - 20 \log (2d_L)] \quad 3.2-6.$$

For our system, the power margin over 2.7 km link distance is approximately 20 dB, so the specific margin of the installation is about 7 dB/km, which allows to compensate an equal atmospheric specific attenuation.

In the winter half year of 2003/04 we could compare three different installations in Graz over seven months. In addition to the very long link, two systems developed by our group were installed over short distances. Figure 3.2-2 shows the availabilities which were achieved in an Ethernet application for these cases.

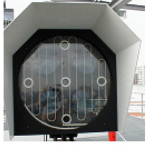
FSO-System	System information	Availability Percentage							
		Oct. 2003	Nov. 2003	Dec. 2003	Jan. 2004	Feb. 2004	March 2004	April 2004	May 2004
	$P_{\text{SYS}} = 53 \text{ dBm}$ $M(0) = 94 \text{ dB}_{\text{opt}}$ $d_L = 2.7 \text{ km}$ $M_{\text{SPEC}} = 7 \text{ dB/km}$	94.53	93.63	86.29	90.25	93.38	95.13	99.94	99.63
	$P_{\text{SYS}} = 13 \text{ dBm}$ $M(0) = 48 \text{ dB}_{\text{opt}}$ $d_L = 80 \text{ m}$ $M_{\text{SPEC}} = 50 \text{ dB/km}$	100	99.34	95.99	94.70	99.47	99.95	99.94	100
	$P_{\text{SYS}} = 27 \text{ dBm}$ $M(0) = 62 \text{ dB}_{\text{opt}}$ $d_L = 80 \text{ m}$ $M_{\text{SPEC}} = 224 \text{ dB/km}$	Not in- stalled	100	100	100	100	100	100	100

Figure 3.2-2: Availability for three different installations during winter and spring.

An availability of 100 % was achieved with 224 dB/km specific margin, while for 50 dB/km still a link failure in 5 % of the time was observed in December and January. This gives evidence that the actual specific attenuation caused by continental fog would be in this range.

### 3.2.1 Weather-influences

Various FSO-systems have been evaluated in regard to different weather conditions. For terrestrial applications it is important to know the influence of the path through the atmosphere, which can be either simulated and modeled or measured over long time periods. The atmospheric path for transmission of a collimated beam of light may be seen as an information channel, to which information is added and on which information gets lost. A variety of effects can be described and several theoretical models are known, but not all of them are relevant to this technology. Once more it is a question of technology used, distance and application to find out relevant impacts on Free Space Optics data transmission.

Ambient light that passes the optics and reaches the detector element, which usually is a PIN-photodiode or an avalanche-photodiode (APD), causes additional current that leads to additional white Gaussian noise in the receiver. Depending on the semiconductor materials and construction principle of the detector there are additional effects as well. Flicker noise produces irregular disturbances which, if we consider data transmission, affects throughput of longer data packets most. At the same time the noise level raises, the impedance of the detector element decreases, which in most receiver principles leads to a level reduction of the received information signal, sometimes also, referred as “burn out”-effect. The dominant source of ambient light for outdoor FSO-Systems is the sun. Therefore the sunlight and the possible positions of the sun have to be considered for

practical applications. For longer FSO-links attenuation is the most critical factor. The contribution of the free atmosphere is comparatively small at the most commonly used wavelengths around 850 and 1550 nanometers. Values for specific attenuation between 0.2 dB/km under very clear atmospheric conditions up to about 10 dB/km due to dust in urban regions are reasonable. Far more critical is the impact of the weather situation. It has been reported, that specific attenuation may temporarily raise to more than 300 dB/km in heavy fog.

### 3.3 Phenomenon of Fog

The phenomenon of fog and haze is constituted of a huge quantity of small water droplets suspended in the air volume.

It is admitted in meteorology, that there is fog when visibility is reduced to less than 1 km and the relative humidity of the air is brought to the saturation level (close to 100 %). Fogs are characterized by several physical parameters such as liquid water content, particle size distribution, average particle size and number per air volume, and visibility reduction. Several types of fog can be distinguished according to their formation mechanism, but generally radiation (convection) fog and (maritime) advection fog are the most typically encountered types in nature [2].

**Radiation fog** is related to the ground cooling by radiation. It appears when the air is sufficiently cool and becomes saturated. So this is a fog which generally appears during the night and at the end of the day. Particle diameters vary weakly around 4  $\mu\text{m}$  and the liquid water content varies between 0.01 and 0.1  $\text{g}/\text{m}^3$ .

**Advection fog** is formed by the movements of wet and warm air masses above colder maritime or terrestrial surfaces. It is characterized by liquid water content higher than 0.2  $\text{g}/\text{m}^3$  and a particle diameter close to 20  $\mu\text{m}$ .

All the optical characteristics of aerosols and in particular those of fog are related to the particle size distribution, which is the most important parameter allowing us to compute the optical properties of a quantity of droplets. Generally this distribution is represented by analytical functions such as the lognormal distribution in the case of aerosols and the modified gamma distribution for the fog, which is widely used to model the various types of fog and clouds.

$$n(r) = ar^\alpha e^{-br} \quad 3.3-1$$

In this equation  $n(r)$  gives the number of particles per volume unit and per increment unit of the particle radius  $r$ ;  $a$ ,  $\alpha$  and  $b$  are parameters which characterize the particle size distribution. The modified gamma distribution is used in simulation software like *Fascod*, *Lowtran* and *Modtran* for modeling the effect of advection and convection fog on

atmospheric transmission. For these two types of fog, the particle size distribution is shown in Figure 3.3-1 & 3.3-2.

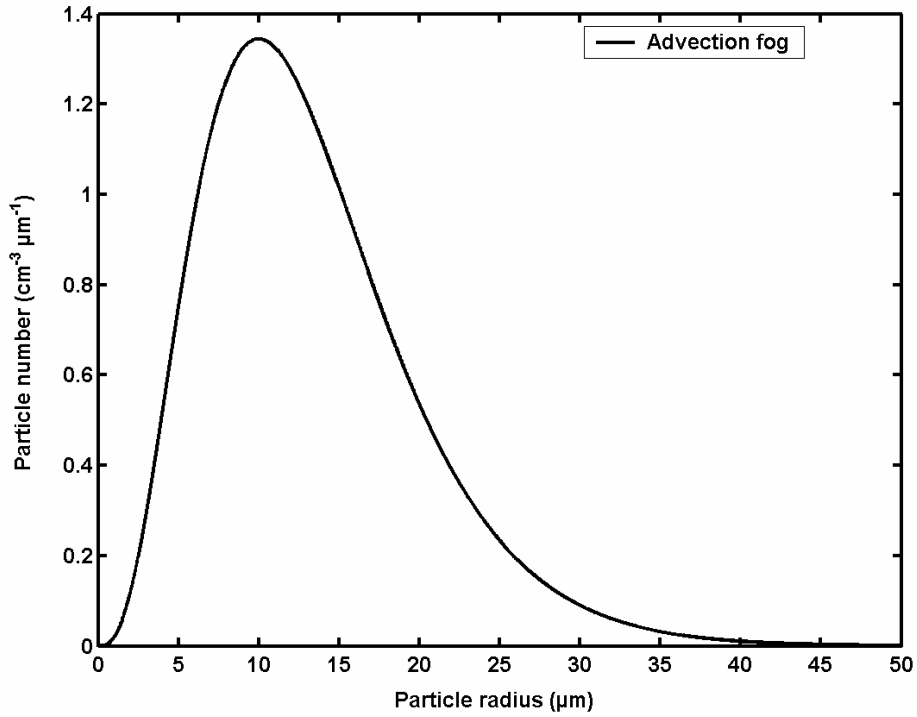


Figure 3.3-1: Particle size distribution for Advection Fog

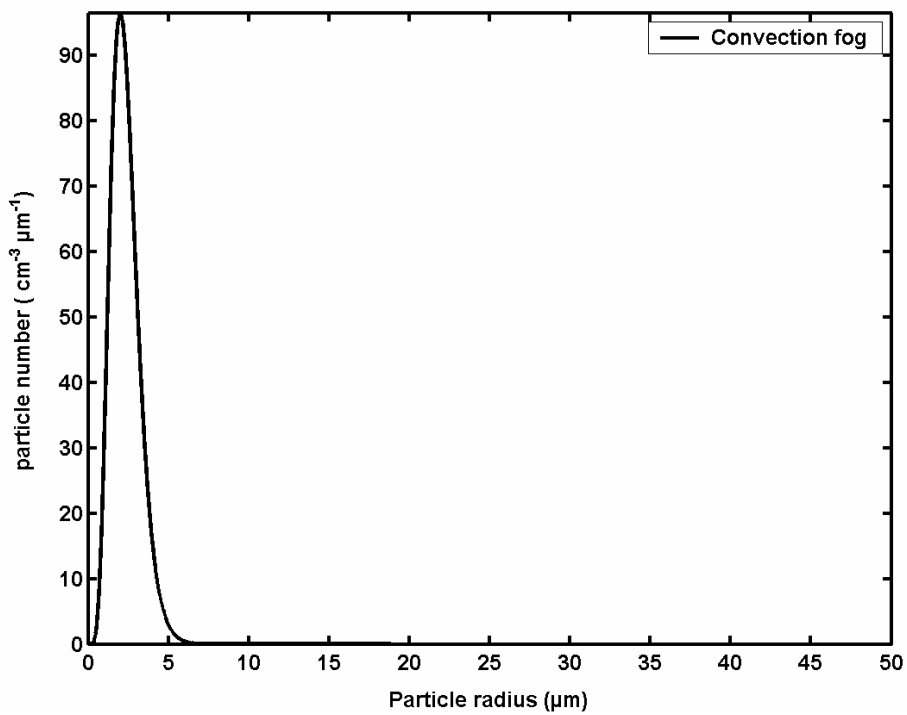


Figure 3.3-2: Particle size distribution for Convection Fog

The transmission of visible light and infrared waves through the atmosphere is described by the Beer-Lambert law

$$\tau(\lambda, d) = \frac{P(\lambda, d)}{P(\lambda, 0)} = e^{-\gamma(\lambda)d} \quad 3.3-2$$

where  $\tau(\lambda)$  is the total transmittance of the atmosphere at the light wavelength  $\lambda$ ,  $P(\lambda, 0)$  is the optical power emitted from the transmitter (without attenuation) at distance 0 and  $P(\lambda, d)$  is the optical power from the transmitter measured at distance  $d$ .  $\gamma(\lambda)$  is the total extinction coefficient per length unit, which represents the attenuation of the light. It is composed of terms for scattering and absorption usually denoted as

$$\gamma(\lambda) = \alpha_m(\lambda) + \alpha_a(\lambda) + \beta_m(\lambda) + \beta_a(\lambda) \quad 3.3-3$$

Here  $\alpha_m$  and  $\alpha_a$  are the molecular and aerosol absorption coefficients, and  $\beta_m$  and  $\beta_a$  are molecular and aerosol scattering coefficients. Absorption by gas molecules like H<sub>2</sub>O, CO<sub>2</sub> and N<sub>2</sub> which are constituents of the air define the main atmospheric transmission windows used for FSO, most important around 850 and 1550 nm, where molecular absorption  $\alpha_m$  is negligible. As the size of the molecular constituents of air is very small compared to the wavelengths of visible and infrared light, the contribution of  $\beta_m$  acting as Rayleigh scattering is negligible too. The aerosol absorption coefficient is small, so the predominant process for light attenuation by fog is Mie scattering, the scattering of aerosol particles and mainly water droplets which are approximately of equal size range as the visible and infrared wavelengths we consider. In other words, this means most of the light power is not absorbed, but it loses directivity. This could be used to reduce attenuation for short-range wide-angle links. In order to predict the attenuation of *directed* or *specular* light radiation in the atmosphere, the Kruse formula was widely used and is often cited in literature. It is given by the following equation:

$$\gamma(\lambda) \approx \beta_a(\lambda) = \frac{\ln(\tau_{TH})}{V} \left( \frac{\lambda}{550 \text{ nm}} \right)^{-q} = \frac{3.912}{V} \left( \frac{\lambda}{550 \text{ nm}} \right)^{-q} \quad 3.3-4$$

In visible and near IR up to about 2.5  $\mu\text{m}$ , this formula relates attenuation to visibility  $V$  (in km) for a given wavelength  $\lambda$  (in nm). Visibility is a parameter which characterizes the opacity of the atmosphere. It is defined as being the distance to an object at which the image contrast drops to a certain percentage of the original contrast of the object, equivalent to a certain transmission threshold  $\tau_{TH}$  over the atmospheric path. Unfortunately two definitions for this threshold exist, 2 % (which is used in the original

Kruse equation), and 5 %, which today is typically used for example at airports to denote the "runway visibility range" RVR. Visibility is technically measured at the center of sensitivity for the human eye, at 550 nm with a spectral band width of typically 250 nm. The visibility range, sometimes also referred as "see-ability", is given by the Koschmieder law to

$$V = \frac{\ln(\tau_{TH})}{\gamma(550nm)} \quad 3.3-5$$

The Kruse equation extends the problem of transmission and visibility to other wavelengths (approx. 0.5 – 2.5  $\mu\text{m}$ ), especially in the IR. The coefficient  $q$  has been subject of many experimental works and theoretical discussions. It depends on the scattering particles size distribution. The original Kruse approach is

$$q = \begin{cases} 1.6 & \text{if } V > 50\text{km} \\ 1.3 & \text{if } 6\text{km} < V < 50\text{km} \\ 0.585V^{1/3} & \text{if } V < 6\text{km} \end{cases} \quad 3.3-6$$

Applying this formula means a significant advantage for longer, IR wavelengths, which seem to be less attenuated for low visibilities in fog. This empirical formula, however, originally was intended for applications in geodesy or meteorology, where dense fog conditions were out of scope. Actually the measurement data it is based on does not include dense fog conditions. Within the community of free-space optic data communications, this is an important question as the link should remain operational under all conditions, if high availability is required. Some investigations indicate no wavelength dependency for visibilities below 500 meters, so the following extension to the  $q$  parameter was proposed by I. Kim, B. McArthur and E. Korevaar

$$q = \begin{cases} 1.6 & \text{if } V > 50\text{km} \\ 1.3 & \text{if } 6\text{km} < V < 50\text{km} \\ 0.16V + 0.34 & \text{if } 1\text{km} < V < 6\text{km} \\ V - 0.5 & \text{if } 0.5\text{km} < V < 1\text{km} \\ 0 & \text{if } V < 0.5\text{km} \end{cases} \quad 3.3-7$$

### 3.3.1 Difference between Kruse and Kim Models

As a practical example to show the difference between the Kruse and Kim model, a visibility of 100 m based on 5 % threshold would mean a specific attenuation of 112.7 dB/km at 950nm wavelength calculated with the Kruse model whereas the Kim model without wavelength dependency it would mean 130 dB/km. This means there is a difference from 16% (of the dB value) between the models.

Other investigations based on Fascod simulation software and Mie scattering even indicate higher attenuation for longer wavelengths under certain fog conditions. Due to the different particle size distributions of different fog types unfortunately a generally valid relation between visibility at 550 nm and wavelength dependent attenuation in the IR seems to be impossible. However, more experimental data especially for the dense fog conditions can help to clarify the situation. In this context we see our own investigations under maritime fog conditions, as presented here.

The attenuation  $a_{dB}$  (in decibels, as conventionally used by technicians for calculating link power budgets) over the link path distance  $d_{LINK}$  in km can then be calculated from the measured transmission  $\tau$  or the extinction coefficient  $\gamma(\lambda)$  (in  $\text{km}^{-1}$ ) according to

$$a_{dB} = 10 \log\left(\frac{1}{\tau}\right) = \frac{10}{\ln(10)} \gamma(\lambda) d_{LINK} \quad 3.3-8$$

Often used is also the specific attenuation, again for the 5 % transmission threshold it can be calculated from

$$a_{SPEC} (dB/km) = \frac{a_{dB}}{d_{LINK}} = \frac{\log(1/\tau_{TH})}{V} \cdot (\lambda / \lambda_0)^{-\alpha} \cong \frac{13dB}{Vkm} \cdot \left(\frac{\lambda \text{ nm}}{550 \text{ nm}}\right)^{-\alpha} \quad 3.3-$$

As a practical example to show the difference between the (original) Kruse and the (modified) Kim model, a visibility of 30 m based on the 5 % threshold would mean a specific attenuation of 392.05 dB/km at 950 nm wavelength calculated with the Kruse model, whereas with the Kim model without wavelength dependency it would mean 433.3 dB/km. These are basically the conditions of our measurement.

## 3.4 System setup (and links)

The optical link for transmission measurement at infrared wavelengths was developed and built by the research group OptiKom at TU Graz. Equipped in a standard housing for OptiKom free-space optic Ethernet data links is a transmitter, able to transmit

two (or more) optical wavelengths each pulse modulated with an individual carrier frequency of 5.5 and 6 MHz. The receiver in the second housing consists of one optical front end for two (or more) wavelengths, which are separated from ambient light and from the other wavelength using an electrical band pass filter which lets only one carrier frequency pass through, associated to one optical wavelength. The received optical power at the optical wavelength is proportional to the electrical signal amplitude, so after rectification and smoothing it can be measured very comfortably as a DC voltage. To achieve sufficient resolution, two stages for each wavelength channel were implemented in the receiver, each covering approx. 15 decibels of dynamics in optical input power. (As an alternative, a logarithmic amplifier could also have been used instead.) The circuit principle is shown in Figure 3.4-1[2].

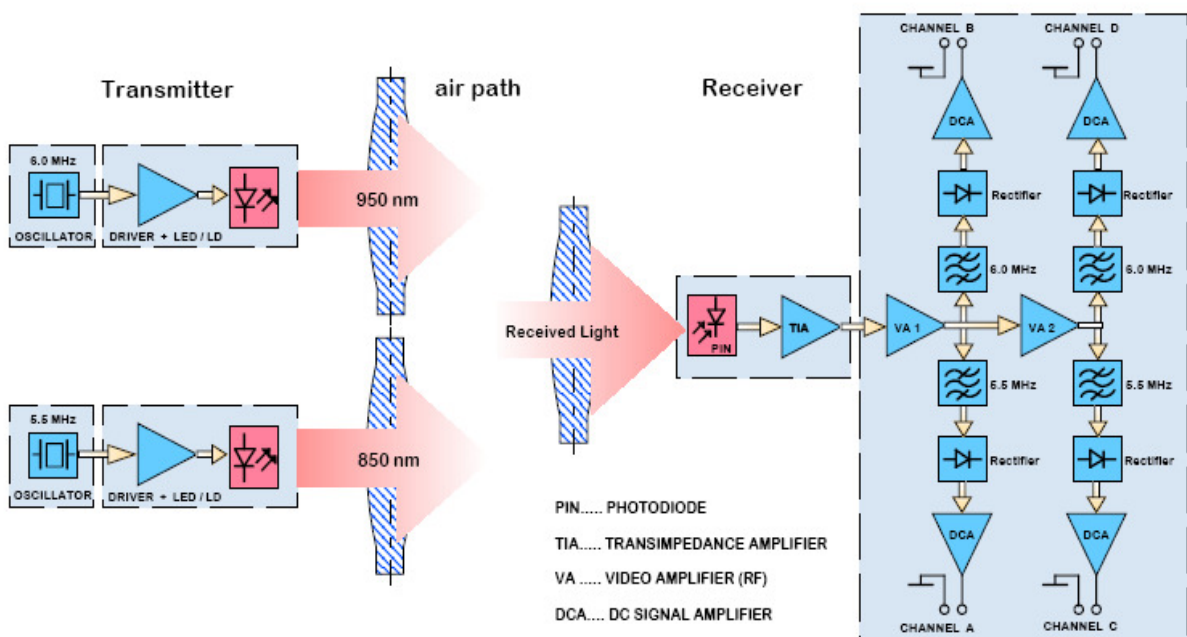


Figure 3.4-1: RF Marker circuit principle for transmitter and receiver.

The system was calibrated in the Lab before any practical fog measurement was performed. First, the crosstalk between the two wavelength channels was found to be sufficiently low in the linear range of the input stage amplifier, resulting in a maximal output change of 0.014 dB (opt) for both channels of the higher power receiver stage (in case of 15 dB optical power difference between the channels) and up to 0.19 dB(opt) change for the lower power receiver stage. Ambient light up to 0.1 mW (more than maximum daylight receiving power) is completely suppressed, resulting in output power change of less than 0.005 dB (opt). Second, the typical relation between received optical power and measured DC voltage for one optical wavelength (associated to one modulation carrier frequency) is shown in Figure 3.4-2.

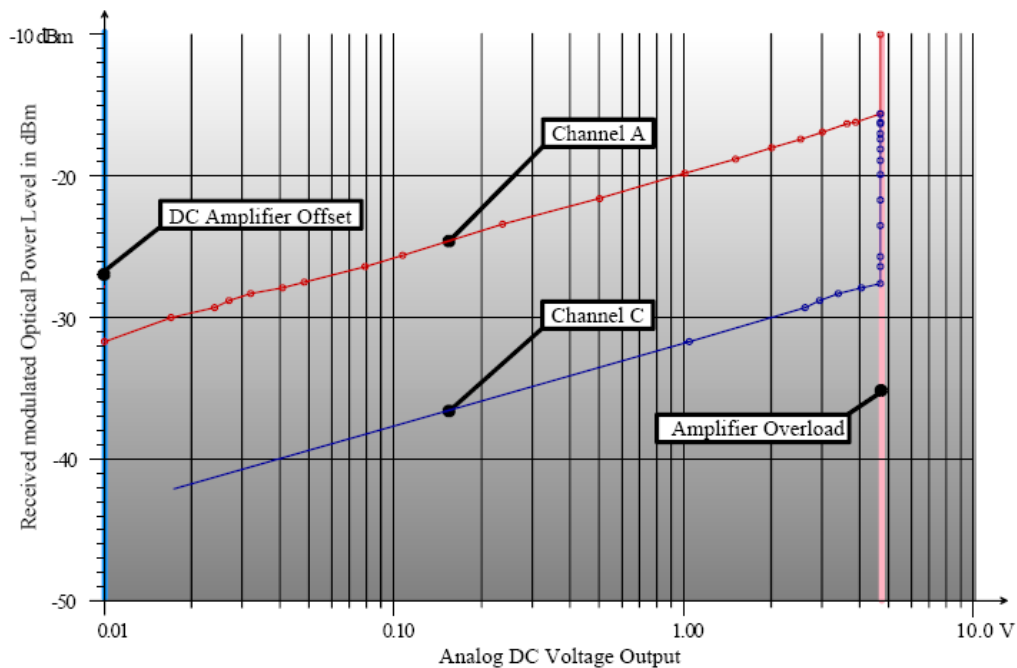


Figure 3.4-2: Typical receiver characteristics for one optical wavelength (950nm).

The main advantages of this RF Marker transmission measurement concept against using un-modulated light and optical band pass filters at the receiver are the possibility to completely suppress ambient light, to have one optical receiver front end only and so – except for chromatic aberration - to have equal optical properties like alignment or acceptance angle for two or several wavelengths, and to have a comparatively cost-effective solution which even allows to use standard FSO systems as a transmitter. For our measurements we use a 950 nm source (SFH495P) and an 850 nm source (L7558-01) as transmitter, and a Si-Pin front end (SFH203FA) for the receiver. Our 850 nm transmitter has a beam divergence of  $2.4^\circ$ , the 950 nm transmitter has  $0.8^\circ$  with 25 mm lens diameter in both cases. Our receiver has  $1.7^\circ$  acceptance angle and a lens diameter of 98 mm. To record the measurement data, a computer with an A/D conversion card operating with LabView software was used. It allows to record one measurement value per second for every channel. The card was a PCI 6023E (12 bit, 200 kS/s). The measured DC voltage value of every channel was stored with a conventional PC together with time and date in a table. The data was processed and evaluated after the measurement in MatLab, resulting in the diagrams shown in the following sections. For our figures we use the specific attenuation (dB/km).

Specific attenuation can simply be calculated from the total attenuation measured over the link distance by

$$\alpha_{SPEC} = \alpha_{ABS} \cdot \frac{1000}{d_{LINK}} \quad 3.4-1$$

$\alpha_{SPEC}$ ...specific attenuation in decibels per kilometer,  
 $\alpha_{ABS}$ ....(total) attenuation in decibels, measured over the link,  
 $d_{LINK}$ ....link distance in meters.

### 3.5 Measurements and Analysis

For the measurements in France, the transmitter and the receiver were mounted on tripods about 3.5 meters above ground over a link distance of 28.3 meters. This campaign was performed from 23rd June, 2004 until 1st July, 2004 and we could observe 3 major fog events within this week, of which one was chosen for detailed analysis. The link distance was selected in a way that our system would be able to record the appearing attenuation for the complete fog event without a broken link, to be sure about the peak values. Having 25 dB dynamics over 28.3 meters allowed us to measure as much as 880 dB/km specific attenuation. The campaign at Graz was started at 29th September, 2005 and is still ongoing; data considered here is until the 30<sup>th</sup> December, 2005. This means we have measured for 93 days and for these days we have data for 99.5% of the time. So far we have observed ten fog events and two snow events, of which we present the analysis of one in this paper. Receiver and transmitter are mounted on tripods on the rooftops of opposite University buildings. Basically we have two links installed at Graz, a shorter one operating over 79.8 m free air distance, and a longer one operating over 650 m free air distance. The shorter link allows us to measure specific attenuation as high as 310 dB/km, the longer one is used for more detailed measurements in haze and light fog and is not considered here. For optical impressions we use a Webcam in addition, which takes a picture every minute. We will try to continue the measurement campaign until April. The campaigns will help to answer many questions concerning availability and specific attenuation for continental and maritime fog conditions[3].

Figure 3.5-1 and 3.5-2 shows the visibility as measured with the transmissiometer during the whole day (3.5-1) and during the fog event in the evening (3.5-2), which is investigated in the following paper. As can be seen, there are different periods in the fog event, and finally the visibility drops to very low values of less than 30 meters in very dense, stable fog. To calculate the attenuation measured at 950 and 850 nm, the maximum received optical power under clear sky conditions around minute 800 was taken as a reference value, and the difference to less power received during the fog event was calculated as attenuation in decibels.

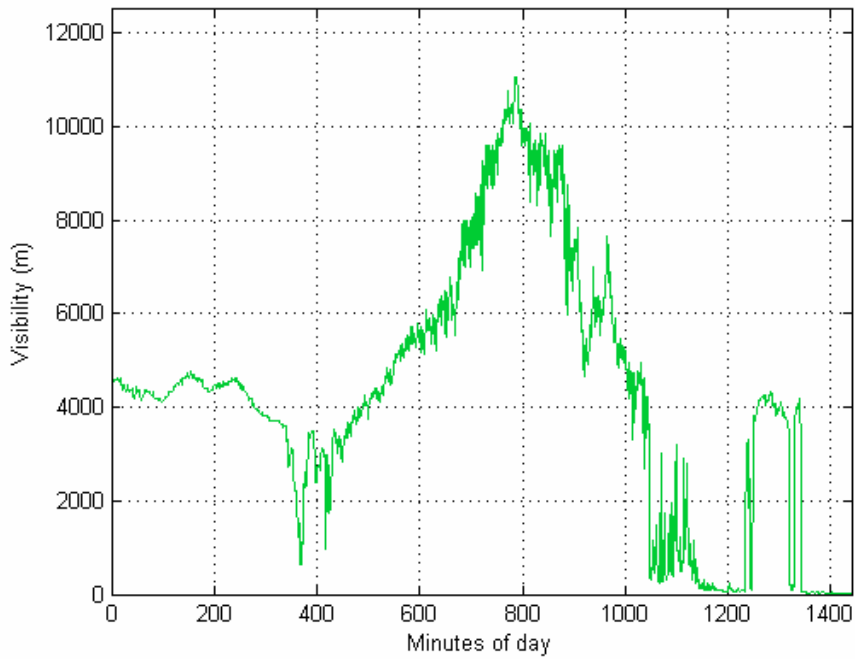


Figure 3.5-1: Visibility during 28.6.2004 (one value per minute) measured with transmissionmeter (whole day).

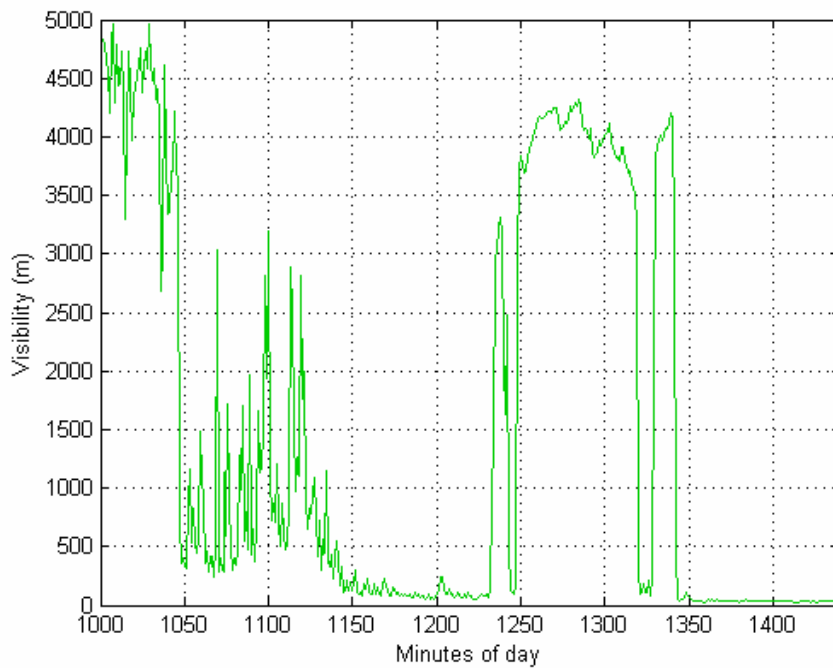


Figure 3.5-2: Visibility during 28.6.2004 (one value per minute) measured with transmissionmeter (whole day).

### 3.5.1 Comparison of fog events at Nice and Graz

We have data of an event of dense maritime fog measured in the evening and night of the 28th June, 2004 at Nice. This allows us to compare the maritime (advection) fog with radiation fog of a typical event at Graz in the evening of the 25th October, 2005. Results of this comparison are shown in the following diagrams. Our first point is the specific attenuation. Figure 3.5-3 and 3.5-4 give the time series of specific attenuation over the two fog events, for Graz on the left hand and for Nice on the right hand. To allow better comparison, the scaling for both diagrams is equal. As can be seen, the peak value is much lower for the Graz event, not exceeding 120 dB/km, whereas the peak value for Nice was up to 480 dB/km. It is a general observation for all fog events measured at Graz so far, that specific attenuation can get close to, but is not exceeding much 120 dB/km [3]. The next points are the time characteristics of the two types of fog. Figure 3.5-3 and 3.5-4 did show the measured specific attenuation averaged over one minute, as it is typical for weather data records, which can be used for FSO availability prediction models. Our measurements actually had higher time resolution.

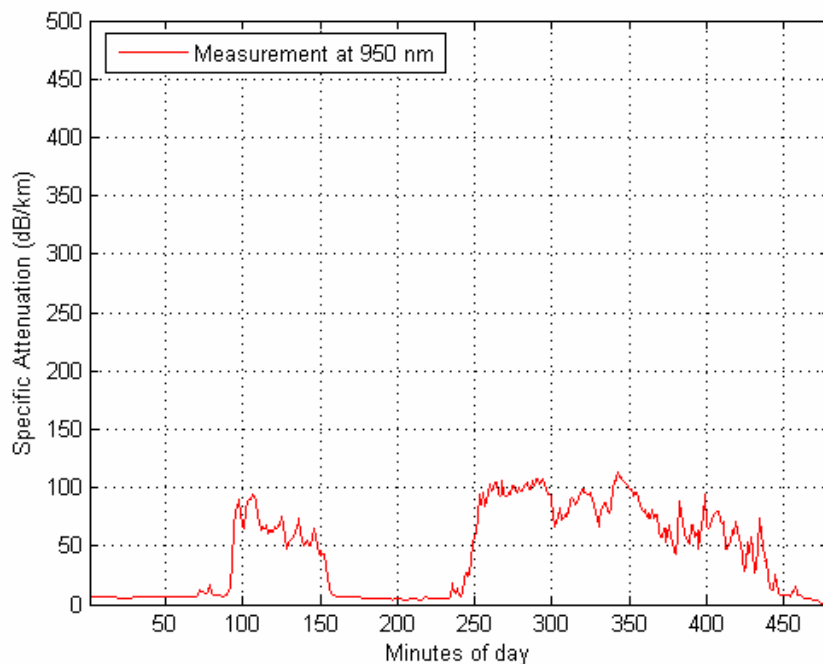


Figure 3.5-3: Specific Attenuation at Graz (average minute values).

In figure 3.5-5 and 3.5-6 we compare the change of the specific attenuation for one second value to the next second value. As can be seen, the fog event at Graz is very stable and shows no major fluctuations, obviously attenuation changes here only gradually over longer time scale. The characteristics of the maritime fog event is very different, with changes of up to 300 dB/km from one second to the next, or variations of more than 45 % of the average value [3]. This point is also shown in figure 3.5-7 and 3.5-8 as a histogram, giving the counts for classes of change in specific attenuation (in different scaling). For low clouds or maritime fog, this means that the peak attenuation can be even much higher

than the average minute value, or lower than that.

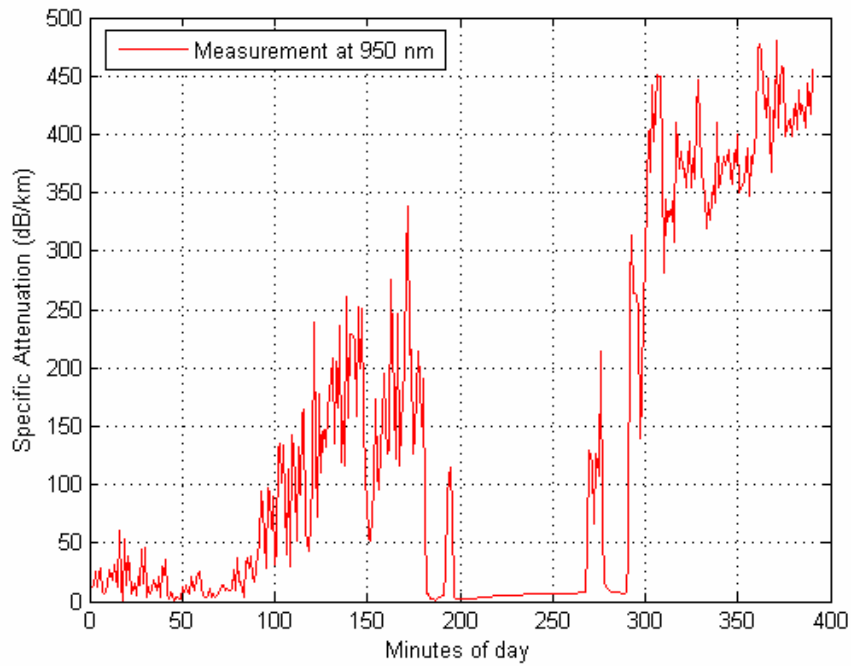


Figure 3.5-4: Specific Attenuation at Nice (average minute values).

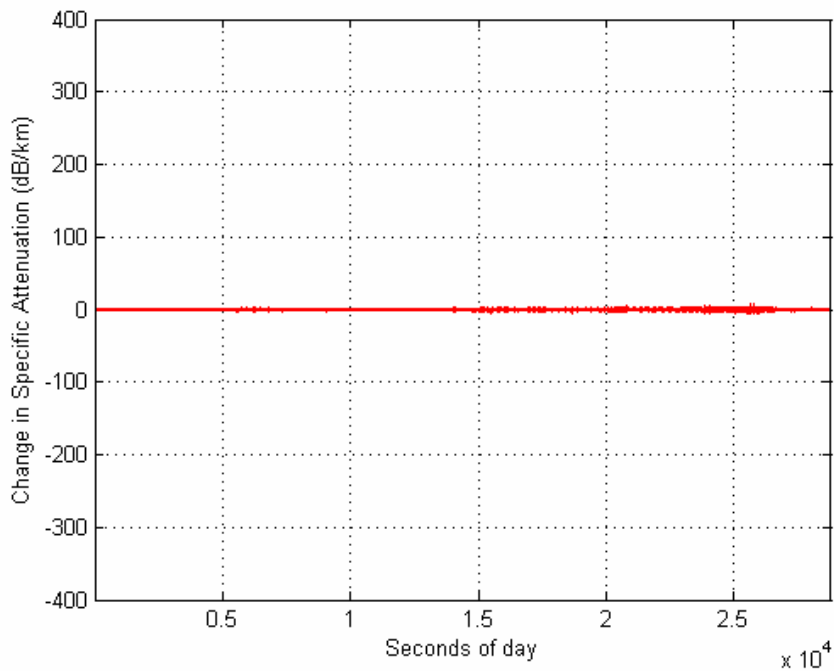


Figure 3.5-5: The change in Specific Attenuation at Graz (second values).

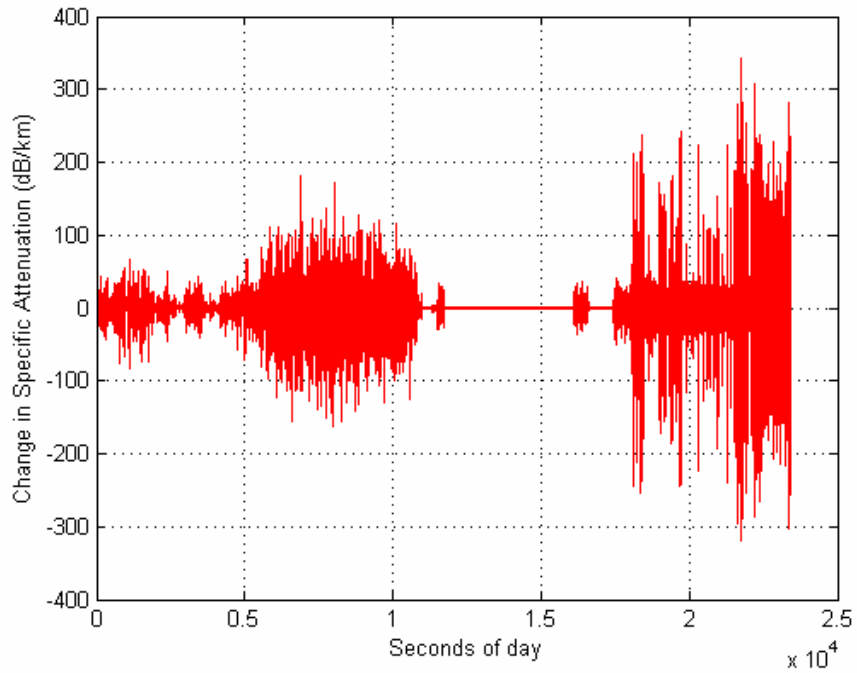


Figure 3.5-6: The change in Specific Attenuation at Nice (second values).

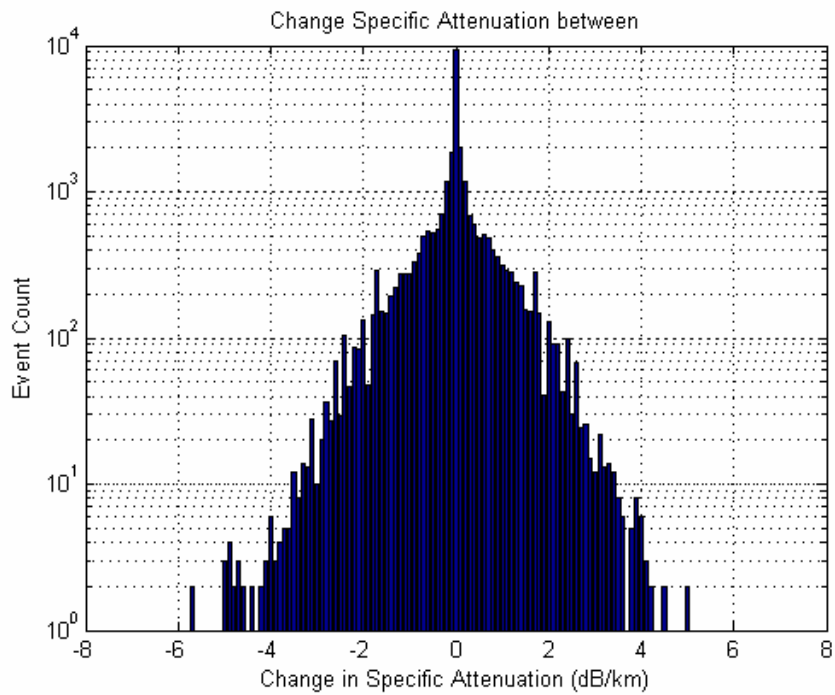


Figure 3.5-7: Histogram for the change of the Specific Attenuation at Graz.

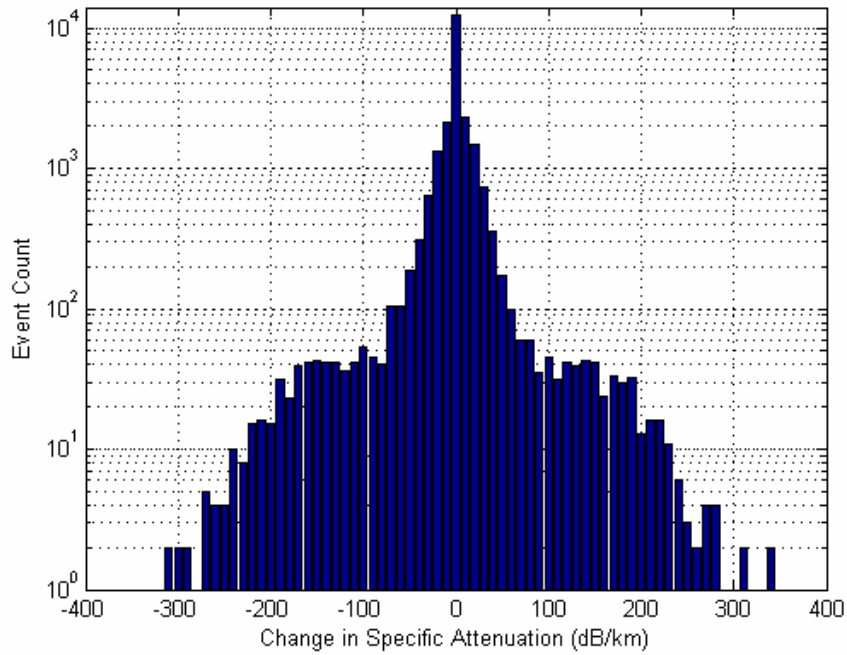


Figure 3.5-8: Histogram for the change of the Specific Attenuation at Nice.

Figure 3.5-9 and 3.5-10 give the value for the minimum and maximum specific attenuation (1 second resolution) within the minute used for the calculation of average attenuation. Our third point is the attenuation effect on different wavelength as used for typical FSO systems, under the same air conditions.

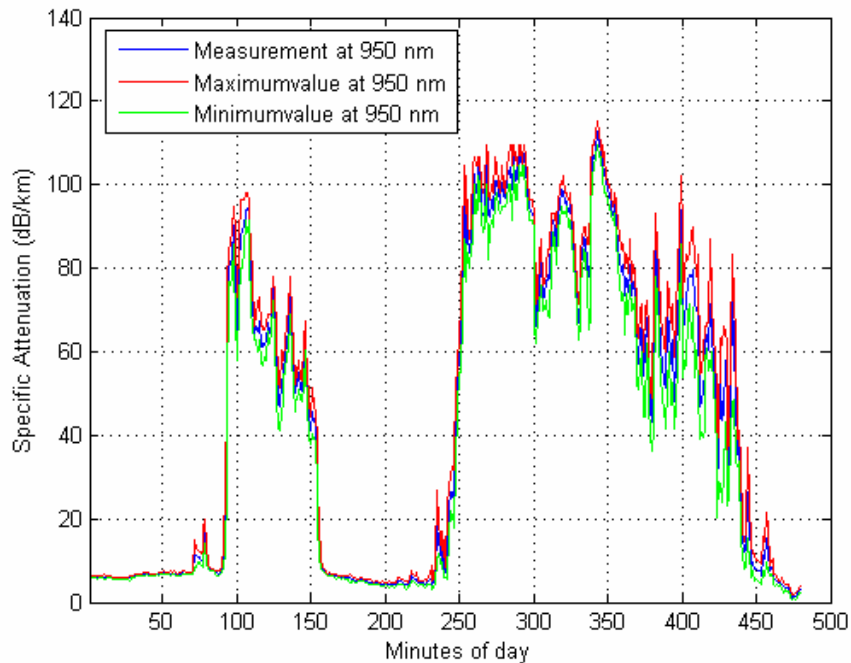


Figure 3.5-9: Specific Attenuation at Graz (minimum, maximum values).

Visibility data collected in meteorological stations or at airports is measured with a transmissiometer, usually operating at 550 nm center wavelengths with 200 nm bandwidth. FSO systems operate at longer wavelengths, mostly at 850, 950 or 1550 nm center wavelength.

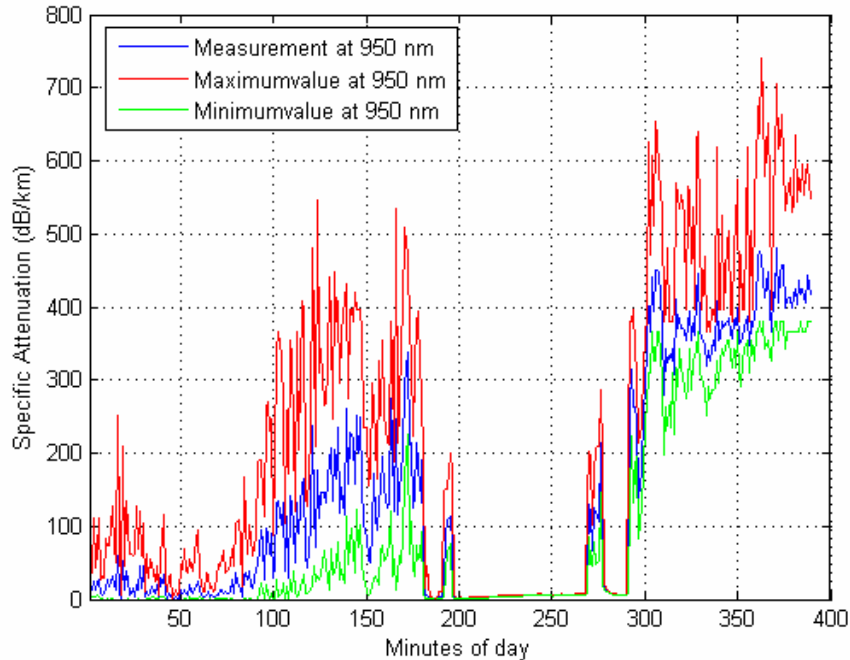


Figure 3.5-10: Specific Attenuation at Nice (minimum, maximum values).

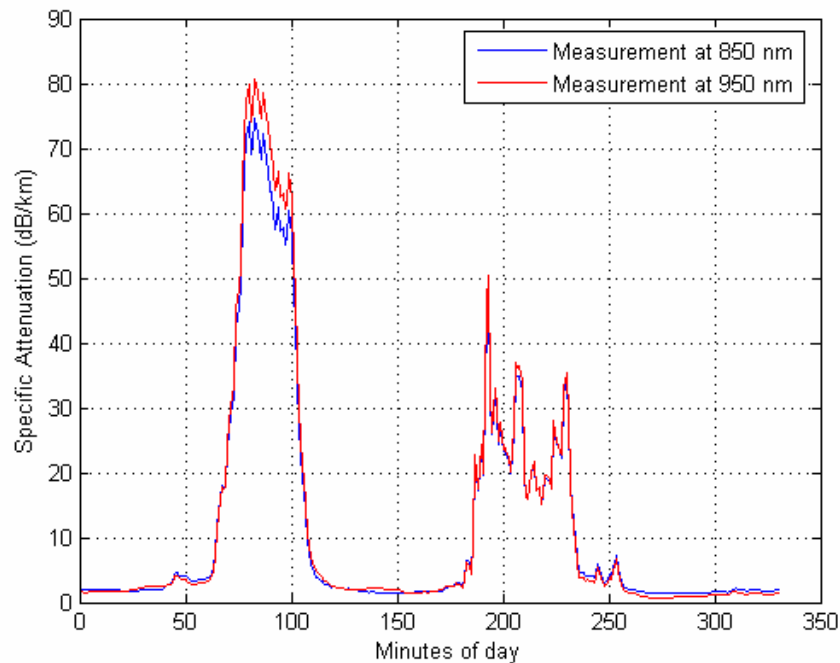


Figure 3.5-11: Specific Attenuation for 850 & 950 nm wavelength (Graz, 30th September, 2005).

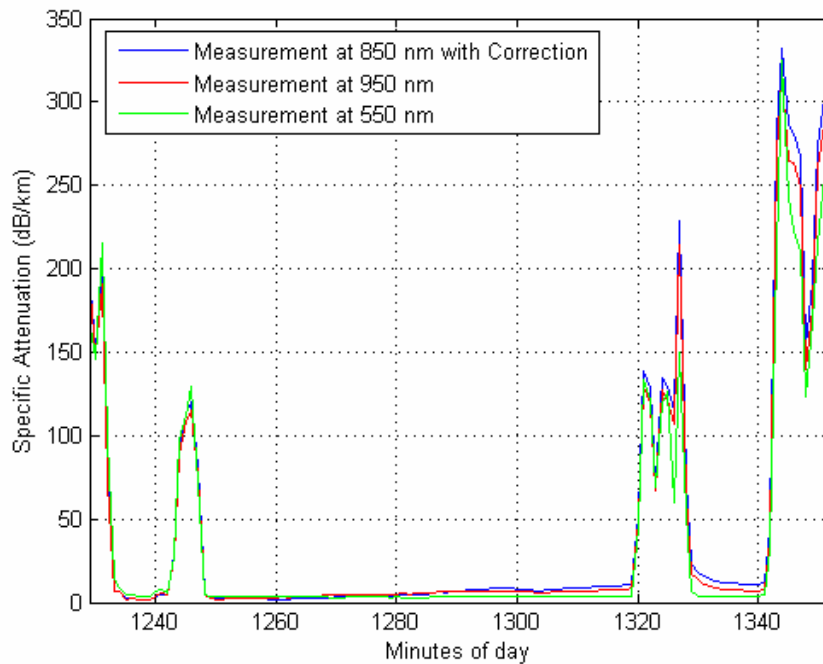


Figure 3.5-12: Specific Attenuation for 550nm (transmissionmeter) and 850 & 950 nm wavelength (Nice detail).

In figure 3.5-12 we compare the specific attenuation for different wavelengths for the dense maritime fog at Nice. As can be seen, we have basically found no wavelength dependency of the attenuation within our measurement accuracy. This is in good agreement with the theory of scattering, as the particle size of dense advection fog is supposed to be several times larger than the optical wavelength used. It is, however, a contradiction to the Kruse model, which in general predicts less fog attenuation for longer wavelengths. Kim et al. has already proposed a modified model, which basically predicts no wavelength dependency for visibilities less than 500 m. In figure 3.5-11 we compare the specific attenuation for 850 and 950 nm wavelength (a transmissionmeter operating at 550 nm is not available for the measurements at Graz). Here we find indications for less attenuation at 850 nm wavelength. One possible explanation for this was proposed by the fog attenuation model of Al Naboulsi et al [4]. For radiation fog particle diameters are in the same order of magnitude than the wavelength, so we observe Mie scattering in the oscillating region. If the diameters are mostly cumulated around a certain value, the shorter wavelength can be less attenuated. Again this would require a modification of the conventional fog model used so far. A second explanation could be based on the spatial transmission properties in this type of fog, as our transmitters for 850 and 950 nm have different beam divergence angles. This kind of influence was proposed by Arnon et al. However, this point should have our attention and will need more thorough investigation in future.

### 3.5.2 Snow Event

Starting on 25th November, 2005 and lasting until 28<sup>th</sup> November 2005 we could also measure a snowfall event. Figure 3.5-13 shows the snow event and the specific attenuation with a peak value of 60 dB/km specific attenuation [3]. This peak value is smaller than the typical peak value for fog measured in Graz (120 dB/km). In figure 3.5-14 we give again the change in attenuation from one second to the next [4]. Here we see also a fluctuation effect caused by the flakes, as one could expect.

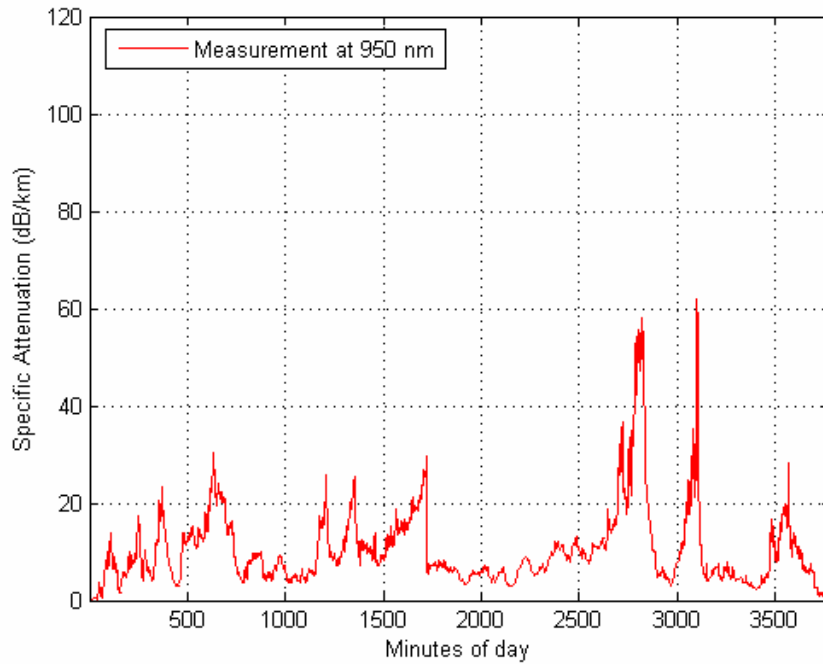


Figure 3.5-13: Specific Attenuation at Graz (average minute values, snow).

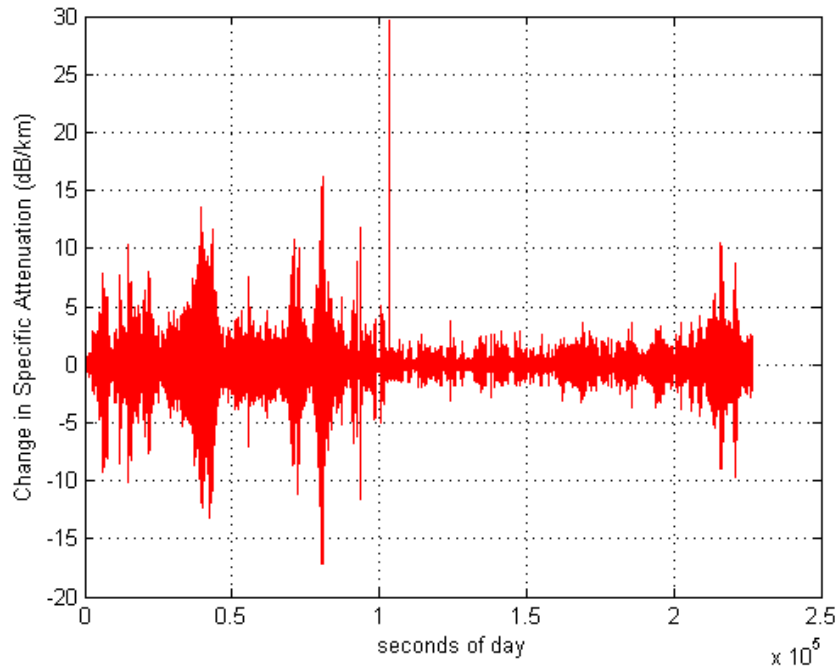


Figure 3.5-14: Change of the Specific Attenuation at Graz (second values, snow).

### 3.6 Summary

Optical Wireless is the nomadic broadband solution (high data rates without any cabling) for connecting the Backbone to the users (Last-Mile-Access). This technology can be an excellent supplement to conventional radio links and Fiber Optics as part of a future evolving broadband network. Terrestrial FSO for short ranges can cover the links between buildings on campus or different buildings of a company, which can be established with low-cost technology. We have demonstrated the use of Optical Wireless for the “last mile” access for special events. Some multimedia applications (like video-conferences, live TV-transmissions, etc.) will illustrate the range of applications for FSO last mile networks. Free Space Optics is an important and integral part of Next Generation high data rate optical networks and will provide the last mile connectivity in order to achieve Gbps transmission to the end user. For the aim to get a highly reliable optical wireless link as part of the future evolving broadband network also standardization, the development of new equipment for Optical Free Space Communication and the use of FSO in combination with microwave backup (i.e. Wireless LAN) are important.

FSO deployments will always remain highly dependent on the location, and the systems may work better in particular climatic regions. System design enhancements will have to accommodate this peculiar weather- and location dependent behavior of the systems. We have provided detailed analysis and comparison for two very different kinds of fog, namely the continental city fog and the maritime fog. The two types of fog behave distinctly different from each other with significant impact on the design of optical

wireless systems Fog is the foremost reason for high light attenuation, but it can have very different characteristics depending on the location. We found a specific attenuation of up to 120 dB/km for the city of Graz, which may be typical for radiation fog in continental cities. Usually the fog appeared to be very stable with very little variations over small intervals of time. In contrast to that, we observed up to 480 dB/km for maritime advection fog or low clouds in a mountainous region at the coast of South France.

Free-space optic links operating in the range of gigabit data rates can have about 50 dB total system power margin in the optimum case, neglecting losses due to geometrical beam spreading. For the case of a continental city like Graz, this would allow link distances up to 400 meters achieving very high availability. As the fog appears to be mostly uniform and stable, coding techniques or space diversity options like multiple beam transmission have very little effect. On the other hand, provided sufficient margin, such links can offer very high data rates with low latency, and allow transmitting fast cable protocol standards without conversion (different to wireless RF links). This also allows larger networks based on segmentation.

For the case of maritime fog or low clouds high link availability would allow FSO link distances of about 100 meters only. The high variability of attenuation can even cause short link breaks if the mean and averaged attenuation could be compensated by the margin of the installation. This provides a chance for improvements by coding techniques. The highest peak specific attenuation in a minute was 739 dB/km, while the lowest was 366 dB/km. This reflects considerable possible improvement by appropriate channel coding or protocol techniques, though also resulting in reduced throughput and increased latency. Except for very short links like street or river crossings, larger networks will require a hybrid approach for such a location.

Few measurements are reported about snowfall. As we observed in the city, the attenuation is less compared to fog, but shows high variability. Multiple transmitter or receiver technology can average out peak attenuations.

## References

- [1] Flecker B., Gebhart M., Leitgeb E., Sheikh Muhammad S. and Chlestil C.: "Results of Attenuation-measurements for Optical Wireless channels under dense fog conditions regarding different wavelengths", Proc. of SPIE, Vol.6303, 63030P, 2006
- [2] Muhammad S., Flecker B., Leitgeb E., Gebhart M.: "Characterization of fog attenuation in terrestrial free space optical links", Optical Engineering Vol.46(6), June 2007
- [3] Gebhart M., Leitgeb E., Sheikh Muhammad S., Flecker B. and Chlestil C.: "Measurement of Light attenuation in dense fog conditions for FSO applications", Proc. of SPIE, Vol. 5891, 58910K, 2005
- [4] Leitgeb E., Gebhart M., Fasser P., Bergenzer J. and Tanczos J.: "Impact of atmospheric effects in free space optics transmission systems," Proc. Of SPIE 4976, pp.86-97, 2003

## **4 WEATHER PARAMETER AND FOG MEASUREMENTS IN MILANO**

(Carlo Capsoni and Roberto Nebuloni)

The activity carried out by the FSO research group in Milan (Politecnico di Milano and IEIIT-CNR) is focused on both theoretical and experimental issues. The experimental work includes the collection and the analysis of continuous measurements over several years of laser attenuation and ancillary atmospheric quantities in the city of Milan, under different weather conditions, including clear-air, rain, snow and fog [Capsoni and Nebuloni, 2006] [Nebuloni and Capsoni 2011]. The analysis of fog measurements has been tailored to:

- Draw conclusions about link availability through the calculation of first-order statistics of path attenuation.
- Look for a correlation between optical attenuation and some atmospheric observables (e.g. visibility) in view of predicting the former from the latter. This is an example of bullet list:

## 4.1 System Setup

The available measurement set-up includes:

- A Terescope 3000 commercial optical system manufactured by Optical Access (now MRV) (see Table 4.1-1)
- A visibility sensor (Belfort 6100)
- An ultrasonic anemometer (Metek-1 USA)
- A weather station (Davis GroWeather)

The optical link is installed within the campus Leonardo of the Politecnico di Milano, in Milan (Italy): the terminals are located on the roof top of two tall buildings (18 m and 29 m above ground, respectively), and the meteorological sensors are positioned at one side of the link.

The station has been recording data almost continuously from 2003 to 2007.

*Table 4.1-1 Terescope 3000 commercial optical system used to measure laser attenuation in Milan.*

<b>Transmitter</b>	
Laser type	Single mode AlGaAs Laser diode
Geometry	Three lasers at 90°
Wavelength	785 nm
Transmitter diameter	50 mm
Beam divergence	2.5 mrad
Mean Power	30 mW (10 mW each laser diode)
<b>Receiver</b>	
Type	APD
Field of view	2.8 mrad
Receiver area	0.021 m <sup>2</sup>
Minimum detectable power	100 nW
<b>Link</b>	
Link length	320 m
Sampling time	1 s
Orientation	65° North-West
Available dynamic range (for weather attenuation)	~21 dB

## 4.2 Measurements and Analysis

The database of measurements carried out in Milan includes the following time series of optical attenuation and atmospheric quantities from October 2003 to June 2007.

- 1-s laser attenuation time series collected by the optical link at the 785 operational wavelength.
- 1-s visibility time series obtained from the visibility sensor (January 2005-June 2007).
- 1-s horizontal and vertical wind speed from the anemometer.
- 1-min temperature, pressure, relative humidity, solar radiation and rain rate from the weather station.

A PC controls the acquisition process of all the sensors and synchronizes the data streams to the CPU internal time. The data are stored into daily files for further (off-line) processing.

A simple data reduction procedure is carried out to identify fog events from the raw time series:

- A 1-min moving average is applied to mitigate noise effects.
- A fog event starts when the visibility falls below 1 km and it ends when visibility increases again above 1 km. The minimum allowable duration of an event is 30 min. No precipitation must occur in the meanwhile.

The 1-km visibility threshold is the upper bound for light fog according to the International Visibility Code. The time window associated to a fog event is extended beyond the time instants when visibility crosses the above threshold to account for transients effects. The time series of all the quantities, cut off as explained above, are saved for further processing, this time on an event-by-event basis. In the following the terms path attenuation (in dB) and specific attenuation (in dB/km) will be used as synonyms, assuming that fog distribution is homogeneous along the measurement path, hence making the conversion trivial. However, this is not always true, even in the case of a relatively short path as the one of the link used here.

### 4.3 Results

Milan is located at 45.27 degree North in latitude, the climate being continental temperate. Fog episodes in the area are frequent during the cold season. The fog formation mechanism is basically radiation. As the occurrence and the intensity of fog depend also on the environment, it is important to state that the Campus of Politecnico di Milano is located in the suburbs of Milan.

Figure 4.3-1 shows an example of the time series of attenuation (1-min averages) over a three-month period during winter. Note that the link goes into outage several times because of the limited dynamic range of the receiver (about 21 dB in the case of the measurement system and up to 35 dB for a more sophisticated equipment). This effect is even more evident in comparison with the one experienced by a microwave link where the dynamic range can be as high as 50-70 dB. To this limit of FSO systems at the receiver end one should add the impossibility of tuning the transmitted power (a technique usually applied at microwaves) because of eye safety limitations in the optical spectrum. All these considerations make FSO not suitable today for one-to-one substitution of microwave relay links.

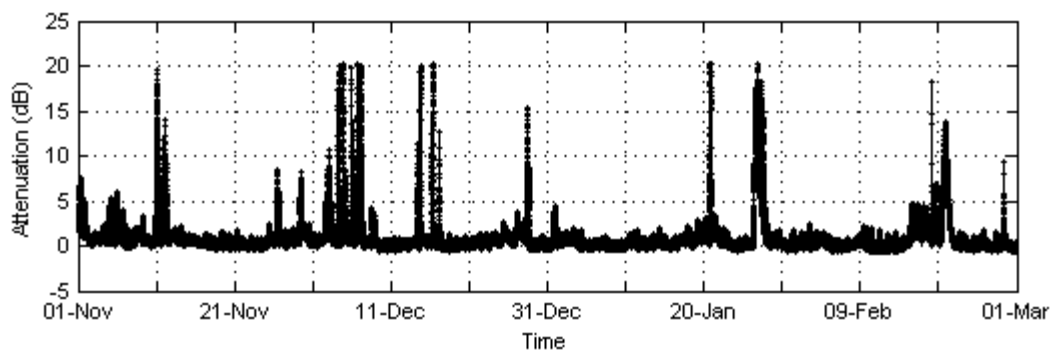


*Figure 4.3-1 1-min averaged data of laser attenuation. The receiver goes into outage when the atmospheric attenuation approaches 20 dB. The peaks in the graph are mainly due to fog.*

The raw time series of attenuation (1-s sampling time), not shown here, highlight rather slow oscillations of the signal, as typical of a continental fogs, which, once the formation phase has completed, are rather stable as there are no temperature variations or abrupt motions of air-masses during the event (as opposed to the case of maritime fogs).

Signal fades produced by fog are long and persistent, resulting in complete beam blockage for a long time. By consequence, the designer has no other option than to reserve enough link budget to achieve the target link availability in statistical terms as the degradation due to fog generally cannot be compensated by such techniques as adaptive coding. A solution to increase system availability would be to use hybrid optical+microwave systems, switching to the slower microwave link when the atmospheric conditions make optical propagation not feasible.

Figure 4.3-2 shows the profiles of visibility and laser attenuation during a fog event occurred on 11-12 January 2005. The optical attenuation, as estimated from visibility through empirical models available in the open literature, has a median value (34.6 dB/km), nearly

equal to the one calculated from the sequence of measured specific attenuation (35.0 dB/km). Moreover, the two time series are usually in good agreement, except in the case of the peak attenuation in the morning of 12<sup>th</sup> January, when the estimated values are much higher than measurements. This behavior could be ascribed to the sharp decrease in the visibility, that, in turn, could be a symptom of non-uniform conditions along the path. In fact, during this short event the two curves have a similar profile, but the measured attenuation curve is slightly delayed in time.

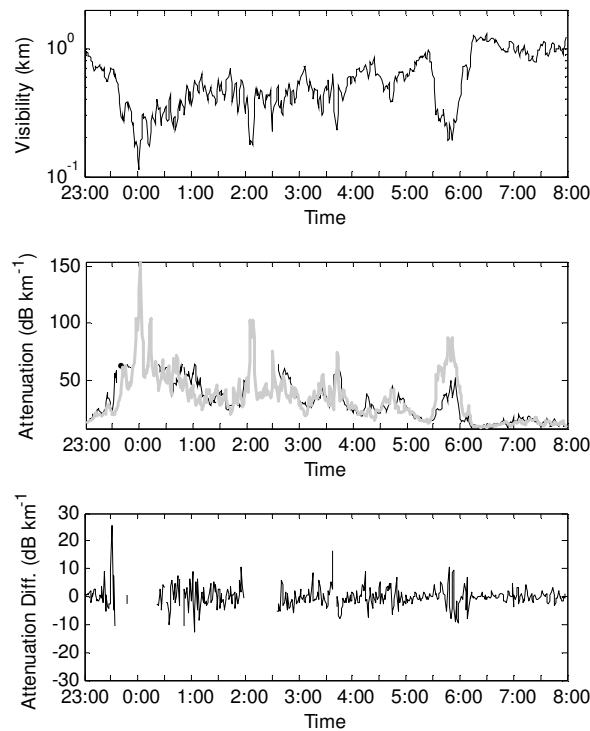


*Figure 4.3-2 Time profiles of (a) visual range; (b) specific attenuation; and (c) differences in specific attenuation during a fog event occurred in Milan on 11 and 12 January 2005. In (b) two profiles are shown: the measured laser attenuation (black curve) and the attenuation as estimated from visual range (gray curve).*

In about half of fog events identified during the measurement period, the attenuation exceeded the dynamic range of the receiver, that is 21 dB, or equivalently 60 dB/km, corresponding to a visual range around 250 m, which is roughly the limit for moderate fog, lower values being associated with thick fog and dense fog. On the whole, specific attenuation was in excess of 60 dB/km during 0.3% of time, a non-negligible value at all, when one considers the availability targets of TLC systems.

Finally, the dynamic of fog and the correlation between some meaningful quantiles of attenuation during single fog events evidence difference patterns for the episodes in Milan from the ones occurring in Graz [Awan et al., 2009] (see also previous chapter). Fog intensity is higher in Graz than in Milan but also the physical processes of fog formation, growth and dissipation seem to be different. The above differences can be explained as follows. Despite Milan and Graz are located in the same temperate area, there are two major differences that

are expected to affect to some extent measurements: (a) the climate during winter is colder in Graz, where daily temperature minima are often below 0°C, while in Milan, temperature rarely falls below 0°C, and (b) Milan is a large city and despite the measurement site is located in the suburb, about 3 km from the center of the city, the microclimate is the one of a dense urban area. On the other side, Graz is a midsize town, with the optical link being located in a suburban environment with no tall buildings and many wide open areas around. Therefore, it is reasonable that fog episodes are heavier in Graz than in Milan.

An overall picture of the optical link performance at the measurement site is in Figure 4.3-3 where different Cumulative Distribution Functions (CDF) of specific attenuation are plotted [Capsoni and Nebuloni, 2006]. Two yearly CDFs are shown (dark solid and dashed lines) for two consecutive years, besides the seasonal CDFs for the year 2005 (dark dotted line for the spring-summer period and dark dot-dashed line for autumn-winter), and finally the CDFs of the worst and best months of the whole two-year period (gray solid and gray dashed curves, respectively). The behaviour of the two years is nearly the same on the average, being the two corresponding curves almost superimposed, although both the best and the worst month occurred in the same year. For  $10^{-2}$  of the yearly time the specific attenuation exceeds 30 dB/km, while it exceeds 60 dB/km for about  $3 \cdot 10^{-3}$  of time. These figures correspond to a measured attenuation of about 10 and 20 dB, respectively, and show the deficiency of this specific set up (although only 320-m long) to provide the performance usually required to a TLC link. As expected, the yearly CDF is mostly determined by the winter months. However, note that the specific attenuation exceeded 1 hour/year ( $10^{-4}$  yearly probability) in the summer months when fog (and snowfall) are absent is above 40 dB/km, a non-negligible value. According to that, a FSO system with a 20 dB dynamic range and designed to provide an yearly outage probability lower than  $10^{-4}$  should not exceed 500 m in length in case it was located in a similar environment as the one of the measurement site. Even if there is a definite influence of foggy periods on the CDF of path attenuation, nonetheless this effect would be even worse if the link were outside the city belt, but definitely less was the equipment installed in the city centre.

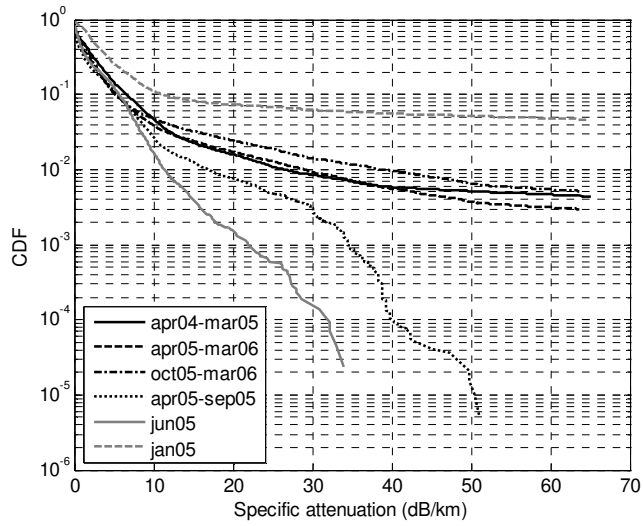


Figure 4.3-3 Cumulative Distribution Functions (CDF's) of the specific attenuation experienced by the optical link.

## References

[Capsoni and Nebuloni, 2006] Capsoni C., Nebuloni R., “Optical Wave Propagation through the Atmosphere in a Urban Area”, Mediterranean Microwave Symposium 2006, Genova, Italy, September 19-21, 2006, pp. 335-338.

[Nebuloni and Capsoni 2011] Nebuloni R., Capsoni C., “Effect of Hydrometeor Scattering on Optical Wave Propagation Through the Atmosphere”, Fifth European Conference on Antennas and Propagation (EuCAP 2011), Rome, Italy, 11-15 April 2011, pp. 2513 - 2517.

[Awan et al., 2009] Awan M.S., Nebuloni R., Capsoni C., Csurgai-Horváth L., Muhammad S. S., Nadeem F., Khan M. S., Leitgeb E.; “Prediction of drop size distribution parameters for optical wireless communications through moderate continental fog”, International Journal of Satellite Communications and Networking, Vol. 27, 2009, pp. 97-116.

## **5 VISIBILITY, ATTENUATION, PRECIPITATION AND RADIOMETRIC MEASUREMENTS IN PRAGUE**

(Vaclav Kvicera, Martin Grabner, Stanislav Zvanovec, Petr Dvorak)

### **5.1 6-year statistics of attenuation and visibility at 860 nm terrestrial FSO path**

#### **5.1.1 Overview**

Statistics of the optical attenuation that have been obtained from 6 years of measurements on a free space optical path, 853 meters long, with a wavelength of 860 nm are presented. The influence of individual hydrometeors on attenuation and statistics of visibility due to the individual hydrometeors are analyzed.

#### **5.1.2 System setup**

The experimental FSO path is located between the Czech Metrology Institute (CMI) and the Institute of Atmospheric Physics of the Academy of Sciences of the Czech Republic (IAP AS CR). The path length is 853 meters. The FSO link is working at 860 nm, the transmitted power is 16 dBm. The divergence angle is 9 mrad and the total receiving area is 515 cm<sup>2</sup>. The recording optical fade margin is 18 dB.

An automatic weather observation system and colour video-camera images of the space between the transmitter and the receiver sites are used for the identification of meteorological conditions. The Vaisala sensors are used for the measurement of temperature, humidity, air pressure and the velocity and direction of the wind. The dynamically calibrated heated tipping-bucket rain gauge with a collector area of 500 cm<sup>2</sup> is used for the measurement of rain intensities. The Vaisala PWD11 device is used for the measurement of visibility in the range from 2000 m down to 50 m. The meteorological data are synchronized in time with the hydrometeor attenuation measurement on the FSO link. Both the received FSO signal level and the meteorological data are recorded synchronously on a PC hard disk.

#### **5.1.3 Measurements and Analysis**

The obtained attenuation data were processed over a 6-year period from December 2003 to November 2009. All the recorded individual attenuation events were carefully compared with the concurrent meteorological conditions recorded by the PWD11 and video-camera images. Identified attenuation events were carefully classified according to the types of occurred hydrometeors. Attenuation events were classified into the following types: rain (R), a mixture of rain with snow (RS), a mixture of rain with hail (RH), snow (S), fog only (F), a mixture of fog with rain (FR), a mixture of fog with snow (FS), and a mixture of fog with rain and snow (FRS). For the better understanding, e.g. a mixture of fog with snow means fog events with occurrence of snow. A mixture of fog with rain means fog events with raining. It should be noted that the RS, RH, FR, FS, and FRS events occurs very rarely and the occurred rain intensities are usually very low (smaller than 15 mm/h). These classified attenuation events were statistically processed and the cumulative distributions (CDs) of attenuation due to hydrometeors were obtained for the individual months and the individual year periods.

### 5.1.4 Results

The obtained CDs of attenuation due to all the hydrometeors combined and to the individual hydrometeors separately on the FSO path over the 6-year period of observation are shown in Figure 1.1-1.

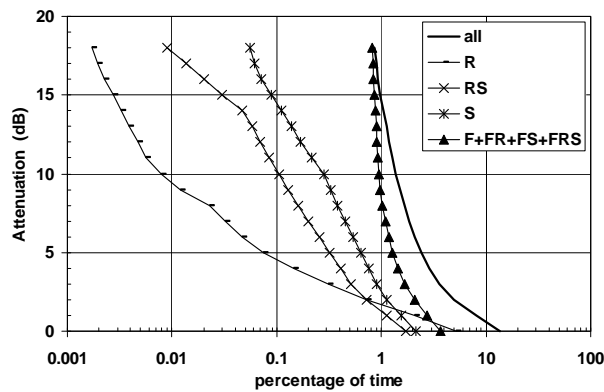


Figure 1: Obtained CDs of attenuation due to all the hydrometeors combined and the individual hydrometeors separately.

The obtained CD of attenuation due to all the hydrometeors combined over the entire 6-year period of observation is drawn by the solid line. This distribution can be considered as the long-term average annual distribution of attenuation due to all the hydrometeors combined in the sense of [ITU, 2009a], [ITU, 2009b]. It follows from Fig. 1.1-1 that the dominant attenuation events were caused by all fog events together, i.e. by F, FR, FS, and FRS events.

The influence of individual fog events on attenuation can be seen in Fig. 1.1-2.

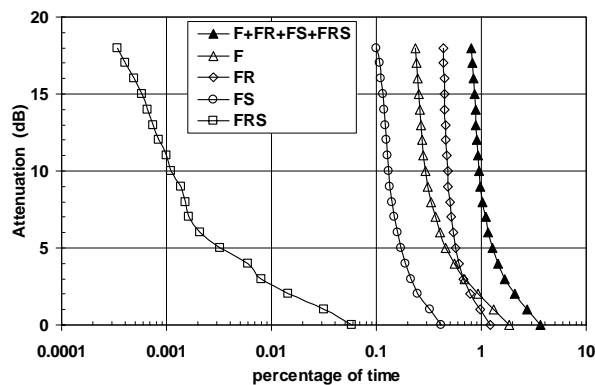


Figure 2: Obtained CDs of attenuation due to individual fog events.

It can be observed that the dominant attenuation events were caused by a mixture of fog with rain but the impact of attenuation due to fog only was also important. Attenuation due to a mixture of fog with snow and attenuation due to a mixture of fog with rain and snow were insignificant because these events occurred for much shorter periods and therefore their CDs are shifted about one decade or more to the smaller percentages of time against the CD of attenuation due to a mixture of fog with rain events.

Fig. 1.1-3 shows the obtained CDs of the average 1-minute rain intensities ( $R(1)$ ) for both all the hydrometeors combined and the individual hydrometeors. For FR events, the maximum value of  $R(1)$  for FR events was about 13.6 mm/h. This value of rain intensity can cause attenuation of about 6 dB/km [ITU, 2009b] which contributes to the fog attenuation during the FR events. The values of  $R(1)$  for RS, RH, S, FS and FRS events do not correspond to reality because, in most cases, it is dependent on the rate of the melting of snow accumulated in the collector of the rain gauge. These  $R(1)$  values are only informative and cannot be used for any calculations of attenuation due to these hydrometeors.

Very small differences can be observed between the CD of  $R(1)$  due to all the hydrometeors combined and the CD of  $R(1)$  due to rain only. The maximum difference is about 5 mm/h for 0.00045% of time.

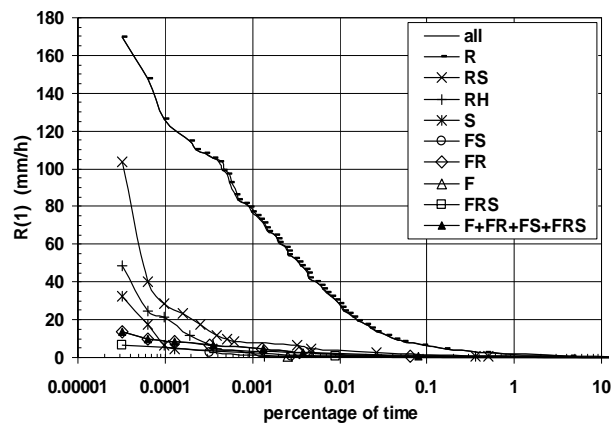


Figure 3: Obtained CDs of the average 1-minute rain intensities.

The obtained CDs of visibility due to all the hydrometeors combined (labelled as all) and to the individual hydrometeors separately are shown in Fig. 1.1-4.

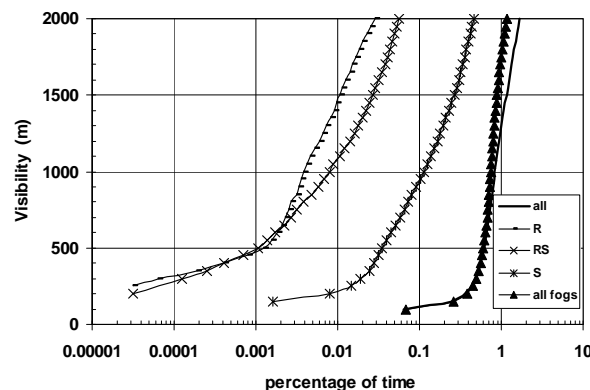


Figure 4: Obtained CDs of visibility due to all the hydrometeors combined and to the individual hydrometeors separately.

It can be seen in Fig. 4 that the visibility is dominantly reduced by all fog events together (F, FR, FS, and FRS events). The influence of snow, rain with snow and rain is insignificant, mainly for visibility shorter than 1000 m.

The obtained CD of visibility due to all of the fog events is shown in Fig. 4. It is composed from the CDs of visibility due to fog only, a mixture of fog with snow, a mixture of fog with rain and a mixture of fog with rain and snow. The corresponding CDs can be seen in Fig. 1.1-5.

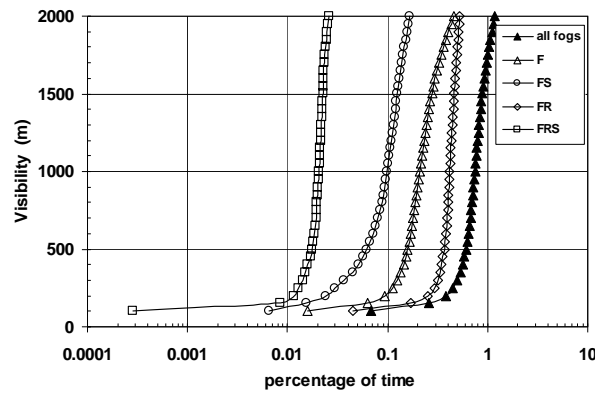


Figure 5: Obtained CDs of visibility due to all the fog events combined and to the individual fog events separately.

It can be seen from Fig. 1.1-5 that both a mixture of fog with rain events and fog only events have a significant influence on visibility, while a mixture of fog with snow events and a mixture of fog with rain and snow events are insignificant because they occur for small percentages of time only and therefore insignificantly only contribute to the CD of attenuation due to all the events combined. More detailed information about the experiment can be found in [Kvicera, 2011].

### 5.1.5 Summary

Attenuation events recorded over a 6-year long measurement campaign on the experimental FSO path in Prague, the Czech Republic, were systematically classified in order to quantitatively demonstrate the impact of different types of hydrometeors on FSO systems. The effects of the atmospheric conditions which are crucially important for the terrestrial FSO system performance were analysed. It was confirmed that, in our climatic region, fog and a mixture of fog with other hydrometeors can significantly degrade the availability performances of used FSO systems.

The dominant attenuation events as well as the significantly reduced visibility correspond to all fog events together, i.e. by F, FR, FS, and FRS events. The occurrences of a mixture of fog with rain and of fog only significantly reduced visibility and caused significant attenuation events.

The long-term results presented can be also regarded as the general reference information for the region of the central Europe. They may be also helpful for the development of new conversion models between atmospheric visibility and optical attenuation.

### Acknowledgment

This research was supported by the Ministry of Education, Youth and Sports of the Czech Republic under the Project No. OC09076 in the framework of COST IC0802.

## **5.2 Fog Attenuation Dependence on Atmospheric Visibility at Two Wavelengths for FSO Link Planning**

### **5.2.1 Overview**

Performance of the models of dependence between fog attenuation and atmospheric visibility is investigated using two-year experimental data measured on parallel FSO links with wavelengths of 830 and 1550 nm. Models fitted to measured data provide better estimation of attenuation for FSO link planning.

### **5.2.2 System setup**

An experimental 830 nm FSO link operates on a 100 m long path in Prague, the Czech Republic and is located 26 meters above the ground level. The transmitted optical power is 13 dBm, the diameter of Fresnel lens is 15 cm. With a fade margin of about 20 dB, it is possible to measure the specific attenuation up to 200 dB/km. The parallel 1550 nm FSO link operates with a transmitted power 3.5 dBm and Fresnel lens diameter of 18 cm. With a fade margin of about 13 dB, it is possible to measure the specific attenuation up to 130 dB/km. On-off keying (OOK) intensity modulation is used on the both links.

Optical calibration was performed before deploying the device. A received power is obtained from the calibrated Received Signal Strength Indicator (RSSI) signal of the FSO link. Meteorological conditions are identified by means of a video camera and an automatic meteorological station located near the receiver. The VAISALA PWD 11 equipment measures the atmospheric visibility (5% definition) values in the range from 50 m up to 2000 m using forward scattered light in the angle of 45°. A distance between the transmitter and the receiver of the visibility detector is about 0.5 m.

### **5.2.3 Measurements and Analysis**

Dense fog events observed during two year period (2008-2009) are analysed and the relation between fog attenuation and atmospheric visibility is derived.

### **5.2.4 Results**

Optical attenuation on the 830 nm FSO link and visibility simultaneously measured during 35 foggy days between January 2008 and December 2009 were selected for the analysis. 15 fog attenuation events were observed on the 1550 nm FSO link in between December 2008 and December 2009. The usual duration of fog events reached from tens of minutes up to several hours. Fig. 1.2-1 shows the scatter plot of average 1-minute optical attenuation values measured during those fog events and 1-minute atmospheric visibility values measured at the same time.

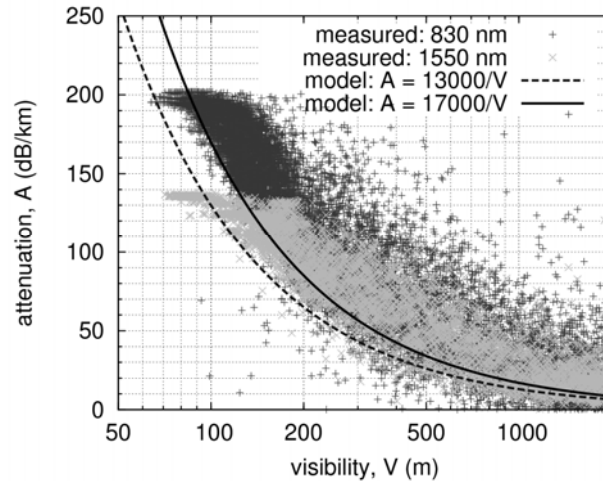


Figure 1: Specific attenuation of optical signal dependence on atmospheric visibility obtained from 01/2008 – 12/2009.

Despite significant dispersion of both plots, the inverse relation of the type (1) can be clearly recognized. Two basic model curves are also drawn in Fig. 1.2-1. The first one is equivalent to (1)  $A = 13/V$  and it gives dominantly lower values of attenuation for a given visibility value than measured ones. The second, higher curve shows relation  $A = 17/V$ , that can be obtained using 2% definition of visibility [Brussaard, 1996]. It gives better estimation of attenuation especially in the case of 1550 nm.

Note also that due to limited dynamical range of the both FSO receivers, measured attenuation values are saturated for the lowest visibilities observed. This is the reason why the attenuation values higher than 195 dB/km measured on the 830 nm link and the values higher than 130 dB/km on the 1550 nm link are excluded from the following analysis.

Fig. 1.2-2 shows comparison of measured data with specific models applied for wavelength of 830 nm. Kruse [Kruse, 1962], Kim [Kim, 2001] and two Al Naboulsi [Al Naboulsi, 2004] models for advection and convection fog are depicted. The results are not much different for Kim and Al Naboulsi models, Kruse model being the worst one. All models underestimate attenuation significantly. They give more or less a minimum value of attenuation expected.

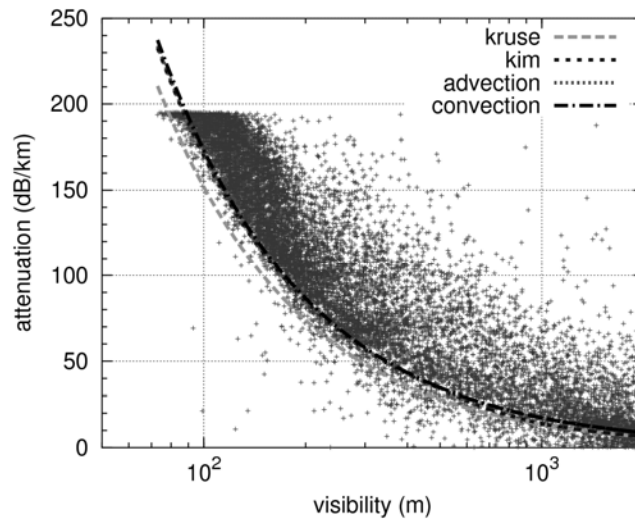


Figure 2: Measured attenuation (830nm)/visibility values and estimation by standard models.

In practice however, in order to estimate reliable statistics of fog attenuation on the FSO links, one should have more realistic relation that would reflect a mean value instead of a minimum value of attenuation for a given visibility. Here we propose two models, a *power-law model*:

$$A = aV^b \quad (6)$$

and a *simple inverse model*:

$$A = c/V \quad (7)$$

where  $a$ ,  $b$ ,  $c$  are model parameters to be optimized by fitting models to measured data.

Fig. 1.2-3 shows the fitted models with parameters  $a = 18.31$ ,  $b = -1.035$ ,  $c = 20.57$ .

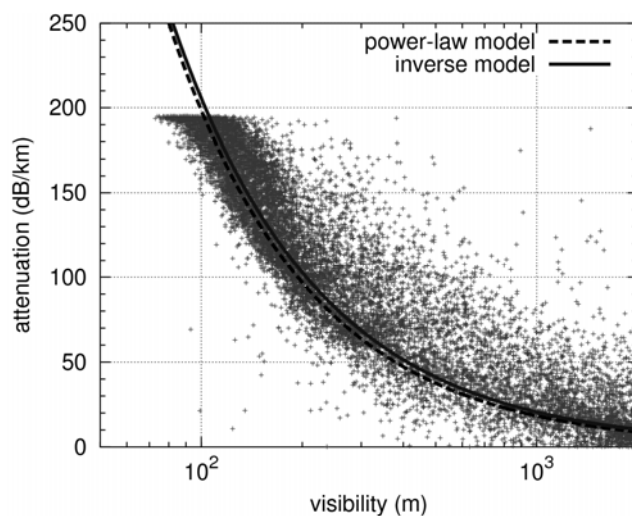


Figure 3: Measured attenuation(830nm)/visibility values and estimation by proposed models.

One can see the both models behave similarly on the dataset from 35 foggy days. Both models with fitted parameters agree very well with “mean” attenuation region for a visibility range between 100 m and 2000 m.

The same comparison is provided for attenuation observed on the 1550 nm FSO link. Fig. 1.2-4 shows the performance of standard models applied for this wavelength.

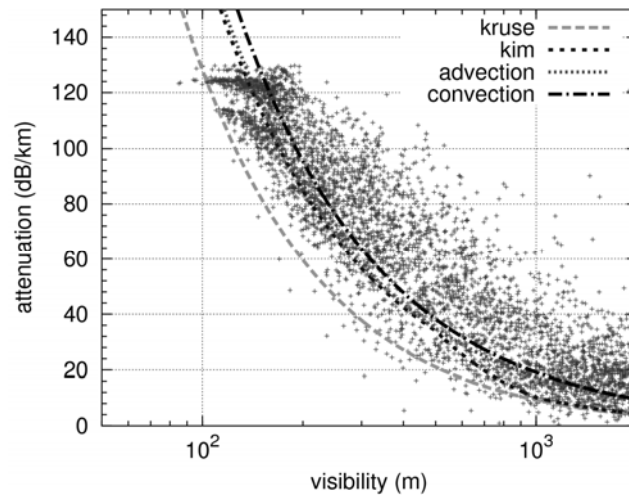


Figure 4: Measured attenuation at 1550nm / visibility values and estimation by standard models.

The classical Kruse model shows the worst agreement with measured data again. Other models fit the measured data better than at wavelength of 830 nm. Note however that Kim model exhibits transient behaviour for visibility between 0.5 and 1 km, which seems to be not observed in the experiment.

Again, very similar performance of the both proposed models is seen in Fig. 1.2-5 on the dataset of 15 foggy days.

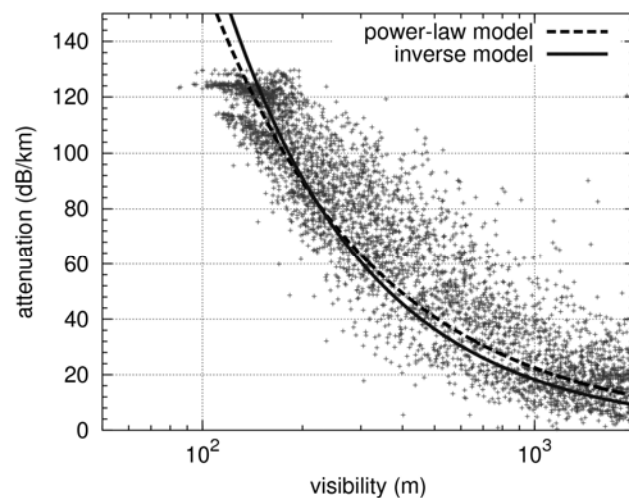


Figure 5: Measured attenuation at 1550nm / visibility values and estimation by proposed models.

It is interesting to compare the fitted value of parameter  $c$  of the inverse model with the result  $c = 10$  derived from 6 foggy day data of 1550 nm attenuation measured in Redmond, USA [Fischer, 2008]. The significant difference suggests that it is not appropriate to use a single value model for different climatic regions. Fig. 1.2-5 shows the fitted models with parameters  $a = 22.44$ ,  $b = -0.8616$ ,  $c = 18.22$ .

Performance of discussed models is compared in Tab. 1 using root mean square errors. Note that stated RMS errors also give useful information about the amount of dispersion of the relation attenuation/visibility.

*Table 1. RMS errors of models*

RMS (dB/km)	wavelength (nm)	
<b>Model</b>	<b>830</b>	<b>1550</b>
Kruse	41.4	32.5
Kim	33.1	21.1
Al Naboulsi advection	32.5	19.5
Al Naboulsi convection	31.7	19.6
Power-law (fitted)	27.0	16.8
Inverse (fitted)	25.7	19.3

Detailed theoretical background can be found in [Grabner, 2010].

### 5.2.5 Summary

The relation between fog attenuation and atmospheric visibility has been studied experimentally using FSO links operating at the two wavelengths of 830 and 1550 nm. These wavelengths fall into the two most utilized bands for FSO systems. The performance of standard models is enhanced by the proposed models with fitted parameters. Long term data of fog events is used so the seasonal variability of fog parameters is taken into account. The results suggest that local climatic conditions may play a more important role than expected. Locally verified models of attenuation/visibility dependence are clearly needed for the reliable design of FSO links with prescribed error performance and availability objectives.

### Acknowledgment

This research was supported by the Ministry of Education, Youth and Sports of the Czech Republic under the Project No. OC09076 in the framework of COST IC0802.

## 5.3 Prague-Ruzyne airport visibility data processing results

### 5.3.1 Overview

Cumulative distributions of visibilities obtained from Prague-Ruzyne airport visibility data processing over 13 years of observation are presented. A great year-to-year variability in accordance with individual synoptic situations occurring during the years is observed.

### 5.3.2 System setup

The visibility measured at airports provides a good estimate for the assessment of fog impairment. Therefore, fog visibility data obtained by the Vaisala transmissometer located at the Prague-Ruzyne airport from January 1996 to December 2008 (13 years of observation) were statistically processed.

### 5.3.3 Measurements and Analysis

Fog visibility data were statistically processed over the individual years, the individual months and the individual hours. The following cumulative distributions (CDs) of visibility were obtained:

- 1) CDs of visibility for individual years,
- 2) CDs of visibility for individual months over the whole period of processing,
- 3) CDs of visibility for the worst hour over the whole period of processing, and
- 4) CDs of visibility for the average year and the average worst month over the entire 13 year period of processing.

### 5.3.4 Results

The obtained CDs of visibility for individual years are given in Fig. 1.3-1. The frequency of fog events shows a great year-to-year variability in accordance with the frequency of individual synoptic situations occurring during the year.

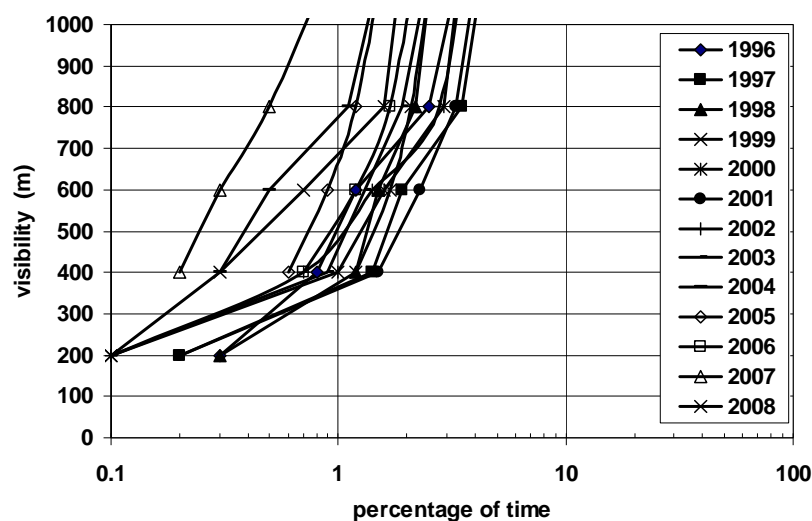


Figure 1: Obtained CDs of visibility for individual years.

As can be seen in Fig. 1.3-2, fog occurred most frequently in November and January due to frequent temperature inversion situations. Fog events occur sporadically during the spring and summer months.

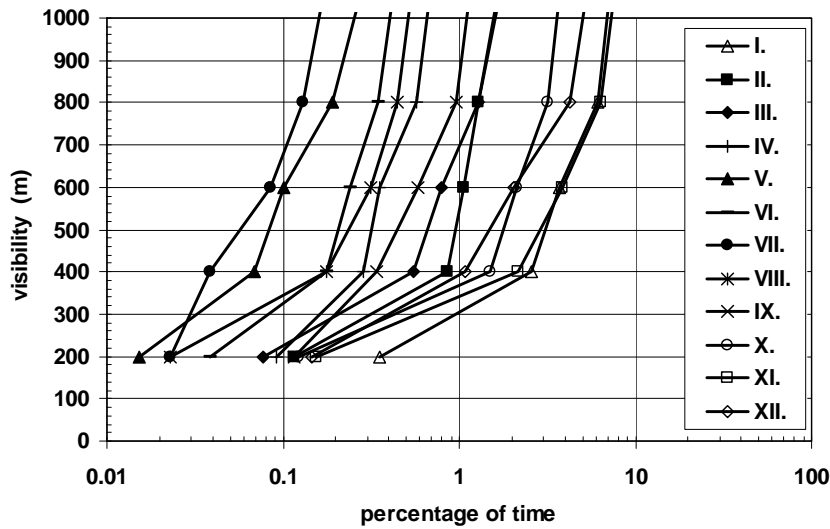


Figure 2: Obtained CDs of visibility for individual months.

The CD for the worst month is formed as for visibility between 1000 m and 600 m by the pertinent part of CD for November, and for visibility smaller than 600 m by the pertinent part of the CD for January.

Fig. 1.3-3 confirms the presumption that the reduced visibility most frequently occur during the sunrise between 4 and 7 a. m. due to the fact that the radiation can cause dense fog events. On the other hand, the reduced visibilities sparsely occur during afternoon between 12 and 16 o'clock.

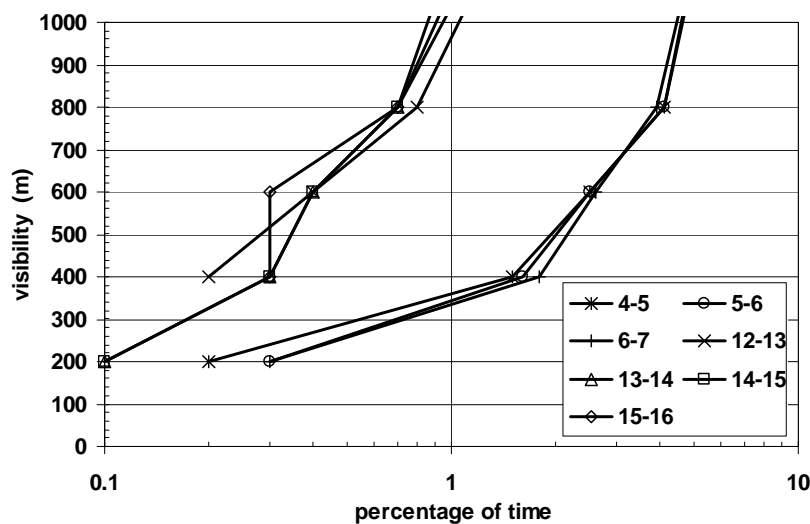


Figure 3: Obtained CDs of visibility for individual hours.

The CD for the worst hour is formed as for visibility between 1000 m and 700 m by the pertinent parts of CDs for hour between 4-5 and 5-6, and for visibility smaller than 700 m by the pertinent part of the CD for hours between 6-7.

The obtained CDs of visibility for the average year and the average worst month over the entire 13 year period of observation, given in Fig. 1.3-4, can be converted to CDs of attenuation due to fog by one of the relevant methods. The CDs obtained can be used for the assessment of availability performance of the FSO link in the climatic region of fog observation.

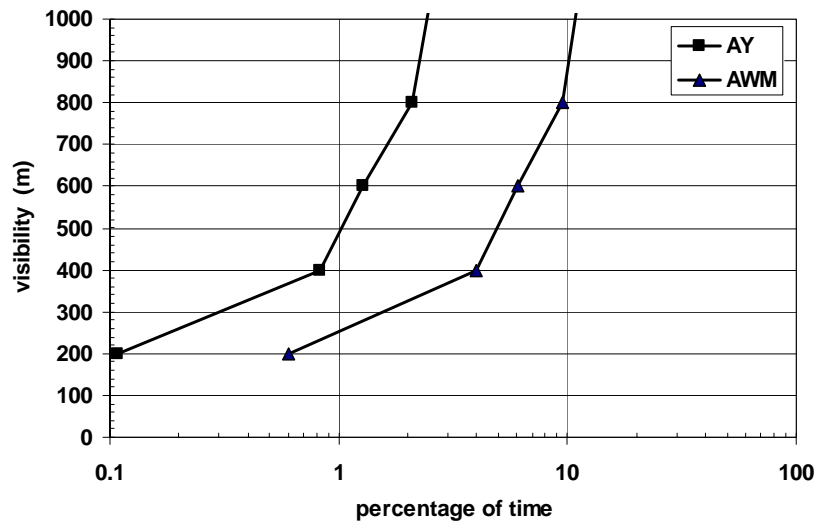


Figure 4: Obtained CDs of visibility for the average year and the average worst month over the entire 13 year period.

The frequency of fog events shows a great year-to-year variability in accordance with the frequency of individual synoptic situations occurring during the years. Fog occurred most frequently in November and January due to frequent temperature inversion situations. Fog events occur sporadically during the spring and summer months. The reduced visibility most frequently occurs during the sunrise due to the fact that the radiation can cause dense fog events.

The obtained CDs of visibility for the average year and the average worst month over the entire 13 year period of processing can be converted to CDs of attenuation due to fog accordance with either the relevant ITU-R Recommendation or other common methods. The obtained CDs of attenuation due to fog can be used for the assessment of availability performances of FSO communication links in the climatic region of fog visibility measurement.

More results obtained were presented in [Kvicera, 2010].

### 5.3.5 Summary

Cumulative distributions of visibilities obtained from Prague-Ruzyne airport visibility data processing over 13 years of observation were presented.

CDs of visibility for individual years, CDs of visibility for individual months over the whole period of processing, CDs of visibility for the worst hour over the whole period of processing, and CDs of visibility for the average year and the average worst month over the entire 13 year period of processing can be converted to CDs of attenuation that can be used for the assessment of availability performances of FSO links.

## Acknowledgment

This research was supported by the Ministry of Education, Youth and Sports of the Czech Republic under the Project No. OC09076 in the framework of COST IC0802.

## 5.4 Joint Characteristics of Microwave Radiometer and Free-Space Optical Link Measured at CTU in Prague

### 5.4.1 Overview

Microwave radiometers have been used as ground or satellite-based instruments for the measurement of temperature radiation emitted by objects, the Earth's surface, and for the monitoring of background space or atmospheric noise for tens of years [Ulaby, 1981]. Even though radiometric measurements have been performed for decades and many phenomena were thoroughly described, today's technological enhancements still open up new research challenges. This is especially true with the movement to higher frequency bands (millimeter, THz, optical or hybrid RF/optical [Nadeem et al., 2009]) allowing the utilization of higher data rates. Nonetheless, the availability of these emerging communication systems is essentially influenced by dynamic atmospheric phenomena such as rain [Zvanovec and Pechac, 2012]. Since radiometric systems can even be built as a monolithic microwave integrated circuits (MMIC) the future high-end wireless communication links could be equipped with a low-cost radiometer [Borgarino et al., 2009] to measure and predict in advance any atmospheric phenomena that might affect the reliability of the link. The aim of this chapter is to introduce results of joint measurement by Microwave Radiometer and Free-Space Optical Link Measured at Czech Technical University in Prague.

### 5.4.2 Measuring equipments

The microwave radiometer was utilized for long term noise temperature monitoring. The radiometer is based on Dicke switch design with working frequency range 10.95 - 12.75 GHz (satellite band). This type of radiometer introduces higher advantage especially by elimination of effects of gain fluctuations. A general description of brightness temperature and rain statistics was presented in [Hogg, 1989]. The dependence of the brightness temperature and rain intensity database (simulated) was analyzed from the air in [Meneghini et al., 1997] using the maximum a posterior probability criterion. The retrieval of rain and cloud parameters from space-borne radiometer measurements was well described in [Pierdicca et al., 1996]. An estimation of rainfall rates and columnar hydrometeor contents from joint measurement data from a spaceborne radiometer and radar was proposed in [Marzano et al., 2005]. Nowcasting of rain events from satellite microwave and infrared sensor imagery (e.g. for emergency issues) was investigated in [Marzano et al., 2007].

A parabolic antenna of the radiometer points horizontally towards tilted planar mirror. In the Dicke design the radiometer switches in turns between the antenna output and the reference (temperature stabilized load). After signal passes through internal amplifiers and a detector, part of signal is detected at the switching frequency by a synchronous detector. The output signal of the synchronous detector is proportional to the difference of noise temperature of an observed object and the reference load.

To fully access optical link performance, two free-space optical transceivers WaveBridge 500 by Plaintree were placed on the roofs of two eight-storied buildings in the CTU campus, approximately 30 meters above ground. This way the optical link having a length around 120 meters was built. The optical wireless system works at the wavelength of 850 nm, transmitted power was set on 20 dBm and beamwidth of LED is 1 degree. Received optical power detected in terms of Strength Signal Indicator (RSSI) is read by adjusted digital voltmeter and stored in a computer – levels of the received optical power corresponding to the voltage were carefully calibrated. Data from two meteorological stations located in the middle of the link and near one of the FSO transceivers were used for further analyses. The both stations collected the temperature and humidity, atmospheric pressure, precipitations, speed and direction of the wind measured by anemometer.

### 5.4.3 Results

Joint statistics between radiometric data and meteorological data were searched for. For the case of short-term measured statistics (from hour up to daily records) of noise temperature and atmospheric temperature a higher correlation was found (correlation coefficients higher than 0.8). These short-term correlations reached such high values only when relatively stable curves of temperature were measured and simultaneously the noise temperature event was distinct. It was proven that these events are caused by shading of particular clouds. It is easy to understand, when a cloud overshadows the Earth surface, the temperature falls. With the temperature decrease all other atmospheric quantities change similarly. Unfortunately, these mentioned events were rarely distinguished. For majority of time, more complicated atmospheric features were observed.

Contrary to short term statistics, no long-term correlation of measured noise temperature and meteorological data was observed. The noise temperature has no statistically significant long-term relationship either with the atmospheric temperature, relative humidity or pressure. Correlations coefficients from the monthly observation varied in the wide range (from negative linear -0.8 up to positive 0.8), so prediction of precipitations from correlation coefficients between noise temperature and other meteorological parameters was impossible.

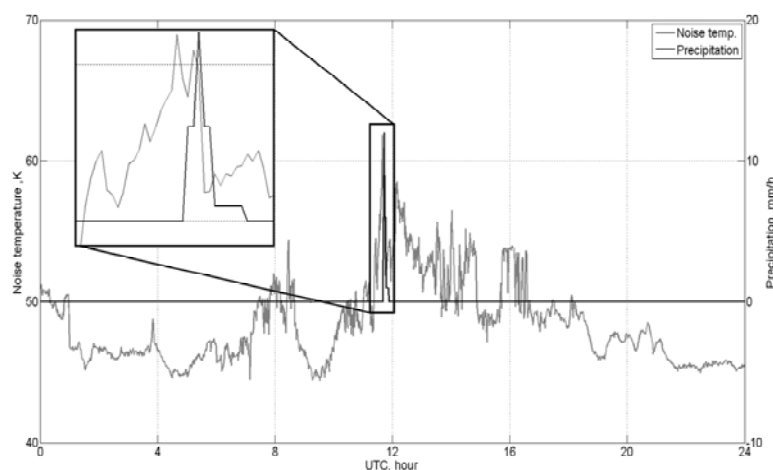


Figure 1: Noise temperature swell at the beginning of the rain measured on 28th of March 2010.

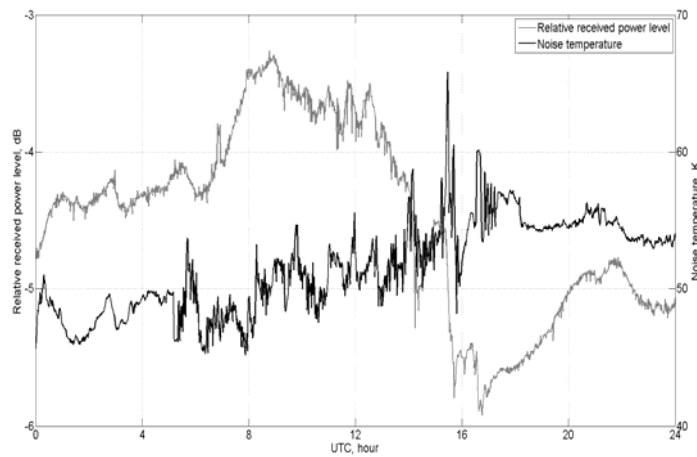


Figure 2: Example of comparison of noise temperature and power level received by FSO receiver on 29<sup>th</sup> of March 2010.

With the ingoing rainfall the vehement and short rise of the radiometer measured noise temperature can be observed. This rises can be observed mostly at the beginning of the rainfall. At this time the devaporation starts and the volume of water drops in the observed area strongly increases. After the burst of rain-fall the changes in the noise temperature vanish and the rain may not be detected by the radiometer even if the rain continues. Detectable transients disappear from measured data after the rain beginning. See the comparison of the measured noise temperature and precipitation in Fig. 1.1-1. Since it was determined that the rapid increase of noise temperature indicates a higher probability of a precipitation, the correlation between the noise temperature and received power of the FSO link was evaluated in next step.

Fig. 1.1-2 depicts the relation between the noise temperature and the received power. If the noise temperature curve is smooth, there can be find sharp fluctuations caused by the rainfall, in which a prediction of oncoming rain is possible and can be properly recognized in 66% of cases. On the other hand, non sharp fluctuations of noise temperature can be used to predict, rain in 43% of cases. Rapid fall of received optical power due to reduced visibility caused by particles scattering is apparent. With the ingoing rainfall the vehement and short rises of the radiometer measured noise temperature were observed. These rises were distinguished mostly at the beginning of the rainfall.

In the measuring period every precipitation started with a noise temperature swell. Noise temperature increased to 150% of the original value in 59% of cases and to 125% of the original value in 82% of cases. All increases correlated to FSO fades were perceptible in average 5.3 min before the precipitations start (with decreasing precision their could be observed up to 10 minutes before start of the event). At this time the devaporation starts and the volume of water drops in the observed area strongly increases. After the burst of rain-fall the changes in the noise temperature vanished and the rain could not be detected by the radiometer even if the rain continued. Detectable transients of measured noise temperature disappeared after the beginning of rain as well. Based on measured statistics our next research is focused to derivation of FSO fade forecasting model capable to on-line precede drops of optical backbone networks.

### 5.4.1 Summary

Due to the complicated and unpredictable nature of the atmospheric weather condition, it is difficult to estimate in advance the lightwave attenuation with a specific weather phenomenon. Based on measured data of the free-space link and adjacent weather stations and microwave radiometer several physical features were distinguished - especially time variant behavior within troposphere at beginnings of the rain events. Results of measurements show good agreement in a noise temperature swell preceding rain event and therefore there is possibility to equip FSO links with additional radiometer detection units.

### References

[Al Naboulsi, 2004] Al Naboulsi M., Sizun H., de Fornel F.: "Fog attenuation prediction for optical and infrared waves", *Optical Engineering*, vol. 43, 2004, pp. 319- 329.

[Borgarino, 2009] Borgarino, M., Polemi, A., Mazzanti, A.: "Low-Cost Integrated Microwave Radiometer Front-End for Industrial Applications", *IEEE Transactions on Microwave Theory and Techniques*, vol.57, no.12, pp.3011-3018, Dec. 2009.

[Brussaard, 1996] Brussaard G. Editor: "Handbook of Radiometeorology", 1st ed, Geneva, Switzerland, 1996, ITU.

[Fischer, 2008] Fischer K. W., Witiw M. R., Eisenberg E.: "Optical attenuation in fog at a wavelength of 1.55 micrometers," *Atmospheric Research*, vol. 87, March 2008, pp. 252-258.

[Grabner, 2010] Grabner M., Kvicera V.: "Fog Attenuation Dependence on Atmospheric Visibility at Two Wavelengths for FSO Link Planning," *Proc. of 2010 Loughborough Antennas & Propagation Conference (LAPC 2010)*, November 8-9, 2010, Loughborough, United Kingdom, pp. 193-196.

[Hogg, 1989] Hogg, D. C.: "Rain, radiometry, and radar", *IEEE Transactions on Geoscience and Remote Sensing*, vol.27, no.5, pp.576-585, Sep 1989.

[ITU, 2009a] Rec. ITU-R P.530-12 "Propagation data and prediction methods required for the design of terrestrial line-of-sight systems," ITU-R Recommendations and Reports, ITU, Geneva, Switzerland, 2009.

[ITU, 2009b] Rec. ITU-R P.841-4 "Conversion of annual statistics to worst-month statistics," ITU-R Recommendations and Reports, ITU, Geneva, Switzerland, 2009.

[ITU, 2009d] Rec. ITU-R P.1814 "Prediction methods required for the design of terrestrial free-space optical link," ITU-R Recommendations and Reports, ITU, Geneva, Switzerland, 2009.

[Kim, 2001] Kim I. I., McArthur B., Korevaar E. J.: "Comparison of laser beam propagation at 785 nm and 1550 nm in fog and haze for optical wireless communications", *Proc. SPIE 4214*, vol. 26, 2001.

[Kruse, 1962] Kruse P. W., McGlauchlin L. D., McQuistan R. B.: "Elements of Infrared Technology", 1st ed., London, UK: Wiley, 1962.

[Kvicera, 2010] Kvicera V., Grabner M., Vasicek J.: "Prague-Ruzyne airport visibility data processing results," *Geophysical Research Abstracts [USB Stick]*, corresponding abstract No. 9338, Volume 12, 2010.

[Kvicera, 2011] Kvicera V., Grabner M., Fiser O.: "6-Year Propagation Statistics Obtained on Terrestrial Free Space Optical 860 nm Path", Proceedings of the 11th International Conference on Telecommunications ConTEL 2011, Graz, Austria, June 15 - 17, 2011.

[Marzano, 2005] Marzano, F. S., D., Cimini, P., Ciotti, R., Ware: "Modeling and Measurement of Rainfall by Ground-based Multispectral Microwave Radiometry", *IEEE Transactions on Geoscience and Remote Sensing*, 43, 5, pp. 1000-1011, 2005.

[Marzano, 2007] Marzano, F. S., et al.: "Rainfall nowcasting from multi-satellite passive-sensor images using a recurrent neural network", *IEEE Transactions on Geoscience and Remote Sensing*, vol. 45, pp. 3800-3812, Nov 2007.

[Meneghini, 1997] Meneghini, R., Kumagai, H., Wang, J. R., Iguchi, T., Koza, T.: "Microphysical retrievals over stratiform rain using measurements from an airborne dual-wavelength radar-radiometer", *IEEE Transactions on Geoscience and Remote Sensing*, vol.35, no.3, pp.487-506, May 1997.

[Nadeem, 2009] Nadeem, F., et al.: "Weather effects on hybrid FSO/RF communication link", *IEEE Journal on Selected Areas in Communications*, , vol. 27, pp. 1687-1697, 2009.

[Pierdicca, 1996] Pierdicca, N., Marzano, F. S., d'Auria, G., Basili, P., Ciotti, P., Mugnai, A.: "Precipitation retrieval from spaceborne microwave radiometers based on maximum a posteriori probability estimation", *IEEE Transactions on Geoscience and Remote Sensing*, vol.34, no.4, pp.831-846, Jul 1996.

[Ulaby, 1981] Ulaby, F. T., et al.: "Microwave remote sensing: active and passive", Reading, Mass.: Addison-Wesley Pub. Co., Advanced Book Program/World Science Division, 1981.

[Zvanovec, 2012] Zvanovec, S., Pechac, P.: "First Results of Rain Spatial Parameters Analyses for Optical Links," Proceedings of the 6th European Conference on Antennas and Propagation (EUCAP 2012) IEEE, 2012, p. 320-322.

## 6 WEATHER PARAMETER AND FOG MEASUREMENTS IN MILEŠOVKA (STARTED IN COST IC0802)

(Ondrej Fiser, Vladimír Brazda, Zuzana Chladová, Petr Pesice, Jiri Pesek)

### 6.1 Overview

Our experimental activity is concentrated to the mountain meteorological observatory “Milešovka.” (see <http://www.ufa.cas.cz/html/meteo/mile.eng.html>). The Milešovka observatory (about 75 km north to Prague) is situated at the summit of an isolated, conically shaped mountain (837 m a.s.l.), overtopping the surrounding terrain by 400 meters. The slopes of the Milešovka Mt. are slanted up to 30° being nearly completely wooded, while birches, lindens, oaks, maples, and beeches create the forest. The conditions on the top of Milešovka are close to the free space one.

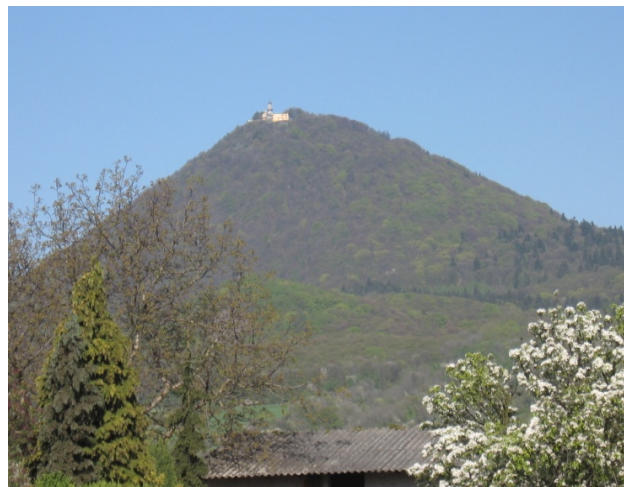


*Figure 6.1-1: Milešovka Mt. (837 m a.s.l.)*

### 6.2 System setup

Our experimental slant dual wave length optical link (FSO) is operating at “Milesovka” for more than 4 years. The link length is 60 m while wave lengths being 830 and 1550 nm. Link operates in simplex transmission. Both wavelengths are switched in periodic intervals. Data are sampled with resolution of 15 seconds and on-line transmitted to Prague. Data are processed to get the FSO statistics of atmospheric attenuation and to compare attenuation on 830 nm and 1550 channels.

We also measure relevant meteorological parameters influencing the FSO attenuation:

- 1) **rain rate** (resolution 1 minute)
- 2) **visibility** through:
  - a) Gerber’s Particle Volume Monitor (PVM-100), measurement of LWC



*Figure 6.2-1: PVM-100*

- b) Vaisala's Present Weather Detector, 2 sensors, first is close to TX (PWD-21), second one at the RX position (PWD-11)



*Figure 6.2-2: Vaisala PWD-21, TX position*

- c) subjective measurement

3) **3D wind velocity vector** using:

two Metek's 3-D sonic anemometers of the USA-1 type. One of them is sited close to the optical transmitter at the height of 4.5 m above the ground level. The second one is placed at the optical receiver station at the observatory's tower.



*Figure 6.2-3: The Metek 3D Ultrasonic anemometers USA1 used for turbulence measurements at the tower (left) and the lamp position (right).*

All wind velocity vector components are sampled and stored at 0.1 s resolution and on-line transmitted to Prague.

#### 4) Structure index

Statistical analysis of measured meteorological data and correlation with attenuation is involved in our research as well as generalisation of results, formulation of methods planning optical wireless links (optical as well as radio ones) is performed.

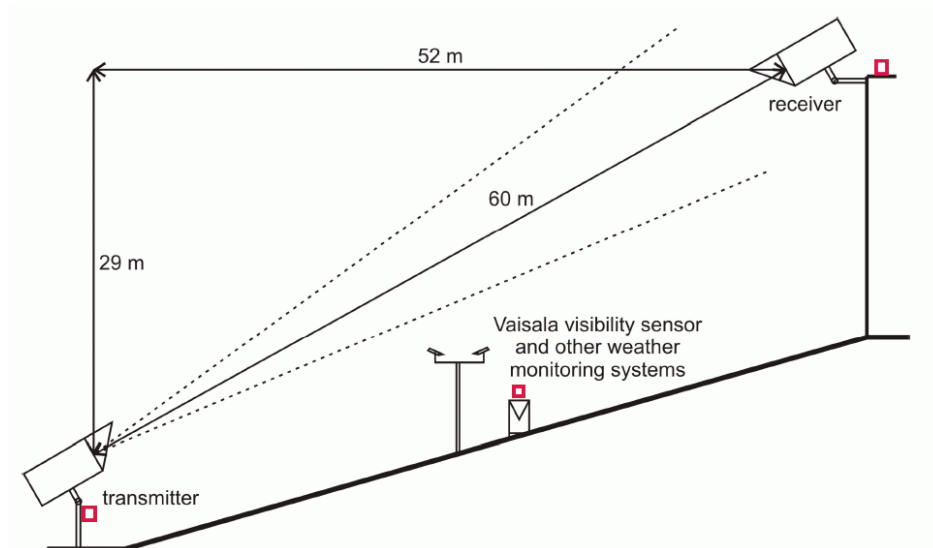


Figure 6.2-4: Arrangement of experimental FSO link at the Milesovka observatory. The humidity and temperature sensors are marked by red squares.

### 6.3 Measurement, analysis and results

In this chapter we present all results corresponding to the 1.1.2009-31.12.2011 period.

#### 6.3.1 General attenuation statistics

For basic illustration to see the statistical behaviour of the FSO experimental link attenuation we have prepared a histogram of all recorded attenuation (fog, rain, wind, refractivity index inhomogeneities etc.). Fig 6.3-1 shows CH2 (830nm) results. Approximately 80% of attenuation values are found in the attenuation interval 0 - 20 dB/km. For higher attenuation values is the probability density decreasing. Attenuation values above 600 dB/km are exceptional ones.

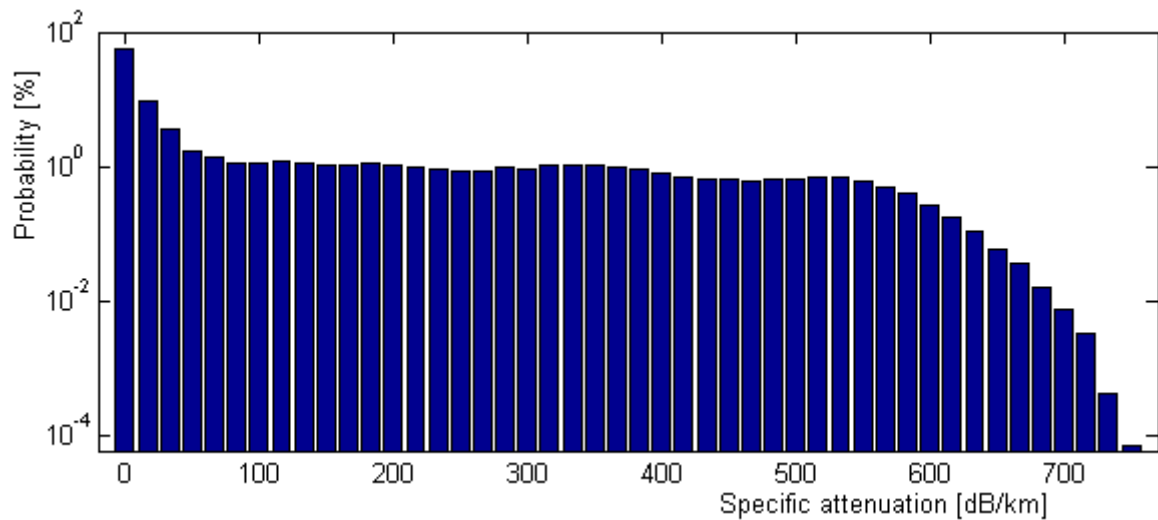


Figure 6.3-1: Probability density of total attenuation on CH2-830nm

Corresponding distribution function (exceedance probability) function of total attenuation derived from our measurement can be seen in Fig. 6.3-2. Surprisingly the attenuation on 1550 nm exceeds the attenuation on 830 nm.

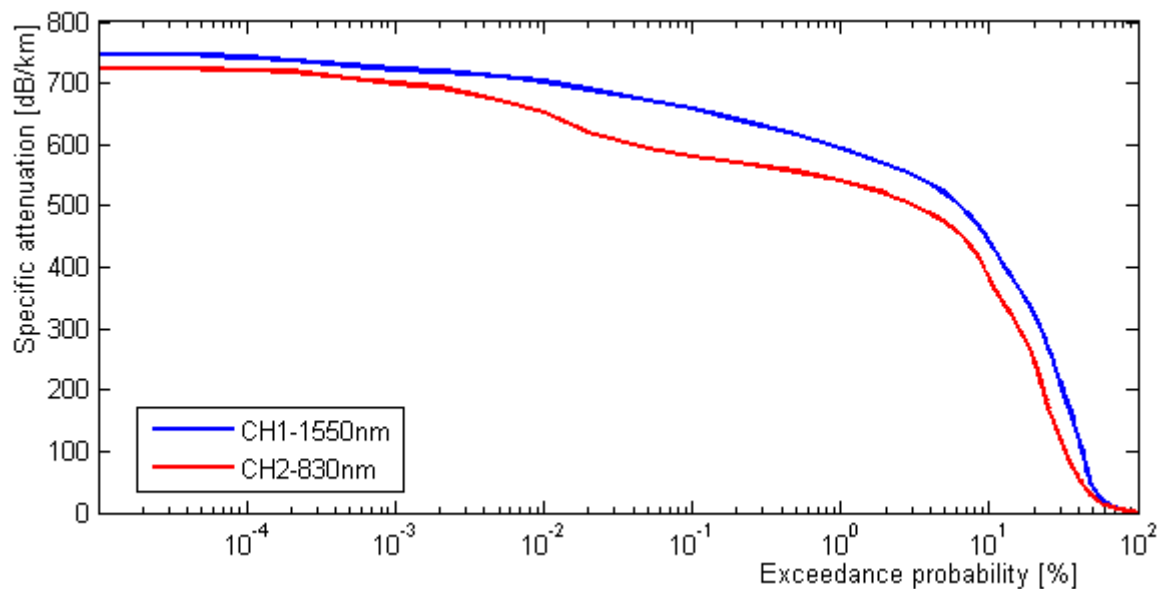


Figure 6.3-2: Cumulative distribution function of attenuation - Milesovka corresponding to the 3 year period (2009-2011)

### 6.3.2 Fog attenuation analysis

One can see the attenuation event example in Fig. 6.3-3. The attenuation on both channels is practically the same in this case. The attenuation is well correlated with the attenuation derived from the Kim formula (black curve). On the other hand the Kim formula underestimates the fog attenuation in the Milesovka case.

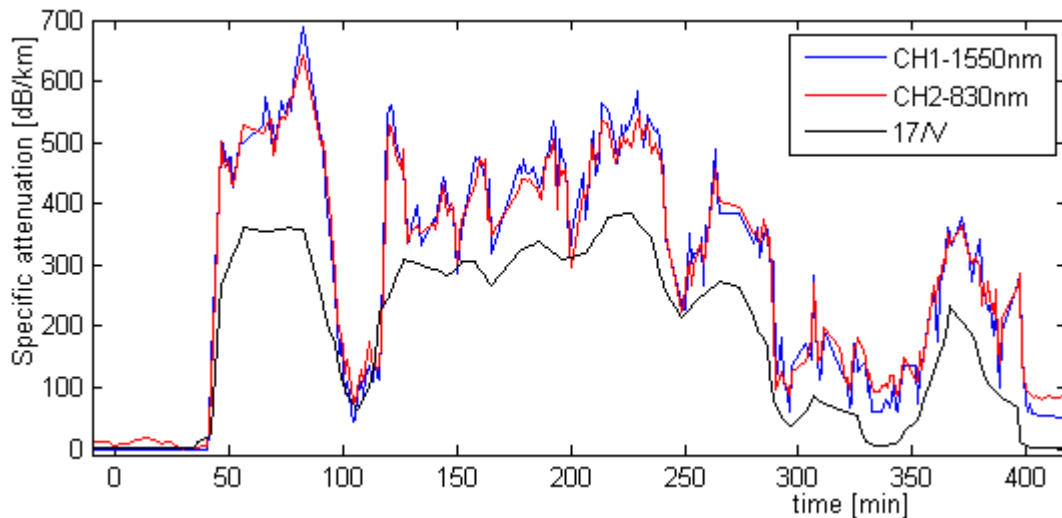


Figure 6.3-3: Fog event in 2011

Next figure expresses the found relationship between the specific fog attenuation and visibility for both channels. The attenuation on 830 nm channel (CH2) is slightly higher as expected. This figure is comparing the measured attenuation dependence on the visibility with the Kim theoretical formula [Kim et al., 2001]. One can see that Kim formula underestimates the observed attenuation values in correspondence to Fig. 6.3-3.

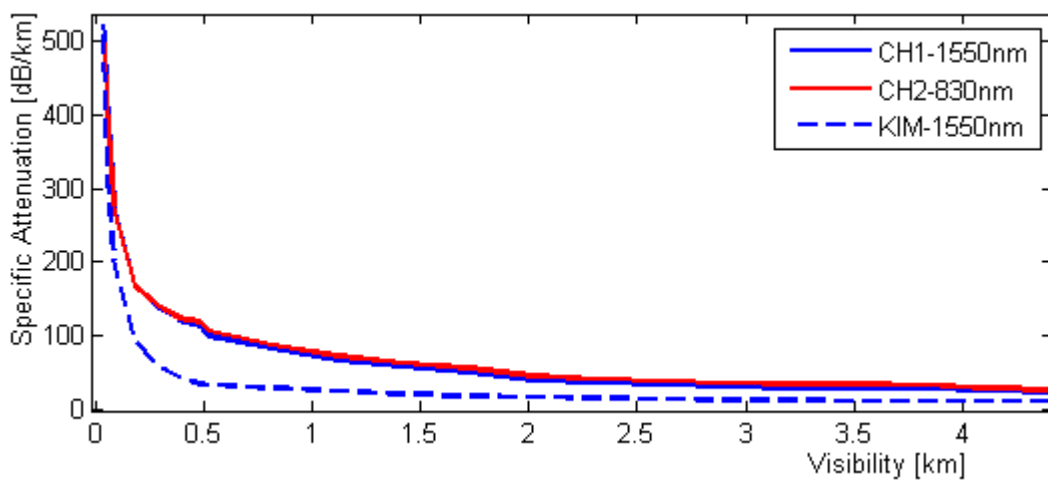


Figure 6.3-4: Scatterplot visibility vs. spec. attenuation

In next figure (Fig. 6.3-5) we show the annual course of the attenuation-visibility dependence. It is interesting that the attenuation values are higher in winter (for the same visibility value) comparing to the results in summer. It is due to worse condition in winter.

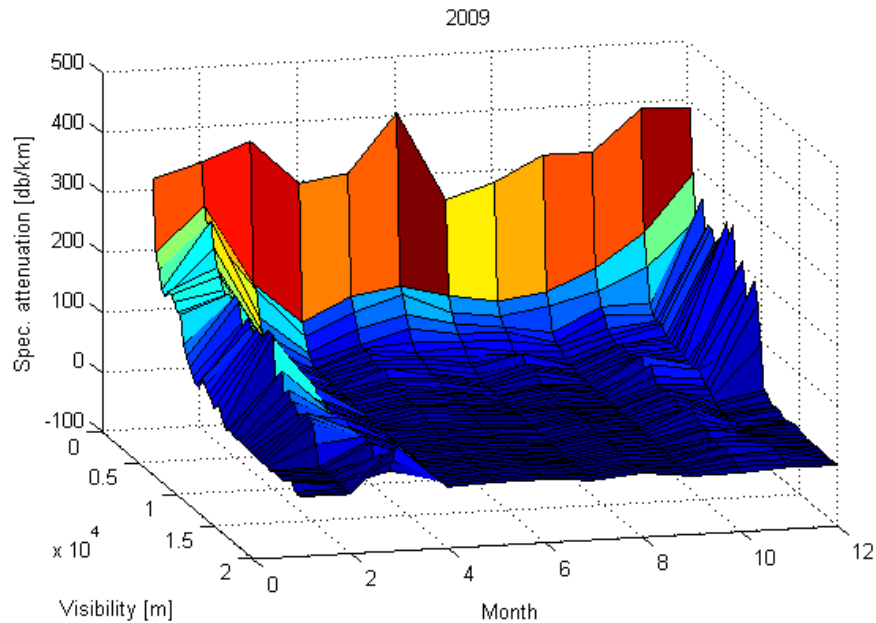


Figure 6.3-5: Scatterplot in each month of 2009

The average diurnal variations of the measured attenuation on both channels are shown in Fig. 6.3-6. Also the inverted visibility ( $1/V$ ) multiplied by a constant of 40 (for the scale purpose) is added. This figure demonstrates very good correlation of attenuation with inverted visibility (corresponding to theoretical assumptions). Further we can see that attenuation on both channels (830 and 1550 nm) is very similar except time period approx. 6.00 - 14.00 UTC when the attenuation at 830 nm distinctly exceeds attenuation at 1550 nm. This diurnal attenuation course corresponds to classical diurnal variations of fog density (inverted visibility). The distinct minimum values of attenuation (as well as inverted visibility) are observed around noon (11.00-16.00 UTC).

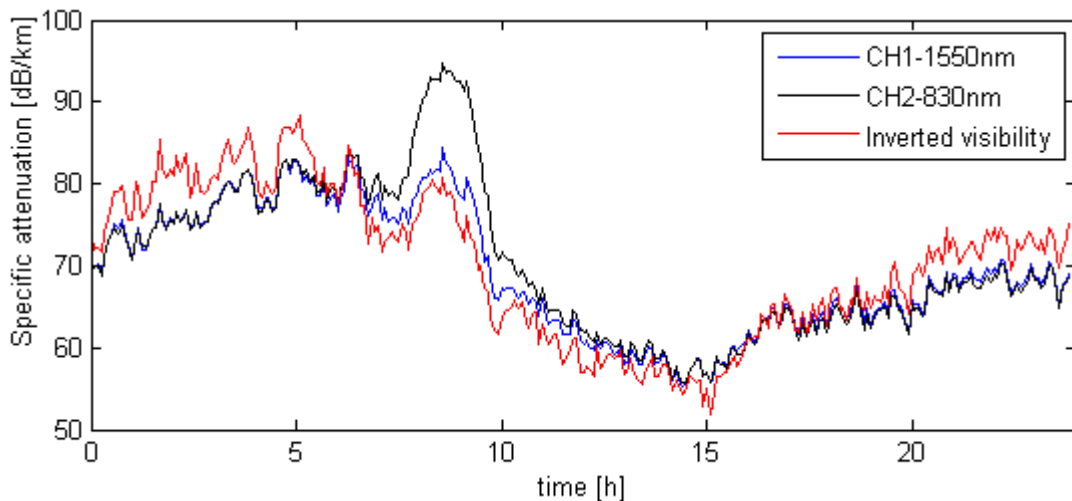


Figure 6.3-6: Diurnal variations of attenuations at 1550 and 830 nm and inverted visibility  $40/V$

Fig. 6.3-7 shows an example of selected interesting time courses of visibilities measured by two visibility sensors (TX and RX positions). Two different situations were observed. First one is occurring from 2 a.m. to 2 p.m. – inverted visibility on the tower (RX position) is

distinctly higher in comparison with the inverted visibility from TX site (2m above ground). It means that more dense fog occurs on the tower. We can explain through low cloudiness.

But after 2 p.m. there was no difference in both visibility values. It means that fog covered whole optical link, i.e. both tower (RX) and ground (TX) sites.

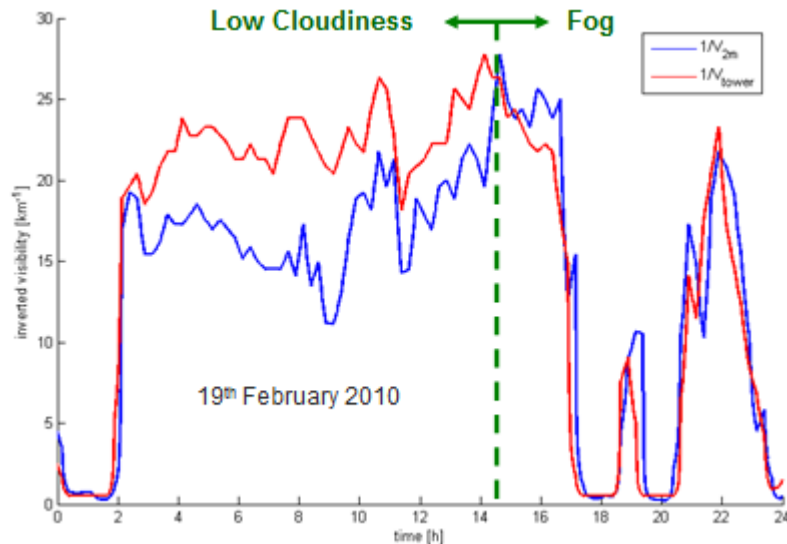


Figure 6.3-7: Time course of inverted visibility derived from sensors at 2 meters above ground (TX site, blue curve) and on the tower (RX site, red colour)

Fig. 6.3-8 shows the comparison of visibility data from both tower and ground positions in the CD form. Visibility of the tower is generally lower because the tower is sometimes hit by clouds unlike the ground position.

The difference between both PWD visibility sensor types at higher visibility values is obvious. It's not a problem for our purpose. We are interested in visibility values where the visibility is low because of fog attenuation. The correlation coefficient between time courses of these two visibilities (tower and ground) is about 0.92 while quantity values are quite different.

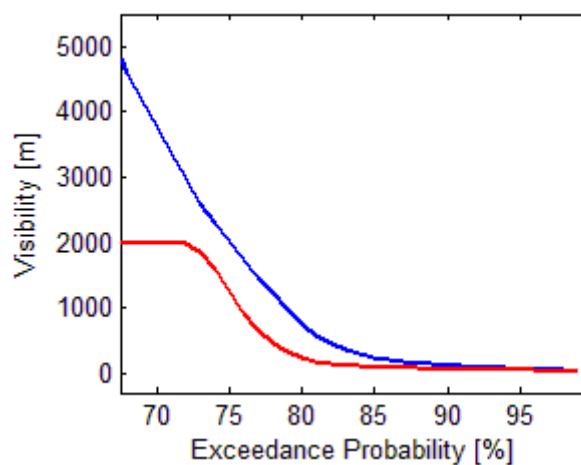


Figure 6.3-8: Distribution function of visibilities from two positions - 2 meters above ground (blue) and on the tower (red)

### 6.3.3 Rain attenuation modelling

To find the attenuations due to rain it is necessary to exclude fog events. We found an ideal value of visibility  $V = 1350$  m where we can declare: if the visibility is higher, the increased attenuation was not caused by the fog. Rain also reduces a visibility but not as much as fog. Besides this, rain and fog are usually exclusive phenomena. When the rain gauge records a rain rate, we know that reduced visibility is caused by rain, and not by fog. It is valid at most of the places, but we discovered that in our mountain observatory Milesovka both phenomena occur often at the same time. The reason is simple – we do not observe decreased visibility due to fog but due to low cloudiness reaching the mountain. If the rain clouds are just in a specific altitude where the rain drops are formed, it is really possible to observe rain and clouds concurrently - clouds have almost the same physical properties as fog. There is an example of attenuation time course in Fig. 6.3-9.

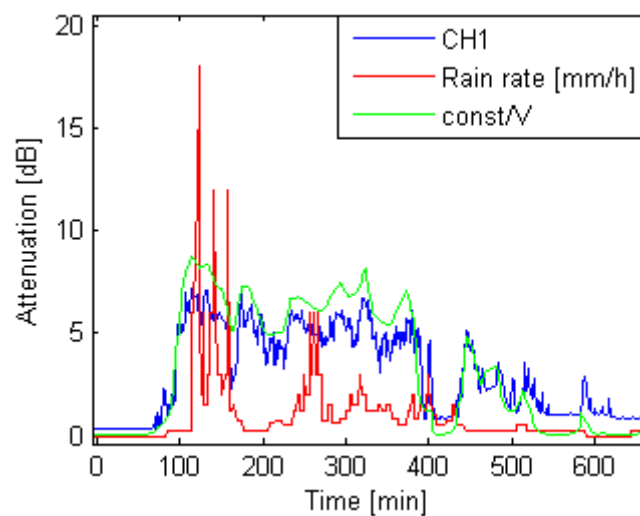


Figure 6.3-9: Selected attenuation event - time course of the FSO link attenuation with rain and clouds concurrently (in dB/60m)

One can see that the attenuation (blue curve) is influenced by visibility mainly (green curve). In Fig. 6.3-9 there is shown the inverted visibility multiplied by a constant (green curve) because it is proportional to the attenuation. But there a rain occurs concurrently. The main consequence is that in such rare cases the hybrid link (FSO link with a radio backup) would have a lower availability than required.

The example of rain attenuation time course is shown in Fig. 6.3-10.

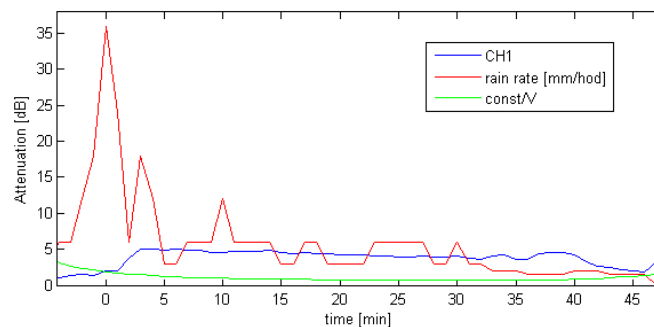


Figure 6.3-10: Attenuation on FSO due to rain

In this case the visibility is high (i.e. inverted visibility is low) and the rain is causing an attenuation up to 5 dB/60m. We can't be sure if attenuation is caused by rain only but in this case the very low inverted visibility indicates that the rain was dominating.

For rain attenuation modeling we use two theoretical formulas. The first one is derived from Mie equations [Brazda et al., 2012]:

$$\alpha_{rain} = 1.6 \cdot R^{0.63} [\text{dB/km}] \quad (6.3-1)$$

where R is rain rate in mm/h.

Similar formula is presented by Carbonneau in [Carbonneau and Wisley, 1998]:

$$\alpha_{rain} = 1.076 \cdot R^{0.67} [\text{dB/km}] \quad (6.3-2)$$

Here the basic statistics of measured rain rates are shown. It is a result of a long-term measurement in period 1.1.2009-30.6.2011. Calibrated precise tipping bucket rain gauge with resolution of 0,1 mm of precipitation amount is used for the measurement. Rain gauge records the precipitation amount every 60 s. Multiplying by 60 we obtain corresponding rain rate in mm/h in each minute. In terms of influence on FSO link attenuation we are interested in actual current rain rate and not, for example, in precipitation amount in whole hour. That's why we use "one-minute rain rate." Cumulative distribution of these rain rates is shown in Fig. 6.3-11 (the blue curve). Theoretical attenuation computed by (1) is represented by green color in Fig. 6.3-11 in correspondence with the right vertical axis.

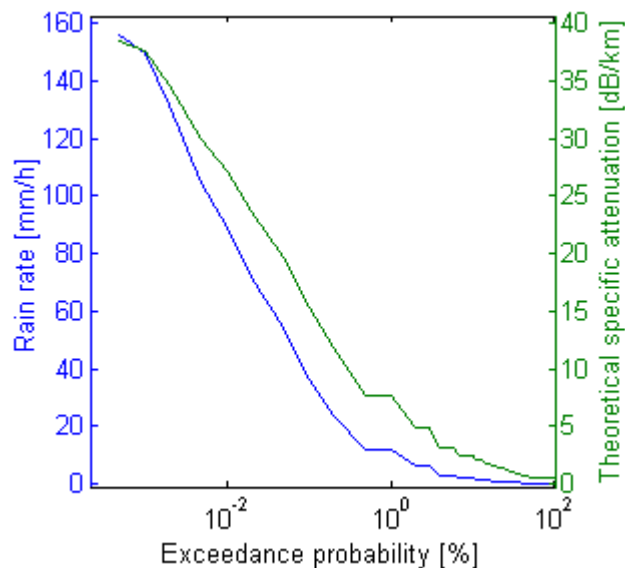


Figure 6.3-11: Cumulative distribution of rain rate and theoretically computed attenuation using Eq. 6.3-1 for the 1.2009-6.2011 period

For example on 1 percent exceedance time probability level there was a rain rate higher than 12 mm/h. One can see that also values over 150 mm/h have been recorded at our observatory. For example, rain rate 156 mm/h have been recorded during strong storm in 2009 (22/5). Attenuation on our FSO link exceeded 20 dB (length being 60 m). But the visibility was lower than 100 m, so we can't say that attenuation was caused by rain only. The right y-axis shows that specific attenuation on our link due to rain reached theoretically a few tens of dB/km, which gives a maximum of 2dB on our 60 m link.

Fig. 6.3-12 shows a maximum rain rates recorded in each month of the year. It proves that strong storms appear only in the summer.

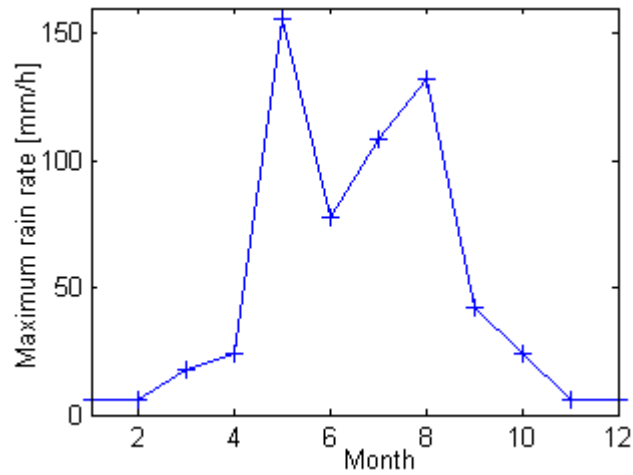


Figure 6.3-12: Maximum rain rate in every month measured at our observatory

An average precipitation amount in each month is displayed in Fig. 6.3-13. It shows that a summer is even rainier than autumn or a spring.

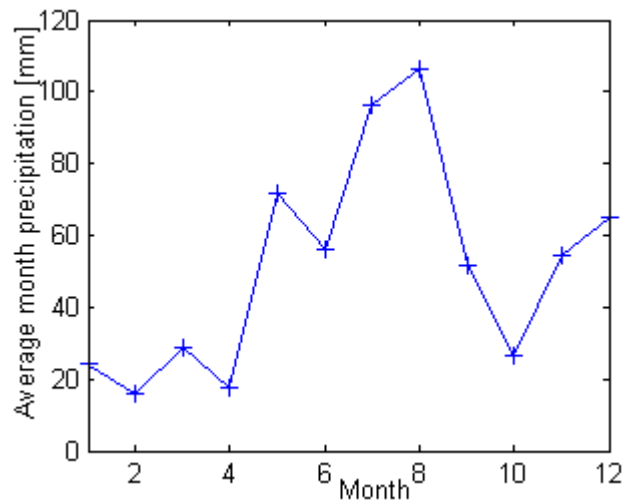


Figure 6.3-13: Average precipitation in every month of the year

The most important result is shown in Fig. 6.3-14. The x-axis is divided into intervals and the mean value of FSO attenuation is computed in each interval.

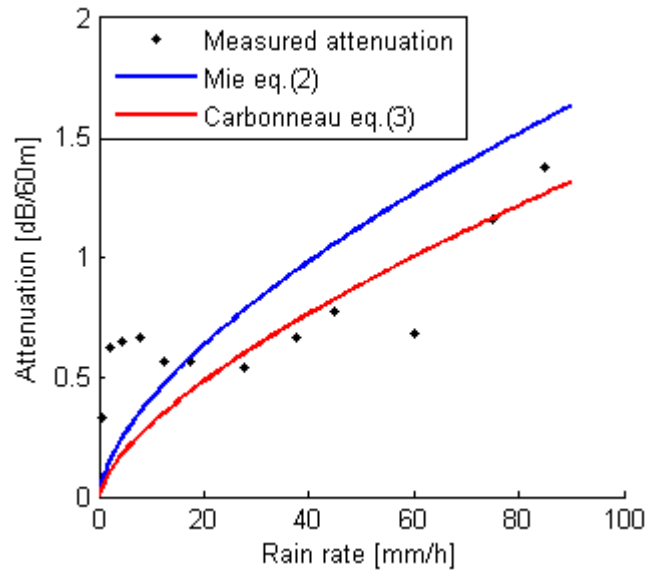


Figure 6.3-14: Averaged scatter plot of measured and theoretical rain attenuation

The measured values are in a good agreement with the theoretical formulas. Deviations are smaller than 0.2 dB. The bigger deviation at the rain rate of 60 mm/h is caused by little amount of data in this interval. We can't say which formula is more accurate, both are more or less right. Important is the fact that there is an obvious dependence attenuation-rain rate. Excluding fog events, the attenuation of our FSO link increases with increasing rain intensity. The quite big relative deviations are caused by the low attenuation absolute values, which is due to the short length of our FSO link. On the other hand we can be sure that the rain covers the entire length of the link which is necessary to investigate the rain impact on FSO.

### 6.3.4 Wind parameters

The wind measurements are performed by two Metek 3D Ultrasonic anemometers USA1. One of them is situated on the top of the observatory tower in the vicinity of the optical receiver, the other one is located on the lamp in the garden in the height of about 5 m above the surrounding terrain. The measurements are performed every 0.1 s because this measurements are the primary source for wind turbulence calculations.

Measurement of the data is continuous and database of all data in the period 1.1.2009 – 31.12.2011 has been made. Wind parameters have been correlated with FSO link attenuation values, according to the integration time 1 minute. For these calculations the data were adjusted. The missing values, values with fog (the visibility is smaller than 1350 meters) and rain were removed.

Next table contents the list of wind parameters. The detailed definitions of few parameters are shown below.

*Table 6.3-1. List of wind parameters*

1. 2D mean of wind direction
2. 2D mean wind speed
3. 2D intensity of turbulence
4. Mean sonic temperature
5. Mean of absolute value of horizontal wind component
6. Turbulent energy
7. Horizontal turbulent energy
8. Standard deviation of horizontal wind speed
9. Standard deviation of vertical wind speed (z axis)
10. Standard deviation of wind direction
11. 3D mean wind speed
12. 3D intensity of turbulence
13. Maximal gust

$$\text{Mean horizontal wind speed [m/s]} : \quad g = \sqrt{(u^2 + v^2)} \quad (6.3-3)$$

$$\text{2D-intensity of turbulence:} \quad I(2D) = \frac{\sqrt{\frac{1}{N} \sum (g - \bar{g})^2}}{\bar{g}} \quad (6.3-4)$$

$$\text{Turbulent energy [m2s-2]:} \quad E_T = 0.5 * \frac{1}{N} \sum ((u - \bar{u})^2 + (v - \bar{v})^2 + (w - \bar{w})^2) \quad (6.3-5)$$

$$\text{Horizontal turbulent energy [m2s-2]:} \quad E_T = 0.5 * \frac{1}{N} \sum ((u - \bar{u})^2 + (v - \bar{v})^2) \quad (6.3-6)$$

where u, v and w are x-, y- and z (vertical)- axis components of the wind speed vector  $\mathbf{v}$ .

For wind measurement illustration, here are figures 6.3-15 and 6.3-16 showing long term diurnal and annual variation of wind speed and wind turbulence. It is obvious that the wind speed is lowest at noon while maxima are reached close to midnight. The intensity of turbulence is maximal at noon in summer months, minimum was observed at midnight in November.

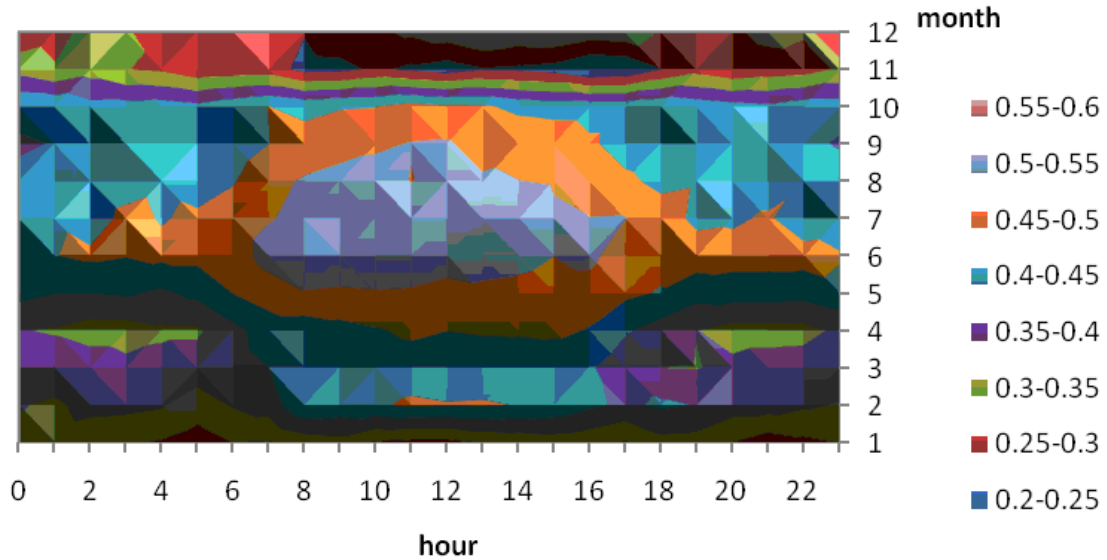


Figure 6.3-15: Annual and daily course of mean 2D intensity of turbulence  $I(2D)$  for year 2009 at the lamp position. One minute mean values were used.

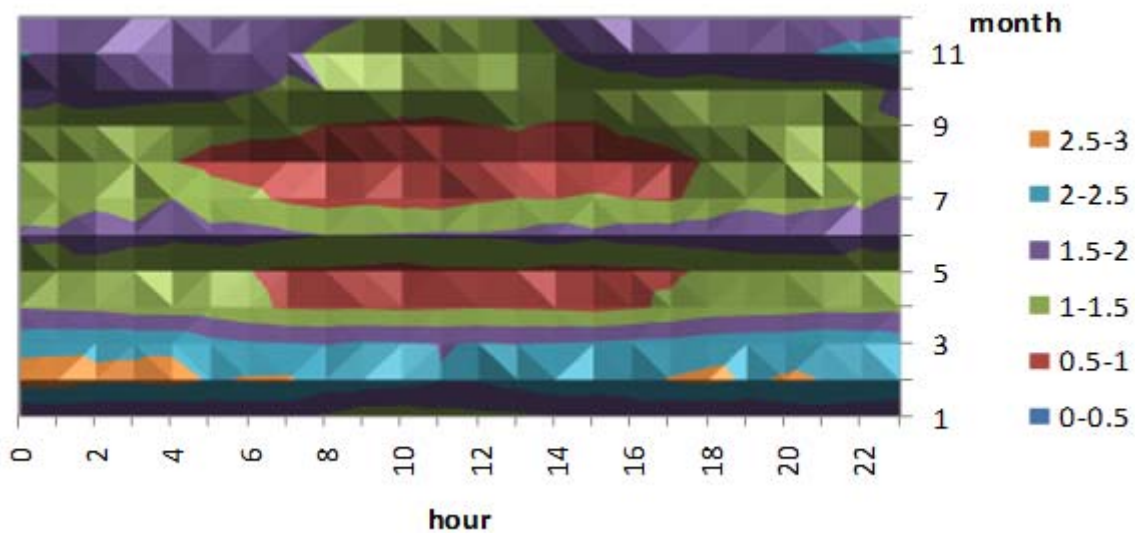


Figure 6.3-16: Annual and daily course of mean horizontal wind speed (g) [m/s] for year 2009 at the lamp position. One minute means were used.

Surprisingly, almost all presented wind parameters were found to be statistically significantly correlated with attenuation at FSO link. On the other hand, the explained variance was very low and it means, that the variables are correlated but their dependence is

very weak (Tables 6.3-2 and 6.3-3). The only one exception represents the sonic temperature. Its value of Pearson's correlation coefficient was very high (negative statistically significant correlation of sonic temperature and attenuation) and the percentage of explained variation was between 13 % for lamp position and 15 % for tower position. The results of this statistic are strongly influenced by high number of measured values (1 minute data) for 3 years (more than 400 000 values for tower position and 800 000 values for lamp position). The critical value for statistical significance is 1.96. This critical value was not exceeded in only one case of maximal gust.

If we don't exclude the fog events, the sonic temperature would be correlated negatively and statistically significantly with standard deviation of T.

*Table 6.3-2. Correlation and its statistical significance between wind parameters (the first column) and attenuation at the tower position. The second column is the value of Pearson's correlation coefficient, third column – the number of data (without fog events, rain events and periods of missing values), critical value for statistical significance (if it is higher than 1.96 it is statistically significant correlation between two quantities with normal distribution). In the last column there is a percentage of explained variance of the data.*

<b>No. of wind parameter</b>	<b>Tower vs. CH1</b>	<b>Number of data</b>	<b>Critical value</b>	<b>Explained variance [%]</b>
1	-0.0475	424377	-30.94	0.225
2	0.0337	424377	21.95	0.113
3	0.0597	424377	38.89	0.356
4	-0.3861	424377	-251.52	14.90
5	0.035	424377	22.80	0.122
6	0.1073	424377	69.89	1.151
7	0.1047	424377	68.20	1.096
8	0.0988	424377	64.36	0.976
9	0.0199	424377	12.96	0.0396
10	0.0307	424377	19.99	0.0942
11	0.0304	429681	19.92	0.0924
12	-0.0075	424377	-4.88	0.0056
13	0.0655	429688	42.93	0.429

Table 6.3-3. The same as Table 6.3-2 for correlation between wind parameters at the lamp position and attenuation of 1550 nm channel.

No. of wind parameter	Lamp vs. CH1	Number of data	Critical value	Explained variance [%]
1	0.0323	802427	28.93	0.104
2	0.0853	802427	76.41	0.727
3	-0.0229	802427	-20.51	0.052
4	-0.3627	802427	-324.9	13.15
5	0.0874	802427	78.29	0.763
6	0.0771	802427	69.06	0.594
7	0.0819	802427	73.36	0.67
8	0.0654	802427	58.58	0.427
9	-0.0486	802427	-43.53	0.236
10	0.0844	802427	75.6	0.712
11	0.0324	916037	31.0	0.104

Next figure shows the dependence of FSO link attenuation on the turbulent energy in 2009. The mean and median values of FSO attenuation are the most fluctuating when turbulent energy values are in an interval 12 – 17 m<sup>2</sup>s<sup>-2</sup> and the mean and median FSO link attenuation are increasing in this interval.

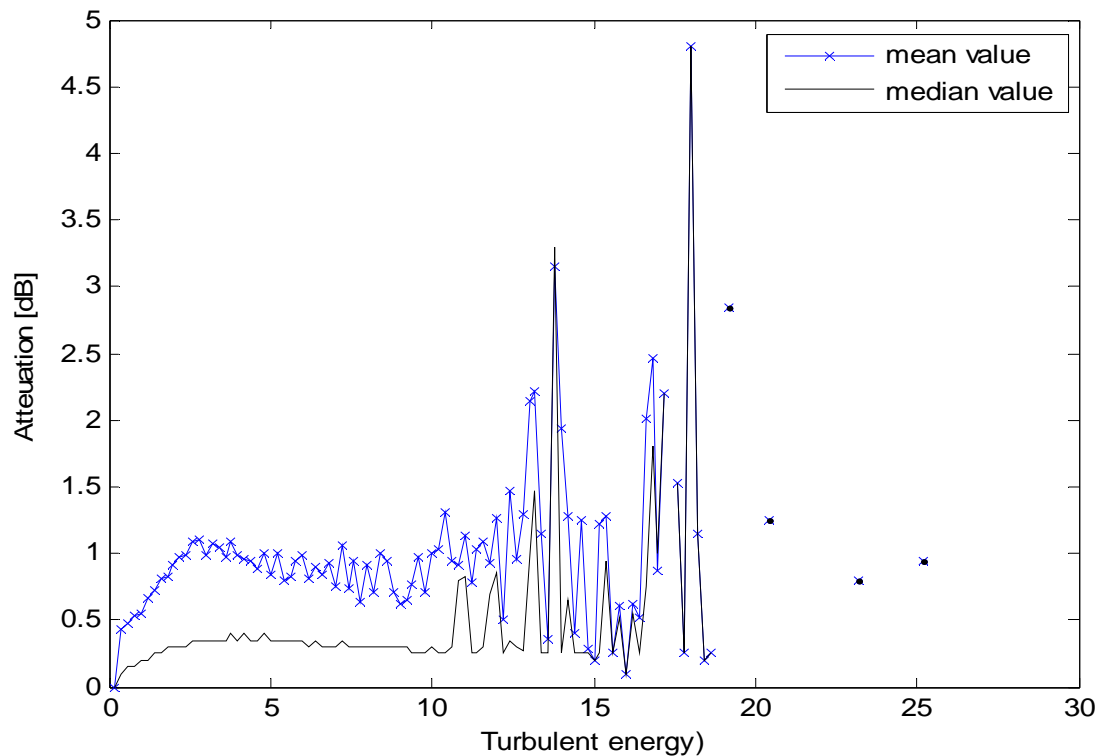


Figure 6.3-17: Attenuation of 1550 nm channel – turbulent energy dependence. Blue line is interval mean value, black line represents the median.

### 6.3.5 Measurement of air refractivity index in optical region

The refractivity index plays an important role in the propagation of FSO signal through the atmosphere. Beside the refractivity index of water (important for attenuation estimation of FSO signal due to fog and cloud droplets and due to rain drops) it is desirable to be familiar with the air refractivity index.

In this study, we have used the formulas published in [Stone and Zimmerman, 2001] while neglecting the influence of CO<sub>2</sub> concentration.

$$n = n_{sp} - 10^{-10}[(292.75)/(t + 273.15)] \times [3.7345 - 0.0401S] \times p_v \quad (6.3-7)$$

$$n_{sp} = 1 + p(n_s - 1)X/D \quad (6.3-8)$$

$$X = [1 + 10^{-8}(E - Ft)p]/(1 + Gt) \quad (6.3-9)$$

$$n_s = 1 + 10^{-8}[A + B/(130 - S) + C/(38.9 - S)] \quad (6.3-10)$$

$$S = 1/\lambda^2, \quad (6.3-11)$$

where  $n$  is the air refractivity index,  $\lambda$  is the wavelength in micrometers,  $p$  is the air pressure in Pascal,  $t$  is the air temperature in °C,  $A, B, C, D, E, F, G$  are constants enumerated in Table 6.3-4.

Partial water vapor pressure  $p_v$  is calculated using following formulas

$$p_v = (RH/100) \times p_{sv}(t) \quad (6.3-12)$$

$$p_{sv}(t) = 10^6 (2C/X)^4 \quad (6.3-13)$$

$$X = -B + \sqrt{B^2 - 4AC} \quad (6.3-14)$$

$$A = \Omega^2 + K_1\Omega + K_2 \quad (6.3-15)$$

$$B = K_3\Omega^2 + K_4\Omega + K_5 \quad (6.3-16)$$

$$C = K_6\Omega^2 + K_7\Omega + K_8 \quad (6.3-17)$$

$$\Omega = T + K_9/(T - K_{10}) \quad (6.3-18)$$

$$T = t + 273.15, \quad (6.3-19)$$

where  $p_{sv}$  is the saturated water vapor pressure in Pascal,  $t$  is the air temperature in °C,  $RH$  is the air relative humidity in percents,  $K1 - K10$  are constants (see Table 6.3-4).

*Table 6.3-4. Table of constants to compute the air refractivity index in optical and infrared region*

<b>Part 1:</b>	<b>Part 2:</b>
a=8342.54	K1= 1.16705214528e3
b=2406147	K2= -7.24213167032e5
c=15998	K3= -1.70738469401e1
d=96095.43	K4= 1.20208247025e4
e=0.601	K5= -3.23255503223e6
f=0.00972	K6= 1.49151086135e1
g=0.003661	K7= -4.82326573616e3
	K8= 4.05113405421e5
	K9=-2.38555575678e-1
	K10=6.50175348448e2

The measurements of air temperature and humidity started in November 2011 and average minute values of temperature and humidity are stored.

Temperature and humidity sensor near the transmitter is located approximately 50 cm above the ground surface, the sensor at the receiver site is placed on top of observatory tower. The measurements of automatic weather station located in the observatory garden were also considered. Air pressure measurements were taken from observatory measurements, the pressure sensor is located in the building.

Five winter month of temperature and humidity measurements were used to evaluate the air refractivity index.

Fig. 6.3-18 shows the monthly means of temperature for three locations. It can be seen that the weather station measurements are colder by tenth of degree than other values. This is probably caused by the position of sensor, which is at the standard 2 m height.

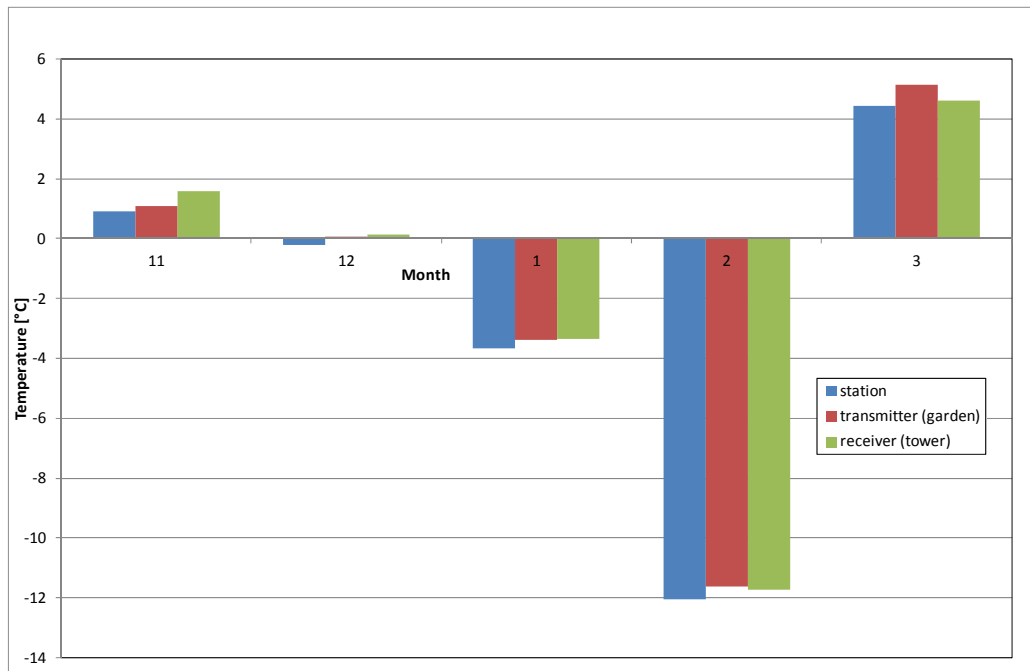


Figure 6.3-18: Monthly mean values of temperature for three evaluated measurements

Fig. 6.3-19 shows the daily courses of temperature and humidity for three considered positions of measurements. The transmitter station has evidently the highest amplitude in temperature as well as humidity and daily maxima are observed earlier. This measurement is influenced by the ground surface which is warmed during the day hours by sun. The receiver station located on top of tower shows the smallest differences between day and night values as it is less influenced by the surface.

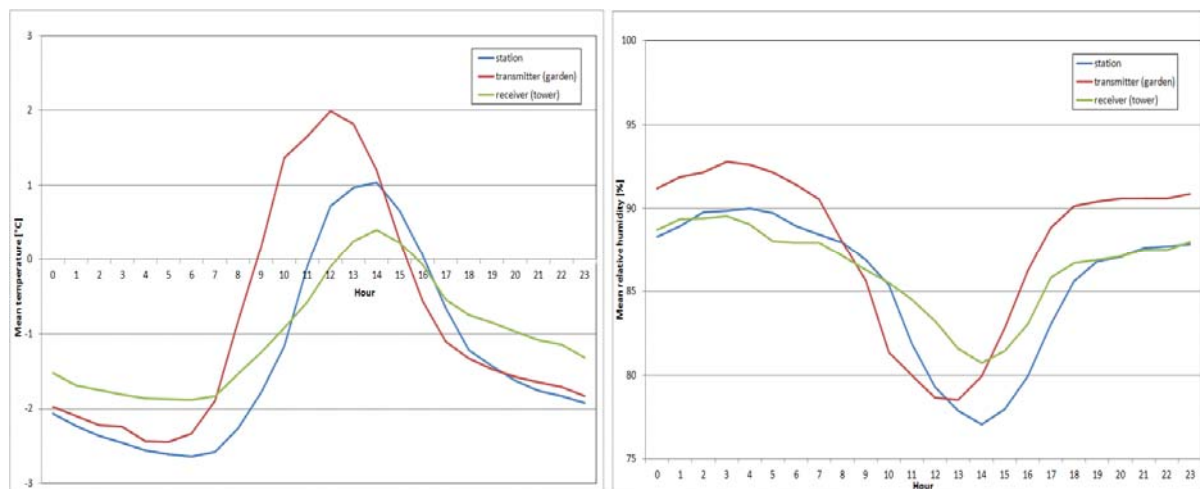


Figure 6.3-19: Daily course of temperature (left hand side) and relative humidity (right hand side) for three considered measurements

The air refractivity index was then evaluated for all three positions of measurement. The air pressure was taken from the observatory measurements. The Edlén formulas described in Chapter 1 were used to calculate the refractivity index values.

Daily course of refractivity index is shown in Fig. 6.3-20. It can be seen that the daily course indicates similar features like measurements of temperature and humidity. The values of refractivity index for different channels (830 nm and 1550 nm) differ while the shape of curves being very similar.

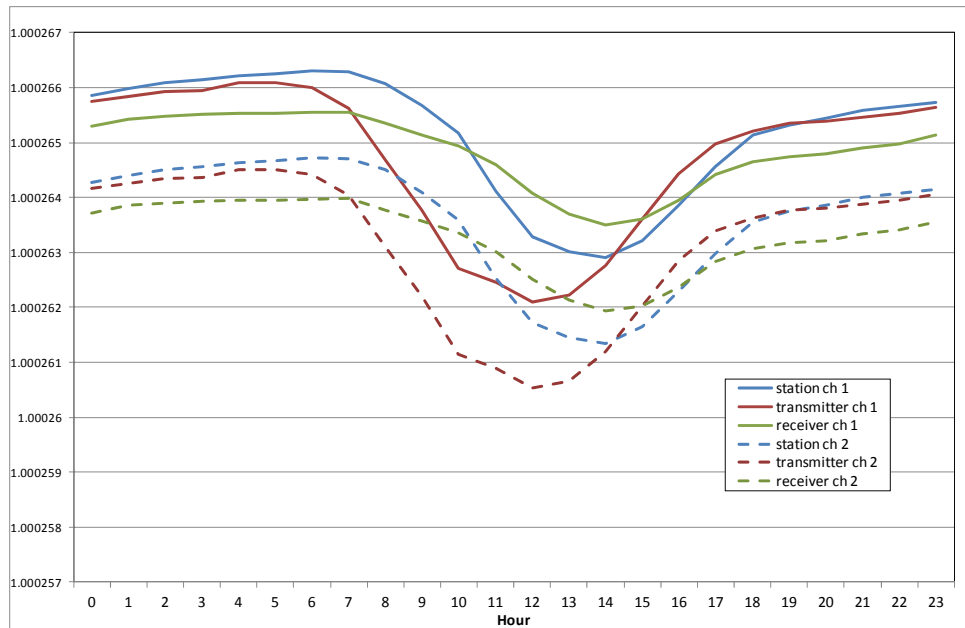


Figure 6.3-20: Daily courses of refractivity index for three considered measurements and two FSO link channels

The vertical gradient of the refractivity index is more important from the FSO signal propagation point of view. We simply evaluated the difference between the refractivity index on the receiver and transmitter sides of the FSO link (tower – garden) while the height difference being 29 m. The difference shows relatively strong diurnal variations with the maximum of difference during the day hours while the negative values of the difference were observed during the night (see Fig. 6.3-21). The difference is almost the same for both optical wavelengths of 830 and 1550 nm.

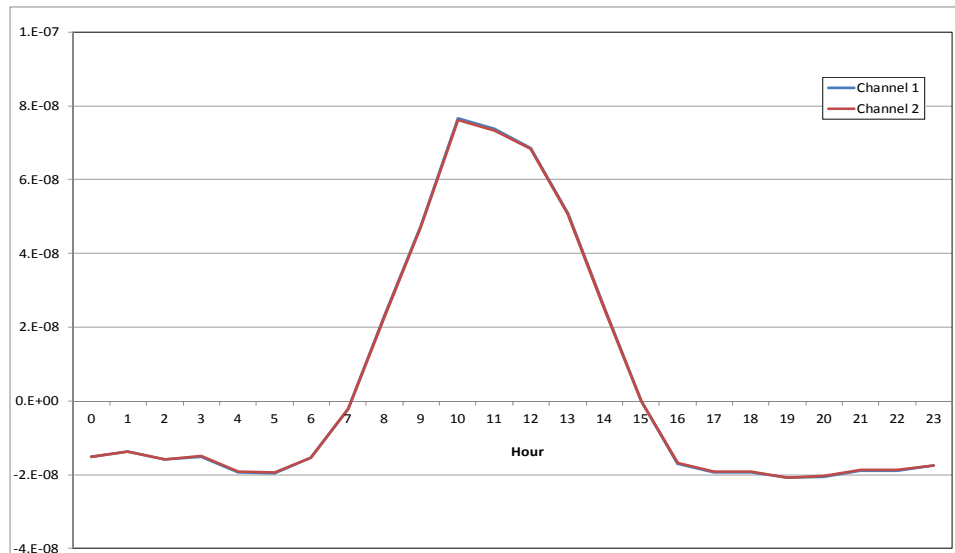


Figure 6.3-21: Daily course of the air refractivity index difference between the receiver (tower) and the transmitter (garden) for both FSO link channels

In Fig. 6.3-22 there is the probability density of "vertical gradient" (in  $\text{m}^{-1}$ ) of the refractivity index. One can see a narrow curve that represents the fact that the vertical gradient is close to zero, symmetrical for both positive and negative values and almost constant.

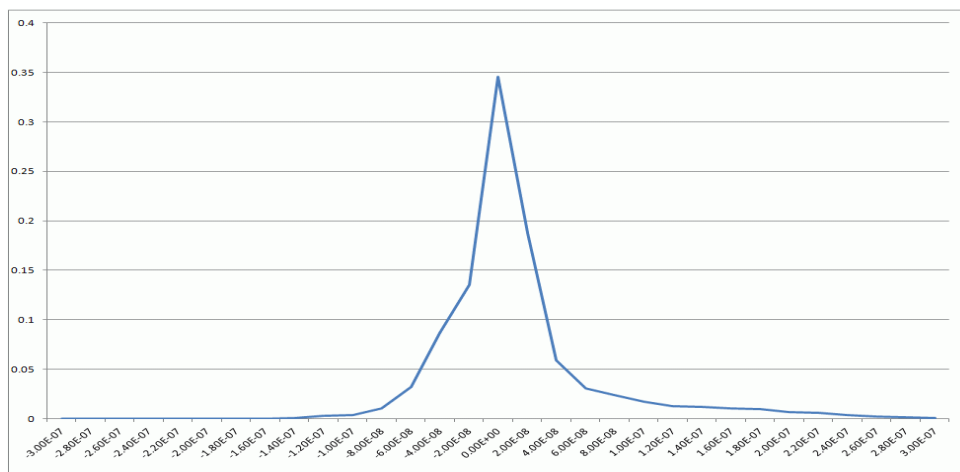


Figure 6.3-22: Daily course of the air refractivity index difference between receiver (tower) and the transmitter (garden) for both FSO link channels

The probability density of the occurrence of the air refractivity index values (Fig. 6.3-23) shows the maxima around the value of 1.000265, but the local maximum around the value of 1.000283 can be seen. The probability density behaves similarly on receiver and transmitter sides of the link. So far we have no explanation for the second local maximum of the refractivity index ("bimodal shape").

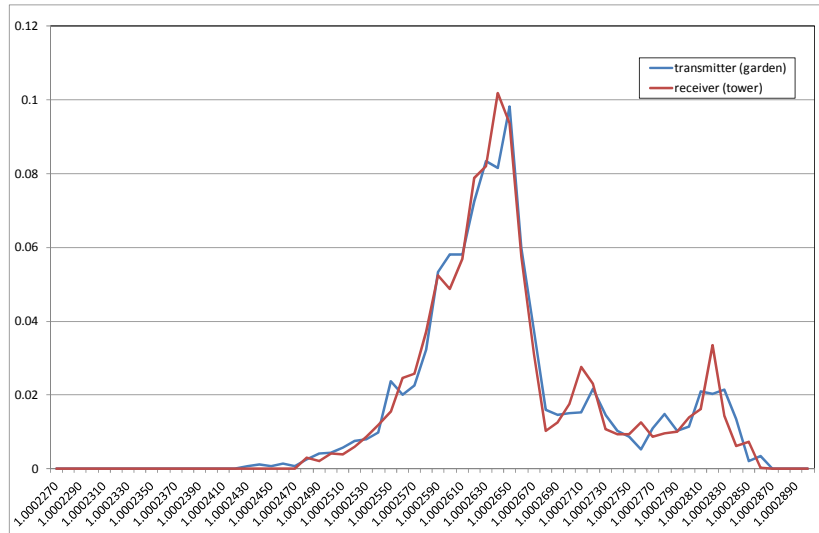


Figure 6.3-23: Probability density of air refractivity index for channel 1

Having values of the refractivity index on both transmitter ( $n_1$ ) and receiver ( $n_2$ ) sites we evaluated the structure index  $c_n^2$  through the following equation:

$$\langle (n_2 - n_1)^2 \rangle = c_n^2 r^{2/3} \tag{6.3-20}$$

where  $r$  is the distance between two sites of the refractivity index measurement (60 m in our case).

Its density of probability is shown in Fig. 6.3-24.

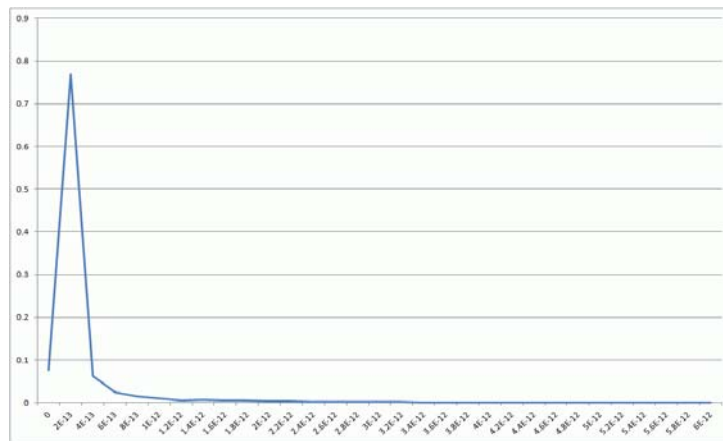


Figure 6.3-24: Probability density function of structure index  $cn^2$ .

The impact of the structure index values on the FSO link attenuation is being studied.

## 6.4 Summary

The main contribution of our experimental activity is the research of FSO signal propagation in severe weather conditions including the impact of wind and atmospheric turbulences on signal attenuation. This is caused through the fact that our observatory is situated on a mountain at the height of 837 m a.s.l.

We measured and presented the CD function of attenuation derived from 3 years measurement as well as scatterplot of the attenuation - visibility dependence. Considering fog only, our attenuation values overestimate the values predicted after well known Kim formula. We explain this phenomenon by severe weather (low temperatures, heavy fogs and low cloudiness).

Certain attention was paid to rain attenuation. After excluding fog events and considering the rain rate record we practically acknowledged the Carboneau formula.

To study the wind turbulences impact on FSO link attenuation we derived many wind parameters and correlated them with the FSO attenuation. Only turbulent energy was found to have a more or less weak impact on the attenuation. Also wind direction related to FSO link orientation was found to be very important.

On the other hand we discovered that the sonic temperature, which is one output parameter of sonic anemometers, is surprisingly well correlated with the FSO attenuation (40%). After analysis of this fact we concluded that the sonic temperature reflects the attenuation due to water vapour.

## 6.5 References

[Kim et al., 2001] Kim I. I., McArthur B., Korevaar E. J.: "Comparison of laser beam propagation at 785 nm and 1550 nm in fog and haze for optical wireless communications", Proc. SPIE 4214, vol. 26, 2001.

[Brazda et al., 2012] Brazda V, Schejbal V, Fiser O.: "Rain impact on FSO link attenuation based on theory and measurement". 6th European Conference on Antennas and Propagation (EUCAP) 2012, pp.1239-1243, 26-30 March 2012

[Carbonneau and Wisley, 1998] Carbonneau T. and Wisley D., "Opportunities and challenges for optical wireless; the competitive advantage of free space telecommunications links in today's crowded market place", in SPIE Conference on Optical Wireless Communications, 1998, pp. 119–128.

[Stone and Zimmerman, 2001] Stone Jr, J. A. Zimmerman, J. H.: "Index of Refraction of Air", The National Institute of Standards and Technology (NIST), USA, 2001

## **7 WEATHER PARAMETER AND FOG MEASUREMENTS ON FSO IN BUDAPEST**

L. Csurgai-Horváth (ed.), I. Frigyes, Budapest University of Technology and Economics

### **7.1 Introduction**

This chapter is the summary of the work carried out in the field of fog density measurements, equipment development and some statistical and modelling work performed at Budapest University of Technology and Economics (BME), Department of Broadband Infocommunications and Electromagnetic Theory.

In section 7.2 we describe the development process and methods of our special device to detect and measure quantitatively the density of fog.

Section 7.3 deals with the impact of fog on FSO, with the path attenuation and provides measurement results as well.

In section 7.4 the effects of the atmospheric turbulence on FSO links is studied, based on the long-term measurements at BME.

### **7.2 Fog density measurements in Budapest**

This section is focusing on the attenuation of radio waves on fixed, V band terrestrial link due to fog. Besides of the V band, fog attenuation measurements on a parallel operating Ka band radio link will be also shown. First of all the appropriate ITU-R recommendation is applied to calculate fog attenuation between moderate and dense fog conditions for different path length and temperatures, and it will be compared with real measurement data. Afterwards a new, simple optical fog density measurement setup will be introduced. The correct operation of the fog sensor is demonstrated by measurements; furthermore the calibration process, which is based on the measured attenuation, will be also shown. It will be proved that the sensor is capable to measure the liquid water content and the attenuation can be predicted from this value. Another outcome of this research is the applicability of this new device in the design process of V or higher band radio and FSO links.

#### **7.2.1 System setup and links**

The high frequency terrestrial radio links which are operating at the 13-38 GHz band are commonly used by mobile radio network operators for plesiochronous digital hierarchy (PDH) connections in order to transfer digital data between the access and the backbone network. As the PDH network consists of fixed terrestrial radio links with line of sight connections, the source of the channel impairments are mainly due to the precipitation. The above mentioned frequency range is mainly influenced by rain or less frequently by sleet. Rain may cause significant attenuation, often above 30 dB, depending on rain intensity [Laurent Castanet (Ed.), 2008].

Nowadays high data rate and wide bandwidth becomes more and more important in the mobile radio networks. Capacity can not be significantly increased by coding or higher bandwidth as the current networks are already reached their limits. Thus the application of higher frequencies is the most feasible solution to solve the expansion of access networks.

Gigabit radio connections are already operating at the 80 GHz radio band in order to fulfil the new requirements [Bridgewave AR80X]. In this frequency range the effect of fog attenuation is worth considering. In this section we study the fog attenuation in the V-band, namely in the 40-75 GHz band according to IEEE Std. 521-2002, based on measurements of terrestrial radio links. A new, low-cost device will be also introduced to measure the density of the fog by estimating the air liquid water content, and the calibration of the device based on the measured attenuation is also demonstrated. The results will be compared and validated with measurement data. Furthermore it is worth to mention the free space optical (FSO) connections, which are very sensitive to the fog attenuation [Sajid S. Muhammad, B. Flecker, E. Leitgeb and M. Gebhart, 2007], therefore the results of this study can be adapted for FSO design and simulation. The application field of the fog sensor besides the measurement of the liquid water content is to create statistics and apply them in the design and availability calculations of high frequency radio and FSO connections.

### 7.2.2 Measurement data applied for the investigations

The department of the authors performs extensive propagation studies of terrestrial radio links and also a measurement system is operated, which continuously collects path attenuation data from several radio connections. This system has recently been extended with a special measurement setup in order to study the attenuation events on V band. Two measurement campaigns has been performed in this year, both of them consists of two parallel radio links on the same physical path with identical polarization. During the first campaign a path with 2.3 km length, during the second with 3.5 km length has been measured. Only the frequencies of the links are different (39.0775 GHz and 72.56 GHz). The goal of this setup is to study exactly the same path on different frequencies. The channel with higher frequency is the main subject of this study, however on the lower frequency was also observable the impact of the fog attenuation. In the next figure the location of the radio links are depicted. They operate in the city area of Budapest, Hungary.

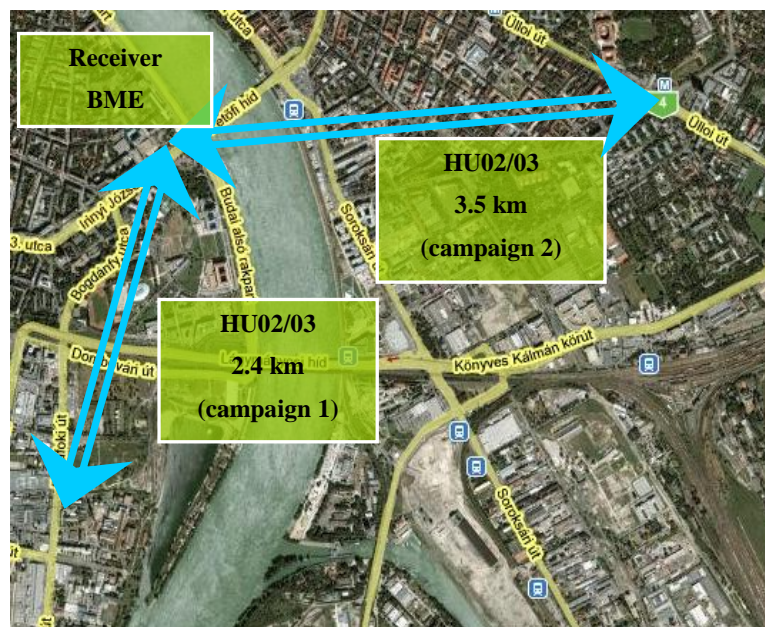


Figure 7.2-1 Measurement locations

The measurement node is equipped also with a meteorological station, which transfers the different weather parameters to the central data collecting computer. Furthermore, a fog sensor is installed at the station and it plays an important role in this study. The sensor has been developed at the Budapest University of Technology (BME), and the principle of its operation will be described later.

The detailed parameters of the measured links and campaigns can be found in Table 7.2-1.

Table 7.2-1 The details of the measurement

Campaign	Receiver location	Height	Name	Length	Frequency	Pol.	Device
1. 17.05.2009-22.07.2009	BME	102 m	HU02	2.3 km	39.0775 GHz	H	Pasolink
	BME	102 m	HU03	2.3 km	72.56 GHz	H	Bridgewave
2. 23.07.2009-still running	BME	102 m	HU02	3.5 km	39.0775 GHz	H	Pasolink
	BME	102 m	HU03	3.5 km	72.56 GHz	H	Bridgewave

Figure 7.2-2 shows the tower with the two radio links. At the top the meteorological station can be seen, assembled with temperature, humidity, wind speed and direction measurement devices. The fog sensor is also depicted, which has a weather-proof housing but allows entering the fog particles in case of foggy weather. During the first campaign no fog events has been detected as it was summer period; however there is an intention to perform further measurements at this path length in the near future in order to record foggy periods.

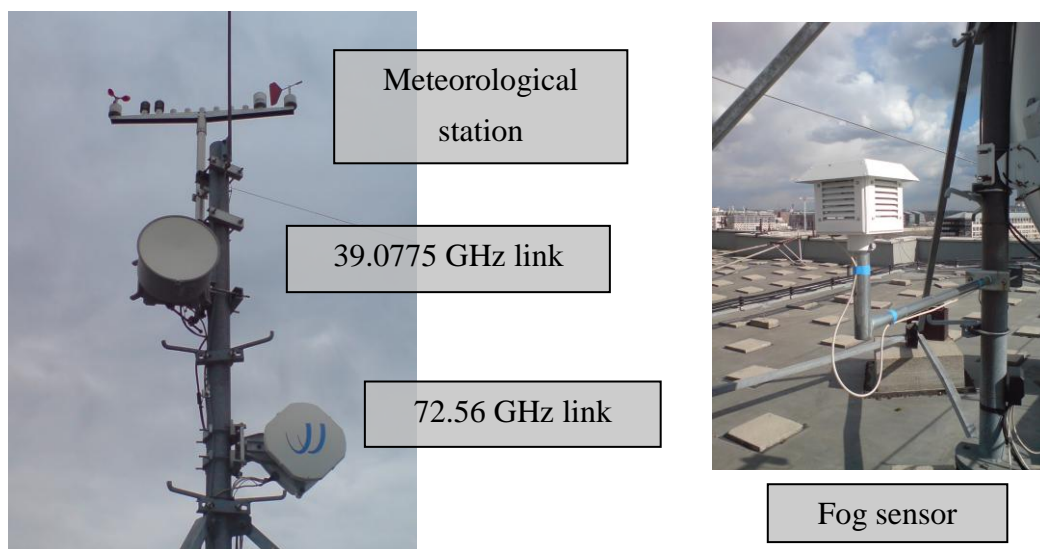


Figure 7.2-2 The radio links and the meteorology sensors

### 7.2.3 Fog attenuation on microwave links

The attenuation due to clouds and fog can be calculated with the appropriate ITU-R P.840 recommendation [ITU-R Rec. P.840-3,1999]. This guidance is applicable from the 10 GHz band, where the fog attenuation becomes well detectable, up to 200 GHz which is the upper

limit of the validity this ITU-R model. Clouds and fog are containing liquid water content entirely as small droplets up to 0.1 mm. The fog has liquid content usually between 0.05 mg/m<sup>3</sup>, (medium fog of the order of 300 m visibility) up to 0.5 g/m<sup>3</sup> (dense fog of the order of 50 m visibility) [Sajid S. Muhammad, B. Flecker, E. Leitgeb and M. Gebhart, 2007]. According to the recommendation a specific attenuation coefficient can be calculated with the following expression, based on Rayleigh-scattering:

$$K_l = \frac{0.819f}{\varepsilon''(1+\eta^2)} [(dB/km)/(g/m^3)], \quad (7.2-1)$$

where  $f$  is the frequency in GHz, and  $\eta = \frac{2 + \varepsilon'}{\varepsilon''}$ . In the latter expression  $\varepsilon'$  and  $\varepsilon''$  are the complex dielectric permittivity of water, also given in the recommendation.

There is also a moderate temperature dependency in the above equations, included in the  $\varepsilon'$  and  $\varepsilon''$  coefficients [ITU-R Rec. P.840-3,1999].

The product of the  $K_l$  attenuation coefficient and the liquid water content  $M$  given in [g/m<sup>3</sup>] express the specific cloud or fog attenuation that can be calculated as it follows:

$$\gamma = K_l M [dB/km]. \quad (7.2-2)$$

By using equation (7.2-1) the attenuation coefficient has been calculated for the frequency range of the two radio links that installed in our measurement setup (30-80 GHz) and depicted in Figure 7.2-3. The temperature range varies in the calculation and its values are representing that the common weather conditions, where the appearance of the fog is the most probable.

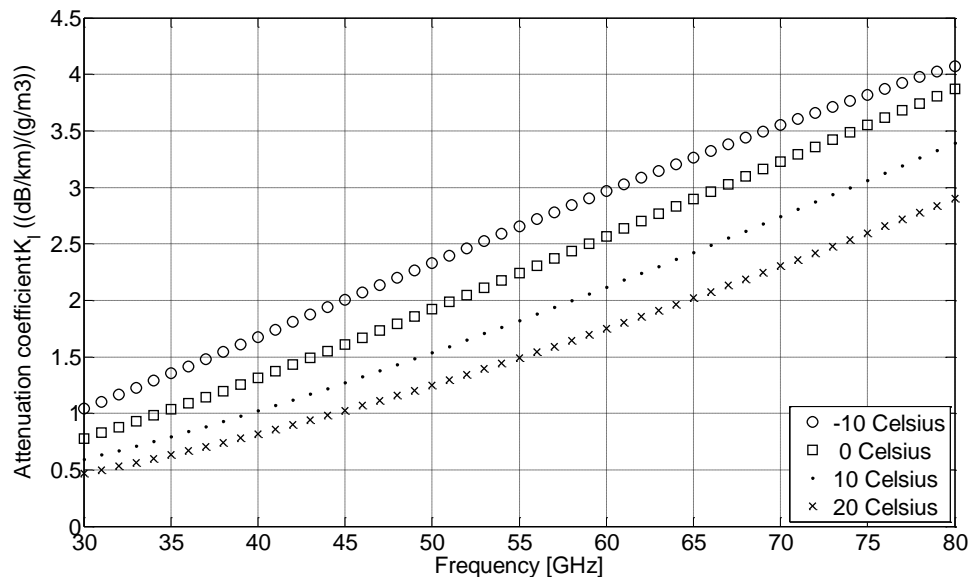


Figure 7.2-3 Attenuation coefficient between 30-80 GHz at different temperatures

This result shows that the coefficient is increasing with the frequency but at higher temperatures will be lower, thus the path attenuation will be higher at high frequencies and at lower temperatures.

Applying the attenuation coefficient and equation (7.2-2), a calculation has been made at the frequencies of the two investigated radio links (39.775 and 72.56 GHz), at 0 °C between 1 km

and 20 km path length for the two extreme values of the liquid water content (0.05-0.5  $\text{mg}/\text{m}^3$ ), at sparse and at dense fog:

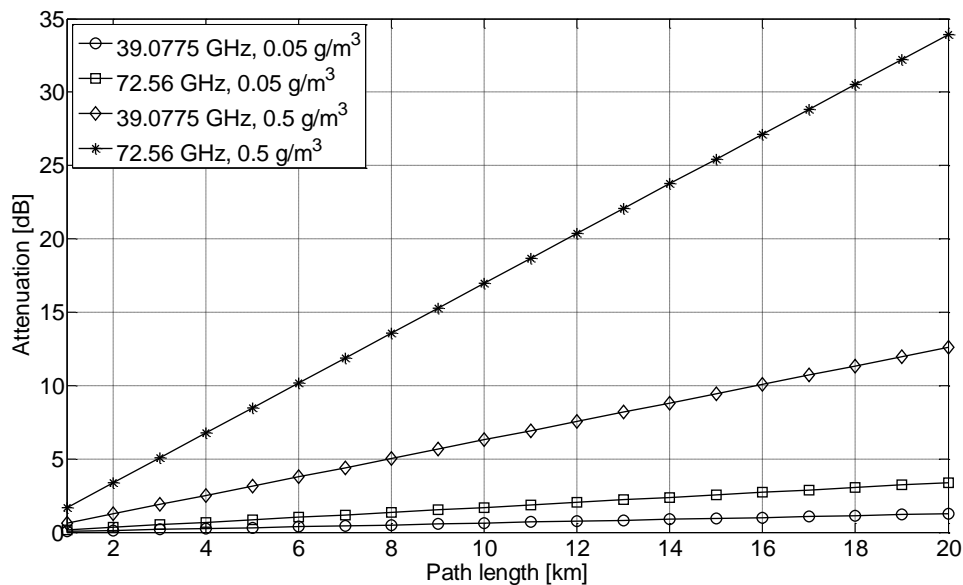


Figure 7.2-4 Fog attenuation at 0 °C as the function of liquid water content and path length

It can be observed that at low liquid water content the path attenuation is not significant even on long radio links, but the dense fog may cause considerable attenuation.

However the range of the gigabit radio links is limited at relative short path length (several, mainly up to 10 km), already on this length the attenuation may reach 16-17 dB during dense fog conditions.

At the Ka band the observable attenuation is not so significant, but it is also well observable as it will be shown in the next section.

#### 7.2.4 A low-cost fog density measurement device

In order to estimate the path attenuation due to the fog, the liquid water content per unit volume should be measured. This task requires quite complicated and expensive measurement devices [Robert G. Knollenberg, 1972], [M. Hagen, S. E. Yuter, 2003]. For experimental purposes a simple and low-cost device has been developed to detect fog events and provide a quantitative value of the air liquid water content. The picture of the fog sensor equipment can be seen in Figure 7.2-2. The device is based on an optical sensor which transmits periodically short infrared light pulses and measures the squarely reflected impulses. The amplitude of the reflected light is correlated with the amount of the reflective material in the sensor area; therefore a good estimation of the liquid water content can be achieved. The construction of the optical sensor and its operation principle is depicted in Figure 7.2-5. Besides the optical fog sensor the device is equipped with temperature and relative air humidity sensors. These parameters are providing also important information and they have characteristic values during foggy weather.

The sensor is built into a rain and sunlight-shielded device box, but allows the free movement of the fog droplets to and from the sensor area. A built-in data processing unit is applied to form the data and transfer the measurement data to the indoor data collecting system.

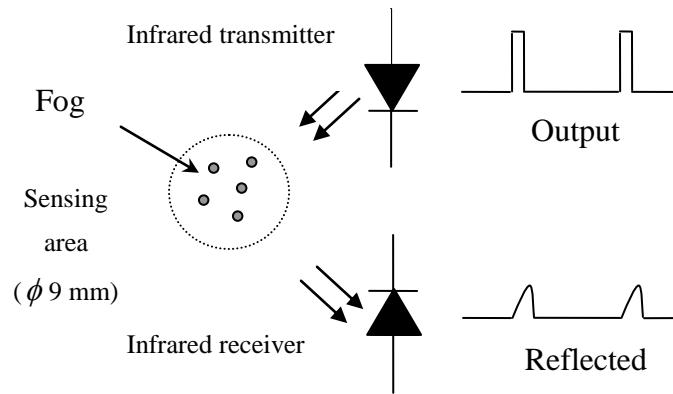


Figure 7.2-5 The principle of the fog density measurement

Several measurement result of detected fog events prove that the device is capable to sense the fog events and give a quantitative liquid content value, as it is shown in Figure 7.2-6. This measurement has been performed on 9-10 of November, 2009. during the campaign 2, on 3.5 km path length. The output of the fog sensor, the received power on the 72.56 GHz and 39.0775 GHz microwave links and the rainfall rate are also graphed. This is a 20 hour long measurement, containing alternating rain and fog events. It can be observed that the rain attenuation events (between the 9<sup>th</sup> and 16<sup>th</sup> hours) can be well distinguished from the fog attenuation events (between the 2<sup>nd</sup> and 5<sup>th</sup> hours), detected by the fog sensor. The output of the fog sensor is denoted here as a relative number, distributing between zero (zero liquid content), and the maximal value of 0.5 (dense fog). Further investigations will be shown in the next section to calibrate the device and find the conversion relationship between device output and liquid water content values. The fog attenuation is very well observable between the 2<sup>nd</sup> and 5<sup>th</sup> hours, its maximal value is approximately 1.5 dB on the V band and less but also visible on the Ka band. Using (7.2-2) the liquid water content can be calculated, which is 0.14 g/m<sup>3</sup> on V band if the attenuation is 1.5 dB. This explains that the output level of the fog density measurement device was below 50 % of its measurement range.

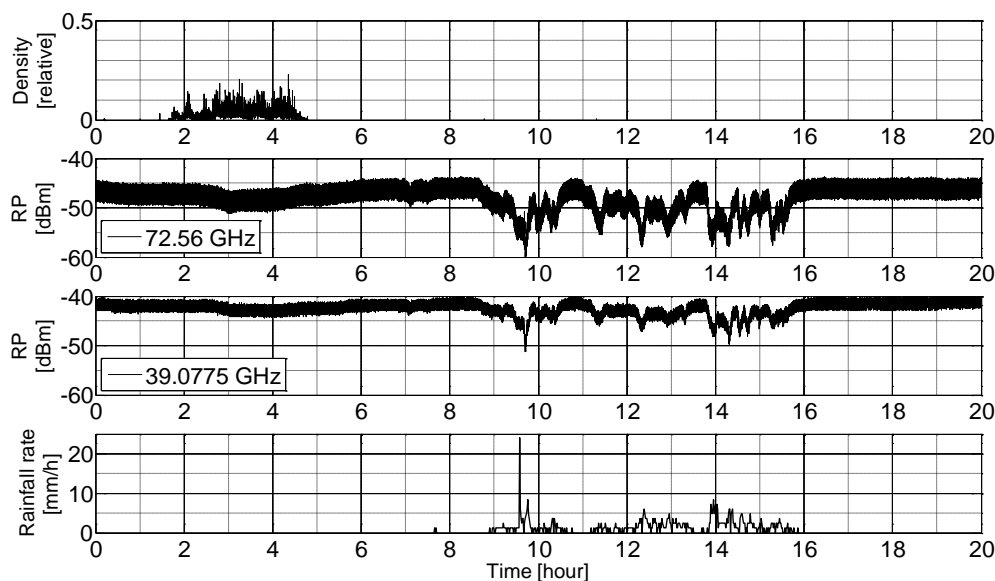


Figure 7.2-6 Measured fog event, received power (RP) at 72.56 and 39.0775 GHz and the rainfall rate

### 7.2.5 Calibration of the fog sensor

Our principle to calibrate the fog sensor is based on the attenuation measurement on the V band radio link. Since the attenuation is the function of the frequency, temperature, path length and liquid water content, the latter can be calculated if we know the other parameters. For the calibration process we applied the fog event that can be seen in Figure 7.2-6. between the 2<sup>nd</sup> and 5<sup>th</sup> hours.

The time varying liquid water content at the  $i^{\text{th}}$  discrete sample time,  $M_i$  is the function of the  $\gamma_i$  specific attenuation, which is also time dependent, and the constant  $K_l$  attenuation coefficient (7.2-2):

$$M_i = \frac{\gamma_i}{K_l} = \frac{A_i / L}{K_l} [g / m^3], \quad (7.2-3)$$

where  $A_i$  is the measured momentary attenuation at the  $i^{\text{th}}$  discrete time in [dB] and  $L$  is the path length in [km].

In order to decrease the effect of scintillation, a 15 sec median filter has been applied on the original measured received power time series. The attenuation is calculated by subtracting the filtered received power values from the median of the received power. As  $K_l$  is temperature dependent, the measured temperature values were also taken into account in the calculations. During this fog event the temperature was slightly changing between 7.9 °C and 9.2 °C. In Figure 7.2-7. this fog event is depicted at high resolution together with the attenuation and the calculated instantaneous liquid water content.

By comparing the output of the fog sensor device and the momentary liquid water content which comes from the measured attenuation, the calibration of the sensor can be done. After the calibration the liquid water content will be provided as a direct parameter from the sensor.

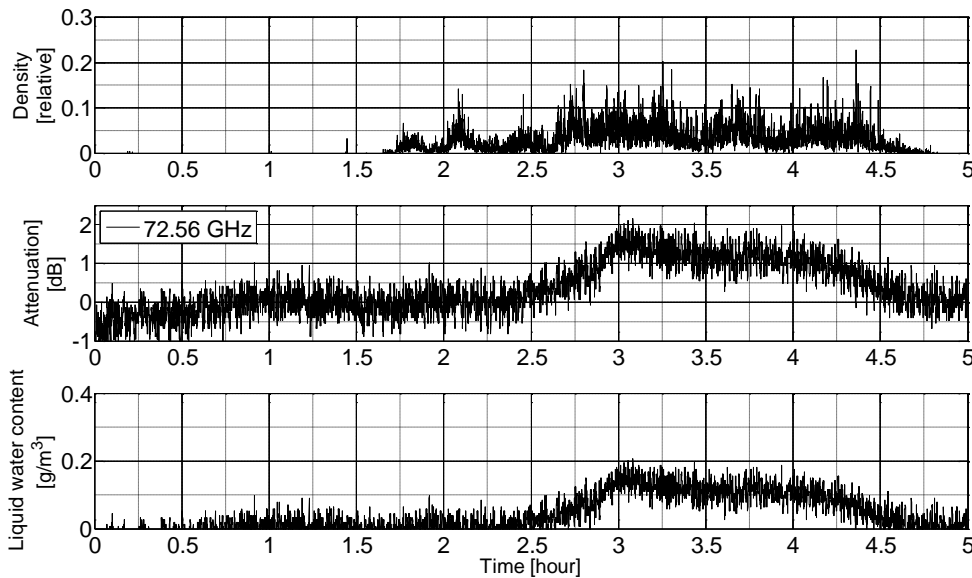


Figure 7.2-7 Fog sensor output, attenuation and liquid water content calculated from attenuation

The ratio between the averaged liquid water content values,  $W_i$  and the fog sensor output values,  $D_i$  gives the following constant:

$$C = \frac{\sum_{i=1}^n W_i}{\sum_{i=1}^n D_i} = 0.7384 [g/m^3] \quad , i = 1 \dots n \quad , \quad (7.2-4)$$

where  $n$  is the number of samples during the whole fog event.

This constant can be used to convert the momentary sensor values,  $D_i$  to momentary liquid water content values:

$$M_i = D_i \cdot C [g/m^3] \quad , i = 1 \dots n \quad . \quad (7.2-5)$$

Using this result, the instantaneous attenuation on the radio path can be calculated directly from the fog sensor output value.

A comparison with another real measured fog event proves that the calibration process was successful and the fog sensor device correctly measures the liquid water content (Figure 7.2-8). This fog event has been recorded at 18.11.2009., on 3.5 km path length. The figure depicts the measured liquid water content calculated with (7.2-4) and (7.2-5), the measured attenuation on the 72.56 GHz link and finally the predicted instantaneous attenuation process, calculated directly from the liquid water content using (7.2-6). The temperature was moderately changing during this event between 8.9°C and 10.3 °C and included in the  $K_l$  constant.

$$A_i = \frac{M_i K_l}{L} [dB] \quad (7.2-6)$$

The CDF of the measured and the predicted attenuation proves that the values are similarly distributed, validating the correct liquid water content estimation.

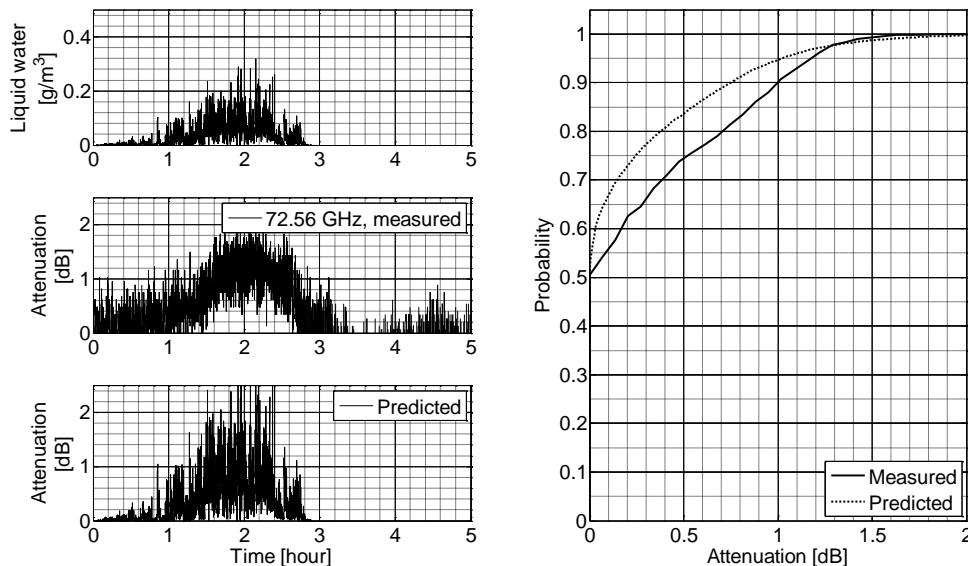


Figure 7.2-8 Measured liquid water content, attenuation, predicted attenuation and their compared CDF

## 7.2.6 Summary

In this section the fog attenuation has been studied on fixed terrestrial microwave links, especially in the V band, but also mentioning the similar, but not so remarkable effects at the Ka band. Using the corresponding ITU-R recommendation we calculated the fog attenuation for different conditions and comparisons has been done with our real measurements. As the main reason of the fog attenuation is the air liquid content, to detect the fog and calculate its density, a simple fog density measurement device has been developed. This optical sensor was tested under foggy weather periods, while the attenuation on microwave links was also recorded. The measured attenuation values are used to calibrate the fog sensor; therefore it is now applicable to measure directly the liquid water content in the air. The calibrated fog sensor output has been tested during measured fog events and it is proved that the measured liquid water content is correct, the attenuation on the microwave link due to fog can be well predicted. Further measurements would be preferable in order to refine the precision of the device, especially during dense fog conditions which was still not recorded during the measurement period. The intention of the authors is to adapt these results in FSO measurements and simulations, where the fog attenuation is even more significant.

## 7.2.7 References

[Laurent Castanet (Ed.), 2008]: "Influence of the Variability of the Propagation Channel on Mobile, Fixed Multimedia and Optical Satellite Communications", The SatNEx E-book, Shaker Publishing, Germany, 2008.

[ITU-R Rec. P.840-3, 1999]: "Attenuation due to clouds and fog", ITU, 1999.

[Robert G. Knollenberg, 1972]: "Comparative Liquid Water Content Measurements of Conventional Instruments with an Optical Array Spectrometer", Journal of Applied Meteorology, Vol. 11, Issue 3, pp. 501–508, 1972.

[M. Hagen, S. E. Yuter, 2003]: "Relations between radar reflectivity, liquid-water content, and rainfall rate during the MAP SOP", Q. J. R. Meteorol. Soc. 129, pp. 477–493, 2003.

[Bridgewave AR80X] users manual, Bridgewave Communications Inc., [www.bridgewave.com](http://www.bridgewave.com)

NEC Corporation, Pasolink] microwave systems, [www.nec.com](http://www.nec.com)

[Sajid S. Muhammad, B. Flecker, E. Leitgeb and M. Gebhart, 2007]: "Characterization of fog attenuation in terrestrial free space links", Journal of OE 46(4) 066001 June 2007.

## 7.2.8 Measurement examples

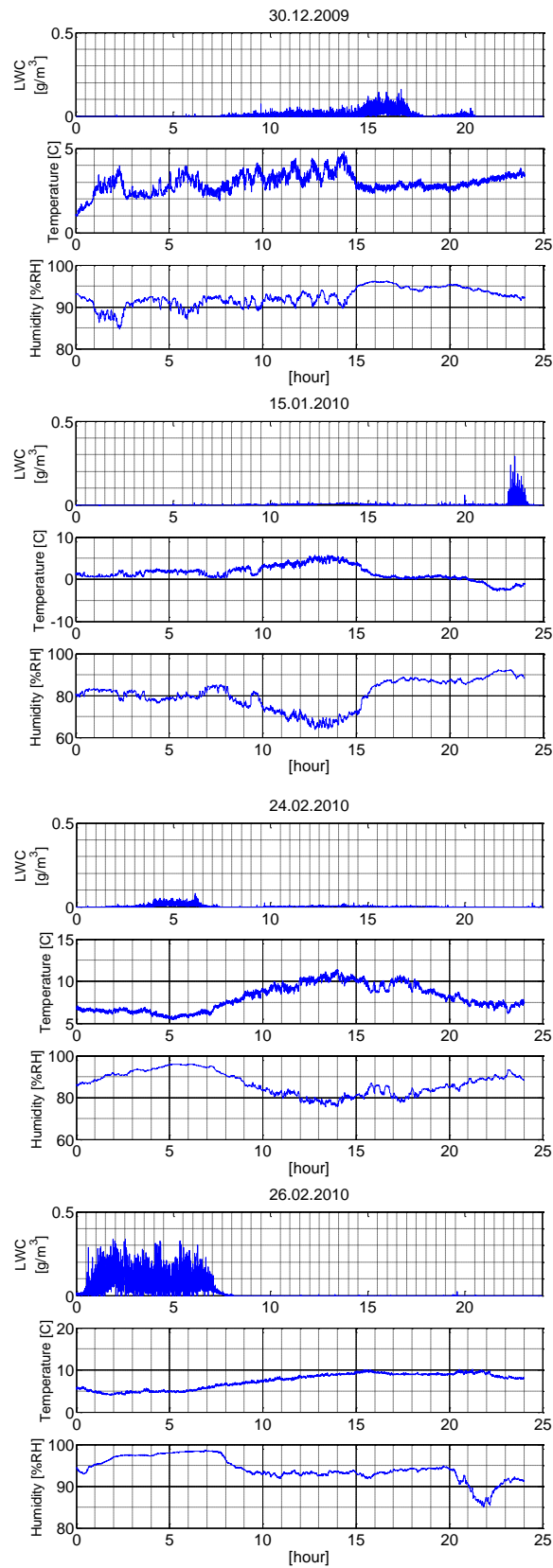


Figure 7.2-9 Measured LWC, temperature and humidity

### 7.3 The impact of Liquid Water Content to Free Space Optical links

Free space optical (FSO) communication became a topic of much interest in recent years. The main reason of that is that it is one of the not too many possibilities making wireless transmission of Gbit/sec and other wideband signals a reality. In the introduction of this section some of the main points relevant to this technique are briefly listed i.e. propagation impairments (including fog effect), practical advantages and application possibilities. The bulk of the section deals with an equipment elaborated in Budapest University of Technology and Economics (BME) measuring one of the parameters characterizing fog i.e. liquid water content (LWC). A method of calibration is given. Results of measurement taken during 6 fog events of total length of about 70 hours show a very high correlation between LWC and fog attenuation along the FSO link.

Also the dependence of measured attenuation from measured LWC has similar characteristics as published relationship of attenuation vs. LWC. Thus LWC as measured with this instrument is a good estimator of fog effect on FSO propagation.

#### 7.3.1 Introduction

The main purpose of this section is to present a simple instrument being able to measure one of the physical quantities characterizing fog; this is of importance as fog is the “public enemy #1” of optical propagation in atmospheric environment. At first, measurements verifying the applicability of this instrument are also presented. However, to put this problem into a communication framework this introductory section discusses some general points of the FSO.

As it is well known interest in Free Space Optics (FSO) techniques in the wireless transmission of wide band signals did much increase since about the beginning of the century. While this technique was virtually nonexistent in representative optical periodicals e.g. in the Journal of Lightwave Technology even in the late nineties, journal-papers, conference-sessions and special workshops and conferences are so to say abundant since then. The reason of this interest is self evident. Possibilities of FSO in high speed wireless are or are nearly unique. Need for high capacity wireless is ever increasing. And, relatively low cost optical components being available due to the maturity of fiberoptic techniques can be applied in FSO as well.

While these possibilities, needs and availabilities exist without doubt, there is one drawback what systems applying free space propagation must take into account, i.e. the severely hostile character of this medium. It can be stated that most of the research work in FSO deals with characterizing the channel on one hand and, even more, to search for countermeasures to these unfriendly characteristics on the other hand.

The mean physical phenomena resulting in temporarily high attenuation – i.e. fading – are: rain, fog, atmospheric turbulence and beam pointing error. Each of these can cause outage of an FSO link, however, with significantly different characteristics.

The main adverse effect is fog, being most responsible for the non-availability of an FSO link. Attenuation of fog, depending on its density, is in the range between 4 dB/km and 300 dB/km. Fog-induced attenuation depends somewhat on the wavelength; it is lower at longer wavelength but the orders of magnitude are similar. An event of very dense fog can last for several hours, resulting thus in very long outage. Among others, Ref. [E. Leitgeb & al., 2009] and [H. Vasseur, C. J. Gibbins, 1996] deal with fog-induced attenuation.

Heavy rain causes high attenuation as well, strongly depending on rain rate (mm/hours). Very heavy rain, 90-100 mm/h, occurring in temperate climate with non-negligible probability can cause attenuation of about 20 dB/km. In Figure 7.3-1. we present a heavy rain event, measured in urban area of Budapest, where the rain intensity was exceeded 100 mm/h for 2.4 minutes, while the received FSO level decreased by nearly 20 dB. This may result in outage as well, however, outage duration is much shorter than fog-induced outage. Duration of a very heavy rain event is usually in the order of minutes as in this presented case.

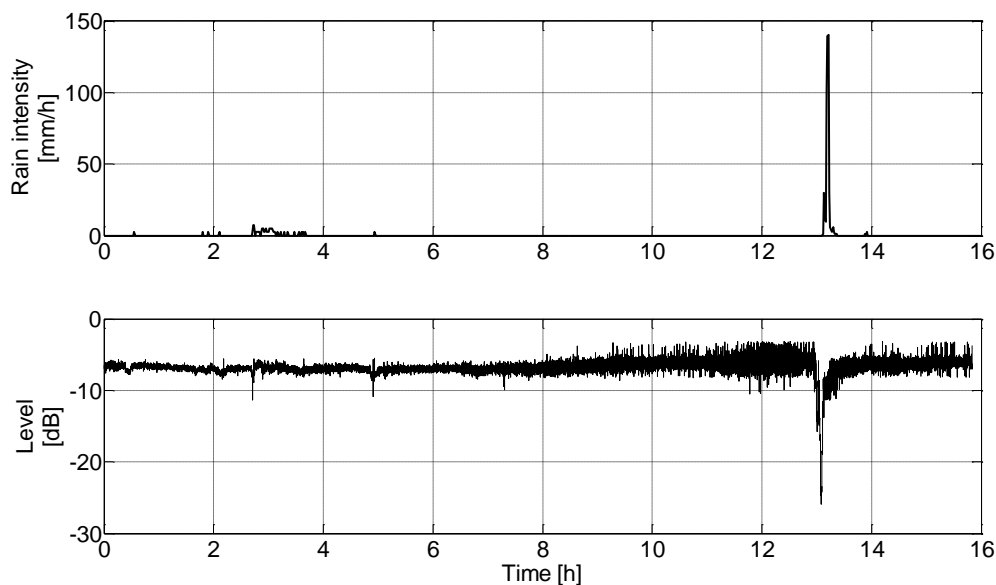


Figure 7.3-1 Rain attenuation on FSO (05.2010)

Atmospheric turbulence causes fluctuation of optical field amplitude and phase, called scintillation. This is a rather slow fading. (“Rather slow” means constant over long strings of symbols; its time constant is in the order of 0.1-1 second.) For short periods it can bring a link into outage condition. Under clear air conditions amplitude scintillation is the main channel impairment. Phase fluctuation, on the other hand, is usually negligible. On turbulence characteristics and its effects see among others [A. Prokes, 2009].

Due to the very narrow width of laser beams carrying information exact pointing of the transmitter toward the receiver is of primary importance. Although usually this is kept fixed by a tracking loop, pointing errors still can appear and these are harmful. Effects of pointing error and scintillation are often jointly investigated (e.g. [D.K. Borah, D.G. Voelz, 2009], [G.K. Karagiannidis & al., 2009]), as these are not simply additive.

Point-to-point FSO equipment available in the time of this writing, i.e. in early 2011, cover the range up to 1-1.25 Gbit/sec. 10 Gbit/sec is foreseen for the not too far future, maybe with an intermediate step of about 3 Gbit/sec. It is also to be noted that while available FSO equipment apply Intensity Modulated/Direct Detection (IM/DD) techniques, optical coherent techniques would be much less vulnerable to channel fading. However, these authors have no knowledge if this theoretical advantage can be realized in practice.

Practical advantages of FSO communications have to be mentioned. An administrative advantage is that optical frequency band is license-free. This is a very important advantage as in some countries fee of license is proportional to the offered frequency band width; thus operating a Gbit/sec mm-wave link is of significant permanent expense while an FSO link can be operated free of charge. And also an advantage: due to the narrow radiated beam width eavesdropping, jamming or even interfering is virtually impossible.

Application possibilities of FSO techniques are rather widespread. These cover good solutions to conventional problems in communications and offer solutions of fully novel ideas. Simple point-to-point FSO links may solve the Last Mile problem, serving as a significantly cheaper version of the Fiber to the Home or the Fiber to the Curb concept. (Although of more modest characteristics.) [A. Gumaste, T. Antony, 2004]. They are very convenient in the backhaul of cellular communication networks [I. Frigyes, L. Csurgai-Horváth, 2010], communication within university or industrial campuses, etc.

Among the novel applications we cite below optical MIMO, the concept of Radio over FSO (RoFSO) and a special application of this latter concept.

MIMO is an efficient countermeasure to scintillation. As an example [A. Puryear, V.W.S. Chan, 2009] proposes a large aperture both in the transmitter and in the receiver containing sparsely located optical radiators resp. receptors. As a result multigigabit/sec transmission is foreseen by the authors for up to 100 km in an even strongly scintillating environment (and, of course, neglecting other sources of fading).

RoFSO is a version of the Radio over Fiber (RoF) concept; in RoF Dense Wavelength Division Multiplexed (DWDM) lightwave carriers are modulated by the RF signals of cellular base stations resulting in extremely simple design of these base stations. Many papers deal with the application of the RoF concept replacing optical fiber(s) with FSO link(s). E.g. [S. Komaki, & al., 2009] reports on the seamless joining of two RoF links via a RoFSO section; *seamless* means in this context that the received DWDM signal is directly focused into the (very small) aperture of the ongoing fiber.

Organization of the rest of this section is as follows. In the next section physical parameters characterizing fog are listed and the applicability of liquid water content (LWC) i.e. one of these is shown. Afterwards the measurement system, that provides data for our model and simulation will be introduced. We will detail the detected relationship between FSO attenuation and LWC, and then summarize our work.

### **7.3.2 Characterization of fog – practical points**

Although water droplets cause in principle both absorption and scattering of the electromagnetic field absorption, however, is usually negligible in the optical frequency range. Thus attenuation depends virtually on scattering only.

It is Mie scattering theory what is relevant for fog effect on optical radiation. However, the application of this theory requires knowledge of so many characteristics and is so complicated that for practical use it is not appropriate. (The required parameters are scatterers' permittivity, their average number and their shape and size distribution; among

these permittivity is known and shape can be assumed to be spherical, but their number and diameter-distribution depends on many factors and are so difficult to determine.)

Due to the above difficulties for practical use estimators have to be found which can be measured and yield sufficiently reliable estimate of fog-induced loss. For this purpose two parameters are appropriate i.e. visibility and LWC. Visibility [F. Nadeem & al., 2009] has some advantages: it can be measured in the actual (i.e. optical) frequency band and also it is permanently measured and published by meteorological services. On the other hand there are some drawbacks as well. Visibility-measuring instruments are rather bulky: transmissiometers require base lines of several tens or even hundreds of meters and the size of instruments measuring optical field scattering is of several meters. For details see e.g. [WMO guide]. And meteorological service reports are not based on in-situ measurements.

Another physical parameter being strictly related to the electromagnetic properties of fog is LWC, also called fog density. Its disadvantage with respect to visibility is that it is not a quantity monitored and reported by meteorological services. Thus for its practical usage it must be measured. However, in BME a rather simple measuring equipment was developed and applied since about a year with success at some institutions. In what follows this equipment, its proposed calibration method and first measuring results achieved in BME on an FSO link are presented.

### 7.3.3 Measurement setup

At BME in the framework of research and industrial cooperation numerous equipments are installed in order to provide important measurement data to study different propagation conditions. Besides of millimeter-wave links and a standard meteorological station, a computer controlled data collection system is operated to collect the fog density and FSO attenuation measurement values. Our measurements are performed in the urban area of Budapest.

The FSO link is formed by commercial equipment, designed for 650-1500 m distances with 100 Mbps transmission rate. In cooperation with the manufacturer, the device has been modified so, that the received optical level can be continuously monitored at the desired rate. In the current measurement campaign we record it at 1 sample/sec rate.

The detailed parameters can be found in Table 7.3-1.

*Table 7.3-1 FSO link parameters*

Wavelength	785 nm
Power	35 mW
Range	650-1500 m
Path length	930 m
Transmission speed	100 Mbps
Manufacturer	GeoDesy

The fog density/LWC is measured with a special device, developed at BME [L. Csurgai-Horváth, J. Bitó, 2010].

This is an optical sensor for detecting fog events and to provide a quantitative value of the air liquid water content. The principle of the operation can be seen in Figure 7.2-5.

The device is based on an optical sensor that transmits infrared light pulses and measures the scattered light. The amplitude of the scattered light is correlated with the amount of the reflective material in the sensor area. The arrangement of the transmitter and the sensor excludes the reflection in case of clear weather condition. When fog appears, the amplitude of the reflected light will increase with the density. In this way a good estimation of the liquid water content can be achieved. Besides the optical fog sensor the device is equipped with temperature and relative air humidity sensors. These parameters are measured with one second sampling rate.

Our principle to calibrate the fog sensor is based on V-band (72.56 GHz) radio attenuation measurements that are also continuously performed at BME [L. Csurgai-Horváth, J. Bitó, 2010], [Bridgeway AR80X]. The attenuation is the function of the frequency, temperature, path length and liquid water content according to the ITU-R P.840 recommendation [ITU-R Rec. P.840-3, 1999]0. In order to determine the LWC-based attenuation, a specific attenuation coefficient should be calculated with the following expression:

$$K_l = \frac{0.819f}{\varepsilon''(1+\eta^2)} [(dB/km)/(g/m^3)] \quad (7.3-1)$$

,where  $f$  is the frequency in GHz, and  $\eta = \frac{2 + \varepsilon'}{\varepsilon''}$ . In the latter expression  $\varepsilon'$  and  $\varepsilon''$  are the complex dielectric permittivity of water, also given in the recommendation., A moderate temperature dependency is also included in the  $\varepsilon'$  and  $\varepsilon''$  coefficients. The product of the  $K_l$  attenuation coefficient and the liquid water content  $LWC$  given in  $[g/m^3]$  express the specific cloud or fog attenuation that can be calculated as it follows:

$$\gamma = K_l LWC [dB/km] \quad (7.3-2)$$

The measured radio attenuation  $A [dB]$  together with the  $K_l$  coefficient allows to express the LWC by applying the  $L [km]$  path length of the radio link:

$$LWC = \frac{A}{K_l L} [g/m^3] \quad (7.3-3)$$

In this manner the output of the optical fog sensor is calibrated, therefore it can be applied as a direct LWC measurement device. In Figure 7.3-2. a typical measured fog event is depicted; at the top is the sensor output, followed by the measured radio attenuation and the LWC, calculated from the attenuation. A strong correlation can be seen between the fog sensor output and the liquid water content.

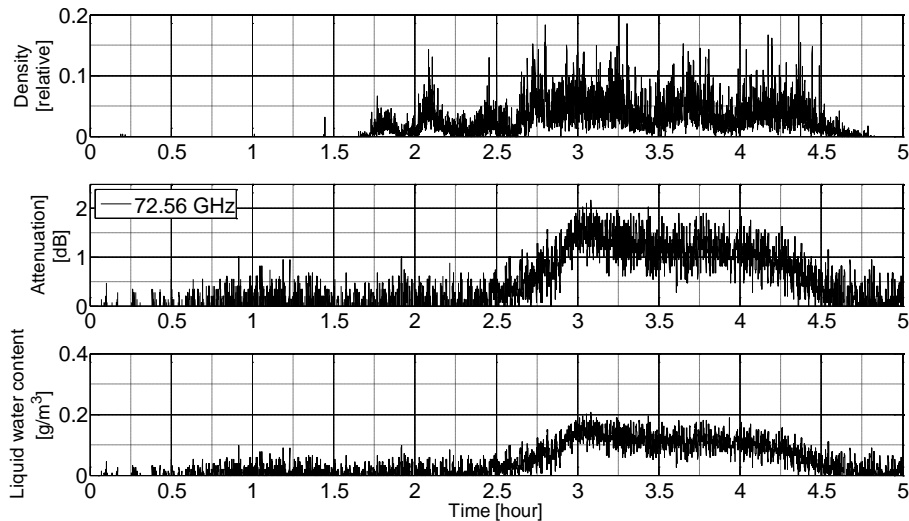


Figure 7.3-2 Fog sensor output, attenuation and LWC

The accuracy of the LWC measurement has been successfully tested also through comparing the FSO attenuation and the attenuation calculated from the LWC [S. S. Muhammad, M. S. Awan, A. Rehman, 2010].

#### 7.3.4 FSO attenuation measurements and model

The FSO connection on 930 m path length and the LWC measurement device were provided several time series of data, recorded between 2010 December and 2011 January. The fog sensor was located at one of the endpoints of the FSO link. The optical link was established between two buildings and located approx. 45 m height from the ground level, as it is a common solution in urban area and it represents the generic application environment. We present in Figure 7.3-3. the time series of measured LWC and the relative optical signal level.

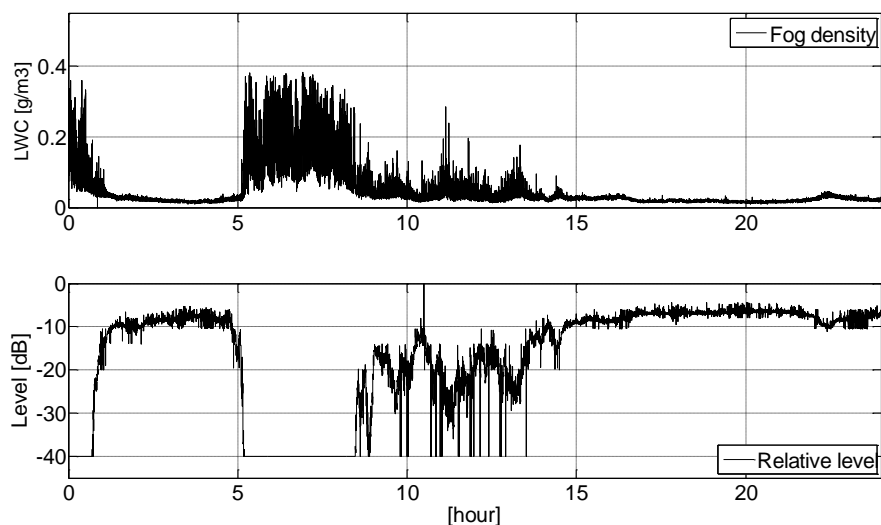


Figure 7.3-3 Measured LWC and FSO received level (23.12.2010)

It should be mentioned here, that the lowest level, that can be detected by this equipment is -40 dB. Therefore under dense fog conditions (approx. above  $0.2 \text{ g/m}^3$ ) we had no measured attenuation data. The FSO attenuation  $A$  [dB] has been calculated from the raw measurement data by subtracting it from the median of the attenuation-free level. Then the specific attenuation  $A_s$  can be calculated with the path length  $L$ :

$$A_s = \frac{A}{L} [\text{dB}] \quad (7.3-4)$$

This value is used during the following modeling process.

Our goal was to find the dependency of the FSO attenuation on the liquid water content. To determine the relationship, several fog events have been processed between December 2010 and January 2011. The total length of the events was 102 hours. In order to eliminate the local fluctuations of the fog density and the fast attenuation variations due to the turbulence, a 30 sec median filter has been applied to smooth the raw measurement data. After this processing, the histograms for LWC and attenuation has been depicted, as it is shown in Figure 7.3-4.

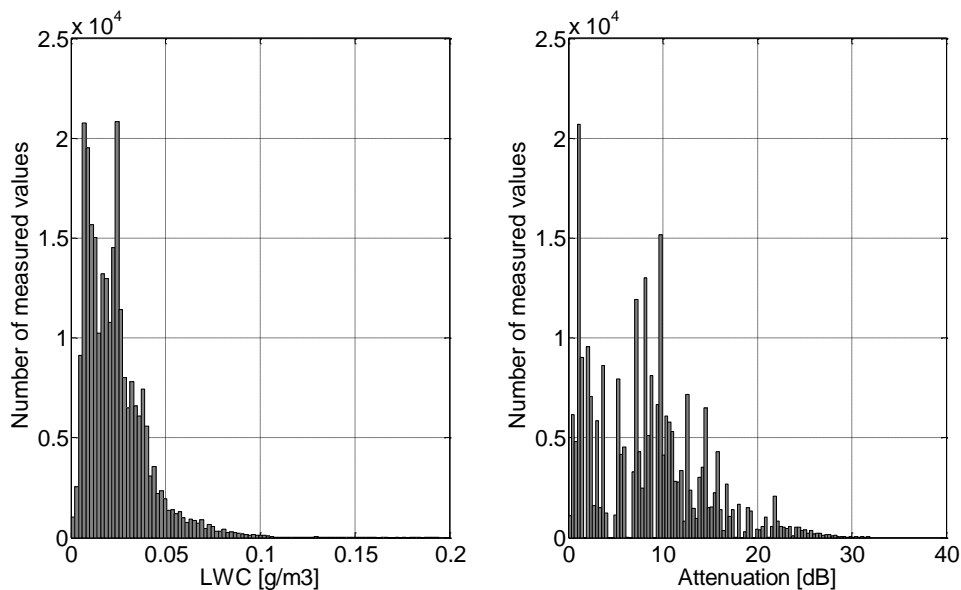


Figure 7.3-4 Histograms of LWC and attenuation

The correlation coefficient between the liquid water content and the attenuation can be applied to estimate the strength of the relationship among these values. The value of the correlation coefficient was calculated as the quotient of the covariance and the standard deviations (7.3-5):

$$R = \frac{\text{cov}(LWC_i, A_i)}{\sigma_{LWC}\sigma_A} \quad (7.3-5)$$

The above calculation was performed for 6 investigated foggy periods, detailed in Table 7.3-2:

Table 7.3-2 Correlation coefficients between FSO attenuation and LWC

Event length [min]	Correlation coefficient
234	0.951
701	0.930
1418	0.919
669	0.907
590	0.928
630	0.852

The average of the correlation coefficients in Table 7.3-2. is 0.915, and as it can be seen the result is a quite high value. In [H. Vasseur, C. J. Gibbins, 1996] the FSO attenuation has been studied at two different wavelength, 630 and 1060 nm. A simple linear function was found to express the infrared attenuation dependence on the LWC. In [O. Bouchet et al., 2006] a power-law expression was published for the specific attenuation at 630 nm:

$$\gamma_{630nm} = 360 \cdot LWC^{0.64} [dB/km] \quad (7.3-6)$$

To find a similar relationship at 785 nm, the measured values were fitted with an equation, as it can be seen in Figure 7.3-5. It should be mentioned, that as the measurement setup was not suitable to detect more than 40 dB attenuation, the high attenuation levels are only extrapolated from the lower values.

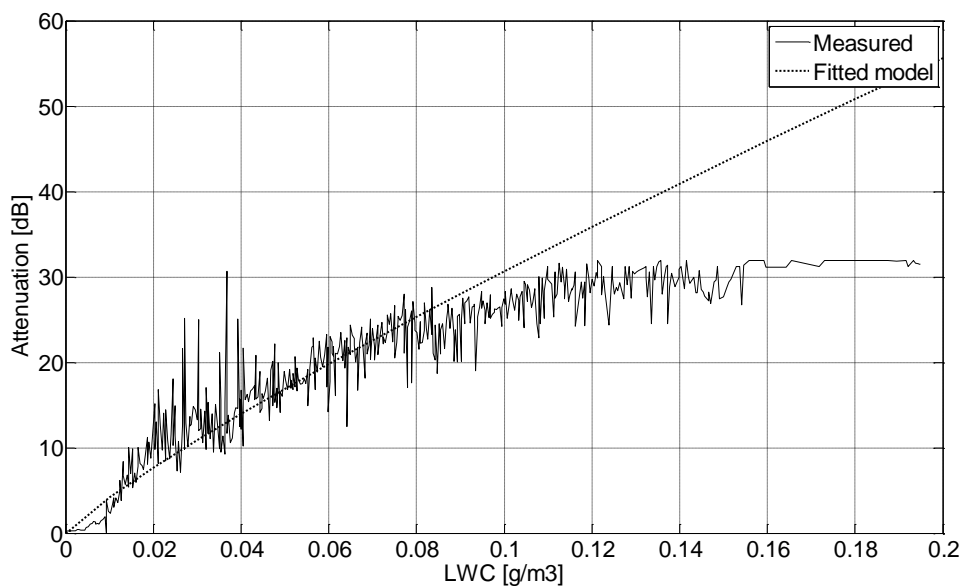


Figure 7.3-5 Fog attenuation as the function of LWC

The figure depicts the result of our measurements and a fitted model, according to the next equation:

$$\gamma_{785nm} = 238 \cdot LWC^{0.86} [dB/km] \quad (7.3-7)$$

This result gives the specific attenuation for 785 nm free space optical links.

To conclude this achievement, it can be stated that a power-law relationship with different parameter-set is applicable to express the 785 nm FSO specific attenuation. Equation (7.3-7) can be used for modeling and simulation purposes.

### 7.3.5 Summary

In this section the propagation characteristics of the free space optical channel has been studied, by focusing to one of the most important environmental influence, the fog attenuation. Our studies are based on real measurements; besides of the standard meteorological devices, a self-developed liquid-water content detector has been applied together with commercial FSO and millimeter-band radio links. According to our calculations a strong correlation has been found between the LWC and the attenuation. This confirms the existence of a relationship between them. At the investigated 785 nm wavelength the FSO attenuation dependency on the LWC has been determined, as a simple power-law equation. In order to compare our results with FSO attenuation models based on visibility measurements, further research work is planned within the COST IC0802 framework.

### 7.3.6 References

[E. Leitgeb & al., 2009]: "Weather effects on hybrid FSO/RF communication link,..." IEEE J. Select. Areas in Comm. VOL. 27, NO. 9, pp. 1687-1697, December 2009

[H. Vasseur, C. J. Gibbins, 1996]: "Inference of fog characteristics from attenuation measurements at millimeter and optical wavelengths", Radio Science, vol. 31, no. 5, pp. 1089-1097, 1996.

[A. Prokes, 2009], "Modeling of atmospheric turbulence effect on terrestrial FSO links", Radioengineering, Vol 18, No1, pp. 42-47, April 2009

[D.K. Borah, D.G. Voelz, 2009]: "Pointing error effects on communication links... J. Lightw.Techn, Vol. 27, No 18, pp. 3965-3973, Sep. 15, 2009

[G.K. Karagiannidis & al., 2009]: "Optical wireless communication with heterodyne detection..." J. Lightw.Techn., Vol. 27, No 20, pp. 4440-4445, Oct. 15, 2009

[A. Gumaste, T. Antony, 2004]: "First mile access networks and enabling technologies", Cisco Press, 2004

[I. Frigyes, L. Csurgai-Horváth, 2010]: "Gbit/sec wireless via Free-Space Optics and E band radio", COST Action IC0802, 26-28 April 2010, Athens, Greece.

[A. Puryear, V.W.S. Chan, 2009]: “Coherent optical communication over the turbulent atmosphere with spatial diversity and wavefront predistortion”, paper #ONS-1, GLOBECOM 2009, Honolulu HA,

[S. Komaki, & al., 2009]: “Performance evaluation of an advanced DWDM RoFSO system for heterogeneous wireless”, paper #ONS-5, GLOBECOM 2009, Honolulu HA

[F. Nadeem & al., 2009]: “Comparison of different models for prediction of attenuation from visibility data”, International Workshop on Satellite and Space Communications (IWSSC 2009) 10th-11th September 2009, Siena-Tuscany, Italy.

[WMO guide] to meteorological instruments and methods of observation, CIMO Guide: <http://www.wmo.int/>

[GeoDesy FSO], [www.geodesy.hu](http://www.geodesy.hu)

[L. Csurgai-Horváth, J. Bitó, 2010]: “Fog attenuation on V band terrestrial radio and a low-cost measurement setup”, Future Network & Mobile Summit, Firenze, Italy, 16-18/Jun/2010. Paper #47.

[Bridgewave AR80X] users manual, Bridgewave Communications Inc., [www.bridgewave.com](http://www.bridgewave.com)

[ITU-R Rec. P.840-3, 1999]: “Attenuation due to clouds and fog”, ITU, 1999.

[S. S. Muhammad, M. S. Awan, A. Rehman, 2010]: “PDF Estimation and Liquid Water Content Based Attenuation Modeling for Fog in Terrestrial FSO Links”, Radioengineering, Vol. 19, No. 2, June 2010. pp. 228-236.

[O. Bouchet et al., 2006]: “Free Space Optics: Propagation and Communication”, Wiley-ISTE, 2006.

## **7.4 FSO link performance under atmospheric turbulence**

### **7.4.1 Observation of atmospheric turbulence on FSO at 785 nm**

This document was written with two purposes in mind. At first, it briefly summarizes the background of the atmospheric turbulence on free space optical (FSO) links. This phenomena causes fluctuation of optical field amplitude and phase called scintillation and it can be observed even at clear sky conditions. Secondly, after outlining the theoretical background measured FSO time series will be presented, also statistics and special observations.

The measurements are carried out at the Budapest University of Technology and Economics (BME), applying a commercial FSO device operating at 785 nm wavelength.

### **7.4.2 The atmospheric turbulence**

Two different class of channel impairment can be observed on FSO systems: the attenuation and the fluctuation of laser power. The attenuation caused by absorption or

scattering, caused by atmospheric gases, water vapour or droplets, precipitation, etc. These effects are out of the scope of this study.

However the main FSO channel impairment is caused by the fog, under clear air conditions amplitude scintillation may cause even significant attenuation. The irradiance fluctuation of the optical wave is caused by the small refraction changes of the atmosphere by deformation the laser beam. The fluctuation of the irradiance is generally centered around the scintillation index:

$$\sigma_I^2 = \frac{\langle I^2 \rangle}{\langle I \rangle^2} - 1 \quad (7.4-1)$$

where  $I$  denotes irradiance (intensity) of the optical wave and the brackets  $\langle \rangle$  denote the a expected value or long-time-average. The scintillation index is the measure of the scintillation magnitude.

The scintillation index is proportional to the scintillation variance, or Rytov-variance, that can be expressed with (7.4-2):

$$\sigma_1^2 = 1.23 * k^{7/6} * C_n^2 * L^{11/6}, \quad (7.4-2)$$

where  $k = 2\pi / \lambda$  is the optical wave number,  $L$  is the path length and  $C_n^2$  is the refractive-index structural parameter [A. Prokes, 2009], [Bouchet et al., 2004].

For constant values of the refractive-index structure parameter (horizontal path with a few kilometers) the scintillation index increases with the path length until it reaches a maximum value.

The intensity of the received optical signal is affected by the turbulence-induced attenuation. Its statistical properties (PDF) is required to establish a high reliable optical connection. Due to the complicated structure of the atmosphere, the various climatic and meteorological situations the modeling of the random attenuation fluctuations is a complex task. In order to simplify the situation, the log-normal distribution is often applied in case of weak fluctuations. For moderate and strong fluctuations the gamma distribution is preferred [Arun K. Majumdar, Jennifer Crider Ricklin, 2008].

### 7.4.3 The measurement setup

At BME an FSO link is operating at 785 nm wavelength and provides measured path attenuation values. The device is installed in the urban area of Budapest, at 45 m height from the ground level, as it is a common solution in urban area and it represents the generic application environment. The link is formed by commercial equipment, designed for 650-

1500 m distances with 100 Mbps transmission rate. In Figure 7.4-1. the location can be seen and a photo about the equipment, while the detailed parameter-set is described in Table 7.4-1.



Figure 7.4-1 Location and picture of the link

Table 7.4-1 Parameters of the measured FSO link

<b>Path</b>	930 m
<b>Wavelength</b>	785 nm
<b>Power</b>	35 mW
<b>Speed</b>	100 Mbps

#### 7.4.4 Results

In order to study the effects of scintillation we applied the measured FSO attenuation time series between 03-05, 2011.

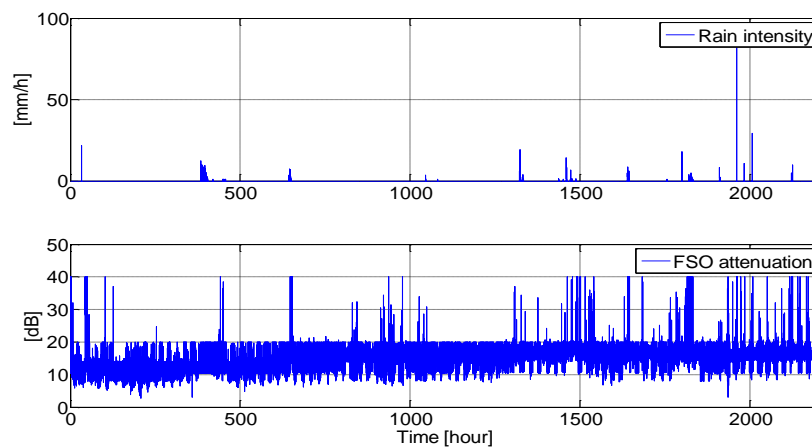
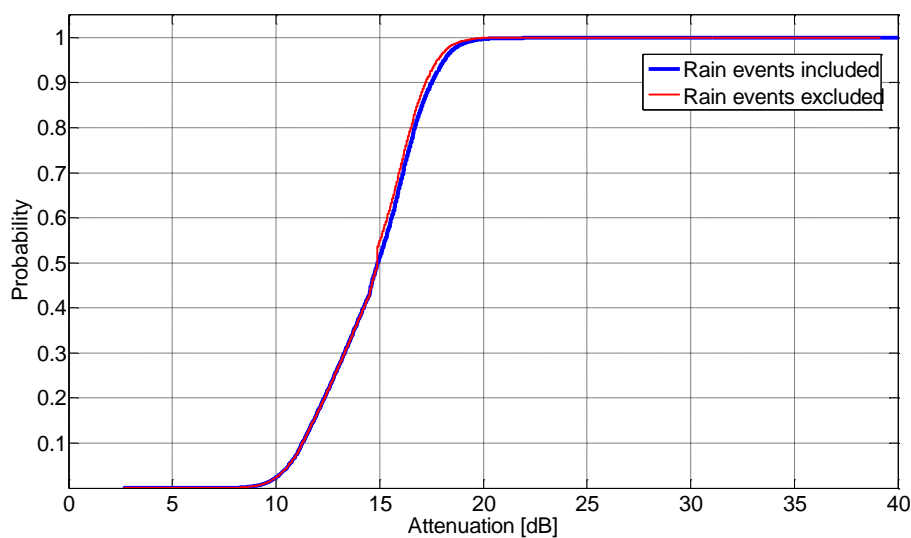


Figure 7.4-2 Measured rain intensity and FSO attenuation

The selected period starts when the probability of fog is very low, practically zero at the location of our equipment. This is the first reason why we selected this starting date. The second reason is that we wanted to study measured data from similar weather condition; in this case the selected 3 month are in spring time, having not too much variable temperature range. Besides the fog, rain may cause also considerable attenuation on FSO. In order to filter out the rain events and allow studying only the scintillation, we applied the measured rain intensity, which is also recorded parallel with the FSO data at BME. In *Figure 7.4-2*. the rainfall rate in mm/h and the attenuation in dB are depicted at the same time scale.

The investigated period of the FSO attenuation time series gives the opportunity to calculate different distribution functions as CDF (*Figure 7.4-3.*) and PDF (*Figure 7.4-4.*).



*Figure 7.4-3 CDF of the FSO attenuation with/without rain events*

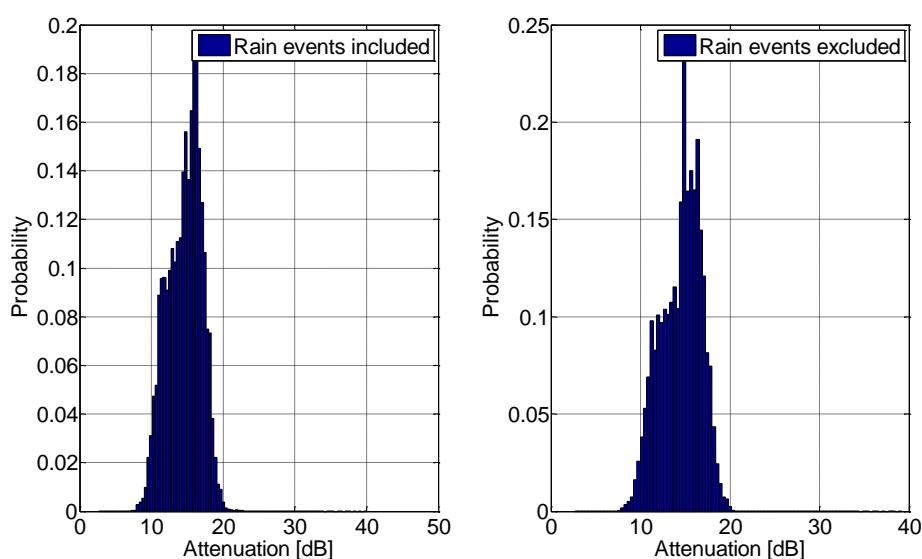


*Figure 7.4-4 PDF of the FSO attenuation with/without rain events*

The CDF of the FSO attenuation can be approximated with lognormal or gamma distributions. The parameters are summarized in Table 7.4-2. and it is depicted in Figure 7.4-5:

Table 7.4-2 Lognormal and Gamma approximation parameters

Lognormal	Gamma
mu: 2.66944	shape: 36.1263
sigma: 0.16948	scale: 0.405078

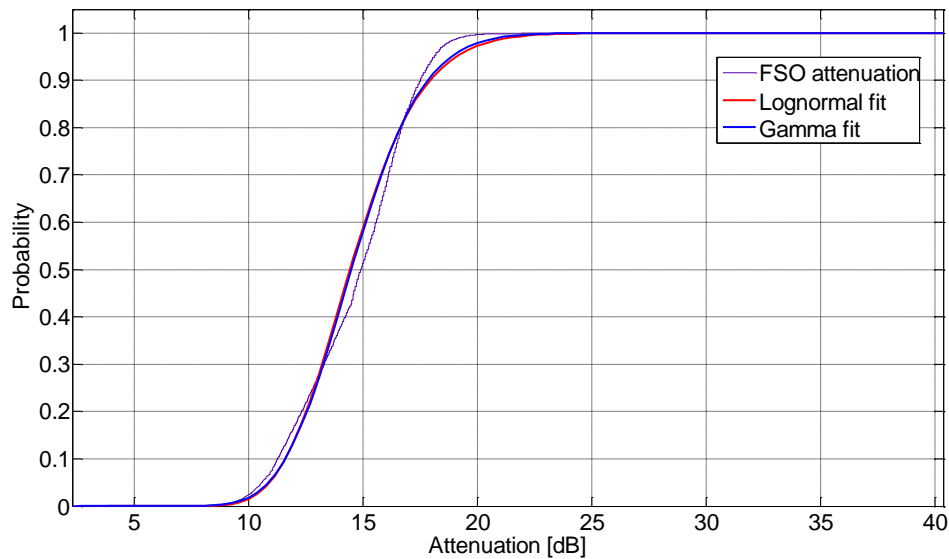


Figure 7.4-5 FSO attenuation approximation with different distributions

For the FSO attenuation time series with filtered rain events can be calculated the scintillation index according to (7.4-1). By applying 60 sec averaging period Figure 7.4-6. depicts the varying of the scintillation index along the time scale. The value of  $\sigma_I^2$  is below 0.1 for the whole period, as it was expected according to [A. Prokes, 2009]. The relative low link distance (930 m) predicts also a low value.

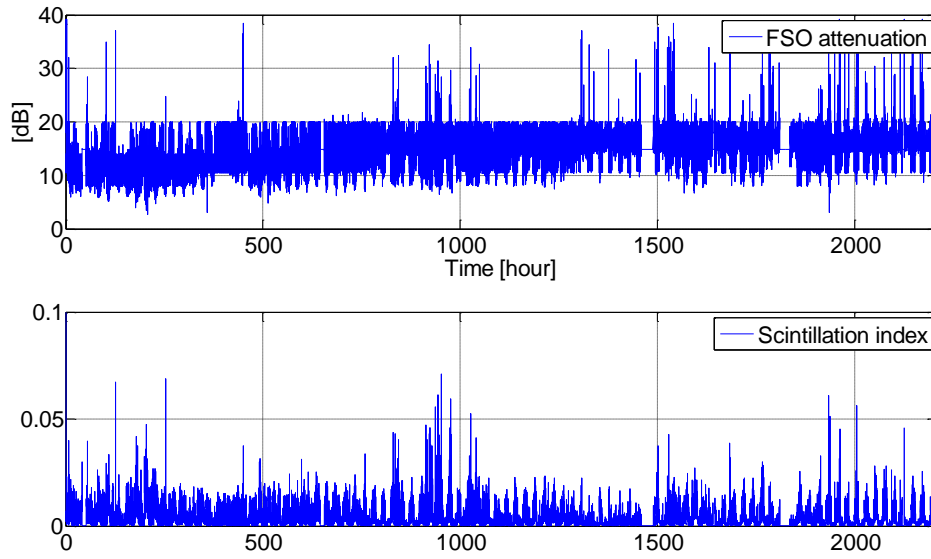


Figure 7.4-6 FSO time series and the scintillation index

The scintillation index shows strong diurnal variation, as it can be observed in Figure 7.4-7. for three consecutive days. The main cause of this effect is the change of the temperature, being low in the evening and increasing midday.

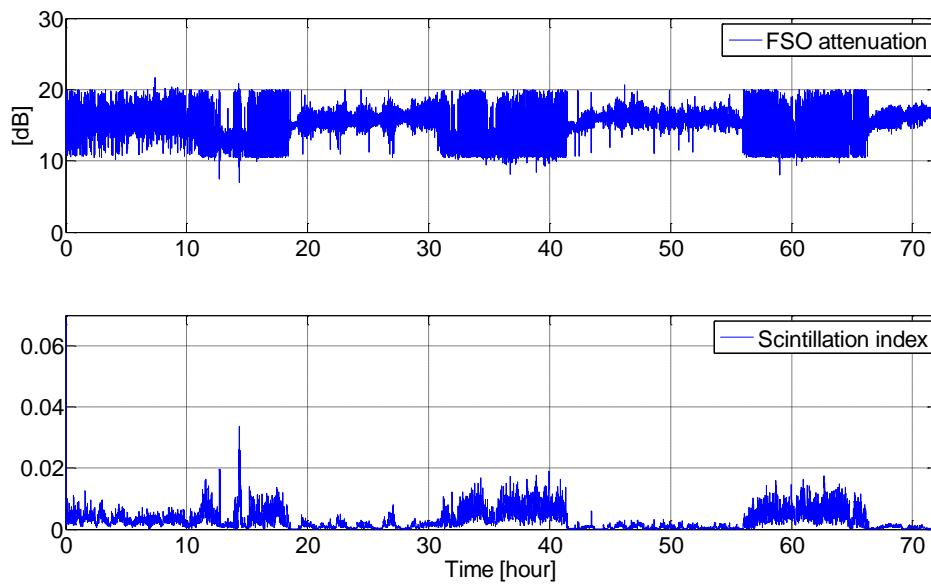


Figure 7.4-7 The diurnal variation of the scintillation index

Furthermore, it can be observed that the rain events may cause -however not in every case- attenuation on the FSO connection (see Figure 7.4-2).

In Figure 7.4-8, a selected rain event and the corresponding attenuation can be seen. The value of the scintillation index increases during the rainy period and it is significantly higher, than during clear sky conditions.

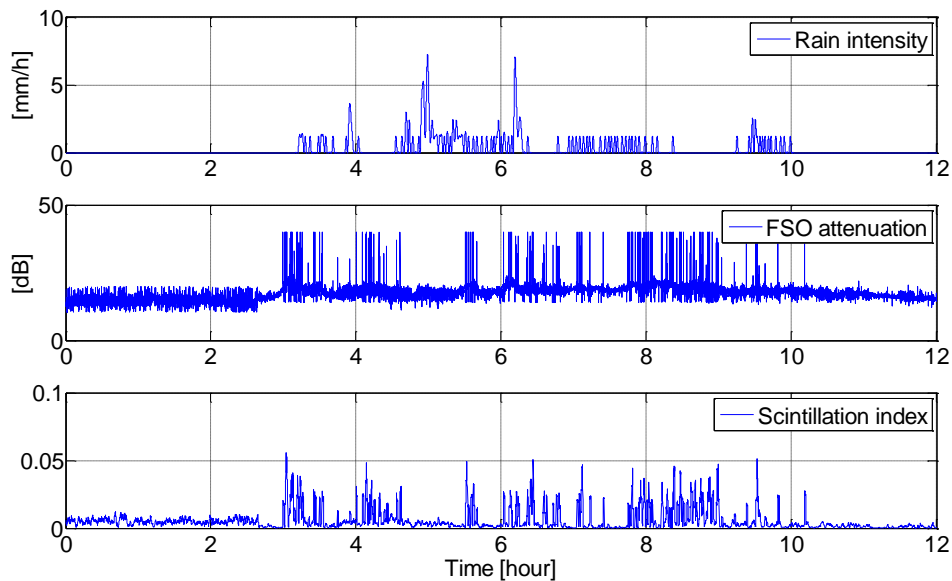


Figure 7.4-8 Rain event with scintillation index

#### 7.4.5 Summary

In this section the effect of atmospheric scintillation has been studied through FSO attenuation measurements at 785 nm wavelength. The phenomenon was classified with CDF and PDF distributions and by calculating the scintillation index. The rainy periods were also studied, as rain intensity measurements were also carried on parallel with the FSO allowing to filter out the rain events and so get more precise statistical and numerical results.

#### 7.4.6 References

[L. Csurgai-Horváth, I. Frigyes, 2011]: “Characterization of Fog by Liquid Water Content for Use in Free Space Optics,” The 11th International Conference on Telecommunications - ConTEL 2011, Graz, Austria, 15-17/06/2011, pp. 189-193, 2011.

[A. Prokes, 2009]: “Modeling of atmospheric turbulence effect on terrestrial FSO links”, Radioengineering, Vol 18, No1, pp. 42-47, April 2009.

[Bouchet et al., 2004]: “Free-Space Optics: Propagation and Communication”, ISTE 2004.

[N. D. Chatzidiamantis, H. G. Sandalidis, G. K. Karagiannidis, M. Matthaiou, 2011], “Inverse Gaussian Modeling of Turbulence-Induced Fading in Free-Space Optical Systems”, Journal of Lightwave Technology, vol. 29, no. 10, May 15, 2011.

[Arun K. Majumdar, Jennifer Crider Ricklin, 2008]: “Free-space laser communications: principles and advances”, Springer, 2008.

## 8 WEATHER EFFECTS AND EXPERIMENTAL MEASUREMENTS USING NEAR-INFRARED FREE-SPACE LINKS IN ROME (STARTED IN COST IC0802)

F.S. Marzano<sup>1</sup>, S. Mori<sup>1</sup>, V. Carrozzo<sup>2</sup>, G.M. Tosi Beleffi<sup>2</sup>

<sup>1</sup> Dipartimento di Ingegneria dell'Informazione, Elettronica e Telecomunicazioni, Sapienza Università di Roma  
Via Eudossiana 18, 00184 Rome (Italy)

{marzano, mori}@diet.uniroma1.it

<sup>2</sup> Ministero dello Sviluppo Economico - Dipartimento per le Comunicazioni, Istituto Superiore C.T.I.

Viale America 201 – 00144 Roma

{valeria.carrozzo, giorgio.tosibeleffi}@sviluppoeconomico.gov.it

Transmission of modulated near-infrared (NIR) beams through the atmosphere is more frequently used to establish optical communications and to interconnect optical fiber networks [Zhu and Kahn, 2002]. FSO is considered as a “wireless” communication system like the ordinary radiofrequency and microwave ones [Majumdar et al., 2008]. The rationale of NIR FSO is the transmission of collimated light beams using low power near-infrared lasers. The FSO collimated light is intercepted by a receiving lens, capable of focusing photons on a highly sensitive detectors. By using single-mode fibers (SMF) directly as light-launchers and light-collectors, the conversion of the optical radiation into the electrical domain can be bypassed and an all-optical treatment of the information can be fully exploited [Carbonneau and Wisley, 1998].

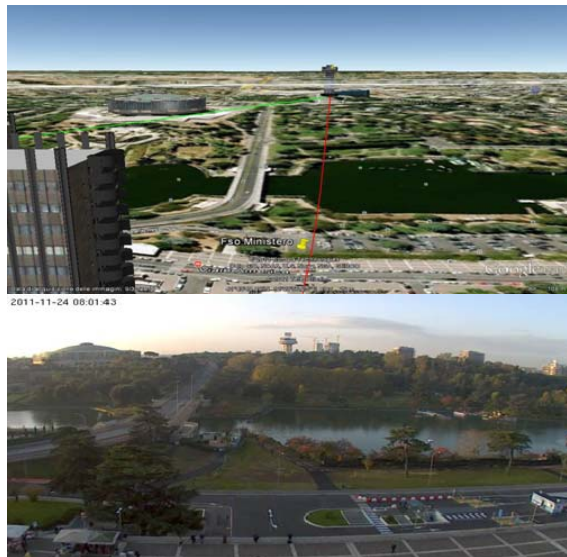


*Fig. 1. Video camera shot (bottom panel) in daytime compared to the “bird view” (top panel), obtained from Google™ earth.*

As long as there is a clear line of sight between the optical source and receiver and enough channel margin, optical wireless systems can cover distances of several km [D’Amico et al., 2003; Nebuloni, 2005; Awan et al., 2010; Nadeem et al., 2009]. Ranges up to 5 km have been tested, even though for shorter link ranges higher QoS (quality of service) performances may be achieved. FSO high data rates, comparable to classical optical fibre

based transmission, can be easily reached with relatively low error rates, while the extremely narrow laser beam-widths may ensure high channel spatial density, potential spatial diversity and high reliability.

This work is devoted to illustrate the improvements of the instrumentation available within the near-infrared (NIR) FSO wide area set up in the Roman area (Italy), operating at 1550 nm (see Fig. 1). FSO channel physical modelling results are described by focusing on rainfall effects and Mie scattering approach. An evaluation of these atmospheric effects is illustrated and a comparison with measurements is carried out for some case studies of moderate and heavy rainfall.

## 8.1 Set up of the Near-infrared free-space link

The FSO set up connects the optical telecommunications instruments on the roof of the Communications Department building of the Italian Ministry of Economic Development (point A, Viale America, height 25 m) and the headquarter of the Department of Foreign Trade (point C, Viale Boston, height 20 m) via two additional optical transceivers on top of the so called “EUR Mushroom” tower (point B, Piazza Pakistan, height 50 m). The distance between location A and B is 750 m, whereas B and C are 900 m far apart [Marzano et al., 2011].

This set up is part of a larger project aimed at testing a full operative mixed wireless-wired (MWW) test bed (see Fig. 2). The FSO experiment should last no less than two years, a sufficiently long period for a scientific assessment of the NIR FSO features.

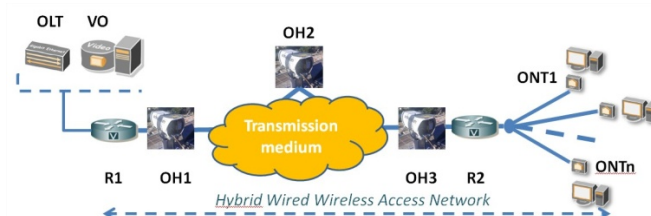


Fig. 2. Towards a full operative Wireless Wired test bed. OLT: Optical Line Termination, VO: Video Overlay, OH: Optical Head, ONT: Optical Network Termination, R: Router.

To monitor the link from A to B, an AXIS P1344-E video camera has been installed in A, pointing towards the “EUR Mushroom” (see Fig. 3) The quality of the link is directly related to the characteristics of the medium the laser beam propagates through. The wide area set up, in fact, faces a quite complex environment: dust, smog, precipitation, turbulence from the traffic, fog, humidity from the lake and the wood, as well as any flying objects, affect the capacity of the channel, thus causing the deterioration of the received signal.

### 8.1.1 Optical transreceiver

The fSONA-SONAbeam® 1250-E optical transceiver device has been installed at sites A and B (see Fig. 3). The transmitting section of such device is driven by 2 lasers characterized by a 160-mW peak power at 1550 nm. The effective clear aperture diameter is 10 cm. The

nominal maximum range in clear air reaches up to 5300 m with transmission rates (transparent and re-clocked) up to 1448 Mbps (OC-3/STM-1, OC-12/STM-4, 270 Mbps, 1064 Mbps, Fast/Gig Ethernet). The maximum power consumption of the device is 50 W, when the heater is on.



*Fig. 3. The AXIS P1344-E video camera installed on the right of the fSONA-SONABeam® 1250-E optical transceiver device.*

### 8.1.2 Meteorological instrumentation

Together with the optical transceiver, there are also available at the site A (see Fig. 4): a meteorological station, a particle disdrometer, a visibilimeter and, optionally, a millimetre-wave radiometer.



*Fig. 4: Location of the video camera and optical transceiver with respect to the meteorological station installed in A (Google© maps).*

The meteorological station is an automatic station able to measure pressure, temperature, wind velocity and direction (through an anemometer), and rainfall through a tipping-bucket rain-gauge. Analyses of the local micro-climate, with measurements made at the meteorological station located in A (see Fig. 5), confirm the peculiarity of the chosen site for urban mixed wired wireless communications experiments.

The visibilimeter is an easy installation and maintenance forward-scatter measurement process: the device measures visibility from 0 to 20 km with a 10% accuracy, employing a 850 nm laser (see Fig. 6). The same device works as an optical disdrometer, too: it is able to provide the size distribution of precipitation particles, measuring their diameter from 0.1 to 30 mm with a 5% accuracy, and their category (drizzle, rain, snow, graupel and sub-species).

Millimetre-wave radiometer is a W-band large bandwidth receiver, still under development and capable of measuring the antenna noise temperature which is related to atmospheric brightness temperature [Marzano, 2006]. The latter is well correlated with the

path-integrated water vapour content and, if present, liquid water content along the pointing direction.

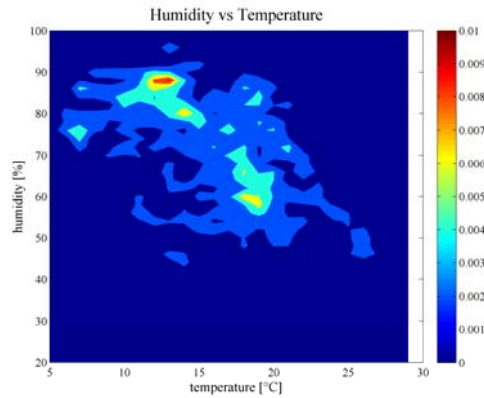


Fig. 5. Temperature and humidity frequency map for the period when both FSO and meteo measurements were performed (20.9.2011 till 1.12.2011).



Fig. 6: The Campbell Scientific PSW 100 particle disdrometer and visibilimeter installed in A.

### 8.1.3 Photovisibilimeter: visibility through video cameras

Atmospheric visibility, measured through a conventional visibilimeter (Fig. 6), is an assessment which is usually carried out at the transmitter or receiver site. Thus it is not representative of the true atmospheric opacity along the FSO link and studies are on going to employ the AXIS P1344-E video camera (see Fig. 2) to estimate visibility along the link direction, from A to B.

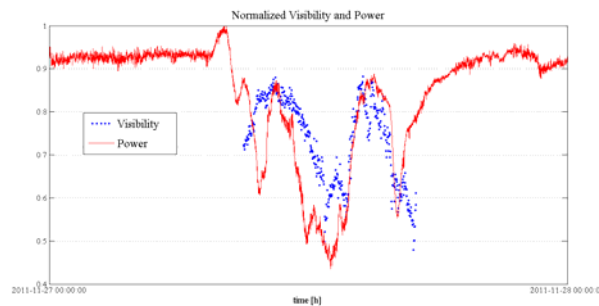


Fig. 7. Estimated atmospheric visibility (blue points) from video camera and FSO received link power (in red) normalized to their maxima during the daytime period.

Visibility appraisal is performed by cross-correlation on the red channel component of the images, using four objects always present in the image and at four different distances as references for each measurement.

Fig. 7 shows the preliminary results where the estimated atmospheric daytime visibility (expressed by the blue dots) is superimposed to the FSO received link power (in red) normalized to their maxima. There is a relatively high correlation between the decrease of FSO power measurement and the trend of estimated visibility which is encouraging.

## 8.2 Channel modelling

Extinction of the FSO laser beam power is mainly due to optical interactions with atmospheric particle distributions, mainly aerosols, snow, fog and rain [Nebuloni, 2005]. Only the raindrop articles will be treated below due to the availability of measured data (shown in the next section).

### 8.2.1 Atmospheric scattering model

In general, the “extinction” law for any electromagnetic radiation intensity  $I$  ( $\text{W m}^{-2} \text{sr}^{-1} \text{Hz}^{-1}$ ) can be written through the “Beer–Lambert–Bouguer” law within the radiative transfer theory [Ishimaru, 1997]:

$$I(r, \theta, \varphi) = I(0, \theta, \varphi) e^{-\int_0^r k_e(r') dr'} = I_0 e^{-\tau(0, r)} = I_0 t(0, r) \quad (8.1)$$

where  $r$  (km) is the range,  $(\theta, \varphi)$  are the incidence angles,  $I_0$  is the incident intensity,  $k_e$  (1/km) is the wavelength- and meteorological-dependent extinction coefficient due to atmospheric gases and particle size distribution,  $\tau$  the optical thickness and  $t$  the intensity transmittance between 0 and the position of the receiver at range  $r$ .

Extinction can be decomposed into scattering coefficient  $k_s$  (1/km) and absorption coefficient  $k_a$  (1/km), so that [Ishimaru, 1997], [Marzano, 2006]:

$$k_e = k_a + k_s, \quad w = \frac{k_s}{k_e} \quad (8.2)$$

where  $w$  is the volumetric albedo. If the angular scattering phase function  $p_s$  is known, than its first moment is expressed by the asymmetry factor  $g$  as follows [Ishimaru, 1997], [Marzano, 2006]:

$$g = \frac{\int \cos \theta_s p_s(\theta, \varphi, \theta_s, \varphi_s) d\Omega_s}{4\pi} \quad (8.3)$$

where  $\Omega_s = \sin \theta_s d\theta_s d\varphi_s$  is the scattering solid angle. The asymmetry factor may be comprised between -1 and +1 indicating dominant backward and forward scattering, respectively. If  $g=0$  then the scattering is angularly isotropic.

## 8.2.2 Atmospheric attenuation and scattering due to rain

The main attenuation factor for optical wireless link is fog, but rain also imposes a non negligible path attenuation  $\alpha$ . As raindrop sizes become large enough to cause reflection and refraction processes, a wavelength-dependent scattering and absorption must be considered within the “geometrical optics” theory limit [Al Naboulsi et al., 2004].

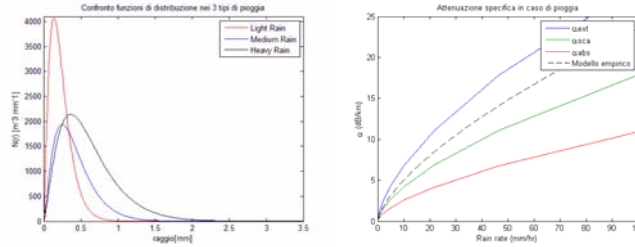


Fig. 8: Rain size distribution for light, medium and heavy rain and model-based absorption, scattering, and attenuation versus rainrate. Empirical attenuation is also shown for comparison.

The Mie theory can be used to simulate the FSO extinction, the albedo and the asymmetry factor by assuming a proper raindrop size distribution  $N$  [Marzano et al., 2007], [Marzano and Ferrauto, 2005]. For light, medium and heavy rain an example is shown in Fig. 8 together with the model-based specific scattering, absorption and total attenuation (extinction) at 1550 nm versus rainrate  $R$ . FSO rain attenuation is basically wavelength independent, as opposite to microwave frequency links  $\alpha$ . Even though for a rain rate of 100 mm/h FSO attenuation can easily exceed 20 dB/km, these values are quite small when compared with attenuation at Ka band and above with the same rain rate  $\alpha$ .

In Fig. 9 the other model-based optical parameters are shown as a function of the simulated liquid water content  $L$ . Rain albedo can be larger than 0.6 whereas  $g > 0.9$  indicates the predominance of an optical forward scattering mechanism.

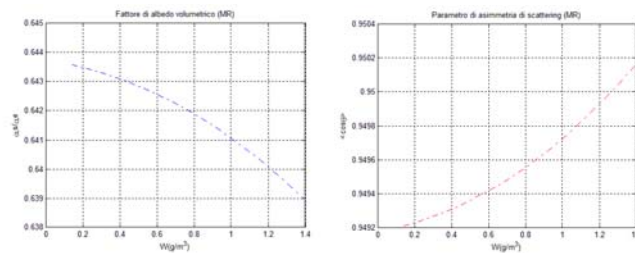


Fig. 9: Model-based rain optical parameters versus liquid water .

Using the Mie simulations with a random variability [Shettle and Weinman, 1970; Marzano and Ferrauto, 2005], the rainfall specific attenuation  $\alpha_{Rain}$  (dB/km) against rain rate of  $R$  (mm/h) for an optical wireless link can be approximated by the following “power law”:

$$\alpha_{Rain} = 10 \log_{10}(k_e) = aR^b \quad (8.4)$$

where from our model simulations  $a=1.150$  and  $b=0.69$ . The latter are similar to those empirically derived and equal to  $a=1.076$  and  $b=0.67$ , as confirmed in Fig. 8. Similar regressive models can be devised for  $w$  and  $g$  and for other hydrometeors as well as not only with respect to rain rate  $R$ , but also to liquid water content  $W$ .

### 8.3 FSO measurement analysis

Recent measurements, carried out in Rome using the FSO link illustrated in Sect. II, are shown here. The temporal trends of temperature and humidity are shown in Fig. 10 for the period going from September 20 till December 1, 2011. The curves tend to confirm the anti-correlation between thermal and wet characteristics of the atmosphere.

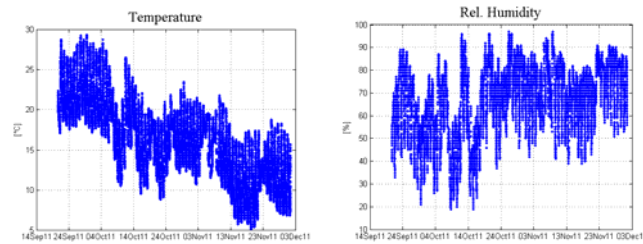


Fig. 10. Temperature and humidity measured at the receiver (point A) from September 20, 2011 till December 1, 2011.

For the considered period Fig. 11 shows the same temporal trend of Fig. 9, but for the measured rainfall and received power at 1550 nm. The received power is anti-correlated with rain intensity: when the latter increases, the received power decreases and viceversa, as expected.

The convective rain event of October 20, 2011 was relatively severe in Rome and characterized by moderate stratiform rain with some embedded convection. Its duration was only a few hours but it caused several damages within the city: see Fig. 12 for its rapid environmental variation.

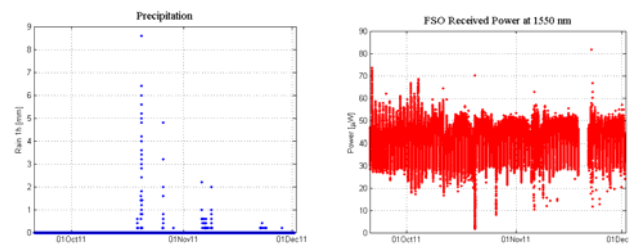


Fig. 11. Same as in Fig. 10, but for rain (mm/h) and received power ( $\square$  W). Sudden drops in received power were often due to birds flying across the FSO link and were observed thanks to the video camera.

Fig. 13 shows the FSO measured path attenuation, derived from the received power in Fig. 12 through a proper temporal windowing and clear-air averaging, and the predicted rain specific attenuation, derived from the model-based regressive expression given in (4) using rain-gauge data as predictors. There is a good agreement in terms of value range, even though a certain dispersion is noted probably due to the rain-gauge sensitivity (about 0.2 mm/h). Moreover, considering the relatively high values of rain albedo and asymmetry factor, some effects due to rain multiple scattering may lead to model-based underestimations [Tam and Zardecki, 1982; Marzano and Roberti, 2003; Marzano and Tosi Beleffi, 2010].

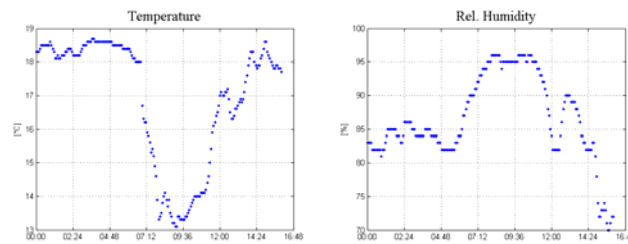


Fig. 12. Temperature and humidity measured on October 20, 2011.

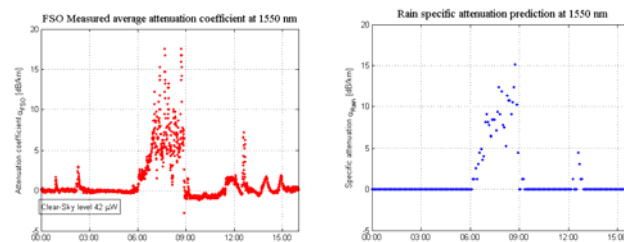


Fig. 13. Same as in Fig. 12, but for FSO measured path attenuation (dB) and model-based predicted specific attenuation (dB/km), using rain-gauge data and equation (4).

## 8.4 Conclusion

The activity devoted to the further development of the free space optics (FSO) link set up in Rome (Italy) has been illustrated. The two-way optical link at 1550 nm is about 1.6 km long and can operate with a transmission rate up to 1.5 Gbps. Among dust, precipitation, turbulence, fog, humidity, and any flying objects, such as birds, affecting the capacity of the optical channel, a set of results have been reported on water particle effects due to raindrops. A numerical evaluation of these atmospheric effects has been illustrated, together with a preliminary FSO channel appraisal based on physically derived propagative models.

Further activity will be devoted to assess data quality, collect longer time series in various meteorological scenarios and optimize the attenuation prediction models. By using the radiative transfer theory, the latter framework can, in principle, take into account multiple scattering effects along the FSO path.

*Acknowledgements.* This work has been carried out within an ISCOM-University La Sapienza funded joint project. Authors are thankful to EUR SpA (Rome, Italy) for its kind availability to install the fSONA-SONAbeam<sup>®</sup> on the so called “EUR Mushroom” tower roof. The authors deeply thank the staff of ISCOM (Department of Communications – Ministry of Economic Development) for the technical support provided, particularly Poalo Nocito, Roberto Dal Molin, Massimo Ferrante, Antonio Spaccarotella, Paolo Balducci and Mauro Piacentini. F. Consalvi of Fondazione Ugo Bordoni (FUB, Rome, Italy) is acknowledged for his support on technical activities.

## 8.5 References

[Zhu and Kahn, 2002] X. Zhu and J. M. Kahn, "Free-space optical communication through atmospheric turbulence channels," *IEEE Trans. Commun.*, vol. 50, pp. 1293–1300, 2002.

[Majumdar et al., 2008] A.K. Majumdar and J.C. Ricklin *Free-Space Laser Communications, Principles and Advantages*. Springer Science LLC, 233 Spring Street, New York, NY 10013, U.S.A., 2008.

[Carbonneau and Wisley, 1998] T. H. Carbonneau and D. R. Wisley, "Opportunities and challenges for optical wireless; the competitive advantage of free space telecommunications links in today's crowded market place," *SPIE Conference on Optical Wireless Communications*, Massachusetts, pp-119-128, 1998.

[D'Amico et al., 2003] M. D'Amico, A. Leva, and B. Micheli, "Free-Space Optics Communication Systems: First Results From a Pilot Field-Trial in the Surrounding Area of Milan, Italy," *IEEE Microwave and Wireless Components Letters*, vol. 13, pp. 305-307, 2003.

[Nebuloni, 2005] R. Nebuloni, "Empirical relationships between extinction coefficient and visibility in fog", *Applied Optics*, vol. 44, pp. 3795-3804, 2005.

[Awan et al., 2010] M.S. Awan, R. Nebuloni, Carlo Capsoni, L. Csurgai-Horva, S.S. Muhammad, F. Nadeem, M.S. Khan, and E. Leitgeb, "Prediction of drop size distribution parameters for optical wireless communications through moderate continental fog," *Int. J. Sat Comm. Networking*, DOI: 10.1002/sat.950, 2010.

[Nadeem et al., 2009] F. Nadeem, V. Kvicera, M.S. Awan, E. Leitgeb, S.S. Muhammad, and G. Kandus, "Weather Effects on Hybrid FSO/RF Communication Link," *IEEE Journal on Selected Areas in Communications*, vol. 27, pp. 1687-1697, 2009.

[Marzano et al., 2011] F. S. Marzano, S. Mori, F. Frezza, P. Nocito, G. M. Tosi Beleffi, G. Incerti, E. Restuccia, and F. Consalvi, "Free-Space Optical High-Speed Link in the Urban Area of Southern Rome: Preliminary Experimental Set Up and Channel Modelling," *Proc. of the 11th International Conference on Telecommunications (ConTEL 2011)*, Graz (Austria), 15-17 June 2011.

[Ishimaru, 1997] A. Ishimaru, *Wave propagation and scattering in random media*, (IEEE Press, Piscataway, NJ, 1997.

[Muhammad et al., 2007] S. Muhammad, B. Flecker, E. Leitgeb, and M. Gebhart, "Characterization of Fog Attenuation in Terrestrial Free Space Optical Links", *J. Optical Eng.*, vol. 46(6) pp. 066001-1 -06601-10, June 2007.

[Kruse, 1962] P. W. Kruse et. al., *Elements of Infrared Technology: Generation, Transmission and Detection*, J. Wiley and Sons, New York 1962.

[Kim et al., 2001] I. Kim, B. McArthur, and E. Korevaar, "Comparison of Laser Beam Propagation at 785 and 1550 nm in Fog and Haze for Optical Wireless Communications," *Proc. SPIE*, vol. 4214, pp. 26-37, 2001.

[Al Naboulsi et al., 2004] M. Al Naboulsi, H. Sizun, and F. de Fornel, "Fog Attenuation Prediction for Optical and Infrared Waves," *Optical Eng.*, vol. 43(2), pp. 319-329, 2004.

[Marzano et al., 2007] F.S. Marzano, D. Scaranari, and G. Vulpiani, "Supervised fuzzy-logic classification of hydrometeors using C-band dual-polarized radars," *IEEE Trans. Geosci. Rem. Sensing*, n. 45, pp. 3784-3799, 2007.

[Tam and Zardecki, 1982] W.G. Tam and A. Zardecki, "Multiple scattering corrections to the Beer-Lambert law. 1. Open detector," *Appl. Opt.*, vol. 21, pp. 2405-2412, 1982.

[Marzano and Roberti, 2003] F.S. Marzano and L. Roberti, "Numerical investigation of intense rainfall effects on coherent and incoherent slant-path propagation at K band and above," *IEEE Trans. Ant. Propagat.*, vol. 28, pp. 51-69, 2003.

[Shettle and Weinman, 1970] E.P. Shettle and J.A. Weinman, "The transfer of solar irradiance through inhomogeneous turbid atmospheres evaluated by Eddington's approximation," *J. Atm. Sci.*, vol. 27, pp. 1048-1055, 1970.

[Marzano and Ferrauto, 2005] F.S. Marzano and G. Ferrauto, "Generalized Eddington analytical model of azimuthally-dependent radiance simulation in stratified media," *Appl. Opt.*, vol. 44, pp. 6032-6048, 2005.

[Marzano and Tosi Beleffi, 2010] F.S. Marzano and G.M. Tosi Beleffi, "An analytical multiple scattering model to characterize free-space millimeter-wave and optical links in presence of atmospheric impairments," *Proc. of the 7th IEEE, IET International Symposium on Communications Systems, Networks and Digital Signal Processing, Newcastle (UK)*, 21-23 July 2010.

[Marzano, 2006] F.S. Marzano, "Modeling antenna noise temperature due to rain clouds at microwave and millimeter-wave frequencies," *IEEE Trans. Antennas and Propagat.*, vol. 54, pp. 1305-1317, 2006.

## 9 CHANNEL MEASUREMENT AND MARKOV MODELLING OF AN URBAN FREE-SPACE OPTICAL LINK

(Ayman Mostafa and Steve Hranilovic, McMaster University, Hamilton ON, Canada.)

Appeared in part *IEEE/OSA Journal of Optical Communications and Networking*, vol. 4, no. 10, pp. 836–846, October 2012.

©2012 IEEE and OSA. Personal use of this material is permitted. Permission from IEEE and OSA must be obtained for all other uses, in any current or future media, including reprinting/republishing this material for advertising or promotional purposes, creating new collective works, for resale or redistribution to servers or lists, or reuse of any copyrighted component of this work in other works. DOI: 10.1364/JOCN.4.000001

*Overview: Free-space optical (FSO) communication links provide high data rates, however, their reliability is heavily dependent on weather conditions. This paper presents our experimental, urban 1.87-km FSO link based on a customized commercial system and develops a library of channel measurements in clear and light rain weather conditions. A channel model for the link is proposed and experimentally quantified. Channel measurements are obtained by modulating a 60-mW laser source. At the receiver, a 2-GSa/s data converter is used and 16 fast-Fourier transform (FFT) cores are implemented in hardware to improve noise immunity. The resulting signal-to-noise ratio (SNR) of the channel samples is around 40~dB under clear weather conditions. Fitting with the log-normal, gamma-gamma, and Erlang distributions are presented and the scintillation index and coherence time are measured. A computationally-efficient finite-state Markov chain is derived for the channel to model both distribution and autocorrelation of the fading and is verified by the measurements. The Markov models and channel measurements in a variety of atmospheric conditions are available for download to permit easy verification of communication algorithms on this urban FSO channel.*

### 9.1 Introduction

Free-space optical (FSO) communication links are a potential solution to the last-mile problem since they combine the flexibility of RF networks and the high data rates of optical links. However, FSO communications are adversely affected by weather conditions such as fog, rain, and snow. Even under clear sky conditions, the non-homogeneity in the atmospheric structure caused by spatial and temporal temperature gradients causes random variations in the refractive index at optical wavelengths. Such non-homogeneity induces fluctuations of the signal intensity at the receiver termed as scintillation [1].

In order to characterize the terrestrial FSO communication link, many experimental investigations have been done, starting from early astronomical studies [2]. More recently, focus has been placed on the development of communication channel models based on experimental measurements. In [3], a 1.5-km link operating at 1550 nm is used to estimate fading distribution for a variety of receiver aperture sizes. The fitting parameters for log-normal and gamma-

gamma fading distributions are compared between the analytical model and experimental data as a function of receiver diameter. All measurements were done using an unmodulated continuous-wave source only 2.1 m above the ground and irradiance measurements made at a rate of 10 kHz in clear weather. The noise was not directly estimated, but rather, an estimate of its mean is removed from all measured samples. Channel measurements on a 1550-nm, 12-km FSO system are reported in [4] to develop estimates of parameters of fading distributions. The transmitter is an unmodulated continuous-wave source and received irradiance were sampled at 10 kHz and noise statistics are measured. Under the assumption of known noise statistics, they develop estimators for parameters of log-normal and gamma-gamma fading distributions considering fading and noise jointly. In [5], channel measurements of attenuation on a 1-km FSO link operating at 1550 nm are reported during a rain event. Although measurement data and atmospheric data are provided, no channel model is presented. A recent work [6] presents measurement results of a 1-km FSO link at 785 nm. The received photocurrent is sampled at 10 kHz for 3-sec intervals. The key contribution of the paper is the development of a Butterworth spectral fit to model the autocorrelation of the atmospheric fading model. The fitting is parameterized by temperature and rain level to give a family of spectra. A good fit in spectra is presented over a wide range of conditions, however, for convenience, the fading is modelled as being gamma distributed and not with more accepted log-normal or gamma-gamma models. In [7], pulses with a frequency of 6 MHz are transmitted for channel measurements over a 2.7-km FSO link. The received samples are bandpass filtered, rectified, and averaged to represent the received optical intensity. Although this process adds more complexity, a key advantage is attained by transmitting away from the DC region with possible coupling issues. The work presents plots of channel scintillation and attenuation but does not provide a comprehensive model for the channel.

This paper presents measurements of a 1.87-km FSO link in an urban environment. Unlike previous work which was done with laboratory equipment or for relatively short periods of time, our measurement system uses customized commercial FSO terminals coupled to a high-speed digitizing system which is able to record continuously. The digitization system uses 2-GSa/s data converters and high-speed FPGAs to collect and filter the incoming samples to improve SNR. After processing, the effective sampling rate is over 100 kHz for a continuous period of nearly 9 hours. An initial library of channel measurements is developed in clear and light rain weather conditions. This library is open for download [8] and will permit more realistic verification of communication algorithms on a commercial urban FSO channel. This work is the initial step in an ongoing campaign of channel measurement in different weather conditions which will be provided to the research community. In addition, a simple Markov model is developed to jointly represent the channel fading distribution and autocorrelation. With a small number of states, it is possible to generate long sequences of fading amplitudes which are close to measurements. Thus, this model will allow for simulation studies of FSO systems without resorting to coarse modelling assumptions of slow, block-independent fading.

Section II presents details of the experiment while Sec. III presents measurements and a bluechannel model for the FSO transceivers. In Section IV, the procedure and measurement results are reported at different time scales and estimates of the fading distribution and coherence time are obtained. blueIn addition, fitting with the log-normal, gamma-gamma, and Erlang distributions are presented. Section V gives a finite-state Markov chain model for the channel which is compared to measured results. Finally, concluding remarks are given in Section VI.

## 9.2 Experimental Details

Given that the objective of this study is a long-term channel measurement in a Canadian environment, the basis of our measurement setup is a commercial FSO terminal, the SONAbeam<sup>TM</sup>-1250-M [9]. This unit was jointly customized with the manufacturer to permit analog transmission and reception functions in addition to the standard digital operation. In addition, two Triton<sup>TM</sup>-V5-VXS digitizer boards [10] are employed on each end of the link.

### A. FSO Terminals

The customized FSO terminals were deployed in August 2010 across McMaster University campus in west Hamilton area as illustrated in Fig. 1. One terminal is installed on the

rooftop of the McMaster Innovation Park (MIP) building (approx. 21 m high) while the other terminal is installed on the rooftop of the Brandon Hall (BH) student residence (approx. 40 m high) at the north-west corner of McMaster University campus. The distance between the two terminals is approximately 1870 meters and the link passes over a major highway and many residential and commercial buildings.

1) Transmitters: Each terminal has four laser diodes at 1550 nm for transmission. Each laser has an independent driver and can operate at one of seven discrete power levels. The maximum radiated optical power of each laser is 60 mW after lenses and filters. The angle of divergence is 2.5 mrad full width at half maximum (FWHM). The optical head satisfies IEC Class-1M eye-safety standards. Only a single laser allows the analog transmission of an electrical signal provided by a standard 50- $\Omega$ , single-ended, AC-coupled SMB plug. Permitted input signal levels are  $\pm 500$  mV.

2) Receiver: The receiver aperture is 20 cm in diameter and has a 2.3-mrad field-of-view. Two spatial and two spectral solar filters are used to minimize the background and radiation noise. An avalanche photodiode (APD) receiver is used. The photodetector is followed by a transimpedance amplifier (TIA) with automatic gain control (AGC). For the experiments reported here, the AGC is disabled and a fixed gain is set via control software. The output voltage is provided directly from the transimpedance amplifier operating in linear mode through a 100- $\Omega$  differential output via a pair of SMB connectors. Typical output levels are  $\pm 30$  mV at a TIA gain of 2000 V/A. B. Digitizer Boards

The core processing units are three Virtex<sup>TM</sup>-5 FPGAs from Xilinx [12]. Each FPGA is supported by two 512-MB DDR3 SDRAM memory banks, giving a total storage capacity of 3 GBytes on-board memory. The analog I/O front-end is supported by a 10-bit, 2-GSa/s ADC and a 12-bit, 2-GSa/s DAC output.

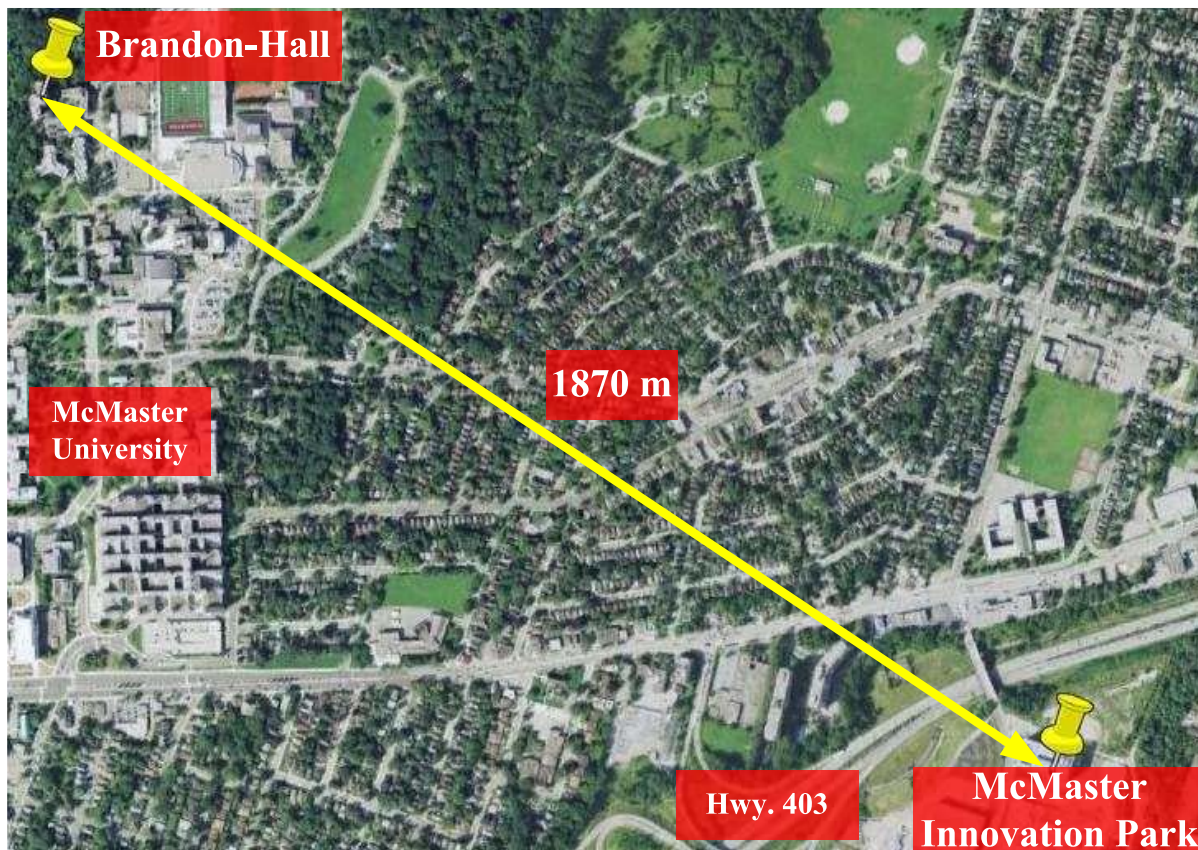


Figure Fehler! Verweisquelle konnte nicht gefunden werden.-1: Aerial view of the FSO link locations (MIP Lat.:  $43^{\circ} 15' 23.75''$  N, Long.:  $79^{\circ} 54' 2.06''$  W, BH Lat.:  $43^{\circ} 15' 57.47''$  N, Long.:  $79^{\circ} 55' 10.99''$  W) (satellite image © 2012 DigitalGlobe Inc. [11]).

### 9.3 Tranceiver Measurement and Characterization

This section presents measurement results to characterize the bandwidth and noise characteristics of the FSO link. The frequency response is used to ensure correct scaling of measured fading. Characterization of the noise is necessary to permit future simulation of communication systems. Details can be found in full journal paper.

### 9.4 Channel Measurements and Data Analysis

Unlike previous work [17], [4], an optical intensity-modulated sinusoid is transmitted through the channel to measure the loss and fading,  $h(t)$ . At the receiver, an FFT is applied as a notch filter to the received samples to minimize the impact of noise corruption.

A block diagram of the signal processing system at the receiver is illustrated in Fig. 6. A sinusoid of frequency 117.187500 MHz is transmitted through the atmosphere from the analog laser. The received signal is sampled at 2 GSa/s and 8192 =  $16 \times 512$  consecutive samples are buffered at a time. These samples are divided into 16 non-overlapping groups where each group undergoes a 512-point FFT implemented in an FPGA [18]. Notice that the transmit frequency is selected so that exactly 30 periods are applied to each 512-point FFT block. The following 11456 samples are discarded due to the latency in the FFT block.

For each FFT block, the real and imaginary coefficients corresponding to the bin containing

the 117.187500-MHz frequency are selected to calculate the magnitude frequency response. Finally, the magnitudes of the 16 segments are averaged and buffered to the on-board memory with an 8-bit resolution. Bit growth during calculations is shown in Fig. 6 along the data path. Using the above measurement parameters produces channel samples at the rate of 101.8 kSa/s.

The FFT acts as a narrow band notch filter which rejects a large portion of the interfering noise. Measuring the spectral density of the received signal in clear weather shows that the average SNR is approximately 40 dB. The FFT bin width can be made narrow by increasing the length of the FFT at the expense of processing time and reduced sampling frequency. As a compromise between noise performance and FFT latency, the data samples are divided into 16 segments with parallel 512-FFT cores instead of a single 8192-FFT core. Such division reduces the overall latency by a similar factor of 16 allowing more samples to be processed.

Details of data analysis can be found in full journal paper. Channel measurements are also available for download from [8].

## 9.5 Markov Modelling

A finite-state Markov chain can be directly applied to model the time-varying behaviour of discrete fading communication channels [23], [24], [25], [26]. The main idea is to divide the set of channel measurements into a finite number of discrete levels which are mapped to states. The transitions between states are then estimated using the measured data to yield a homogeneous Markov chain representation of the fading process.

Details of the model are available in full journal paper and can be downloaded from [8].

## 9.6 Summary

This work presents measurement results and channel modelling of an urban FSO channel. Unlike earlier work, we employ modified commercial transceivers and have collected a library of channel measurements in blueclear and light rain weather conditions. Thus, all of the trade-offs inherent in the design of a commercial FSO product are reflected in our measurements. The measurement system was implemented on a high-speed FPGA board where FFT cores were used to achieve measurement SNRs of approximately 40 dB. blueFitting to the log-normal, gamma-gamma, and Erlang distributions and measurements of the coherence time in clear weather are also presented. The channel gain is measured in light rain and clear weather conditions and a complete library of these measurements is available for download [8]. We intend to post new channel measurements to this database on a continuing basis under a greater variety of weather conditions. It is our sincere hope that this data set will aid FSO communication system designers to evaluate the performance of their algorithms using realistic channel data.

A finite-state Markov chain model is derived from the channel measurements and shown to model both the distribution and autocorrelation properties of the turbulence-induced fading. In particular the 64-state model showed good agreement and is also available for download [8].

The developed channel measurement system will be run continuously throughout the year to produce a large database of channel measurements under different weather conditions. Such a database will be used to build comprehensive statistical models and empirical formulas that directly relate the weather parameters with the channel statistics and the performance of the

communication link.

## 9.7 References

- . [1] L. C. Andrews and R. L. Phillips, *Laser Beam Propagation through Random Media*, 2nd ed. Bellingham, Washington: SPIE, 2005.
- . [2] M. E. Gracheva and A. S. Gurvich, "Strong fluctuations in the intensity of light propagated through the atmosphere close to the earth," *Radiofiz.*, vol. 8, no. 4, pp. 717–724, 1965.
- . [3] F.S.Vetelino,C.Young,L.Andrews,andJ.Recolons,"Apertureaveragingeffectsontheprobabilitydensityofirradiance fluctuations in moderate-to-strong turbulence and spherical waves in the atmosphere," *Journal of Applied Optics*, vol. 46, no. 11, pp. 2099–2108, April 2007.
- . [4] A. Khatoon, W. G. Cowley, and N. Letzepis, "Channel measurement and estimation for free space optical communica- tions," in *AusCTW 2011*, January - February 2011.
- . [5] F. S. Marzano, S. Mori, F. Frezza, P. Nocito, G. M. T. Belevfi, G. Incerti, E. Restuccia, and F. Consalvi, "Free-space optical high-speed link in the urban area of southern Rome: preliminary experimental set up and channel modelling," in *Proceedings of the 5th European Conference on Antennas and Propagation (EUCAP)*, April 2011, pp. 2737 – 2741.
- . [6] K.-H. Kim, T. Higashino, K. Tsukamoto, and S. Komaki, "Optical fading analysis considering spectrum of optical scintillation in terrestrial free-space optical channel," in *International Conference on Space Optical Systems and Applications*, Santa Monica, CA, May 2011, pp. 58–66.
- . [7] M. Gebhart, E. Leitgeb, and J. Bregenzner, "Atmospheric effects on optical wireless links," in *Proceedings of the 7th International Conference on Telecommunications, ConTEL 2003*, vol. 2, Zagreb, Croatia, June 2003, pp. 395 – 401.
- . [8] "Free-Space Optical Communication Algorithms Laboratory (FOCAL), McMaster University." [Online]. Available: focal.mcmaster.ca
- . [9] fSONA Networks, Inc. (2011) fSONA: free Space Optical Networking Architecture. [Online]. Available: <http://www.fsona.com/>
- . [10] TEK Microsystems, Inc., "TekMicro." [Online]. Available: <http://www.tekmicro.com/>
- . [11] DigitalGlobe, Inc. (2012) Satellite Imagery and Geospatial Information Products. [Online]. Available: <http://www.digitalglobe.com/>
- . [12] Xilinx, Inc. (2011). [Online]. Available: <http://www.xilinx.com/support/documentation/virtex-5.htm>
- . [13] S. M. Kay, *Modern Spectral Estimation: Theory And Application*. Prentice Hall, Englewood Cliffs, New Jersey, 1988.
- . [14] "The Weather Network." [Online]. Available:

<http://www.theweathernetwork.com/weather/caon0289>

- . [15] H. Willebrand and B. S. Ghuman, *Free Space Optics: Enabling Optical Connectivity in Today's Networks*. Sams Publishing, 2002.
- . [16] I. Kim, J. Koontz, H. Hakakha, P. Adhikari, R. Stieger, C. Moursund, M. Barclay, A. Stanford, R. Ruigrok, J. Schuster, and E. Korevaar, "Measurement of scintillation and link margin for the terralink laser communication system," *Proceedings of the SPIE*, pp. 100–118, January 1998.
- . [17] F. S. Vetelino, B. Clare, K. Corbett, C. Young, K. Grant, and L. Andrews, "Characterizing the propagation path in moderate to strong optical turbulence," *Journal of Applied Optics*, vol. 45, no. 15, pp. 3534–3543, May 2006.
- . [18] "Xilinx LogiCORE IP Fast Fourier Transform v7.1," March 2011. [Online]. Available: [http://www.xilinx.com/support/documentation/ip\\_documentation/xfft\\_ds260.pdf](http://www.xilinx.com/support/documentation/ip_documentation/xfft_ds260.pdf)
- . [19] G. R. Osche, *Optical detection theory for laser applications*. Wiley-Interscience, 2002.
- . [20] "NIST/SEMATECH e-handbook of statistical methods." [Online]. Available: <http://www.itl.nist.gov/div898/handbook/>
- . [21] M. A. Al-Habash, L. C. Andrews, and R. L. Phillips, "Mathematical model for the irradiance probability density function of a laser beam propagating through turbulent media," *Optical Engineering*, vol. 40, pp. 1554–1562, August 2001.
- . [22] M. L. B. Riediger, R. Schober, and L. Lampe, "Multiple-symbol detection for photon-counting MIMO free-space optical communications," *IEEE Transactions on Wireless Communications*, vol. 7, no. 12, pp. 5369–5379, December 2008.
- . [23] H. S. Wang and N. Moayeri, "Finite-state Markov channel - a useful model for radio communication channels," *IEEE Transactions on Vehicular Technology*, vol. 44, no. 1, pp. 163–171, February 1995.
- . [24] Q. Zhang and S. Kassam, "Finite-state Markov model for Rayleigh fading channels," *IEEE Transactions on Communications*, vol. 47, no. 11, pp. 1688–1692, November 1999.
- . [25] V. Bhaskar, "Finite-state Markov model for lognormal, chi-square (central), chi-square (non-central), and K-distributions," *International Journal of Wireless Information Networks*, vol. 14, no. 4, pp. 237–250, October 2007.
- . [26] X. Zhu and J. M. Kahn, "Markov chain model in maximum-likelihood sequence detection for free-space optical communication through atmospheric turbulence channels," *IEEE Transactions on Communications*, vol. 51, no. 3, pp. 509–516, March 2003.

## 10 FSO LINK PROPAGATION MEASUREMENTS AND CHANNEL MODEL UNDER FOG CONDITIONS DEVELOPED AT NORTHUMBRIA UNIVERSITY

(Zabih Ghassemlooy, Joaquin Perez, Muhammad Ijaz)

### 10.1 Introduction

Optical Communications Research Group (OCRG) at Northumbria University has started a measurement campaign in order to unveil and support the available FSO link propagation models regarding fog and smoke conditions. In this case OCRG is interested in the visibility ( $V$ ) range with poor viewing conditions due to the high attenuation over the FSO propagation path, using Kruse and Kim propagation models [Kim, McArthur et al., 2001] at a link range less than 500 m. In order to provide a fair comparison in terms of the different transmitted optical wavelengths, this campaign of measurements is carried out in an indoor atmospheric chamber for low visibility range for light to dense fog and smoke conditions. The indoor atmospheric chamber is of 6 meter long where the injected fog is controlled using air vents and fans positioned along the chamber, thus allowing careful monitoring of the FSO transmission. The chamber allows repetitive measurements under identical conditions for specific FSO link configurations. Thus avoiding the long waiting time experienced in outdoor FSO links mostly determined by the weather conditions that could vary from location to location. Visibility is measured using the wavelength of 0.55  $\mu\text{m}$  along the length of an FSO channel rather than at one location as is the case in traditional outdoor FSO links [Fischer, Witiw et al., 2008; Naboulsi, Forne et al., 2008], thus enabling to relate the measured visibility with an exact empirical value of fog attenuation at any FSO wavelengths.

Finally, this campaign offered a complete set of results for the FSO link under the visible-NIR wavelength spectrum for fog and smoke conditions. The main outcome of this measurement campaign is development of a new empirical model showing that both fog and smoke attenuation are wavelength dependent rather than visibility dependent as has been reported [Kim, McArthur et al., 2001].

### 10.2 Modelling the Fog Attenuation for FSO Links - Overview

Fog is composed of very fine spherical water particles of various sizes suspended in the air, causing humidity to reach 100% as reported in [Awan, Horwath et al., 2009; Yang, Niu et al., 2010]. Fog particles reduce the visibility near the ground and the meteorological definition of fog is when the visibility drops to near 1 km [(WMO), 2008]. Two types of fog are well categorized in literature, which are the convection and the advection fog [Cereceda, Osses et al., 2002]. Assuming fog particles have spherical shape, one can apply the exact Mie scattering theory to measure the scattering cross section  $C_s$  of the particle by knowing the particle radius  $r$ . Thus, we can estimate the theoretical value of the normalized scattering efficiency  $Q_s$  as [Bohren and Huffman, 1983]:

$$Q_s = \frac{C_s}{\pi r^2} \quad (10.2-1)$$

The total attenuation induced by particles in the atmosphere is the sum of molecular absorption and scattering of light. However, the wavelengths used in FSO links are almost

selected in the atmospheric transmission windows where the molecular absorption cross-section  $C_a$  due to gases is negligible, i.e.  $C_a \sim 0$  [Bohren and Huffman, 1983]. The atmospheric attenuation coefficient  $\beta_\lambda$  of the optical signal due to the scattering of fog particles is given by [(WMO), 2008]:

$$\beta_\lambda = \int_0^\infty \pi r^2 Q_s \left( \frac{2\pi r}{\lambda}, n' \right) n(r) dr \quad (10.2-2)$$

where  $n'$  is the real part of the refractive index,  $2\pi r/\lambda$  is the size parameter, and  $n(r)$  is the particle size distribution function. Generally this distribution is represented by analytical functions such as the log-normal distribution for aerosols and is given by [Weichel, 1990]:

$$n(r) = ar^\alpha \exp(-br) \quad (10.2-3)$$

where,  $a$ ,  $b$  and  $\alpha$  are the parameters that characterize the particle size distribution. Since,  $Q_s$  is mainly dependent on the size parameter, which is dependent on  $\lambda$  and  $r$ . The size parameter is ratio of the size of the fog particle to the incident wavelength. Therefore, the resultant fog attenuation will be remarkably dependent on the selected wavelength. However, the particle radius of the fog varies in the spatial domain in the atmosphere, due to lack of the fixed particle size along the FSO link. This introduces a complexity to predict the fog induced attenuation by using the theoretical approach in the FSO channel. Generally, due to the complexity involved in the physical properties of the fog, like particle size and the non-availability of particle distribution, the fog induced attenuation of the optical signal can be predicted using empirical models. Empirical models use the visibility data in order to estimate the fog induced attenuation. The original empirical relationship which relates  $V$  with the fog attenuation has been given by the Kruse model [Kruse, McGlauchlin et al., 1962]:

$$V(km) = \frac{10 \log_{10} T_{th}}{\beta_\lambda} \left( \frac{\lambda}{\lambda_o} \right)^{-q} \quad (10.2-4)$$

where  $T_{th}$  is the visual threshold taken as 2%,  $\lambda_o$  is the maximum spectrum of the solar band and  $q$  is the coefficient related to the particle size distribution in the atmosphere. Kruse model estimates the fog attenuation from visible – NIR wavelengths and the  $q$  value, which is a function of visibility, is defined as:

$$q = 0.585V^{1/3} \quad \text{for } V < 6 \text{ km} \quad (10.2-5)$$

However, the estimation of the fog attenuation using the Kruse model is considered to be inaccurate for fog [Kim, McArthur et al., 2001]. This is because the value of  $q$  has been defined from haze particles ( $V > 1$  km) present in the atmosphere rather than fog ( $V = 1$  km). Kim modified the Kruse model using theoretical assumptions for the fog by defining  $q$  values as follows [Kim, McArthur et al., 2001]:

$$q = \begin{cases} 1.6 & \text{for } V > 50 \text{ km} \\ 1.3 & \text{for } 6 < V < 50 \text{ km} \\ 0.16V + 0.34 & \text{for } 1 < V < 6 \text{ km} \\ V - 0.5 & \text{for } 0.5 < V < 1 \text{ km} \\ 0 & \text{for } V < 0.5 \text{ km} \end{cases} \quad (10.2-6)$$

The values of  $q$  indicate that the atmospheric attenuation coefficient  $\beta_\lambda$  is wavelength independent in the fog condition for  $V < 0.5$  km. However, recent experimental data at selective wavelengths of 0.83 and 1.55  $\mu\text{m}$  shows a different behaviour than is predicted by the Kim model especially for the dense fog conditions with visibility  $V < 0.5$  km [Nadeem, Javornik et al., 2010; Grabner and Kvicera, 2012; Ijaz, Ghassemlooy et al., 2012; Ijaz, Ghassemlooy et al., 2012]. This demonstrates that in spite of a significant number of investigations, the model presented in (10.2-6) needs to be explicitly verified experimentally, not for the selective or specific wavelength but for the entire spectrum of the visible – NIR range.

### 10.3 Empirical Characterization of a FSO Link under Fog and Smoke Conditions using an Indoor Atmospheric Laboratory Chamber

The link visibility (i.e. the meteorological visual range) is used to characterize the fog and smoke attenuation. The visibility  $V$  parameter is defined in [Pierce, Ramaprasad et al., 2001] as the distance to an object at which the visual contrast of the object drops to 2% of the original visual contrast (100 %) along the propagation path – commonly known as the Koschmieder law. This 2 % drop value is known as the visual threshold  $T_{th}$  of the atmospheric propagation path. The 2% visual threshold value is adopted here in order to follow the Koschmieder law as opposed to the airport consideration of  $T_{th} = 5\%$  [Prokes, 2009]. The meteorological visibility  $V$  (km) can be therefore expressed in terms of the atmospheric attenuation coefficient  $\beta_\lambda$  and  $T_{th}$  at a 0.55  $\mu\text{m}$  wavelength and is given as:

$$V = -\frac{10 \log_{10}(T_{th})}{\beta_\lambda}, \quad (10.3-1)$$

where  $\beta_\lambda$  is normally expressed in (dB/km), and is mathematically defined by knowing the transmittance  $T$  of the optical signal and the propagation distance  $L$  (km) using the Beer-Lambert law as [Ricklin, Hammel et al., 2006; Prokes, 2009]:

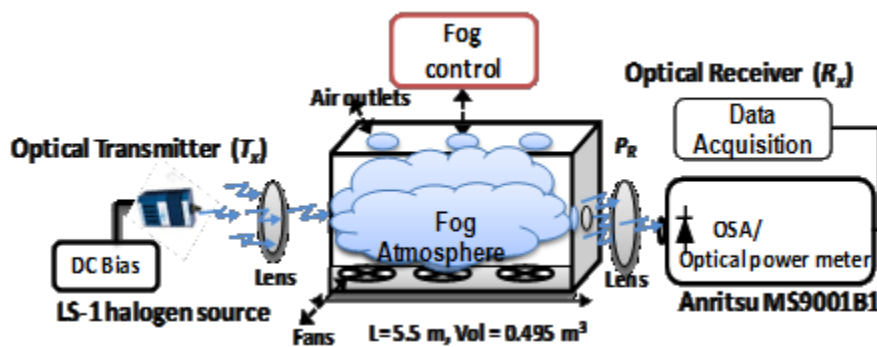
$$\beta_\lambda = -\frac{10 \log_{10}(T)}{4.343L}. \quad (10.3-2)$$

The FSO link propagation measurement campaign at OCRG is based using the indoor atmospheric chamber. This design is described in the previous chapter where it is used to characterize the turbulence effect on FSO communications links [Ghassemlooy, Le Minh et al., 2012]. The chamber design is depicted in the snapshots of the Fig. 10.3-1. This allows investigation of fog and smoke effects on FSO links, such as the scattering of the optical signal at 0.55  $\mu\text{m}$  in the presence of dense fog as shown in Fig. 10.3-1(c). In order to evaluate these impairments two types of aerosols were generated by a smoke machine (dry particles)

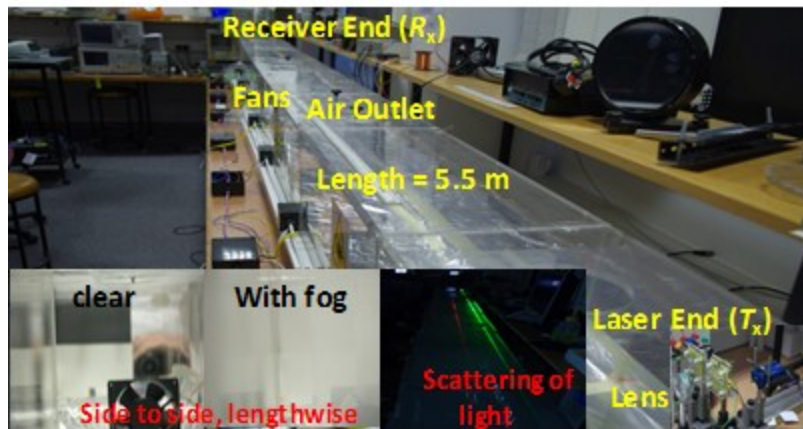
and a fog machine (water steam, with 100% humidity) [Awan, Horwath et al., 2009] with an output of  $0.94 \text{ m}^3/\text{sec}$ . In order to evaluate different propagation models two experimental approaches are used to characterise fog and smoke attenuation, (i) a continuous LS-1 tungsten halogen source with a broad spectrum ( $0.36$  to  $2.5 \text{ }\mu\text{m}$ ) and an Anritsu MS9001B1 optical spectrum analyser (OSA) with a spectral response of  $0.6$  to  $1.75 \text{ }\mu\text{m}$  and (ii) a number of laser sources at wavelengths of  $0.55$ ,  $0.67$ ,  $0.83$ ,  $1.31$  and  $1.55 \text{ }\mu\text{m}$  with the average transmitted optical powers  $P_T$  of  $-3.0 \text{ dBm}$ ,  $0 \text{ dBm}$ ,  $10 \text{ dBm}$ ,  $6.0 \text{ dBm}$  and  $6.5 \text{ dBm}$ , respectively and an optical power meter.

The amount of aerosols in the atmospheric chamber is controlled by a number of fans and a ventilation system. Aerosol particle sizes are very fine and light, and are slowly moving within the chamber. A time duration of 30 seconds is sufficient enough for fog/smoke particles to settle down homogeneously within the chamber prior to data acquisition (DAQ). An automated DAQ system which uses a LabVIEW frontend with the OSA is used to control wavelengths under the test, the sampling frequency and the optical loss estimation. In order to measure the effect of fog on different wavelengths, the average received optical power  $P_R$  is measured using the OSA at  $R_x$  before and after the injection of fog into the atmospheric chamber. The fog density is easily controlled via small size outlets. Measurements of the optical power are carried out at one second time interval until the chamber is free from fog with a clear view. The normalized transmittance  $T$  is calculated from  $P_R$  with and without fog. Since the goal is to characterise the optical attenuation, having identical powers at different wavelengths are not essential. The geometric and other losses are not taken into account for  $T_x$ , as  $P_R$  is measured both before and after fog and smoke at  $R_x$  to attain the wavelength dependent losses.

The value of  $\beta_\lambda$  is determined using (10.3-2), which corresponds to the measured  $T$  from light to dense fog condition for all wavelengths. Simultaneously the link visibility is measured in the same FSO link path along the chamber using a laser diode at  $0.55 \text{ }\mu\text{m}$  to ensure maximum transmission to the human eye, thus relating the visibility to human eye perception.



(a)



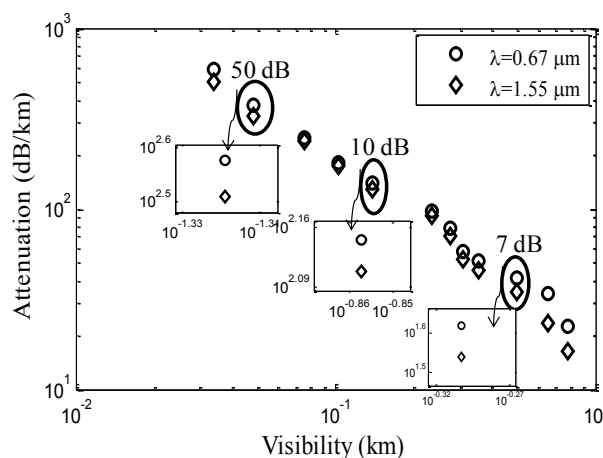
(b)

Figure 10.3-1: (a) The experimental set up to measure the fog attenuation and visibility and (b) the laboratory controlled atmospheric chamber and FSO link setup, and the inset, shows the presence of fog and the scattering of light in the atmospheric chamber.

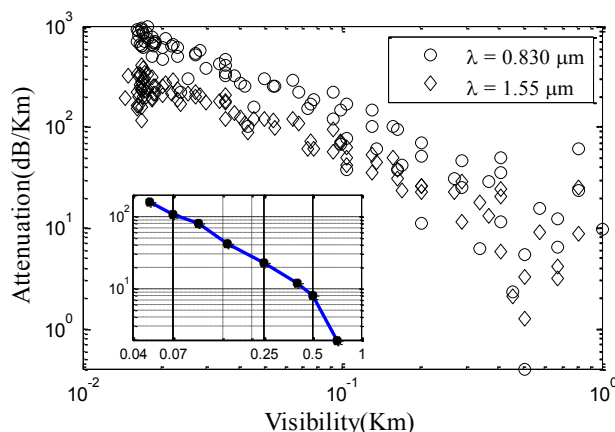
### 10.3.1 Experimental Attenuation Measurements for Fog and Smoke

The measured average fog attenuation (in dB/km) against the measured visibility for 0.67  $\mu\text{m}$  and 1.55  $\mu\text{m}$  wavelengths are shown in Fig. 10.3-2(a). In this graph the measured attenuation is notably higher for 0.67  $\mu\text{m}$  than at 1.55  $\mu\text{m}$  for the given visibility range ( $0.032 \text{ km} < V < 1 \text{ km}$ ). There is an attenuation difference of 50 dB/ km, 10 dB/ km and 7 dB/ km at  $V$  of 0.048 km, 0.103 km and 0.5 km, respectively. This difference contradicts the wavelength independency predicted by Kim model for  $V < 0.5 \text{ km}$  [Kim, McArthur et al., 2001].

Furthermore, the measured attenuation of smoke (dB/ km) against the visibility for 0.83  $\mu\text{m}$  and 1.55  $\mu\text{m}$  wavelengths are depicted in Fig. 10.3-2(b). The experimental result clearly demonstrates the dependency of the wavelength on the smoke attenuation. In general, the smoke attenuation difference is stronger than the fog attenuation. For smoke the difference in attenuation values are 108 dB/ km, 23 dB/km and 8 dB/ km for 0.83  $\mu\text{m}$  and 1.55  $\mu\text{m}$  at  $V$  of 0.07 km, 0.25 km and 0.5 km, respectively as shown in Fig 10.3-2(b) inset. The results show that 1.55  $\mu\text{m}$  wavelength is more favourable for the dense ( $V < 0.07 \text{ km}$ ), thick ( $V = 0.25 \text{ m}$ ) and moderate fog and smoke ( $V = 0.5 \text{ km}$ ) conditions.



(a)



(b)

Figure 10.3-2: The measured attenuation (dB/km) and visibility (km) (a) fog and (b) smoke.

## 10.4 New Empirical Model for Fog and Smoke Channels

The attenuation due to the scattering and absorption is highly dependent on the size parameter, according to (10.2-2). However, Kim had also defined values of  $q$  for fog, equation 10.2-6, illustrating the wavelength dependency of the attenuation and the type of scattering. The values of  $q$  are -4, -1.6 and 0 for Rayleigh scattering ( $r \ll \lambda$ ), Mie scattering ( $r \sim \lambda$ ), and geometric scattering ( $r \gg \lambda$ ), respectively [Kim, McArthur et al., 2001]. In order to come up with an appropriate model for the attenuation of fog and smoke based on the measured data the following were carried out. Using (10.2-4) values of  $q$  were obtained for individual wavelengths from 0.60 – 1.6  $\mu\text{m}$  using the empirical curve fitting method with a reference wavelength of 0.55  $\mu\text{m}$  as shown in Table 10.4-1. Values of the root mean square error (RMSE) and  $R^2$  confirm the curve fitting is in a good correlation with the measured data for both fog and smoke. The value of  $q$  is found to be within 0 to 0.6 for fog and smoke indicating Mie scattering ( $r \sim \lambda$ ). This verifies that in the ( $r \sim \lambda$ ) region for the dense fog condition, the  $q$  value is function of the wavelength not the visibility.

Table 10.4-1: Values of  $q$  obtained for different wavelength from measured fog and smoke data.

For Fog			
Wavelength ( $\mu\text{m}$ )	$q$	$R^2$ -value	RMSE
0.6	0.002	0.9670	0.1950
0.8	0.020	0.9850	0.1400
0.9	0.030	0.9846	0.1470
1	0.045	0.9827	0.1560
1.1	0.050	0.9813	0.1620
1.2	0.070	0.9803	0.1590
1.3	0.093	0.9802	0.1690
1.4	0.105	0.9800	0.1750
1.5	0.130	0.9760	0.1760
1.6	0.135	0.9751	0.1890

For Smoke			
0.55	0	0.9985	0.0467
0.67	0.100	0.9628	0.2000
0.83	0.180	0.9220	0.3100
1.31	0.580	0.9121	0.2100

The plot of predicted  $q$  values against the wavelength against the wavelength range of  $0.6 - 1.6 \mu\text{m}$  for fog and smoke conditions as well as the linear fit plot are shown in Fig. 10.4-1 and Fig. 10.4-2, respectively. The best curve fit does satisfy the equation 10.4-1 with  $R^2$  and RMSE values of 0.9732 and 0.0076, and 0.9797 and 0.0497 for fog and smoke, respectively.

$$q(\lambda) = \begin{cases} 0.1428\lambda - 0.0947 & \text{Fog} \\ 0.8467\lambda - 0.5212 & \text{Smoke} \end{cases} \quad (10.4-1)$$

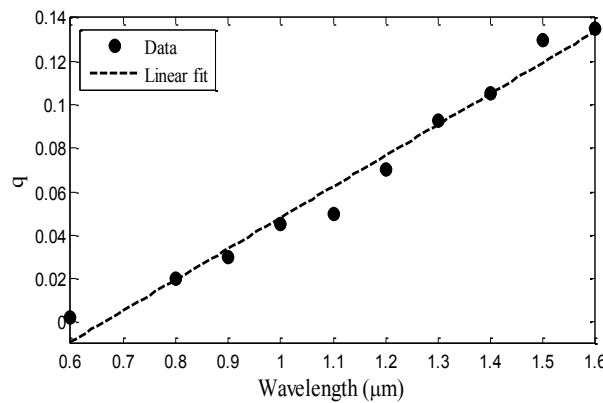


Figure 10.4-1: The predicted  $q$  value and linear curve of best-fit against wavelength for fog.

Therefore, the new proposed model for predicting the attenuation due to fog and smoke for  $0.55 \mu\text{m} < \lambda < 1.6 \mu\text{m}$  and  $0.15 \text{ km} < V < 1 \text{ km}$  can be presented as:

$$\beta_{\lambda} (\text{dB} / \text{km}) = \frac{17}{V(\text{km})} \left( \frac{\lambda}{\lambda_0} \right)^{-q(\lambda)} \quad (10.4-2)$$

The associated function for  $q(\lambda)$  for the fog and smoke is expressed in (10.4-1). The experimental data shows that as  $V \rightarrow 0$  for the very dense fog condition, the received optical signal is significantly lower than the OSA minimum sensitivity at  $V = 0.0135 \text{ km}$ . This validates that measurements below  $0.015 \text{ km}$ , however are not very practical to show the wavelength dependency of the fog attenuation. Thus, confirming the validity of the model for the visibility range of  $0.015 \text{ km} < V < 1 \text{ km}$ .

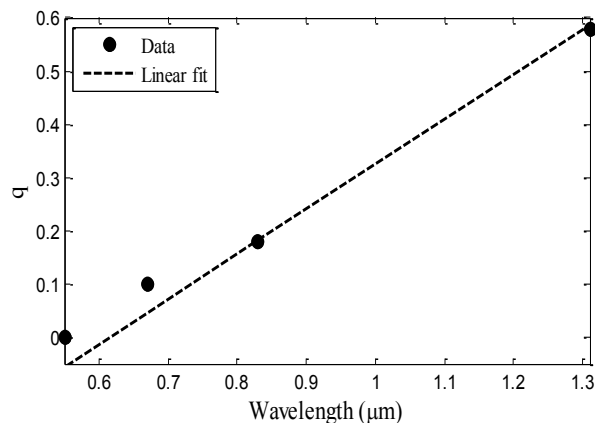


Figure 10.4-2: The predicted  $q$  value from proposed model and linear curve of best-fit against wavelength for smoke.

#### 10.4.1 Comparison of the measured visibility and attenuation data with the proposed model

Fig. 10.4-3 shows the measured fog attenuation against the concurrent visibility data for the selected wavelengths of 0.67, 0.83, 1.1, 1.31 and 1.55  $\mu\text{m}$  for the modified and Kim fog models. The log-log plot of the attenuation curve obtained from the proposed model defined by (10) and the comparison with the measured data shows a good agreement. However, the comparison of Kim model at  $\lambda = 1.55 \mu\text{m}$  with the measured data for  $V < 0.5 \text{ km}$  shows clearly that the Kim model overestimates the fog attenuation. The main reason for this is that Kim model does not take into account the wavelength to estimate the fog attenuation. However, Kim model fits well with the experiment data for  $V > 0.5 \text{ km}$  (see inset in Fig. 10.4-3). On the other hand, Fig. 10.4-4 displays the measured smoke attenuation against the concurrent visibility data for the selected wavelengths of 0.55, 0.67, 0.83, and 1.31  $\mu\text{m}$ . The comparison of the proposed smoke model illustrates a good agreement between the measured data for selected wavelengths. This figure clearly indicates the dependency of the smoke attenuation on the wavelength. The figure shows a difference of  $> 50 \text{ dB/km}$  observed between 1.31 and 0.83  $\mu\text{m}$  for the dense smoke condition ( $V < 0.07 \text{ km}$ ), with a progressive reduction in the attenuation difference for thick and moderate smoke conditions, thus, clearly indicating suitability of the NIR wavelengths for dense smoke conditions.

The proposed new model, where the available visibility data needs to be considered instead of the liquid water content (LWC) and the particle radius, is most suitable for the FSO link budget analysis in urban areas where fog and smoke are more likely to occur all year round.

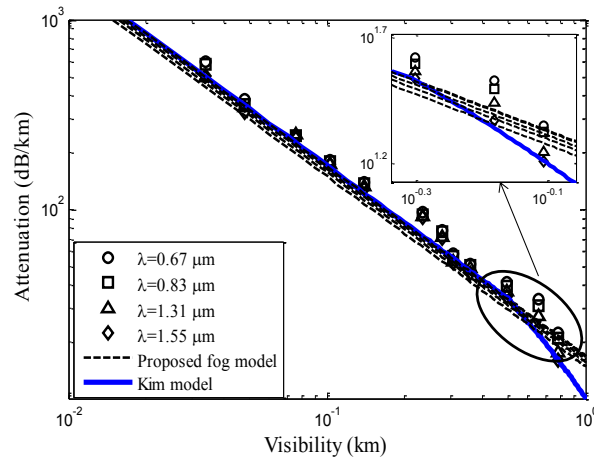


Figure 10.4-3: Real time measured fog attenuation versus visibility ( $V = 1$  km) and curves of modified fog and Kim model for different wavelengths.

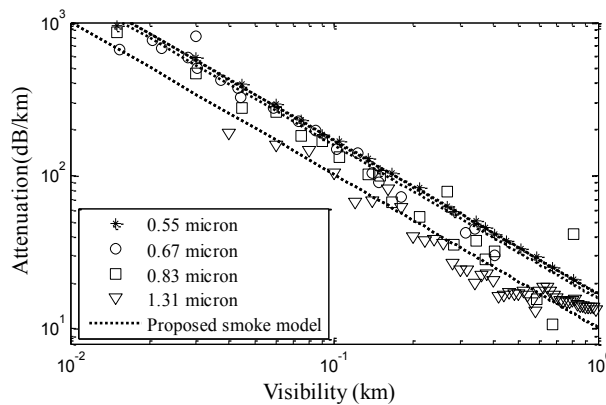


Figure 10.4-4: Real time measured smoke attenuation versus visibility ( $V = 1$  km) and curves of smoke model for different wavelengths.

### 10.4.2 Comparison of the proposed model with visible-NIR spectrum attenuation

The measured attenuation for the visible – NIR spectrum under test (SUT) at the very dense fog condition ( $V \sim 0.05$  km), as depicted in Fig 10.4-5(a), shows three possible attenuation windows, (i)  $0.60 \mu\text{m} - 0.85 \mu\text{m}$ , which has an attenuation range of  $375 \text{ dB/km} - 361 \text{ dB/km}$  with the peak attenuation of  $382.4 \text{ dB/km}$  at  $0.72 \mu\text{m}$ , (ii)  $0.85 \mu\text{m} - 1.0 \mu\text{m}$  showing that  $0.830 \mu\text{m}$  has a lower attenuation ( $360 \text{ dB/km}$ ) than  $0.925 \mu\text{m}$  and with a peak attenuation of  $383.6 \text{ dB/km}$ , whereas at  $0.940 \mu\text{m}$  the peak attenuation is the lowest at  $354 \text{ dB/km}$ , and (iii)  $1.0 \mu\text{m} - 1.55 \mu\text{m}$ , with an attenuation range of  $360 \text{ dB/km} - 323 \text{ dB/km}$ .

These results show that at  $1.33 \mu\text{m}$  the highest attenuation is at  $357 \text{ dB/km}$  compared to  $1.05 \mu\text{m}$  with a peak attenuation of  $347.6 \text{ dB/km}$ . However,  $1.55 \mu\text{m}$  wavelength has the lowest attenuation of  $324 \text{ dB/km}$  in the very dense fog condition at  $V = 0.05$  km.

Table 10.4-2 shows the suitable possible wavelengths and associated attenuation values for fog. The behaviour of the attenuation spectrum is similar for  $V = 0.3$  km with the peak attenuation values of  $\sim 59.5 \text{ dB/km}$  to  $53.5 \text{ dB/km}$  for  $0.6 \mu\text{m}$  and  $1.55 \mu\text{m}$ , respectively (see Fig. 10.4-5 (b)).

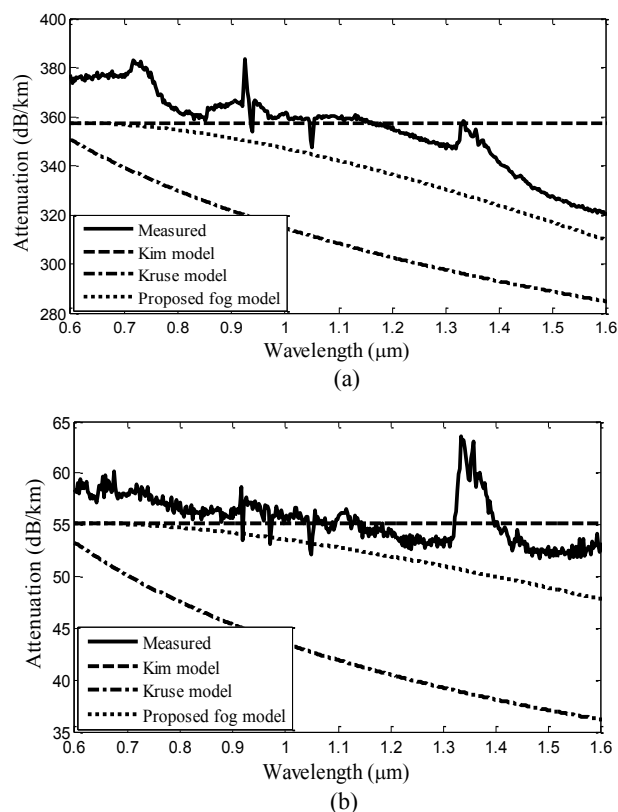


Figure 10.4-5: The measured fog attenuation (dB/km) from the visible – NIR spectrum and the comparison with the selected empirical models (a) for  $V = 0.048$  km, and (b) for  $V = 0.3$  km.

Table 10.4-2: Suitable wavelengths to operate FSO in a foggy channel, measured at  $V = 0.048$  km.

Wavelength Window ( $\mu\text{m}$ )	Attenuation at $\lambda$ Window Range (dB/km)	Peak Attenuation (dB/km)	Suitable Operational Wavelengths ( $\mu\text{m}$ )
0.6 – 0.85	375 – 361	382.4	0.830
0.85 – 1.0	361 – 360	383.3	0.940
1.0 – 1.55	360 – 323	357.0	1.55

In order to correlate the proposed model with the outdoor FSO channel, Kim and Kruse models are selected, which are widely used in literature. Kim model at  $V \sim 0.05$  km and 0.3 km show that the fog attenuation for SUT is wavelength independent contradicting the experimental data. The Kruse model underestimates the fog attenuation at  $V \sim 0.05$  km and 0.3 km for SUT (see Figs. 10.4-5 (a) and (b)). However, the new proposed model for fog shows a close correlation for SUT. This verifies that the proposed model estimates the fog attenuation more accurately than both Kim and Kruse models for  $V < 0.5$  km.

In the case of smoke, the measured smoke attenuation (in dB/km) at  $V \sim 0.185$  km and 0.245 km for SUT is shown in Fig. 10.4-6. The resultant smoke attenuation at  $V = 0.185$  km is almost 90 dB/km for the visible range dropping to 43 dB/km at the NIR range of SUT. For  $V = 0.245$  km the smoke attenuation starts at 70 dB/km at the visible range decreasing to 33 dB/km at the NIR range of SUT, see Fig. 10.4-6 (b). For smoke Kim model overestimates the measured attenuation and shows that wavelength is independent of attenuation for  $V < 0.5$  km. However, Kruse model underestimates the smoke attenuation for  $0.7 \mu\text{m} < \lambda < 1 \mu\text{m}$  and overestimates the smoke attenuation for  $1.1 \mu\text{m} < \lambda < 1.6 \mu\text{m}$  (see Figs. 10.4-6 (a) and (b)). On the other hand the new proposed model fits well the experimental data and shows a close

co-relation with the measured smoke attenuation spectrum, thus verifying the validity of the proposed model for smoke conditions for the visible – NIR SUT.

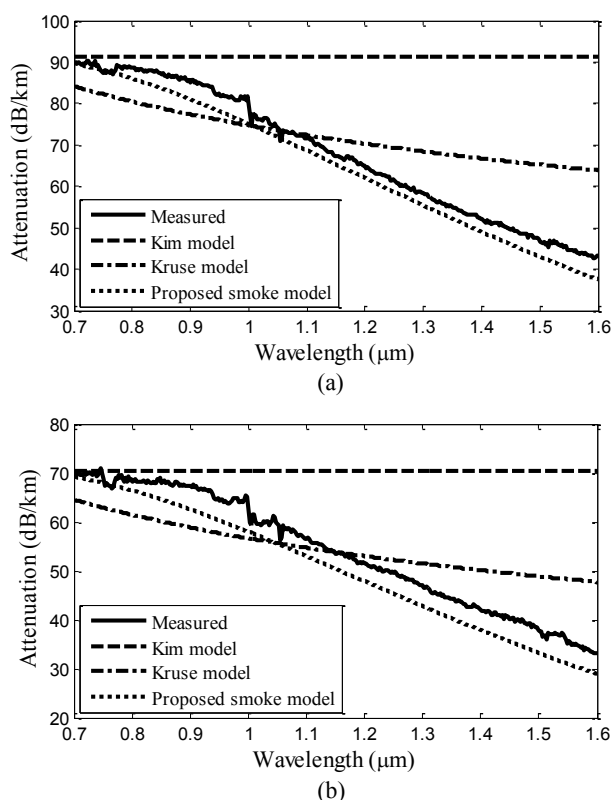


Figure 10.4-6: The measured smoke attenuation (dB/km) from the visible – NIR spectrum and the comparison with the selected empirical models (a) for  $V = 0.185$  km, and (b) for  $V = 0.245$  km

## 10.5 Summary

The OCRG at Northumbria University has demonstrated the impact of fog and smoke on the FSO link performance using a continuous wavelength spectrum range of  $0.6 \mu\text{m} < \lambda < 1.6 \mu\text{m}$  under controlled laboratory conditions. The result of this campaign has led to proposal of a new wavelength dependent model for the atmospheric fog and smoke, which is valid for the visible – NIR range over the visibility range of 1 km. Moreover, the experimental results have established that the most robust wavelengths that could be adopted in foggy atmospheric conditions to minimize the outdoor FSO link failure. Furthermore, to validate the behaviour of the proposed empirical model for the selected wavelengths, a complete comparison with the continuous attenuation spectrum for the same fog and smoke conditions has been carried out showing that the attenuation is almost linearly decreasing towards the NIR wavelengths for fog and smoke. The proposed model is calibrated for outdoor FSO links using Kim model, thus validating the laboratory-based empirical model.

## 10.6 References

[(WMO), W. M. O., 2008], (WMO), W. M. O., "Guide to Meteorological instruments and methods of observation, WMO No. 8", 2008.

[Awan, M. S., L. C. Horwath, et al., 2009], Awan, M. S., L. C. Horwath, et al., "Characterization of Fog and Snow Attenuations for Free-Space Optical Propagation", Journal of Communications; Vol 4, No 8 : Special Issue: Optical Wireless Communications, 2009.

[Bohren, C. F. and D. R. Huffman, 1983], Bohren, C. F. and D. R. Huffman, "Absorption and scattering of light by small particles ", John Wiley and sons, New York,1983.

[Cereceda, P., P. Osses, et al., 2002], Cereceda, P., P. Osses, et al., "Advective, orographic and radiation fog in the Tarapacá region, Chile", Journal of Atmospheric Research, 64,2002, 261-271.

[Fischer, K. W., M. R. Witiw, et al., 2008], Fischer, K. W., M. R. Witiw, et al., "Optical attenuation in fog at a wavelength of 1.55 micrometers", Atmospheric Research, 87,2008, 252-258.

[Ghassemlooy, Z., H. Le Minh, et al., 2012], Ghassemlooy, Z., H. Le Minh, et al., "Performance Analysis of Ethernet/Fast-Ethernet Free Space Optical Communications in a Controlled Weak Turbulence Condition", Lightwave Technology, Journal of, 30(13),2012, 2188-2194.

[Grabner, M. and V. Kvicera, 2012], Grabner, M. and V. Kvicera, "The wavelength dependent model of extinction in fog and haze for free space optical communication", Journal of Optics express, 19(4),2012, 3379-3386.

[Ijaz, M., Z. Ghassemlooy, et al., 2012] Ijaz, M., Z. Ghassemlooy, et al. "Analysis of Fog and Smoke Attenuation in a Free Space Optical Communication Link under Controlled Laboratory Conditions"." 1st International Workshop On Optical Wireless Communications, IWOW 2012". Pisa, Italy, IEEE:2012 1-3.

[Ijaz, M., Z. Ghassemlooy, et al., 2012] Ijaz, M., Z. Ghassemlooy, et al. Comparison of 830 nm and 1550 nm based free space optical communications link under controlled fog conditions. Communication Systems, Networks & Digital Signal Processing (CSNDSP), 2012 8th International Symposium on. 2012

[Kim, I. I., B. McArthur, et al., 2001] Kim, I. I., B. McArthur, et al. Comparison of laser beam propagation at 785 nm and 1550 nm in fog and haze for optical wireless communications. Proc. SPIE 4214, Boston, MA, USA 2001

[Kim, I. I., B. McArthur, et al., 2001] Kim, I. I., B. McArthur, et al. Comparison of laser beam propagation at 785 nm and 1550 nm in fog and haze for optical wireless communications. SPIE Proceedings, Boston, MA, USA, SPIE. 2001

[Kruse, P. W., L. D. McGlauchlin, et al., 1962], Kruse, P. W., L. D. McGlauchlin, et al., "Elements of infrared technology: Generation, transmission and detection", J. Wiley and sons(New York, ),1962.

[Naboulsi, M. A., F. d. Forne, et al., 2008], Naboulsi, M. A., F. d. Forne, et al., "Measured and predicted light attenuation in dense coastal upslope Fog at 650, 850 and 950 nm for free space optics applications. ", Journal of Optical Engineering, 47(3),2008, 036001-036001-036001-036014.

[Nadeem, F., T. Javornik, et al., 2010], Nadeem, F., T. Javornik, et al., "Continental fog attenuation empirical relationship from measured visibility data", Radio Engineering, 19 (4)( ),2010.

[Pierce, R. M., J. Ramaprasad, et al., 2001], Pierce, R. M., J. Ramaprasad, et al., "Optical attenuation in fog and clouds", Proc. SPIE 4530, 58 2001.

[Prokes, A., 2009], Prokes, A., "Atmospheric effects on availability of free space optics systems", Journal of Optical Engineering, 48(6),2009, 066001-066010.

[Ricklin, J. C., S. M. Hammel, et al., 2006], Ricklin, J. C., S. M. Hammel, et al., "Atmospheric channel effects on free-space laser communication", Journal of Optical and Fiber Communications Research, 3(2),2006, 111-158.

[Weichel, H., 1990] Weichel, H. Laser beam propagation in the atmosphere. Bellingham,1990 SPIE Optical Engineering.

[Yang, J., Z. Niu, et al., 2010], Yang, J., Z. Niu, et al., "Microphysics of atmospheric aerosols during winter haze/fog events in Nanjing", Journal of Environmental Science, 31(7),2010, 1425-1431.

## 11 FSO LINK PERFORMANCE UNDER ATMOSPHERIC TURBULENCE

(Zabih Ghassemlooy, Joaquin Perez, Sujan Rajbhandari, Muhammad Ijaz, Hoa Le Minh)

### 11.1 Overview

The free space optics (FSO) communications harness the richness of huge available bandwidth in infrared wavelength, which can effectively elucidate last mile access network problem for a foreseeable future. The FSO systems are largely deployed as large the primary, back-up and disaster recovery links offering a range of speed from 10 Mbits/s – 10 Gbit/s. Due to the inherent unpredictability of atmospheric conditions, the FSO system encounters a number of challenges, which limits the link availability as well as reliability. Among a number of challenges, substantial optical signal losses due to the atmospheric absorption and scintillations are key issues that requires a serious considerations. The scintillations is large caused by variation in reflective index caused by temperature and pressure fluctuations which results in random variations in light intensities in both space and time at the receiver plane. In clear weather conditions, theoretical and experimental studies have shown that scintillation could severely affect the FSO link reliability and disrupt the connectivity [Zhu and Kahn, 2002; Gappmair, 2011].

Scintillation has been investigated extensively and a number of theoretical models have been proposed to describe scintillation induced fading [Khalighi, Schwartz et al., 2009; Tsiftsis, Sandalidis et al., 2009; Gappmair, 2011]. In practice, it is however very challenging to measure the effect of the atmospheric turbulence under diverse weather conditions. This is mainly due to the long waiting time to observe and experience reoccurrence of different atmospheric events, which sometimes can take weeks or months. In addition in an outdoor environment the weather effect, could be a mixture of a number of atmospheric conditions (rain, turbulence, fog, smoke, dust, etc.). Therefore, carrying out a proper link assessment under specific weather conditions becomes a challenging task. Because of this reason, we have developed a dedicated indoor laboratory atmospheric chamber that enables us to assess the performance of the FSO link under controlled environment [Rajbhandari, Perez et al., 2011; Perez, Ghassemlooy et al., 2012]. The chamber offers the advantage of full system characterization and assessment in much less time compared with the outdoor FSO link, where it could take a long time for the weather conditions to change therefore prolonging the characterization and measurement.

### 11.2 Turbulence Models

The random fluctuation in the atmospheric temperature from point-to-point along the optical beam propagation path results in variation in the atmospheric refractive index  $n_{as}$  [Pratt, 1969]. The rate of change of the atmospheric refractive index  $n_{as}$  depends on the atmosphere temperature and pressure as given by [Karp, Gagliardi et al., 1988]:

$$n_{as} = 1 + 77.6(1 + 7.52 \times 10^{-3}\lambda^{-2})\frac{P_{as}}{T_e} \times 10^{-6} \quad (11.2-1)$$

$$-dn_{as}/dT_e = 7.8 \times 10^{-5} P_{as}/T_e^2 \quad (11.2-2)$$

where  $P_{as}$  is the atmospheric pressure in millibars,  $T_e$  is the effective temperature in Kelvin and  $\lambda$  the wavelength in microns. Near the sea level,  $-dn_{as}/dT_e \cong 10^{-6} \text{ K}^{-1}$  [Karp, Gagliardi et al., 1988]. The contribution of humidity to the refractive index fluctuation is not accounted for in (1) because this is negligible at optical wavelengths [Osche, 2002].

In atmospheric turbulence, an important parameter for characterising the amount of refractive index fluctuation is the index of refraction structure parameter  $C_n^2$  introduced by Kolmogorov [Kolmogorov, 1961], which is a function of the wavelength, pressure and temperature as given by [Andrews and Phillips, 2005]:

$$C_n^2 = \left(86 \times 10^{-6} \frac{P_{as}}{T_e^2}\right)^2 C_T^2, \text{ at } \lambda = 850 \text{ nm}, \quad (11.2-3)$$

where the temperature structure constant  $C_T^2$  is related to the universal 2/3 power law of temperature variation as given in:

$$D_T = \langle (T_1 - T_2)^2 \rangle = \begin{cases} C_T^2 l_0^{-4/3} L_p^2 & \text{for } 0 \ll L_p \ll l_0 \\ C_T^2 L_p^{2/3} & \text{for } l_0 \ll L_p \ll L_0 \end{cases}, \quad (11.2-4)$$

where  $T_1$  and  $T_2$  are the temperatures at two points separated by the propagation distance  $L_p$ .  $C_n^2$  can vary from  $10^{-17} \text{ m}^{-2/3}$  up to  $10^{-12} \text{ m}^{-2/3}$  for weak and strong turbulence regimes, respectively.

By their random nature, turbulent media are extremely difficult to describe mathematically due to the presence of non-linear mixing of observable quantities [Osche, 2002]. A number of statistical models to describe optical intensity variation under various turbulence strengths had been proposed and studied. The two most popular among them is the log-normal and Gamma-Gamma model, which are summarized below.

The extent of field amplitude fluctuation in atmospheric turbulence can be characterized by the log-amplitude variance  $\sigma_x^2$ , commonly referred to as the Rytov parameter.  $\sigma_x^2$  is related to  $C_n^2$ , the horizontal distance  $L_p$  travelled by the optical field/radiation as:

$$\sigma_x^2 = 0.56k^{7/6} \int_0^{L_p} C_n^2(x)(L_p - x)^{5/6} dx, \text{ for a plane wave} \quad (11.2-5)$$

where  $k = (2\pi/\lambda)$  is the spatial wave number. For a field propagating horizontally through the turbulent medium, as is the case in most terrestrial applications, the refractive index structure parameter  $C_n^2$ , is constant, and the log irradiance variance (scintillation index) for a plane wave becomes:

$$\sigma_I^2 = 1.23C_n^2 k^{7/6} L_p^{11/6} \quad (11.2-6)$$

where the log-intensity variance  $\sigma_I^2 = 4\sigma_x^2$ .

In the weak fluctuations region, the statistics of the irradiance fluctuations have been experimentally found to obey the log-normal distribution. The irradiance pdf is the log-normal distribution function given by:

$$p(I) = \frac{1}{\sqrt{2\pi\sigma_l^2}} \frac{1}{I} \exp \left\{ -\frac{\left( \log(I/I_0) + \sigma_l^2/2 \right)^2}{2\sigma_l^2} \right\} \quad I \geq 0 \quad (11.2-7)$$

The log-normal pdf is plotted in Figure 11.2-1 for different values of log-irradiance variance  $\sigma_l^2$ . As the value of  $\sigma_l^2$  increases, the distribution becomes more skewed with longer tails in the infinity direction. This denotes the extent of fluctuation of the irradiance as the channel inhomogeneity increases.

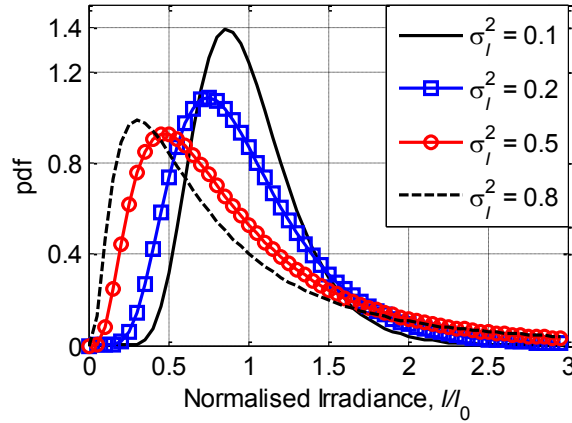


Figure 11.2-1: Log-normal probability density function with  $E[I] = 1$  for a range of log irradiance variance  $\sigma_l^2$ .

As the strength of atmospheric turbulence increases log-normal statistics display large deviations compared to the experimental data [Andrews, Phillips et al., 2001; Uysal, Navidpour et al., 2004]. The turbulent eddies resulted due to multiple scatterings were not accounted by Rytov in his approximation and hence Andrews *et al.* [Andrews, Phillips et al., 2001] proposed a Gamma-Gamma Turbulence Model, which take accounts of both small scale (scattering) and large scale (refraction) effects. The gamma-gamma irradiance distribution function is given by:

$$p(I) = \frac{2(\alpha\beta)^{(\alpha+\beta)/2}}{\Gamma(\alpha)\Gamma(\beta)} I^{\left(\frac{\alpha+\beta}{2}\right)-1} K_{\alpha-\beta}(2\sqrt{\alpha\beta I}); \quad I > 0 \quad (11.2-8)$$

where  $\alpha$  and  $\beta$ , respectively represent the effective number of large- and small-scale eddies of the scattering process.  $K_n(\cdot)$  is the modified Bessel function of the 2<sup>nd</sup> kind of order  $n$ , and  $\Gamma(\cdot)$  represents the Gamma function. If the optical radiation at the receiver is assumed to be a plane wave, then the two parameters  $\alpha$  and  $\beta$  that characterise the irradiance fluctuation pdf are related to the atmospheric conditions by [Popoola, Ghassemlooy et al., 2007]:

$$\alpha = \left[ \exp \left( \frac{0.49\sigma_l^2}{(1 + 1.11\sigma_l^{12/5})^{7/6}} \right) - 1 \right]^{-1} \quad (11.2-9)$$

$$\beta = \left[ \exp \left( \frac{0.51\sigma_l^2}{(1 + 0.69\sigma_l^{12/5})^{5/6}} \right) - 1 \right]^{-1} \quad (11.2-10).$$

While the scintillation index is given by:

$$\sigma_N^2 = \exp \left[ \frac{0.49\sigma_l^2}{(1 + 1.11\sigma_l^{12/5})^{7/6}} + \frac{0.51\sigma_l^2}{(1 + 0.69\sigma_l^{12/5})^{5/6}} \right] - 1 \quad (11.2-11).$$

A plot of Gamma-Gamma distribution for three different turbulence regimes, namely weak, moderate and strong is given Figure 11.2-2. The plot shows that as the turbulence increase form weak to strong regime, the distribution spreads out more, with an increase in the range of possible values of the irradiance.

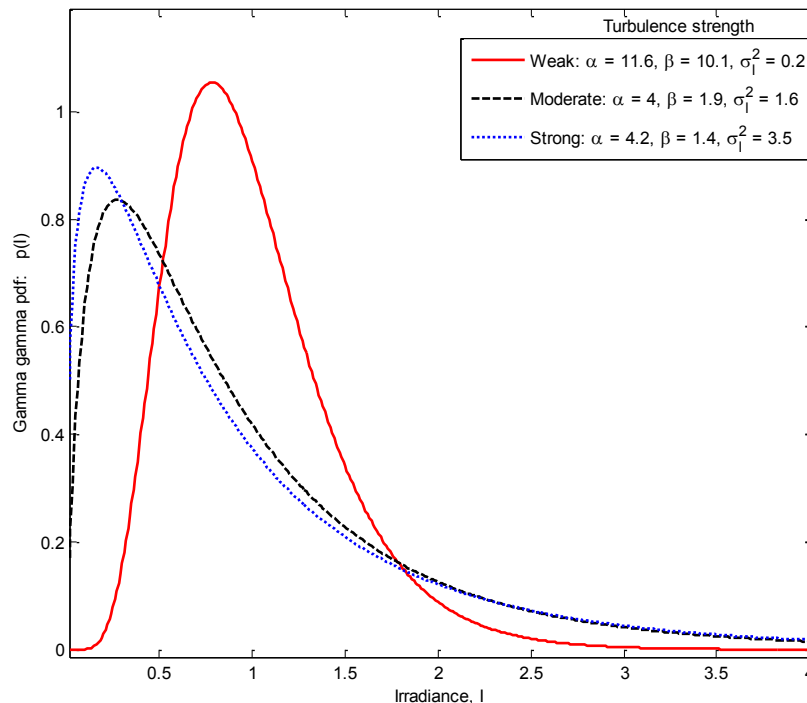


Figure 11.2-2: Gamma-gamma probability density functions for three different turbulence regimes, namely weak, moderate and strong.

### 11.3 Laboratory based FSO Test Bed

Depending upon the location and environment, assessing and characterizing the FSO link performance in different weather conditions is difficult as the dynamics of the atmospheric conditions can change within a short duration as well as the performance depends on a number of interdependent parameters such as fog, rain, snow and turbulence. Thus there is a need for an indoor atmospheric test-bed where measurement and research can be carried out in a controlled environment. A typical FSO laboratory-based link set-up for data communication in a turbulence environment is shown in Figure 11.3-1 (a). As in common optical communication systems, in this FSO laboratory environment set-up the transmitter

consists of a laser source which can be modulated with an electrical signal and the receiver consists of an optical collimator and photodiode, followed by transimpedance amplifier. The different parameters of transmitter and receiver are summarized in Table 11.3-1. The laboratory based FSO channel is an enclosed glass chamber with a number of air vents and hot-plates in order to control the temperature, as depicted in Figure 11.3-1 (c). In order to compensate for shorter link length, temperate gradient between transmitter and receiver is made up to 7 K/m. The other parameters including chamber dimension, temperature range, wind speed are given in Table 11.3-1. The different modulation format including on-off keying (OOK) is generated using an arbitrary waveform generator (AWG), which can directly modulate the laser. At the receiver, the signal is acquired using data acquisition system and further processed and analyzed at Matlab environment.

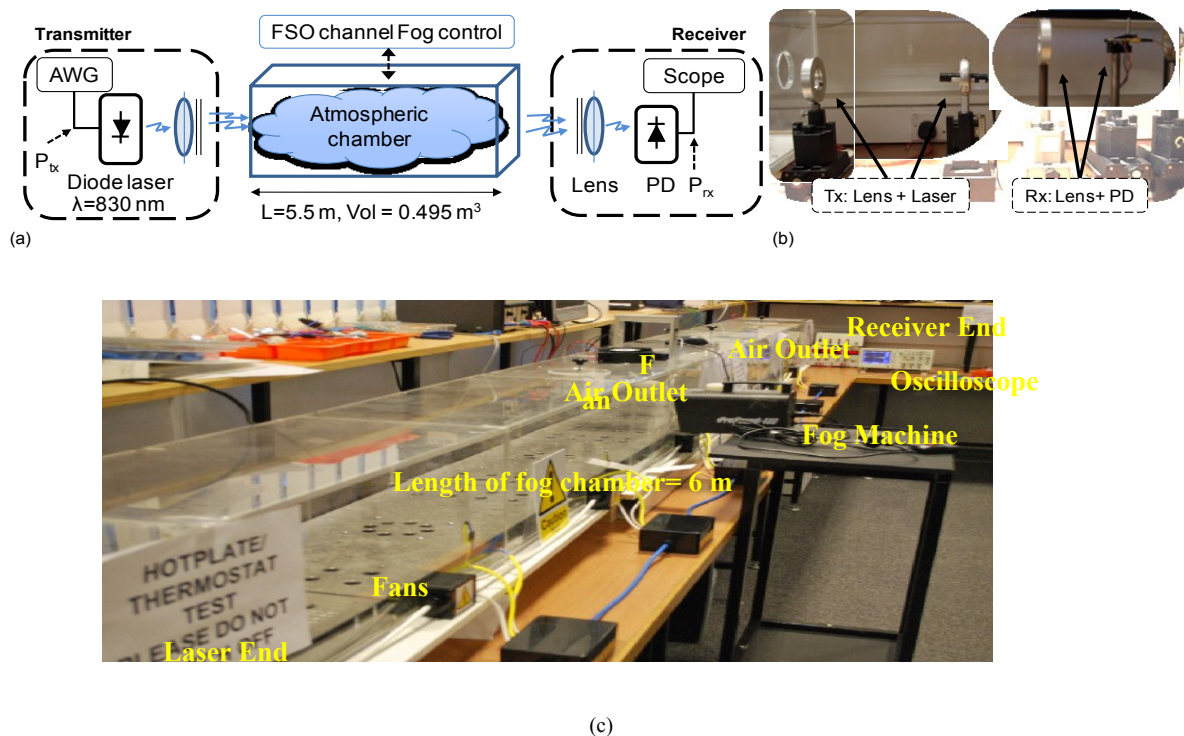


Figure 11.3-1: (a) Block diagram of the FSO experimental set-up, (b) the simulation chamber, and (c) the laboratory chamber set up.

Table 11.3-1. Parameters of the FSO Link

Parameter		Value
<b>Transmitter</b>		
Data source	Data rate ( $R_b$ )	5 Mbit/s 12.5 Mbit/s 125 Mbit/s
	Format	OOK, PPM, BPSK
	Line coder	4B5B
Laser diode	Peak wavelength	830 nm
	Maximum optical power	10 mW
	Class	3B
	Beam size at aperture	5 mm × 2 mm
	Beam divergence	5 mrad
	Laser beam propagation model	Plane
	Modulation bandwidth	75 MHz
Optical lens	Diameter	3.4 cm
	Focal length	20 cm
Channel	Dimension	550×30×30 cm <sup>3</sup>
	Temperature range	20 - 65 °C
	Temperature gradient $\Delta T/\Delta L$	7 K/m
	Wind speed	<10 m/s
	Link segment $\Delta R$	1.5 m
	Rytov variance	<0.23
<b>Receiver</b>		
Photodetector	Spectral range of sensitivity	750 - 1100 nm
	Active area	1 mm <sup>2</sup>
	Half angle field of view	± 75 Deg
	Spectral sensitivity	0.59 A/W at 830 nm
	Rise and fall time	5 ns
Amplifier	Transimpedance amplifier	AD8015
	Bandwidth	240 MHz
	Transimpedance amplifier gain	15 kΩ
	Filter bandwidth	$R_b$

## 11.4 Link Evaluation

In order to evaluate the validity of the measurement under the influence of the weak atmospheric turbulence, the channel is characterized both theoretically and experimentally. We measure scintillation index from the received optical intensity and compare it with the theoretical predictions. In order to quantify the scintillation index, the non-zero size of the receiver photodiode has to be taken into account the fading effect is reduced significantly if the receiver aperture  $A_{rx}$  greater than the coherence distance (i.e. by the process known as the aperture averaging). The aperture averaging factor, which is widely used to quantify the fading reduction, is given by:

$$A = \frac{\sigma_I^2(D)}{\sigma_I^2(0)}, \quad (11.4-1)$$

where  $\sigma_I^2(D)$  and  $\sigma_I^2(0)$  denote the scintillation index for a receiver lens of diameter  $D$  and a “point receiver” ( $D \approx 0$ ), respectively.

For the plane wave propagation with a smaller inner scale  $l_0 \ll (L/k)^{0.5}$ , the scintillation index is given by [Andrews and Phillips, 2005]:

$$\sigma_I^2(D) = \exp \left[ \frac{0.49\sigma_I^2}{\left(1+0.65d^2+1.11\sigma_I^{\frac{12}{5}}\right)^{\frac{7}{6}}} + \frac{0.51\sigma_I^2 \left(1+0.69\sigma_I^{\frac{12}{5}}\right)^{-\frac{5}{6}}}{1+0.90d^2+0.62d^2\sigma_I^{\frac{12}{5}}} \right] - 1, \quad (11.4-2)$$

where the scalar parameter  $d = \sqrt{kD^2/4L_p}$ .

In the presence of turbulence, the instantaneous irradiance is fluctuated, thus leading to the variation in instantaneous signal-to-noise ratio (SNR). Here we use the average value of SNR to evaluate the FSO link performance. The ensemble mean of SNR can be expressed as [Majumdar and Ricklin, 2008]:

$$\langle \text{SNR} \rangle = \frac{\text{SNR}_0}{\sqrt{\sigma_I^2(D)(\text{SNR}_0)^2 + I_0/I}}, \quad (11.4-3)$$

where  $\text{SNR}_0$  is for the turbulence free condition. With no turbulence  $\langle \text{SNR} \rangle = \text{SNR}_0$ .

#### 11.4.1 Channel Characterization

In order to compensate for the short chamber length the temperature gradient is set to  $\Delta T/\Delta L \sim 7$  K/m, the temperature measured at each point along the chamber is maintained within the tolerance margin of  $\pm 1$  K. The average temperatures recorded to within  $\pm 1$  K at four different locations along chamber are given in Table 11.4-1.

Table 11.4-1: Measured temperatures over five experiments at four positions within chamber

	T <sub>1</sub> (°C)	T <sub>2</sub> (°C)	T <sub>3</sub> (°C)	T <sub>4</sub> (°C)
Set 1	28	25	23	23
Set 2	33	28	24	23
Set 3	37	30	24.2	23.4
Set 4	45	34	25	24
Set 5	54	40	27.3	25

In order to predict the scintillation index  $\sigma_I^2$  in the indoor chamber, we have assumed that  $C_n^2$  is constant between two measured temperature points. Here we have measured the temperatures at four positions, to predict the scintillation index and used (5) to calculate the overall scintillation index. Figure 11.4-1 depicts both predicted and measured total scintillation index  $\sigma_I^2$  showing a good agreement, which is used to calibrate the chamber.

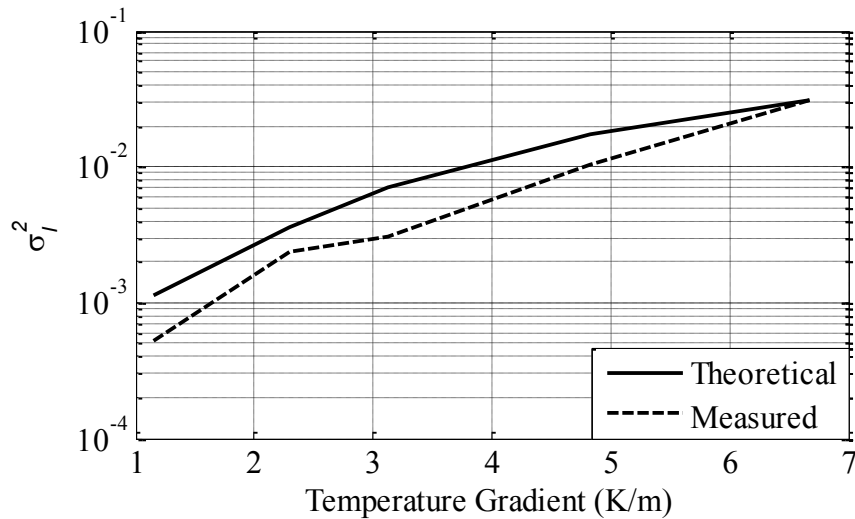
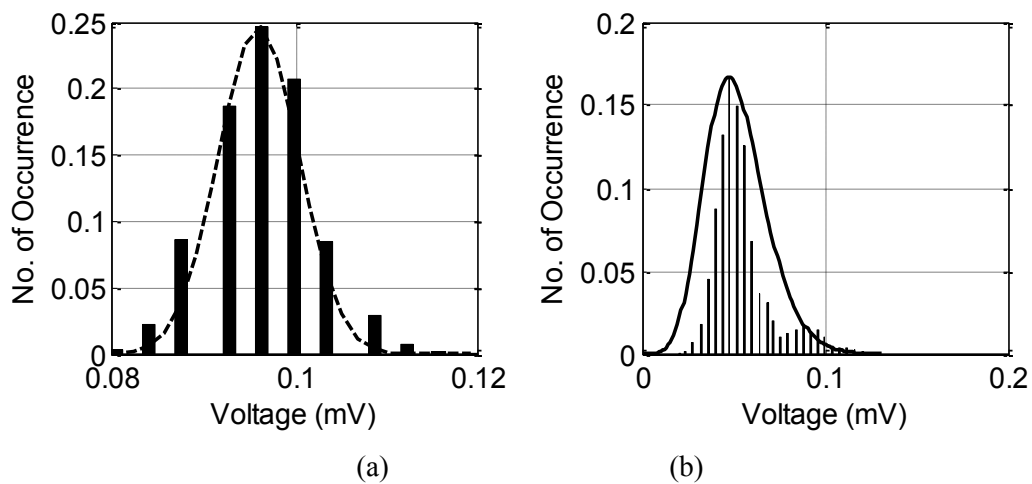


Figure 11.4-1: The theoretical and measured scintillation index  $\sigma_I^2$  against the temperature gradient for the controlled atmospheric chamber.

### 11.4.2 Signal Probability Distribution

It is found that the noise variance due the ambient light is  $< 3.35 \times 10^{-5}$  mW, which is significantly lower (by up to 7000 times) than the log-normal variance, hence the effect of ambient light can be ignored in the presence of turbulence. Figure 11.4-2 shows histograms for the received signal without and with turbulence, respectively. Notice that the total number of occurrence is normalized to the unity. Unlike the case with no turbulence case (Figure 11.4-2 (a)) where the distribution is a Gaussian shape, the signal distribution in the presence of the turbulence is skewed towards infinite, clearly showing a log-normal distribution. For the comparisons, log-normal curve of best fit is also show for all the cases. Since the measured values of  $\sigma_I^2$  fall within the range of [0, 1], the turbulence experimented is classified as weak.



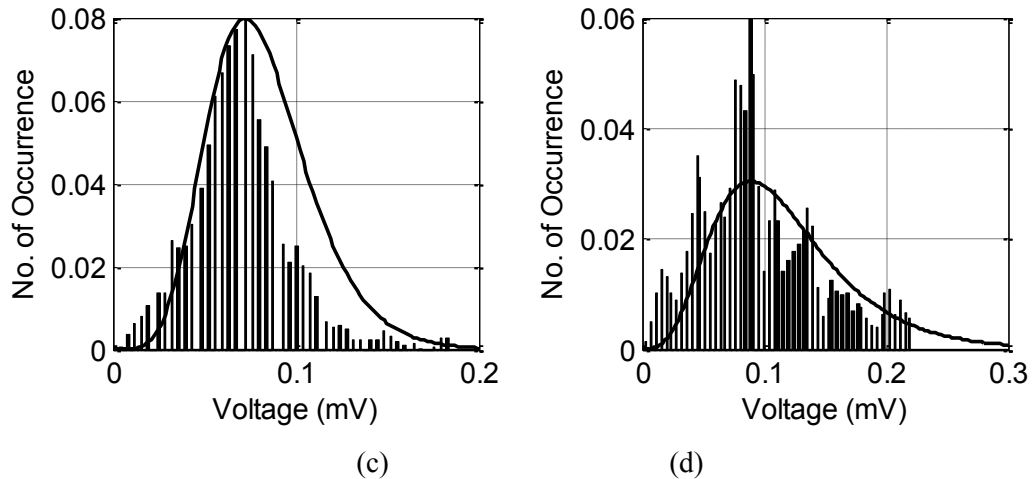


Figure 11.4-2: Received signal distribution a) without turbulence, and with turbulence b)  $\sigma_I^2 = 0.009$  c)  $\sigma_I^2 = 0.067$  and d)  $\sigma_I^2 = 0.240$  (the curve fitting is shown by solid lines).

### 11.4.3 FSO Link Evaluation

The measured eye-diagrams for the received OOK signal at 12.5 Mbps are depicted in Figure 11.4-3 (a) with no turbulence and in Figure 11.4-3 (b) in the case of weak turbulence. Note that the eye opening is smaller in the presence of turbulence, which results in a considerable level of signal intensity fluctuation. This is due to the substantial increase of the width at the top (bit 1) and base (bit 0) of the eye-diagram.

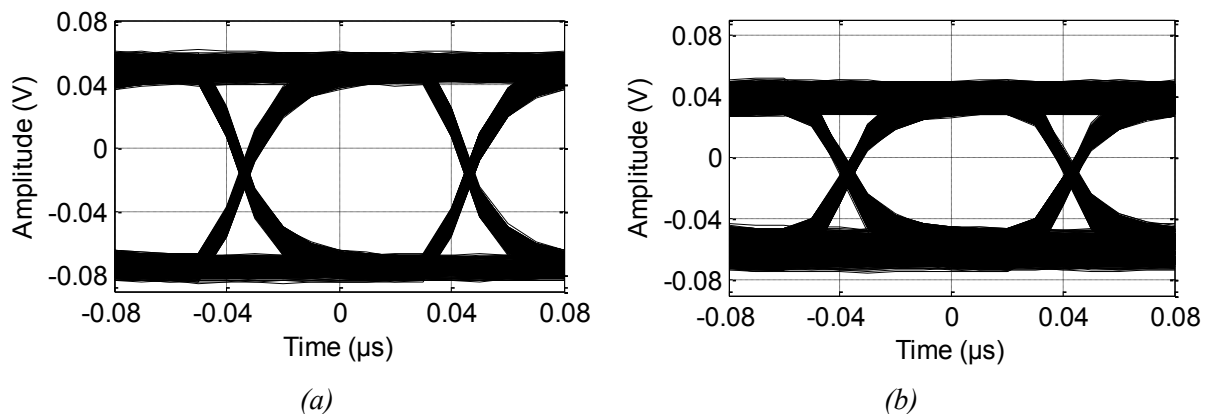


Figure 11.4-3: The measured eye-diagram of received signal at 12.5Mbit/s in the condition of (a) no turbulence and (b) weak turbulence with the scintillation index  $\sigma_I^2 = 0.0164$ .

Under the same turbulence condition, we transmitted OOK signal at 125 Mbit/s through the FSO channel and obtained the eye-diagrams at the receiving end, see Figure 11.4-4. The eye opening in this case is very close to the one obtained for the 12.5 Mbps link as the data rate is not sensitive to the turbulence.

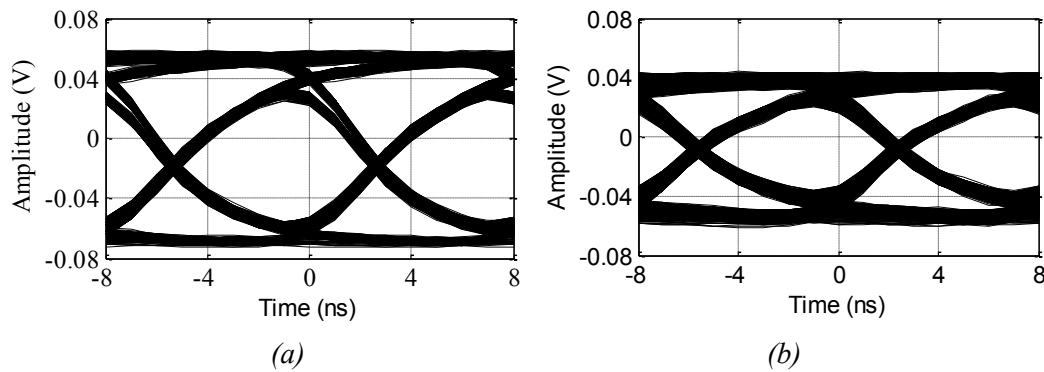


Figure 11.4-4: The measured eye-diagram of received signal at 12.5 Mbit/s in the condition of (a) no turbulence and (b) weak turbulence with the scintillation index  $\sigma_I^2 = 0.0164$ .

The measured  $Q$ -factor against a range of scintillation index  $\sigma_I^2$  values is shown in Figure 11.4-5. For the clarity of the figure, the  $x$ -axis is in the logarithmic scale. Figure 11.4-5 presents a good match between the predicted and experimental data. The  $Q$ -factor decreases exponentially with the increase of scintillation index values. In fact, the drop in the  $Q$ -factor does not depend on the data rates but it depends on  $Q_0$  and values of the scintillation index.

Although  $Q_0$  values are about 28 and 8 for 12.5 and 125 Mbps links, respectively, the obtained  $Q$ -factors show that they are almost identical as  $\sigma_I^2 > 0.05$ . This indicates that the increment in transmit optical power will have a little effect to mitigate the increased turbulence level. A number of techniques have been proposed in literature to deal with the turbulence including the aperture averaging, the spatial diversity, and the cooperative diversity.[Khalighi, Schwartz et al., 2009; Tsiftsis, Sandalidis et al., 2009; Pedireddi and Srinivasan, 2010]

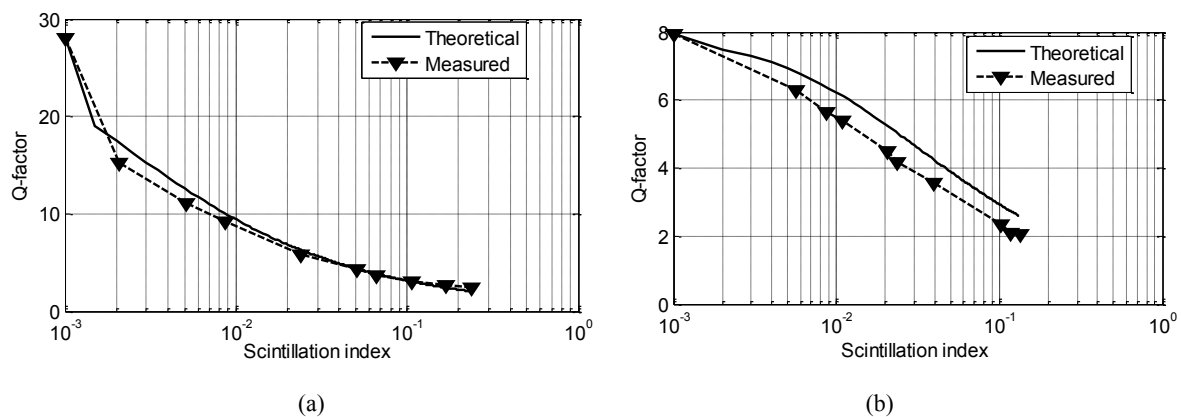


Figure 11.4-5: The predicted and measured  $Q$ -factor against different scintillation index values for (a) 12.5 Mbps and (b) 125 Mbps.

## 11.5 Summary

In this chapter, the performance of FSO system under turbulence conditions is evaluated. A number of performances metric are evaluate including reflective index structure, histogram, eye-diagram and  $Q$ -factor is evaluated. Methods to generate turbulence and control its level were discussed and practically implemented. The paper also pointed out the relation between the experimental environment and the outdoor. The obtained results showed that turbulence can severely affect the link availability of the FSO systems due to the sharp

response in BER performance of the link. The analysis and demonstration presented have shown a step forward to characterize the atmospheric channel in an indoor environment, which is by nature complex and unpredictable. On the other hand an interesting approach to FSO outdoor measurements on a real link has been reported.

## 11.6 References

[Andrews, L. C. and R. L. Phillips, 2005] Andrews, L. C. and R. L. Phillips, Eds. Laser Beam Propagation through Random Media, SPIE Press.2005

[Andrews, L. C., R. L. Phillips, et al., 2001] Andrews, L. C., R. L. Phillips, et al. Laser beam scintillation with applications. Bellingham,2001 SPIE.

[Gappmair, W., 2011], Gappmair, W., "Further results on the capacity of free-space optical channels in turbulent atmosphere", Communications, IET, 5(9),2011, 1262-1267.

[Karp, S., R. M. Gagliardi, et al., 1988] Karp, S., R. M. Gagliardi, et al. Optical Channels: fibers, clouds, water and the atmosphere. New York,1988 Plenum Press.

[Khalighi, M. A., N. Schwartz, et al., 2009], Khalighi, M. A., N. Schwartz, et al., "Fading Reduction by Aperture Averaging and Spatial Diversity in Optical Wireless Systems", Optical Communications and Networking, IEEE/OSA Journal of, 1(6),2009, 580-593.

[Kolmogorov, A., 1961] Kolmogorov, A., Ed. Turbulence. Classic Papers on Statistical Theory. New York, Wiley-Interscience.1961

[Majumdar, A. K. and J. C. Ricklin, 2008] Majumdar, A. K. and J. C. Ricklin. Free-Space Laser Communications: Principles and Advances. New York,2008 Springer.

[Osche, G. R., 2002] Osche, G. R. Optical Detection Theory for Laser Applications,2002 Wiley-Interscience.

[Pedireddi, L. B. and B. Srinivasan, 2010], Pedireddi, L. B. and B. Srinivasan, "Characterization of atmospheric turbulence effects and their mitigation using wavelet-based signal processing", Communications, IEEE Transactions on, 58(6),2010, 1795-1802.

[Perez, J., Z. Ghassemlooy, et al., 2012], Perez, J., Z. Ghassemlooy, et al., "Ethernet FSO Communications Link Performance Study Under a Controlled Fog Environment", Communications Letters, IEEE, 16(3),2012, 408-410.

[Popoola, W. O., Z. Ghassemlooy, et al., 2007], Popoola, W. O., Z. Ghassemlooy, et al., "Free-space optical communication using subcarrier modulation in gamma-gamma atmospheric turbulence", 9th International Conference on Transparent Optical Networks (ICTON '07) 3,2007, 156-160.

[Pratt, W. K., 1969] Pratt, W. K. Laser Communication Systems. New York,1969 John Wiley & Sons, Inc.

[Rajbhandari, S., J. Perez, et al., 2011] Rajbhandari, S., J. Perez, et al. A fast ethernet FSO link performance under the fog controlled environment. ECOC. 2011

[Tsiftsis, T. A., H. G. Sandalidis, et al., 2009], Tsiftsis, T. A., H. G. Sandalidis, et al., "Optical wireless links with spatial diversity over strong atmospheric turbulence channels", Wireless Communications, IEEE Transactions on, 8(2),2009, 951-957.

[Uysal, M., S. M. Navidpour, et al., 2004], Uysal, M., S. M. Navidpour, et al., "Error rate performance of coded free-space optical links over strong turbulence channels", IEEE Communication Letters, 8(10),2004, 635-637.

[Zhu, X. and J. M. Kahn, 2002], Zhu, X. and J. M. Kahn, "Free-space optical communication through atmospheric turbulence channels", IEEE Transactions on Communications, 50(8),2002, 1293-1300.

## 12. Hybrid FSO/RF links: answer to the different weather influence

### Contributors

I. Frigyes (chapter editor), L. Csurgai-Horváth, O. Fiser, Z. Ghassemlooy, M. Grabner, V. Kvicera, I E Lee, and W. P. Ng

### 12.1 Overview of chapter 12

Since the early days of outdoor FSO communication it was recognized that the most critical adverse propagation effects are due to meteorological phenomena. In particular dense fog, impeding visibility makes communication via FSO virtually impossible. A plausible countermeasure to this type of fading could be a special hybrid *diversity* system, i.e. an FSO link operated parallel to an RF link. In principle the latter could operate either at millimetre waves or at microwaves. Both have pros and cons. A microwave link is virtually not influenced by weather while its bandwidth (and so its capacity) is certainly much lower than that of the FSO link; on the other hand, a millimetre wave system can have the same bandwidth as an FSO link (or at least the same order of bandwidth) while it is also sensitive to some meteorological phenomena. Thus the effectiveness of such a hybrid system is not self-evident and needs investigation. The three sections of this subchapter report on investigations of this type.

The first of these (12.2) is written by V. Kvicera, and M. Grabner of the Czech Metrology Institute (CMI) and O. Fiser of the Institute of Atmospheric Physics, both in Prague. It reports on three years of measurement of attenuation due to rain, snow and fog over a hybrid mm-wave/FSO link. Based on these measurements availability of such a link is simulated, under the assumption that FSO is not influenced by rain and mm-wave is not influenced by fog. Main findings are: i. unavailability of the hybrid system is about 3 orders of magnitude lower than that of the FSO alone link and ii. there is a very large yearly variability in hydrometeors.

The second (12.3) section is written by I. Frigyes and L. Csurgai-Horváth of the Budapest University of Technology and Economics; similarly hybrid mm-wave/FSO link is investigated with equal capacity of both. Outage capacity is determined based on realistic system characteristics (IM/DD and PSK-QPSK) and known channel models. Performance metric here is maximal hop length with prescribed outage capacity. Main findings are: i) maximal hop length of the hybrid system is determined by the loss of the FSO signal caused by *rain*; ii) this is by about 10% longer than that of the E-band-only system if IM/DD is used; and iii) but about 2-times longer in the case of coherently detected BPSK or QPSK.

The third, (12.4) written by Z. Ghassemlooy, I. E. Lee, and W. P. Ng of the University of Northumbria at Newcastle, UK deals with the problem from a different context. It investigates the environmental effects of the increasing capacity of wireless networks and concludes that the application of *green technologies* is a must. FSO is proposed as an appropriate means to achieve that and hybrid FSO/RF seems to be able to mitigate the harmful effects of meteorological/atmospheric phenomena.

### 12.2 Availability performance assessment for a simulated terrestrial hybrid 850 nm/58 GHz system

#### 12.2.1 Introduction

Free space optical links can be used as affordable last mile broadband solutions. Their advantages are easy installation, rapid deployment time and significant cost savings. The disadvantages of FSO links are that their availability performances are seriously affected by lower atmospheric visibility which

is significantly influenced mainly by fog, snow and their combinations [Korevaar & al. 2003], [Gebhart & al, 2005]. Novel radio frequency (RF) digital systems operating in the frequency bands above 50 GHz are able to transmit a signal with a bit rate of up to 10 Gbit/s [http-1], [http-2]. In contrast to FSO systems, heavy rainfalls have a significant impact on the availability performance of RF systems. A hybrid FSO/RF system, i.e. an FSO link backed up by an RF link, uses the strengths of each system to overcome each others' weaknesses. It can achieve a higher link availability performance than a particular FSO or RF link due to the fact that the RF part of a hybrid FSO/RF system can mitigate the influence of dense fog events and the FSO part can mitigate heavy rainfall events [Leitgeb & al., 2004]. The selection and calculation of certain design parameters of a hybrid FSO/RF system, switching and some results obtained during short-term experiments are given in [Akbulut & al., 2003], [Nadeem & al., 2009].

Fog seems to be the most important impairment factor for FSO links. Fog-only events as well as combinations of fog with hydrometeors like fog with rain, fog with snow or fog with rain and snow significantly reduce the atmospheric visibility [Kvicera & al., 2008]. Long-term measurements of visibility are carried out at meteorological stations and airports by means of transmissometers or diffusiometers and therefore these visibility data are usually used for the assessment of fog attenuation. However, these measurements do not differentiate between fog-only events and the combination of fog with other hydrometeors. Fog-only visibility data should be used for the conversions of visibility to the specific attenuation due to fog. Conversely, both the fog-only events and the combinations of fog with other hydrometeors should be used for the assessments of availability performances of FSO links. Therefore, the influence of combinations of fog with hydrometeors on the total fog attenuation is shown.

The parallel experimental FSO/RF paths are realized in a collaboration of the CMI with the Institute of Atmospheric Physics of the Academy of Sciences of the Czech Republic (IAP AS CR). Both propagation characteristics and availability performances of the FSO link, an RF link and a simulated hybrid FSO/RF system were examined on our experimental paths.

### *12.2.2 Experimental set-up*

The experimental set-up consists of an FSO path, a parallel RF path, meteorological measurements near the receiver sites, data gathering and data processing.

#### *12.2.2.1 FSO Path*

The commercially available FSO system operates at 850 nm on a path about 853 metres long. The transmitted power is about 16 dBm, the divergence angle is 9 mrad and the optical Rx aperture is 515 cm<sup>2</sup>. The recording optical fade margin is about 17 dB.

#### *12.2.2.2 RF Path*

The commercially available RF system operates at 57.670 GHz with V polarization on the same experimental path as the FSO system. The transmitted power is about 5 dBm and the recording fade margin is about 27 dB.

#### *12.2.2.3 Terrain Profile*

The terrain profile of the path between the IAP AS CR and the CMI is line-of-sight. The elevation angle from the IAP AS CR to the CMI is about 2.2°, and the difference of altitudes is about 33 m.

#### *12.2.2.4 Meteorological Measurements*

Meteorological conditions were identified by means of data obtained from a weather observation system located near the receiver sites and from colour video-camera images of the space between the transmitter and the receiver sites. The system uses Vaisala sensors for the measurement of temperature,

humidity, air pressure and the velocity and direction of the wind. The rain intensities were measured using a dynamically-calibrated heated tipping-bucket rain gauge with a collector area of 500 cm<sup>2</sup>, and the rain amount per tip was 0.1 mm. The Vaisala PWD11 device was used for the measurement of visibility in the range from 2000 m up to 50 m. The meteorological data were synchronized in time with the measurement of hydrometeor attenuation.

12.2.2.5 Data Processing

Both the received FSO and RF signal levels were measured, recorded synchronously on a PC hard disk, and statistically processed. All the recorded individual attenuation events were compared with the concurrent meteorological conditions and were carefully categorized according to the types of individual hydrometeors that occurred. Attenuation events due to individual types of hydrometeors, i.e. rain (R), rain with snow (RS), snow (S), fog only (F), fog with rain (FR), fog with snow (FS), fog with rain and snow (FRS) were identified. Rain intensities contained in the observed FR events, FS events and FRS events were always smaller than 3 mm/h. On the FSO link this rain intensity, however, could cause the maximum attenuation of about 2.5 dB/km during an FR event, about 8.6 dB/km for a wet snow event and about 25.3 dB/km for a dry snow event during the FS events, respectively [ITU-R P.1814. Therefore, the fog events were ranked minutely. Only those attenuation events which were unambiguously identified due to their origin were statistically processed. It should be noted that the cumulative distributions of attenuation due to snow as well as due to rain with snow might be influenced by additional attenuation due to snow particles settled down on both the shield of the FSO system’s lens and the RF system’s antenna radomes.

The obtained attenuation data were processed over a 3-year period from December 2006 to November 2009. The cumulative distributions of attenuation due to hydrometeors were obtained for the individual months and the individual year periods over the 3 year period of data processing.

12.2.3 Attenuation due to hydrometeors on FSO path

The obtained monthly cumulative distributions (CDs) of attenuation due to all of the hydrometeors combined (R, RS, S, F, FR, FS, FRS) for the individual 1-year periods of observation on FSO path are given in Figs. 12.2-1...12.2-3.

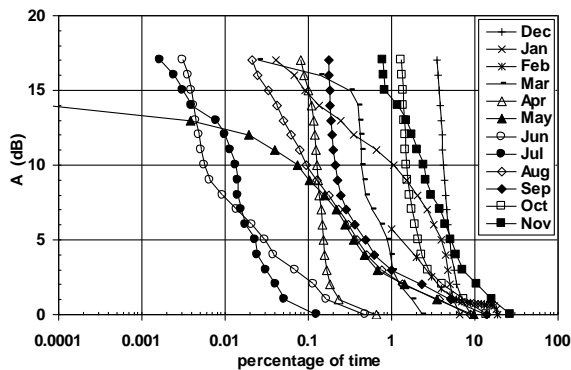


Figure 12.2-1 Obtained monthly CDs of attenuation all of the hydrometeors combined on the FSO path for the 1<sup>st</sup> year period

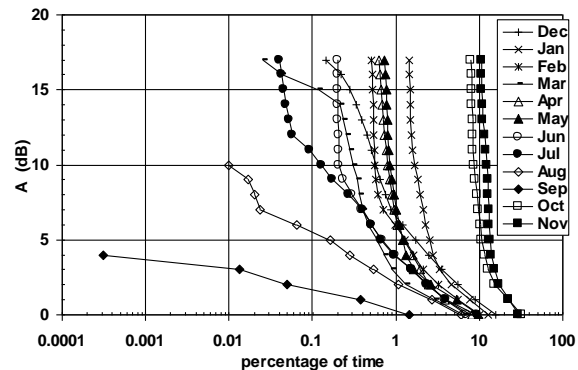


Figure 12.2-2 Obtained monthly CDs of attenuation due to all of the hydrometeors combined on the FSO path for the 2<sup>nd</sup> year period

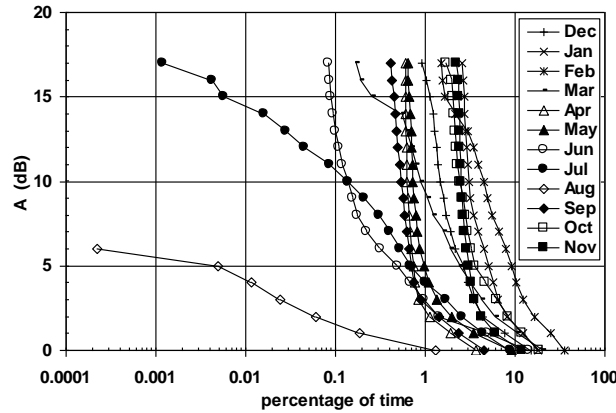


Figure 12.2-3 Obtained monthly CDs of attenuation due to all of the hydrometeors combined on the FSO path for the 3<sup>rd</sup> year period

The large month-to-month variability of these distributions can be observed. The CD of attenuation due to all of the hydrometeors combined for the worst month of the 1<sup>st</sup> year period is formed by the pertinent parts of the CDs for November and December. For the 2<sup>nd</sup> year period, the CD of attenuation due to all of the hydrometeors combined is formed by the CD for November. The CD of attenuation due to all of the hydrometeors combined for the worst month of the 3<sup>rd</sup> year period is formed by the pertinent parts of the CDs for February and January. It can be seen that the dominant attenuation events occurred mainly during the period from November to February, i.e. during the winter months. The insignificant attenuation events, i.e. the small or short-term attenuation events occurred from May to September.

The obtained annual CDs of attenuation on the FSO path due to both all of the hydrometeors combined and the individual hydrometeors separately are shown in Figs. 12.2-4-12.2-6.

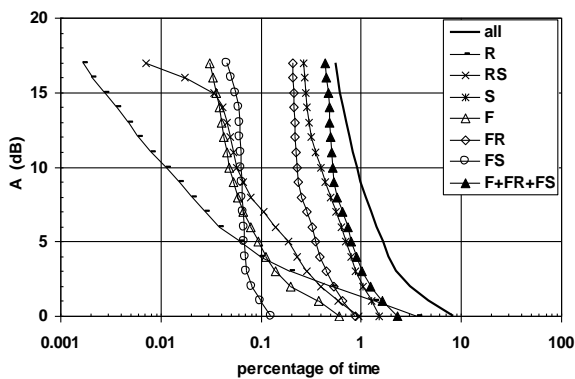


Fig.12.2-4 CDs of attenuation due to individual hydrometeors on the FSO path for the 1<sup>st</sup> year period

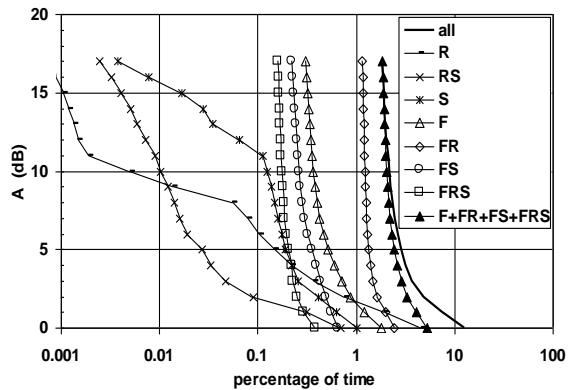


Fig. 12.2-5 CDs of attenuation due to individual hydrometeors on the FSO path for the 2<sup>nd</sup> year period

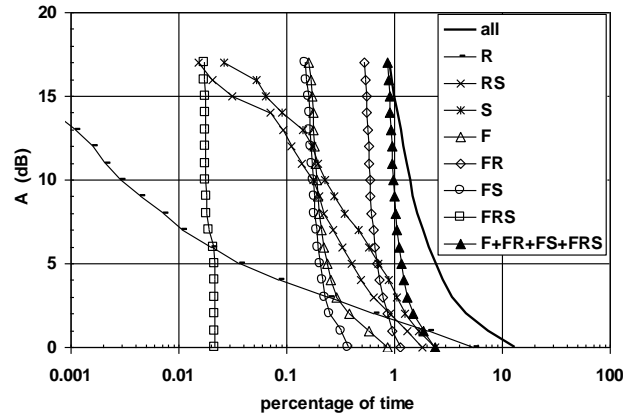


Figure 12.2-6 CDs of attenuation due to individual hydrometeors on the FSO path for the 3<sup>rd</sup> year period

It follows from Figs.12.2. 4-6 that the dominant attenuation events were caused by fog events combined (F+FR+FS+ FRS) while the FR events were most significant of these for the 2<sup>nd</sup> and the 3<sup>rd</sup> year period. For the 1<sup>st</sup> year period, the snow events were more significant than the fog-only events.

12.2.4 Attenuation due to hydrometeors on the RF path.

The obtained monthly CDs due to all of the hydrometeors combined (R, RS, S, F, FR, FS, FRS) for the individual 1-year periods of observation on the RF path are given in Figs. 12.2-7 12.2-9.

The large month-to-month variability of these distributions can also be observed. The CD of attenuation due to all of the hydrometeors combined for the worst month of the 1<sup>st</sup> year period is formed by the pertinent parts of the CDs for March and September. For the 2<sup>nd</sup> year period, the CD of attenuation due to all of the hydrometeors combined is formed by the pertinent parts of the CDs for March and November. The CD of attenuation due to all of the hydrometeors combined for the worst month of the 3<sup>rd</sup> year period is formed by the pertinent parts of the CDs for October and February.

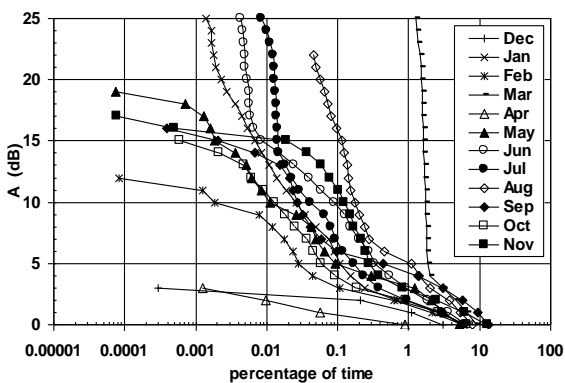


Fig 12.2-7 Obtained monthly CDs of attenuation due to all of the hydrometeors combined on the RF path for the 1<sup>st</sup> year period

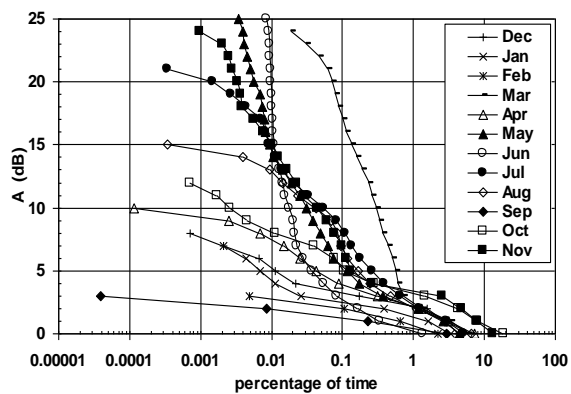


Fig 12.2-8 Obtained monthly CDs of attenuation due to all of the hydrometeors combined on the RF path for the 2<sup>nd</sup> year period

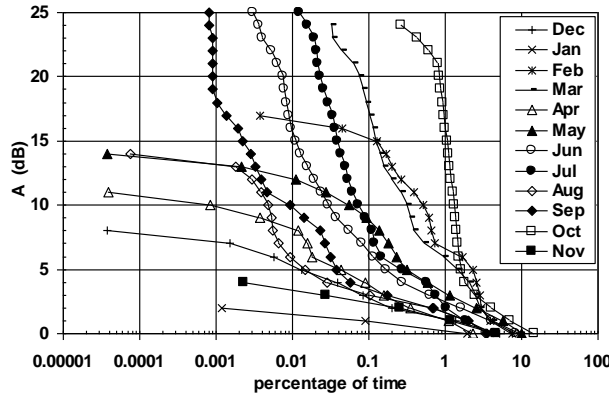


Fig. 12.2-9 Obtained monthly CDs of attenuation due to all of the hydrometeors combined on the RF path for the 3<sup>rd</sup> year period

The insignificant attenuation events, i.e. the small or short-term attenuation events occurred during the winter months, i.e. from November to February.

The obtained annual CDs of attenuation on the RF path due to both all of the hydrometeors combined and the individual hydrometeors separately are shown in Figs. 12.2-10-12.2-12.

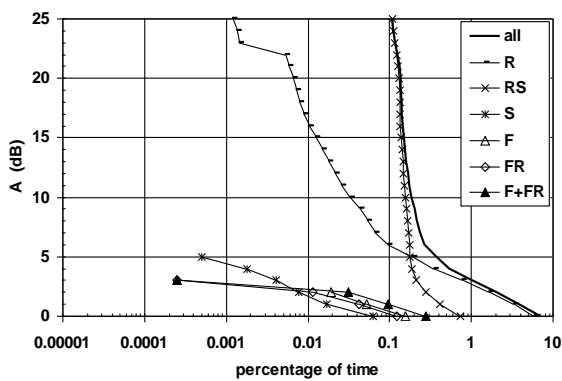


Figure 12.2-10 Obtained CDs of attenuation due to individual hydrometeors on the RF path for the 1<sup>st</sup> year period

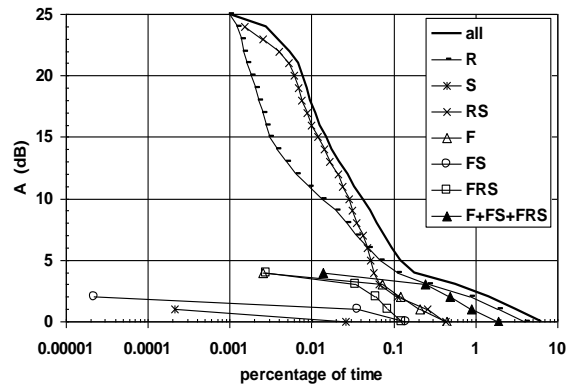


Figure 12.2-11 Obtained CDs of attenuation due to individual hydrometeors on the RF path for the 2<sup>nd</sup> year period

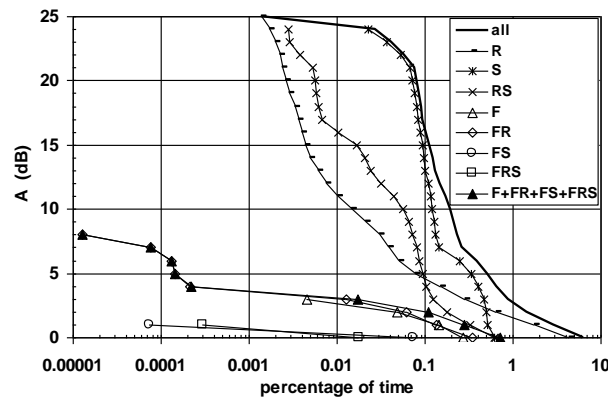


Figure 12.2-12 Obtained CDs of attenuation due to individual hydrometeorson the RF path for the 3<sup>rd</sup> year period

It follows from Figs. 10-12 that the dominant attenuation events were caused by RS and R events for the 1<sup>st</sup> and 2<sup>nd</sup> year period and by S, RS and R events for the 3<sup>rd</sup> year period. It can be seen that the F, FR, FS and FRS events only caused insignificant attenuation events.

### 12.2.5 Yearly CDs of attenuation due to hydrometeors on FSO and RF paths

The obtained CDs of attenuation due to all of the hydrometeors combined on the FSO and RF paths for the individual year periods and the average year over the 3-year period are displayed in Figs. 12.2-13 and 12.2-14.

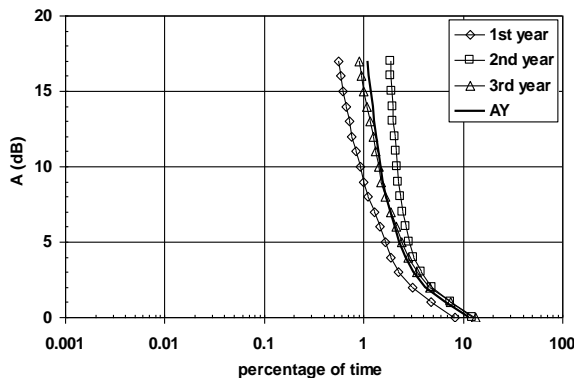


Fig. 12.2-13 Obtained CDs of attenuation due to all of the hydrometeors combined on the FSO path for the individual year periods and the average year

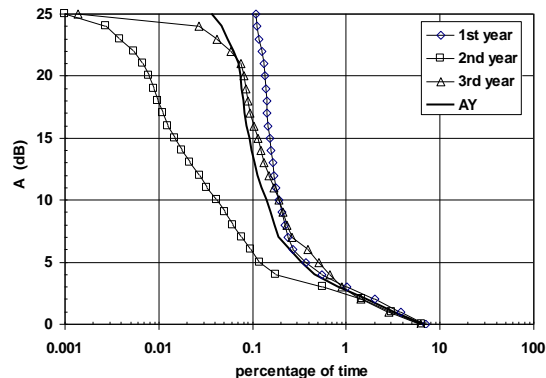


Fig. 12.2-14 Obtained CDs of attenuation due to all of the hydrometeors combined on the RF path for the individual year periods and the average year

It can be seen that the dominant attenuation events occurred on the FSO path during the 2<sup>nd</sup> year of observation while the dominant attenuation events on the RF path occurred during the 1<sup>st</sup> year of observation.

### 12.2.6 Availability performance of hybrid FSO/RF system

Availability performances [ITU-R F.592] of FSO links are mainly limited by dense fog events while availability performances of RF links are influenced predominantly by heavy rainfall events. A simple diversity technique can be simulated, so either the FSO part or the RF part of the hybrid FSO/RF system is active depending on instantaneous values of the optical and radio path attenuation. It can be assumed that the RF part of the system mitigates non-rain events and the FSO part mitigates rain events. The availability performances of the FSO link, the RF links and the simulated hybrid FSO/RF system can be assessed from the CDs of attenuation due to all of the hydrometeors combined which are given in Figs. 15-17 for the individual year periods of observation.

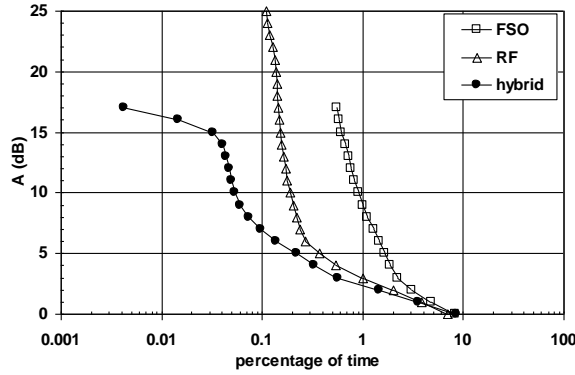


Fig. 12.2-15 Obtained CDs of attenuation due to all of the hydrometeors combined for the FSO path, RF path and simulated hybrid FSO/RF system for the 1<sup>st</sup> year period

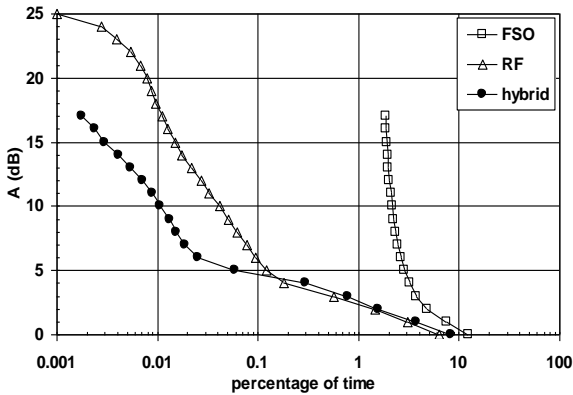


Fig. 12.2- 16 Obtained CDs of attenuation due to all of the hydrometeors combined for the FSO path, RF path and simulated hybrid FSO/RF system for the 2<sup>nd</sup> year period

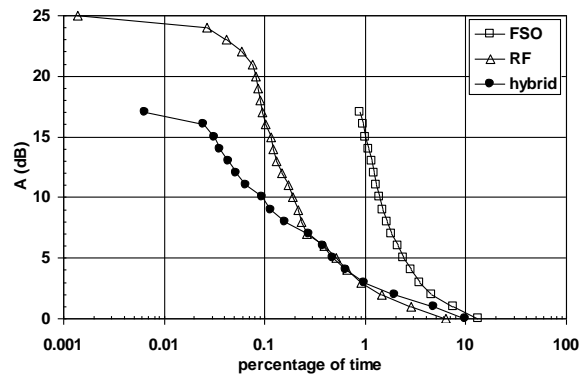


Fig. 12.2-17 Obtained CDs of attenuation due to all of the hydrometeors combined for the FSO path, RF path and simulated hybrid FSO/RF system for the 3<sup>rd</sup> year period

The great year-to-year variability of these distributions can be observed in the 2<sup>nd</sup> year period. For the 2<sup>nd</sup> year period, the dominant attenuation events occurred on the FSO path while the attenuation events on the RF path were most favourable over the 3-year period. This is confirmed by Figs. n.12.2-13 and 12.2-14. Therefore, the simulated hybrid FSO/RF system was the most efficient for the 2<sup>nd</sup> year period.

The obtained CDs of attenuation due to all of the hydrometeors combined for the FSO path, RF path and the simulated hybrid FSO/RF system over the 3-year period are shown in Fig. 12.2-18. The long-term availability performances of the FSO, RF and hybrid FSO/RF systems can be assessed from the Figure.

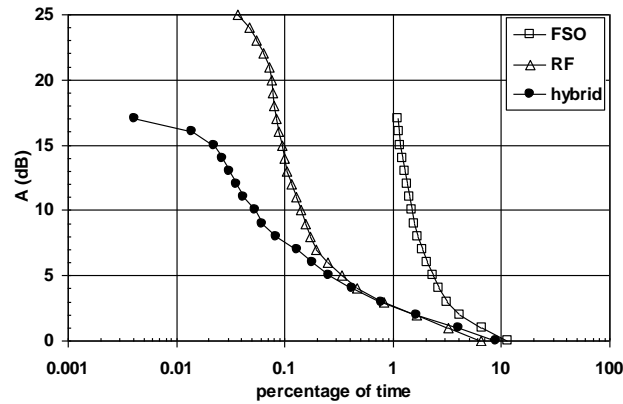


Fig. 12.2-18 Obtained CDs of attenuation due to all of the hydrometeors combined for the FSO path, RF path and simulated hybrid FSO/RF system over the 3-year period

Let us consider a hybrid system where both the FSO link and the RF link have the same fade margin  $FM = 17$  dB. The obtained availability performances (AP) of the FSO link, the RF links and the simulated hybrid FSO/RF system are given in Table 1.

Table 12.2-1 Availability performances of FSO, RF and simulated hybrid FSO/RF system

System	AP (%)
FSO	98.9000
RF	99.9171
hybrid FSO/RF	99.9958

It can be seen that a significant improvement of the availability performance (practically 2 decades) was achieved for the simulated hybrid FSO/RF system in comparison with the FSO system alone.

### 12.2.7 Conclusions

The results of a propagation study on a free space optical link at 850 nm on a path 853 metres long and on a parallel 58 GHz radio link obtained over a 3-year period of observation are presented. Individual attenuation events were compared with the concurrent meteorological situations and were carefully classified according to the causes of their origin. The cumulative distributions of attenuation due to all of the hydrometeors combined for the individual months as well as due to individual hydrometeors for individual year periods were obtained for both paths. The yearly CDs of attenuation due to all of the hydrometeors combined for individual year periods and the average year over the 3-year period were also obtained. The large month-to-month and year-to-year variability of these CDs were observed on both paths. The availability performances of the FSO link, the RF link and the simulated hybrid FSO/RF system were assessed from the CDs of attenuation due to all of hydrometeors combined. For the 2<sup>nd</sup> year period, the dominant attenuation events occurred on the FSO path while the attenuation events on the RF path were most favourable over the 3-year period. Therefore, the simulated hybrid FSO/RF system was the most efficient for the 2<sup>nd</sup> year period when the dense fog attenuation events

were eliminated by the RF system and heavy rain attenuation events were eliminated by the FSO system.

Up to about two decades of higher availability performance was achieved for the simulated hybrid FSO/RF system than for the FSO link alone. The diversity improvement factor reached significant values for attenuation greater than 5 dB and the significant diversity gain was obtained for the percentages of time smaller than 2%.

It was proved that a radio link working in the 58 GHz band can be used as a hitless backup for an FSO link. Limitations due to dense fog and heavy rain are significantly eliminated. The availability performance of the obtained hybrid FSO/RF system is much improved over that of either the FSO or 58 GHz systems. The utilizations of radio systems working in the higher frequency bands have other advantages such as small antennas and broadband transmission. Therefore, the high bit rate transmission need not be reduced.

It should be noted that the results obtained in Prague with the temperate climate of Central Europe are climatically dependent. Long-term experimental research is needed to obtain more detailed information about the influences of individual hydrometeors on attenuation and more reliable results about the availability performances of hybrid FSO/RF systems.

## **12.3 Gbit/sec wireless via FSO and E-band<sup>1</sup> radio**

### *12.3.1 Introduction<sup>2</sup>*

This section deals with Gbit/sec wireless links. The transmission rate of equipment available at the time of this writing (early 2010) is 1 to 1.25 Gbit/sec. 10 Gbit/sec is foreseen in the not too far future, maybe with an intermediate step of about 3 Gbit/sec. In principle, microwave i.e. radio at <30 GHz, mm-wave and FSO bands would equally be appropriate for Gbit/sec transmission, with radio below 10 GHz very likely yielding the best characteristics. Surprisingly, microwave performance is inadequate, as we will explain later. Among mm-waves E-band is allotted to high-speed fixed-service digital transmission with two half-bands for forward and return channels, respectively: 71-76 and 81-86 GHz. The explicitly formulated reason to allocate this band was to make possible Gbit/sec point-to-point transmission via mm-waves. In the optical frequency band practical rather than technical or regulatory factors determine the applicable wavelengths, among these available components and eye safety; these lead to 850 nm and 1550 nm.

It turns out that both FSO and mm-waves have rather adverse propagation characteristics. Interestingly enough, they are similar from the equipment point of view and complementary from the channel point of view. Therefore they offer themselves, self evidently, as two diversity routes of one link. The purpose of this paper is to describe the adverse propagation effects which make this diversity necessary and to discuss these heterogeneous diversity links.

FSO characteristics are widely discussed in relevant literature. A detailed description of meteorological effects is given in [Nadeem & al., 2009] together with a discussion of parallel FSO/millimeter-wave links. A tutorial summary of turbulence effects on FSO beams is given in [Prokes, 2009]. Among others [Borah, Voelz, 2009] and [Karagiannidis 2009] deal with the joint effect of

---

<sup>1</sup> Wikipedia definition: "The newer designation of "E-Band" lies in the extremely high frequency bands from 71 to 76 GHz, 81 to 86 GHz and 92 to 95 GHz. It is being used for short range, high bandwidth communications."

<sup>2</sup> This paper is a somewhat extended version of [Frigyes & Csurgai-Horváth, 2010]

turbulence and pointing errors, [Borah, Voelz, 2009] dealing with OOK/DD and [Karagiannidis 2009] with PSK/coherent detection. Our discussion will deal with both optical DD and heterodyne detection.

The mm-wave propagation characteristics are, for example, described in the European Union sponsored COST reports [Hall, 1996] and [Arbesser-Rastburg, 2002] on terrestrial and satellite aspects respectively; [Castanet, 2008] deals with various aspects of propagation characteristics of satellite links with a detailed discussion of mm-waves. For characteristics of hybrid FSO/microwave-mm-wave links see [Nadeem & al., 2009] and [Luna & al, 2009].

### 12.3.2 Summary of the application and main characteristics of wireless gigabit/sec links

#### 12.3.2.1 Application

In cellular mobile networks backhaul sub-networks are very often – nearly always – realized via point-to-point digital radio. This is the simplest and most economic solution in 2G and maybe also in 3G networks. While in 3G systems the capacity of these is only in exceptional cases >100 Mbit/sec, in NGN (Next Generation Networks) the backhaul links will have to provide significantly higher bit rates, say 1 Gbit/s at least. Fig. 12.3-1 shows an example of network topology in which wireless links serve to connect aggregating points to base sites.

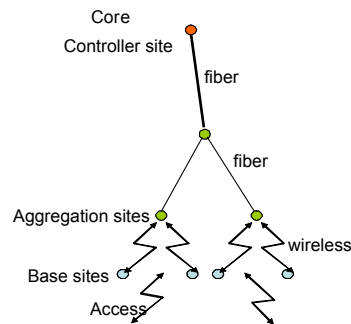


Figure 12.3-1 Wireless network with wireless link

While this type of application seems to be the most demanding both in hop-length and in reliability requirements several other applications are mentioned by equipment producers and other sources.

To cite a few examples, “last mile” application is one of these. The concept of FTTH (Fiber To The Home) and FTTC (Fiber To The Curb) is long since known but very rarely applied only – mainly due to financial reasons. The role of these can much cheaper be fulfilled by wireless links of appropriate (Gbit/sec) transmission capacity.

A second example is campus-application: in intra-nets of university, hospital or industrial campuses the high rate wireless links are economic and appropriate alternative of wired systems. Ad-hoc applications as emergency communications or temporary systems, among these battlefield communications are a further group of application. And also connecting distinct networks and systems such as LAN-s (Local Area Networks) or fiberoptic links with a trace crossing a river, a motorway, tracks, form a further group.

Note that each of these requires high bitrate and high availability and can be realized both by FSO and E-band links.

#### 12.3.2.2 FSO main characteristics

##### 1) Modulation

As usual in optical communications most FSO systems operate with OOK/DD (On-Off Keying/DD). Consequently most investigations relate to that. However, due to better power economy the application of coherent methods is not excluded. Among these, differentially encoded PSK (Phase Shift Keying) with heterodyne detection would be the primary candidate. OOK-PPM/DD (PPM: Pulse Position Modulation) could also have some advantages.

## 2) *Adverse channel characteristics [Nadeem & al., 2009], [Karagiannidis 2009],*

The most important among these are rain, fog, atmospheric turbulence and beam pointing error.

The main adverse effect is fog, being most responsible for the non-availability of FSO links. As usual in meteorology, intensity of fog is characterized by visibility. Just to state some indicative values, valid for 850 nm wavelength: light fog – visibility of about 10 km – causes low attenuation, about 1 to 4 dB/km. The attenuation of heavy fog – visibility of < 0.5 km – produces very high loss, > 40 dB/km, and up to 300 dB/km if the fog gets denser. Fog-induced attenuation depends somewhat on the wavelength; it is lower at longer wavelength but the orders of magnitude are similar.

Heavy rain causes high attenuation as well, strongly depending on rain rate (mm/hours). Very heavy rain, 90-100 mm/h, occurring in temperate climate with non-negligible probability can cause attenuation of about 20 dB/km. Both fog- and rain-induced fading is flat both in time and in frequency.

Atmospheric turbulence causes fluctuation of optical field amplitude and phase, called scintillation. This is a rather slow fading. (“Rather slow” means constant over long strings of symbols; its time constant is in the order of seconds.) For short periods it can bring a link into outage condition. Under clear air conditions amplitude scintillation is the main channel impairment. Phase fluctuation, on the other hand, is usually negligible (both in DD and in differentially encoded PSK).

Taking into account that the laser beam carrying information is very narrow, exact pointing of the transmitter toward the receiver is of primary importance. Although usually this is kept fixed by a tracking loop, pointing errors are still harmful. Effect of pointing error and scintillation are often jointly investigated, as these are not simply additive.

### 12.3.2.3 *E-band radio main characteristics*

#### 1) *Modulation*

E-band systems, similarly to FSO apply simple modulation, although for a different reason. Present day technology of mm-wave circuits is not very much evolved. Transmitters of very low phase noise and receivers of very high linearity are non-existing (at least at sufficiently low prices). On the other hand this frequency band is sparsely used and antennas have rather narrow beams. Consequently equipment of higher level modulation (e.g. MQAM with  $M > 4$ ) are neither available nor needed. OOK, BPSK, BFSK or, at most, QPSK is applied in present-day 1 Gigabit/sec systems. (Note that a significant change in transmission rate (e.g. up to 10 Gigabit/sec) will certainly need higher level modulation, mainly due to the width of the frequency band available in E-band, i.e.  $2 \times 5$  GHz.)

#### 2) *Adverse channel characteristics*

Fog is to some extent lossy, however, its loss, in contrast to FSO is more or less negligible at least in short links. Loss depends on the liquid water content of air and on temperature. Measured and predicted loss values of a particular fog event are compared in Fig.2. Data were taken in December 2009 at BME: loss was measured on a 3.5 km link and liquid water content with our sensor. As seen, prediction and measurement values are close to identical.

In contrast to FSO heavy rain is primary cause of outage for mm waves. In E-band attenuation can be as high as 30-35 dB/km (rain rate: 90 mm/h) and it depends only slightly on frequency. Some E-band measurement results are described in [Tjelta & Breivik, 2009].

Atmospheric turbulence-caused scintillation has some effect on mm-wave links being, however, negligible if the hop length is less than about 20 km [McMillan & al, 1997].

#### 12.3.2.4 Parallel FSO/radio links; application aspects

Against the adverse effect of fog in FSO a backup *radio* link offers itself as countermeasure. Its application is really foreseen since the early days of FSO. From this point of view there is a significant difference between the pre-E-band era and today. Gigabit/sec radio did not exist in the pre-E band era. Therefore all of the publications in this field, including [Nadeem & al., 2009]], [Luna & al, 2009] assume radio backup for increasing link availability during foggy periods at significantly lower rate. However, reasonable rate reduction must be less than, say 10-fold. E.g. [Luna & al, 2009] takes 10-fold and 5-fold reduction into account.

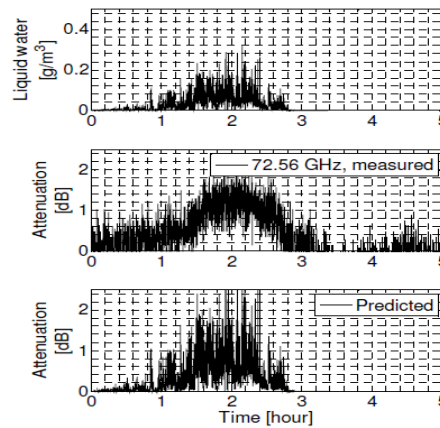


Fig. 12.3-2 Predicted and measured fog-induced loss at E-band; prediction is based on water-content sensing

From the availability point of view a lower-than-10 GHz backup link would be preferable (proposed e.g. by [Luna & al, 2009]) as this is influenced neither by fog nor by rain. However, in reality this solution does not exist, for various reasons. The frequency band is congested; to find not-used frequencies is nearly impossible. The transmission rate of this backup link would have to be at least 100 Megabit/sec, possibly later as high as 300-1000 Megabit/sec which is at or over the limit of actual technical possibility. One of the advantages of FSO is being license free while this freedom does not exist for the proposed backup frequency. (While this is not valid for the 2.4 and 5 GHz ISM/UNII bands, congestion of these is extremely heavy.)

Mm-wave backup is much more applicable and often proposed (e.g. by [Nadeem & al., 2009] and others). Two frequency bands were proposed, with different characteristics, i.e. about 60 GHz and about 40 GHz. 60 GHz is license free virtually also free from intersystem interference and the bandwidth is sufficiently high even for Gbit/sec transmission. On the other hand this frequency band can only be applied to short links, typically below 1 km. 40 GHz is in principle an applicable choice. Details are given e.g. in [Nadeem & al., 2009].

According to the opinion of the authors the appearance of E-band Gbit/sec systems may result in a breakthrough in parallel FSO/radio application: transmission rate is about the same as already mentioned; somewhat longer hops than those of 60 GHz are possible; and, as seen, to some extent characteristics are complementary. E-band is not unlicensed but a simplified licensing procedure applies.

#### 12.3.3 Parallel FSO/E-band links; technical aspects

### 12.3.3.1 General

If an FSO link is operated in parallel to a radio link, in our case parallel to an E-band link, this system can be regarded as a special case of a MIMO (Multiple Input Multiple Output) system, forming actually a  $2 \times 2$  MIMO. Its dissimilarity from a conventional MIMO system is that both receive antennae “see” the opposite transmit antenna only and don’t see the neighbouring one. This so-called *parallel MIMO system* was introduced (by Horváth and one of these authors) and investigated, relative to a quite different problem, in [11]. It is characterized by a diagonal channel matrix

$$\mathbf{H} = \begin{pmatrix} h_1 & 0 \\ 0 & h_2 \end{pmatrix} \quad (12.3-1)$$

where  $h_i$ ,  $i=1,2$  is the transfer coefficient *related to fading*.

We’ll apply this model and relevant methods for the present case.

As seen in (1) the number of diversity routes is only 2. This is in contrast to more conventional MIMOs, in which a  $2 \times 2$  system would produce up to 4 diversity routes. However, if we regard the two (rather special) diversity routes as one entity the concepts of Space Time (ST) trellis coding can be applied. The ST encoder-decoder serve as the innermost codec, applied concatenated with the presumably also existing channel encoder – e.g. LDPC; the role of ST coding is to yield additional coding gain (and that with code rate 1). The block schematic is shown in Fig. 3. Note that coding aspects will not be dealt with here; for some details on ST codes optimized for a parallel MIMO channel see also [11].

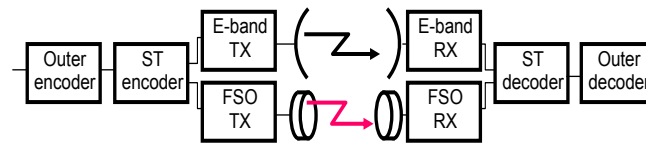


Fig. 12.3-3 Block schematic of a parallel FSO/E-band system with ST coding

In the present discussion we are interested in channel capacity. As this channel is non-ergodic (channel is virtually constant during thousands or millions of symbols) it is the *outage capacity* that is of interest. Channel capacity can be determined from the standard MIMO capacity formula (with some modifications), written below for the deterministic case:

$$C = \log_2 \det \left( \mathbf{I}_m + \frac{\rho}{n} \mathbf{H} \mathbf{H}^H \right) \quad (12.3-2)$$

with  $\rho$  the *unfaded* signal-to-noise ratio (SNR)

$n$  the number of transmit antennae

$m$  the number of receive antennae

$\mathbf{I}_m$  the unity matrix of order  $m$  and

superscript  $H$  meaning the Hermitian transpose.

Some modifications are needed for application of this formula. First note that  $\rho$  is the *electrical* SNR. In optical *DD* this is proportional to the optical power *squared*; in optical heterodyne detection SNR is proportional to the optical power while noise power in that case is that of the local oscillator shot noise. Second, in the electrical case for sake of fairness it is reasonable to apply  $\rho/n$ . In the present case the same approach would have not too much sense: electrical and optical powers are independent. Thus

in our numerical evaluations rather than being “fair” we’ll take reasonable SNR-s both for the FSO and for the E-band link. SNR of the E-band link will be designated as  $\rho_1$  and that of the FSO link as  $\rho_2$ .

To specify the optical SNR in DD, the received optical power is approximately given as [Prokes, 2009]

$$P_{r,opt} = P_{t,opt} \left( \frac{\phi}{D\mathcal{G}} \right)^2 \quad (12.3-3)$$

with  $P_{t,opt}$ , the transmitted optical power

$\phi$  the receiver lens diameter

$D$  the hop length and

$\mathcal{G}$  the angle of divergence of the propagating beam (defined as usual for a Gaussian beam).

Then the *electrical* SNR is

$$\rho_2^2 = \left( \frac{i_{signal}}{i_{noise}} \right)^2 = \left( \frac{R_d P_{r,opt}}{i_{noise}} \right)^2 \quad (12.3-4)$$

$i_{noise}$  is the (mainly thermal) noise current of the electrical amplifier (specified by the manufacturer).

Thus applying (12.3-2...-4) we get for DD

$$C = \log_2 \left( \left( 1 + \rho_1 |h_1|^2 \right) \times \left( 1 + \rho_2^2 |h_2|^4 \right) \right) \quad (12.3-5)$$

In the case of heterodyne detection electrical SNR is proportional to the received optical power (not to its square). Its magnitude is

$$\rho_2 = \frac{\eta_q P_{r,opt}}{hf_c B} \quad (12.3-6)$$

where  $\eta_q$  is the detector quantum efficiency,  $h$  is Planck’s constant,  $f_c$  is the carrier frequency,  $B$  is the bandwidth and  $R_d$  is the photodetector’s responsivity.

We have for this case

$$C = \log_2 \left( \left( 1 + \rho_1 |h_1|^2 \right) \times \left( 1 + \rho_2 |h_2|^2 \right) \right) \quad (12.3.3-7)$$

The next section investigates behaviour in the case of heavy rain, of fog and of turbulence. Antenna pointing error effects are not discussed.

### 12.3.3.2 Functioning in the case of heavy rain

Note that rain is usually *the* determining phenomenon of link outage as both propagation media – optics and mm-wave – are sensitive to it, however, to a different scale.

According to [Nadeem & al., 2009] and [ITU-R P.837, 2007] the attenuation of rain, both in mm-waves and in FSO can be expressed as

$$A = \gamma \cdot D = kDR^\alpha \text{ dB} \quad (\text{n-12.3-8})$$

Where  $A$  is the rain-induced attenuation in dB,  $\gamma$  the loss/km,  $R$  the rain rate in mm/hours, and  $D$  the effective hop-length in km.

In distances of interest here it is just slightly shorter than the true distance.

$k$  and  $\alpha$  frequency- and polarization-dependent parameters. For 80 GHz the following apply:

$$k_{\text{horiz}} = .955; k_{\text{vert}} = .888; \alpha_{\text{horiz}} = \alpha_{\text{vert}} = .772$$

In the optical bands of interest

$$k = 1.076; \alpha = .67$$

As an example of rain effect see Table 12.3-1 for Budapest

Table 12.3-1 Rain effects in FSO and E-band; Budapest

Probability	10 <sup>-4</sup>	10 <sup>-5</sup>
R, mm/h	35.9	96.2
$\gamma_1$ , dB/km	15.15	32.4
$\gamma_2$ , dB/km	11.75	22.94

$|h_i|^2$  values are given as

$$|h_i|^2 = 10^{-\gamma_i D/10} / D^2 ; i = 1, 2 \quad (12.3-9)$$

### 12.3.3.3 Functioning in the case of fog

As seen in section II fog – in spite of the fact that its effect on the FSO link is detrimental – is not very harmful for the whole parallel system. Therefore a rather rough ad-hoc fog model can be adequate. So assume that 16% of days is foggy; duration of one fog event is 6 hours in the average; and with equal probability these are of very light, light and heavy density with FSO attenuation of 4 dB/km,  $\leq 20$  dB/km and  $>120$  dB/km, respectively. Fog attenuation at 80 GHz for radio in the same situations is 0, 0.25 dB/km and 3 dB/km, respectively.

Simultaneous occurrence of fog and heavy rain is improbably and can be excluded. Therefore – assuming the above fog attenuation at E-band – the radio equipment must insure required link availability by itself for about 1% of time and for further 1% together with a strongly and 1% with a lightly reduced quality FSO link, respectively.

### 12.3.3.4 Effect of turbulence on parallel link capacity

Atmospheric turbulence causes fluctuation of received optical field amplitude and phase. Depending on the strength of fluctuation instantaneous received intensity (or power) follows either lognormal or gamma-gamma distribution [Prokes, 2009]. The former is valid for weak turbulence (to be defined later) with cumulative distribution function

$$F_{h_a}(h_a) = \frac{1}{2} \operatorname{erfc} \left[ -\frac{\ln h_a + \sigma_R^2/2}{\sqrt{2}\sigma_R} \right] \quad (12.3-10)$$

Here  $h_a = |h_2|^2$  in the atmospheric turbulence case and  $\sigma_R^2$  is the so-called Rytov variance, defined as

$$\sigma_R^2 = 1.23 C_n^2 \beta^{7/6} D^{11/6} \quad (12.3-11)$$

Where  $C_n^2$  is the *structure parameter* of the index of refraction and its magnitude in optical frequencies is in the range of  $10^{-15} \dots 10^{-13}$ ,  $\beta$  is the wave number measured in 1/m unit, And  $D$  is the hop length, now measured in m unit (in contrast to km units applied in the preceding).

The scintillation is called weak if the Rytov-variance is less than 0.3...0.5. While the lognormal distribution of (12.3-10) is strictly valid for this case only, it gives quite good results if the receiver lens is rather large; in this case the large aperture integrates to certain extent the fluctuations on that surface.

#### 12.3.3.5 System specification

The primary specification is  $K$ , the number of *bits per channel use* supported by the parallel system. (This form of capacity description is in diversity systems more appropriate than (bit/sec)/Hz. Namely *one* channel is formed by the whole diversity system, whether it occupies one or more than one frequency bands.) The choice of  $K$  takes into account the code rate of the outer code (see Fig. 12.3-3.) The rate of the ST code is 1.

The definition of outage probability is

$$P_{out} \hat{=} \Pr\{C < K\} \quad (12.3-12)$$

As  $C$  is given as a function of SNR, (12.3-12) is equivalent to

$$P_{out} = \Pr\{SNR < C^{-1}(SNR_{C=K})\}, \quad (12.3-13)$$

i.e. the cumulative distribution at  $C^{-1}(SNR_{C=K})$ .

In principle the joint distribution of each disturbing physical phenomenon could be formed. However, as the rainy, foggy, periods are not stationary this would be a formal approach without much meaning. Instead we could express the outage probability as follows

$$P_{out} = \Pr\{\text{clear air}\} \cdot \Pr\{\text{out} | \text{clear air}\} + \Pr\{\text{fog}\} \cdot \Pr\{\text{out} | \text{fog}\} + \Pr\{\text{out} | \text{rain}\} \quad (12.3-14)$$

The contribution of the E-band link to the first and second term of (14) is very low (as we shall see it is zero). Thus system design can be based on the third term – i.e. heavy rain assumed – and the possible effect of the first two terms subsequently determined.

Binary modulation is selected with optical direct detection: OOK in the FSO and BPSK in the E-band. With heterodyne FSO, we can alternatively use QPSK.

12.3.4 A numerical example

12.3.4.1 Hop length vs. specified maximal  $P_{out}$

To get an idea about the performance of parallel FSO/E-band links, the effect of various phenomena will be calculated for a prototype equipment. The parameters of the FSO link are specified in Table 12.3-2. For the E-band link no detailed link parameters are given; a reasonable reference fade margin of 45 dB (for a 1 km link) is assumed.

Table 12.3-2 FSO link parameters

Wavelength	1550 nm
Transmit power	40 mW
Angle of divergence	2 mrad
Modulation level	Binary or quaternary
Receiver diameter	25 cm
Responsivity	1 A/W (i.e. $\eta_q=0.8$ )
Optical detection	DD or heterodyne
Receiver noise current	200 nA
Reference hop length	1 km ( $\rho_2=35$ dB in DD, 65 dB in heterodyne)

Table 12.3-3 Outage capacities vs. hop length; binary mod. DD

$P_{out}=10^{-5}; \rho_1=45$ dB; $\rho_2=35$ dB							
D/km	1	1.125	1.25	1.312	1.38	1.44	1.5
$C_{out;Eband}$	4.3	2.8	1.5	1.0	0.39	0.30	0.25
$C_{out;FSO}$	8.0	5.5	3.0	2.0	1.2	0.67	0.33
$C_{out;parall}$	12.3	8.3	4.5	3.0	1.6	0.97	0.58
Limiting D for:				Eband		FSO	Parallel
$P_{out}=10^{-4}; \rho_1=45$ dB; $\rho_2=35$ dB							
D/km	2	2.25	2.4	2.5	2	2.7	
$C_{out;Eband}$	3.1	1.1	1.0	0.86	0.60	0.47	
$C_{out;FSO}$	3.8	1.6	0.75	0.42	0.22	0.15	
$C_{out;parall}$	6.9	2.7	1.75	1.28	0.86	0.62	
Limiting D for:				FSO	Eband		Parallel

Maximal hop length is computed for outage probabilities of  $10^{-4}$  and  $10^{-5}$  for various situations: FSO only, E-band only and parallel link. This is done for DD binary and for heterodyne binary *and* quaternary modulation.

Table 12.3-3 contains virtual magnitudes of outage capacities vs. path length  $D$ . Virtual if  $C > 0.5$ , as no higher order than binary modulator is foreseen.

In Table 12.3-4 similar data are given for heterodyne optical detection. In this case  $\rho_2$  is so much larger than  $\rho_1$  that hop length is uniquely determined by the FSO link while during heaviest rain periods the E-band link is in outage.

Table 12.3-4 outage capacities vs. hop length; binary & quaternary detection

Pout=10-5; $\rho_2=65$ dB					
D/km	2.3	2.4	2.5	2.6	2.7.
Cout;FSO	2.0	1.4	0.94	0.59	0.35
Limiting D for:	quaternary			binary	
Pout=10-4; $\rho_2=65$ dB					
D/km	4.0	4.2	4.4	4.6	4.65
Cout;FSO	2.3	1.6	1.07	0.66	0.58
Limiting D for	quaternary				binary

#### 12.3.4.2 Operation under heavy fog

In principle outage due to fog could be determined from (12.3-14). The ad-hoc fog model of section 12.3.3.3 shows that  $\Pr\{\text{out}|\text{fog}\}=0$  as the E-band link, even in the worst case, is never in outage due to fog. Even in the longest hop and heaviest fog, E-band-link SNR is 17 dB, corresponding (virtually) to 6 bit/channel use.

(Note that the FSO-alone link would be in outage in the case of fog of light or of heavy density – i.e. for about 10.5% of time according to our ad-hoc model described in section 12.3.3.3)

#### 12.3.4.2 Effect of turbulence

According to section 12.3.3.3 lognormal distribution can be applied to turbulence characterization. So outage probability of the FSO link can be computed from (12.3-10). It turns out – not surprisingly – that for long paths and medium strength of turbulence the outage probability is very high. (In the case of the quaternary example with 4.2 km it can be as high as 1.2 %.) On the other hand scintillation has *some* effect in E-band (and in mm-waves, in general), but its magnitude does not exceed a few dB [McMillan & al, 1997] and is so negligible. Thus this phenomenon is also negligible in parallel links.

#### 12.3.5 Conclusions

While the complementary character of propagation effects on FSO and RF links was recognized in the early days of FSO, recent development in E-band changed the exploitation possibilities of this complementarity. The novelty described here is that E-band links yield the same transmission rate as FSO links, thus in up to date parallel FSO/E-band links the two technologies are of equal rank. The main consequence of that is that in such parallel systems it is not only availability that is increased due to this

design but high availability does not require settling for lower backup transmission rate and also quality is improved. Our main findings are:

i. Practical considerations exclude the application of a backup RF link in the microwave (in particular below-10-GHz) frequency band, as proposed by some investigations.

ii. In contrast to FSO-alone systems, in parallel links rain, rather than fog, is the main cause of unavailability. Rain is the only environmental effect to which such parallel links are sensitive (determining availability, or inversely, hop-length), regardless of other effects being detrimental to FSO-alone links. Taking the last points into account it could be stated that if an E-band link is operating in parallel to an FSO link it is more the FSO serving as backup to the E-band link than the converse

iii. By recognizing that such a parallel link can be regarded as a special, so-called *parallel* MIMO system, quality can be improved by applying Space-Time trellis coding, in addition to the usual channel coding. ST coding with code rate 1 can yield additional coding gain.

iv. Among optical technologies heterodyne detection has much better performance than Direct Detection at the expense of being much more complex; perhaps an optical low-noise input amplifier could yield a much less expensive intermediate solution;

v. While FSO is fully license-free, a license is needed for E-band. However, it enjoys a much simpler licensing procedure than microwave bands.

## **12.4 Green-inspired hybrid FSO/RF wireless backhauling for next generation Metrozones**

### *12.4.1 Introduction*

The unequivocality of global man-made climate change has attracted substantial conservation efforts, to promote greener technology options (Consortium 2010; GreenTouch 2011; VCE 2011), energy-efficient solutions (Vereecken, Van Heddeghem et al. ; Vadgama 2009; Research 2010; Tuttlebee, Fletcher et al. 2010), and carbon emissions savings opportunities (Fehske, Fettweis et al. ; (GeSI) 2008; Forster, Dickie et al. 2009), toward realizing a global low carbon society. Statistics released by the Global eSustainability Initiative (GeSI) ((GeSI) 2008) reveal that the worldwide carbon emissions will rise from 40 billion tonnes (Gt) carbon dioxide equivalent (CO<sub>2</sub>e) per annum (pa) in 2002 to approximately 53 GtCO<sub>2</sub>e by 2020. The information and communications technology (ICT) sector has been identified as one of the key areas in mitigating the world's carbon footprint, due to its astounding direct contribution of 2%, by consuming 3% of the worldwide energy with a growth rate of 6% pa (Vereecken, Van Heddeghem et al. ; Forster, Dickie et al. 2009; Vadgama 2009). The explosive growth in the number of mobile, fixed and broadband subscribers on a global basis, which is attributable to the emerging ICT demand in developing countries ((GeSI) 2008), inevitably requires extensive mobile networks supported by greater amount of power-hungry base transceiver stations (BTSs) and mobile switching centres. Consequently, enormous stress would be incurred upon network operators to suppress the resulting infrastructure carbon footprint with a projected growth from 133 million tonnes (Mt) CO<sub>2</sub> to 299 MtCO<sub>2</sub> by 2020 at an annual incremental rate of 5%.

Greenfield deployment of macro-cellular networks requires up to tens of thousands of BTSs, for providing ubiquitous coverage and seamless communication, while coping with the capacity demand for voice and high-speed data and video traffic. At present, an estimated 24,000 BTSs are deployed in the existing third generation (3G) network throughout the UK with a total power consumption of 300 GWh/year, for providing coverage to a population in excess of 80%, in which these statistics would double up to extend the network for national coverage (Forster, Dickie et al. 2009). The roll-out of the 4G cellular wireless standards in the near future is poised to set the peak capacity requirements up to 1 Gbps (Fehske, Fettweis et al.). This is in order to provide a comprehensive and secure all-internet

protocol (IP) based solution to various mobile broadband facilities, such as the ultra-broadband internet access, voice over IP (VoIP), online gaming and streamed multimedia applications. The incessantly exploding mobile data traffic volumes due to burgeoning smart devices, applications and changing user behaviour has resulted in severe bandwidth capacity crunch, in which the peak-to-average gap is forecasted to rise to ~90 times its current size by 2015 with the adoption of 4G technologies (Research 2010).

## 12.4.2 The green Metrozones concept

### 12.4.2.1 The rationale

The diffusion of smaller cells into traditional macro-cellular networks presents a feasible, energy-efficient and cost-effective alternative, to shift the access network closer to the mobile user terminals (MUTs) as compared to other methods, such as improving spectrum efficiency and increasing cell site transmit power (Research 2010; VCE 2011). Correspondingly, a manifold gain in the mobile data capacity can be achieved to curtail the impact of the prevailing bandwidth capacity crunch phenomena. Inevitably this will drive the deployment of at least an order-of-magnitude more micro-/picocells for providing a uniformly distributed capacity density across a mobile service area (VCE 2011). Thereby, addressing the requirement for new data-centric RAN architecture solutions with a higher degree of network flexibility and reconfigurability.

On the other hand, the existing macro-cellular BTS infrastructures are retained and upgraded to enhance the network performance and scalability, while promoting a significant reduction in the site costs. These BTSs with integrated routing and mesh networking capabilities can be deployed at the macro tier, to enable rapid, flexible and low-cost connectivity to the core network via the packet-based multi-hop communication, as compared to wired backhaul solutions, such as leased T1/E1 copper lines and optical fiber links (Tipmongkolsilp, Zaghloul et al. 2011). The evolving trends in emerging 4G wireless mobile broadband networks reveals preferences for smaller cells to boost the capacity and migration towards cost-effective packet-based wireless backhauling solutions. This has led to the interdependency between macro- and sub-cells, which has attracted the Metrozones concept to cope with the massive growth in the number of mobile subscribers and high-speed data services, while complementing the operators' escalating deployment and operational costs.

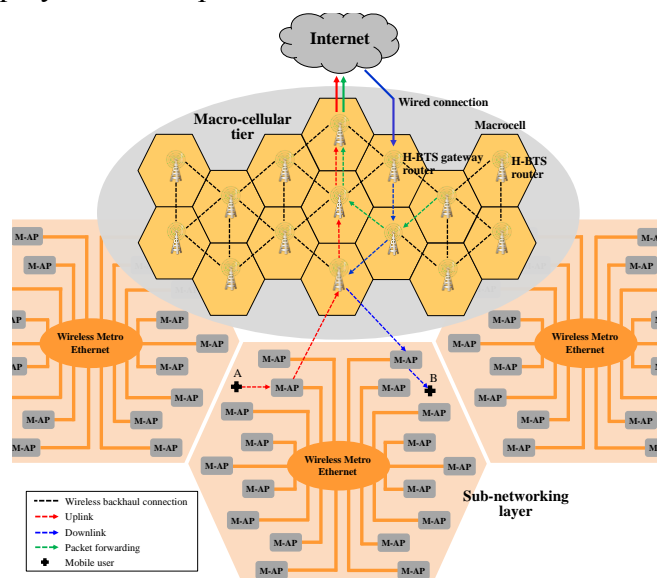


### **Figure 12.4-1** Network architecture of the green Metrozones concept.

#### *12.4.2.2 Network architecture*

In principle, the network topology of Metrozones is conceptually similar to a two-tier infrastructure/backbone wireless mesh network (WMN) ([Akyildiz, Wang et al. 2005](#); [Research 2010](#)), which comprises two main hierarchy – the macro-cellular tier and sub-networking layer (see Figure 12.4-1).

The macro tier is populated by the BTS infrastructures with no mobility, less power constraint, sophisticated computational functions and integrated routing capabilities to perform wireless mesh backhauling. A fraction of BTSs with the gateway (GW) or the bridge functions has wired connection to the Internet, representing sources/sinks in the WMN, thereby enabling connectivity to the wired backbone facilities at a much lower cost and with flexible networking options ([Akyildiz, Wang et al. 2005](#); [Tipmongkolsilp, Zaghoul et al. 2011](#)). These BTSs automatically establish and maintain the connectivity among themselves, to form interconnected self-configuring, self-healing wireless backhaul links within the WMN. The data traffic is en route to and from the wired Internet entry points via multi-hop communication among mesh nodes using efficient routing protocols, thus promoting link reliability and load balancing in the macro tier.

At the sub-networking layer, M-APs provide coverage to smaller micro-/picocells within each macrocell form a cluster, which is connected to the BTS via the wireless Metro Ethernet ([Networks 2011](#)), thereby forming a point-to-multipoint connection. Inter-cell coordination is managed in an autonomous manner based on the Self Organizing Network (SON) ([NEC 2009](#); [Networks 2009](#)) principles, whereby the M-APs form self-configuring, self-optimizing and self-healing clusters, to maximize network performance and deliver enhanced user perceived quality through numerous integrated approaches. These include optimization of the network parameters under interference and overload conditions; mitigation of quality degradation that may arise from inaccuracies of network planning or equipment faults; and rapid and efficient fault identification and compensation.

#### *12.4.2.3 The proposed green approach*

Gigabit Ethernet (GigE) backhauling solutions in next generation 4G networks will largely be based on the millimeter-wave (MMW) and licensed E-Band technologies (i.e., 50/60 GHz and 80 GHz bands, respectively), for supporting bandwidth-intensive data operations in the enterprise and urban markets with shorter link requirements of 3-5 km ([Tipmongkolsilp, Zaghoul et al. 2011](#); [WiMAX.com 2011](#)). The high operating frequencies of these technologies promotes antenna directivity with a very narrow beamwidth (4.7° and 1.2° at 60 GHz and 80 GHz, respectively). This unveils numerous technical advantages in mesh-configured wireless backhaul networks, such as the throughput enhancement, interference mitigation, superior security and a high frequency reuse rate ([WiMAX.com 2011](#)). Nonetheless, the high susceptibility of MMW radios to the rain attenuation presents a greater challenge to network operators in optimizing their backhaul solutions, to deliver GigE speeds with a desired carrier-grade availability of 99.999%, not affected by local meteorological conditions ([Jones 2008](#); [WiMAX.com 2011](#)).

FSO communications is a promising broadband wireless access candidate in complementing the RF solutions to resolve the existing “last mile” access network problems. This is due to FSO’s superior characteristics including (i) no licensing requirements or tariffs for its utilization; (ii) virtually unlimited bandwidth for providing near-optimal capacity and supporting high-speed applications; (iii) extensive link range of > 5 km; (iv) high energy efficiency due to low power consumption, reduced interference and fading immunity; and (v) minimal cost and time for deployment ([Mahdy and Deogun 2004](#)). The performance of both FSO and RF links are susceptible to the adverse effects of meteorological and other

natural conditions. Therefore, hybrid FSO/RF systems ([Kim and Korevaar 2001](#); [Bloom and Hartley 2002](#); [He and Schober 2009](#); [Zhang, Hranilovic et al. 2009](#)) present the most prominent alternative to enable these technologies in complementing one another's weaknesses, since fog and rain drastically affect the FSO and RF links, respectively, but only insignificantly vice versa, and rarely occur simultaneously.

Based on concepts described in this section a H-BTS can be designed for the green Metrozones, which takes advantage of the symbiotic relationship between the FSO and RF technologies, by integrating these communication links at the macro tier. No details are given here as this COST Action deals mainly with propagation issues, networking concepts being outside of the field of interest. Main requirements, however, are briefly mentioned below.

The new H-BTS system architecture corresponds to high data-rate transmission with lower transmit power and less susceptibility to interference, thereby delivering high-capacity, power-efficient wireless backhauling solution under most weather conditions and varying data traffic load. A *radio resource management (RRM) module* encompassing a *resource prioritization mechanism* is designed and introduced into the system hub of the proposed H-BTS architecture. This is to maintain a good control and optimal on-demand resource allocation to both the wireless backhaul and RF access networks, taking into account various factors such as the fluctuating traffic demand, spectral bandwidth occupancy, network load, quality of service (QoS), channel conditions, etc. Furthermore, we consider a *BAS scheme* employing a default low data-rate, low-power radio, which necessitates the discovery, registration and monitoring of active M-APs, to enable two distinctive features: the *SWoD mechanism* and *cooperative inter-cell support*. The *SWoD mechanism* minimizes the number of operating radio access interfaces (RAIs) and enhances potential energy savings by putting idling/under-utilized RAIs and M-APs into sleep mode, particularly in low traffic scenarios. The *cooperative inter-cell support* offloads the M-APs located at the macrocell edge to neighbouring H-BTSs with more resource availability, thus enabling more even distribution of the network load across a particular topology.

### 12.4.3 Feasibility studies

We carry out preliminary feasibility studies to examine the time-varying characteristics of the macro-cellular BTSs daily traffic load, and the performance of the proposed hybrid FSO/RF systems under different weather conditions.

#### 12.4.3.1 Daily traffic profile of the BTS

The daily traffic pattern of a BTS can be approximated by a modified sinusoidal profile given by ([Hossain, Munasinghe et al.](#))

$$\lambda(t) = \frac{1}{2^\gamma} \left[ 1 + \sin\left(\frac{\pi}{12} + \varphi\right) \right]^\gamma + n(t) \quad (12.4-1)$$

where  $\lambda(t)$  denotes the instantaneous normalized traffic (in unit of Erlangs),  $\gamma = \{1, 3\}$  determines the abruptness of the traffic profile,  $\varphi$  is a uniform random variable with interval  $[0, 2\pi]$ , which determines the distribution of the traffic pattern among the BTSs, and  $n(t)$  is a Poisson distributed random process which models the random fluctuations of the traffic ([Hossain, Munasinghe et al.](#)).

Our simulation studies indicate that the above approximation does not model the random fluctuating behavior of the data traffic in a realistic manner, compared to real measurements ([Correia, Zeller et al. ; Heegaard 2007](#)). We suggest that the abruptness in the traffic profile can be generated as a sum of sinusoids, in which the modified expression is given by

$$\Lambda(t) = \sum_{i=1}^N \lambda_i(t). \quad (12.4-2)$$

In our studies, the traffic pattern is adequately modelled as a sum of eight sinusoids (i.e.,  $N = 8$ ).

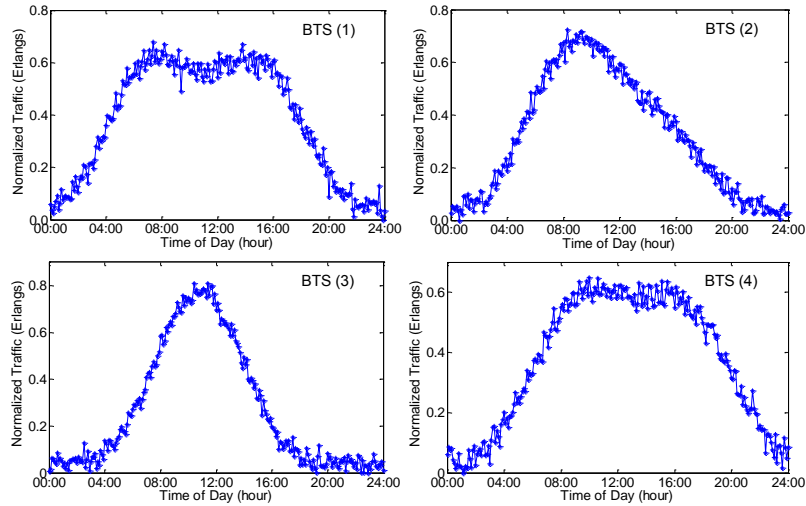


Figure 12.4-2: The resulting daily traffic pattern approximated for four BTSs

Figure 12.4-2 shows the daily traffic pattern approximated for four BTSs, in which it is noted that BTSs generally exhibit a lower traffic requirement in the early morning (0:00 hr to 4:00 hr) and the late evening (20:00 hr to 24:00 hr) with a normalized traffic  $< 0.3$  Erlangs, compared to peak hours during the day (i.e., 9:00 hr to 16:00 hr) with data traffic approaching the maximum load. These observations suggest that the proposed SWoD mechanism and cooperative inter-cell support would be of great benefit in promoting potential energy savings during the low traffic period, by placing idling/under-utilized RAIs and M-APs into sleep mode. Under heavy traffic scenarios, the proposed features of the H-BTS architecture would enable best decision-making for on-demand resource allocation, thereby maintaining even distribution of network load across a particular topology.

#### 12.4.3.2 Performance of the hybrid FSO/RF system

The outage probability  $P_{\text{out}}$  is an appropriate performance measure for the system under study, which denotes the probability that the instantaneous channel capacity  $C$ , for a channel state  $h$ , falls below a desired transmission rate  $R_0$ , given by the relation (Farid and Hranilovic 2007)

$$P_{\text{out}} = \text{Prob}(C(\text{SNR}(h)) < R_0) \quad (12.4-3)$$

Figure 12.4-3 depicts the  $P_{\text{out}}$  for the FSO and RF links at varying link distance  $L$ , under different weather conditions. The weather effects are characterized through numerous parameters including the visibility  $V$ , rain attenuation  $a_{\text{rain}}$ , and turbulence strength  $C_n^2$  (Farid and Hranilovic 2007; He and Schober 2009; Zhang, Hranilovic et al. 2009). An average transmit power of 40 mW is assumed for the sub-systems (Farid and Hranilovic 2007). Our results show that the FSO system is capable of maintaining a link range in excess of 2.0 km at  $P_{\text{out}} = 10^{-6}$  for  $R_0 = 0.5$  bits/channel use, under moderate (12.5 mm/h) and heavy (25.0 mm/h) rain conditions, while the RF link suffers significant link reduction with  $L < 0.5$  km. This reveals the vast potential of the FSO link in enabling a very high-speed wireless backhauling under the adverse effects of rain. Under the low visibility ( $V = 0.642$  km)

condition, the FSO link suffers severe performance degradation with  $L < 1.0$  km at  $P_{out} = 10^{-6}$ , and experiences system outage probability of 1 for  $L > 1.5$  km. The RF link can be employed as a complementary alternative to establish backhaul communication, albeit at a relatively lower data rate and link quality. Hence, the inherent advantage of both FSO and RF systems in complementing one another under the effects of rain and fog, respectively, reflects the symbiotic relationship between these technology options.

12.4.4 Conclusions

With the adoption of the fourth generation (4G) technologies, the green Metrozones concept presents a viable approach to address the non-negligible presence of power-hungry base transceiver stations (BTSs), and the mushrooming of metro access points (M-APs); and their contributions to the world’s carbon footprint. The *hybrid free-space optical and radio frequency (FSO/RF) system* can be integrated at the macro-cellular tier, to enable high-capacity, power-efficient wireless backhauling. Preliminary feasibility studies are carried out to examine the time-varying characteristics of the BTS daily traffic profile, and the performance of the proposed hybrid FSO/RF systems under different weather conditions.

12.5 Summary of chapter 12

The most important findings of chapter 12.2 are: i) unavailability of the hybrid system is about 3 orders of magnitude lower than that of the FSO alone link and ii) there is a very large yearly variability in hydrometeors.

Most important findings of chapter 12.3: i) maximal hop length of the hybrid system is determined by the loss of the FSO signal caused by *rain*; ii) this is by about 10% longer than that of the E-band-only system if IM/DD is used; and iii) but about 2-times longer in the case coherently detected BPSK or QPSK.

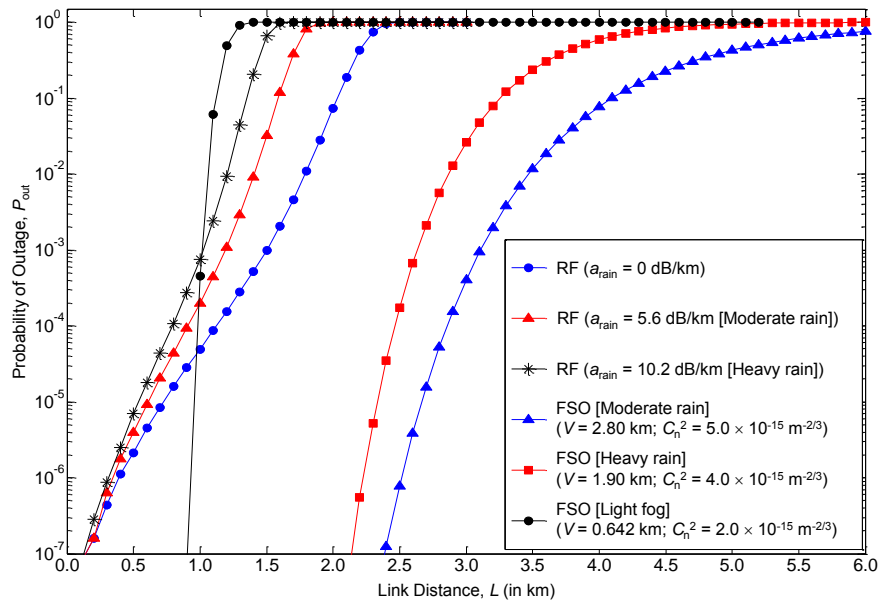


Figure 12.4-3 Outage probability of the FSO and RF links at varying link distance  $L$ , for  $R_0 = 0.5$  bits/channel use, under different weather conditions.

Most important findings of chapter 12.4 are: i) the green Metrozone concept introduced here is an important way to decrease the power consumption of wireless networks of ever increasing capacity; ii) application of FSO is an appropriate technology in realizing these concepts; and iii) hybrid FSO/RF systems are able to minimize the effects of hostile propagation characteristics.

## References

- [Akbulut & al., 2003] Akbulut, A., M. Efe, A. M. Ceylan, F. Ari, Z. Telatar, H. G. Ilk, and S. Tugac, "An Experimental Hybrid FSO/RF Communication System," *Proc. (393) Communication Systems and Networks* 2003. <http://www.actapress.com/PaperInfo.aspx?PaperID=13974&reason=500>.
- [Akyildiz, I. F., X. Wang, et al. (2005)]. "Wireless mesh networks: a survey." *Computer Networks* 47(4): 445-487.
- [Arbesser-Rastburg, 2002] B. Arbesser-Rastburg ed., Final Report, COST Action 255, Nordwijk, The Netherlands, ESA Publication, 2002.
- [Bloom, S. and W. Hartley (2002)]. The last-mile solution: hybrid FSO radio. Whitepaper, AirFiber Inc.
- [Borah, Voelz, 2009] D.K. Borah, D.G. Voelz, "Pointing error effects on communication links... J. Lightw. Technol., Vol. 27, No 18, pp. 3965-3973, Sep. 15, 2009.
- [Castanet, 2008] L. Castanet ed., Influence of the Variability of the Propagation Channel on Mobile, Fixed Multimedia and Optical Satellite Communications, Aachen, Germany, Shaker Verlag, 2008.
- [Consortium, E. (2010)]. "<https://www.ict-earth.eu/>."
- [Correia, L. M., D. Zeller, et al]. "Challenges and enabling technologies for energy aware mobile radio networks." *Communications Magazine, IEEE* 48(11): 66-72.
- [Farid, A. A. and S. Hranilovic (2007)]. "Outage Capacity Optimization for Free-Space Optical Links With Pointing Errors." *Lightwave Technology, Journal of* 25(7): 1702-1710.
- [Fehske, A., G. Fettweis, et al]. "The global footprint of mobile communications: The ecological and economic perspective." *Communications Magazine, IEEE* 49(8): 55-62.
- [Forster, C., I. Dickie, et al. (2009)]. Understanding the environmental impact of communication systems.
- [Frigyes, Csurgai-Horváth, 2010] I. Frigyes, L. Csurgai-Horváth, "Free-space optics and E-band radio: complementary techniques for Gbit/sec wireless", in *IEEE WCNC'10 Workshop*, April 2010, Sydney, NSW, Australia.
- [Gebhart & al, 2005] Gebhart, M., E. Leitgeb, S. S. Muhammad, B. Flecker, and C. Chlestil, "Measurement of light attenuation in dense fog conditions for FSO applications," *Proc. of SPIE*, vol. 5891, pp. 1-11, 2005.
- [GeSI, G. e.-S. I. (2008)]. SMART 2020: Enabling the low carbon economy in the information age.
- [GreenTouch, S. (2011)]. "<http://www.greentouch.org/>."
- [Hall, 1996] M. Hall ed., Final Report, COST Action 235, Luxembourg, European Commission Publishing, 1996.
- [He, B. and R. Schober (2009)]. "Bit-interleaved coded modulation for hybrid RF/FSO systems." *Communications, IEEE Transactions on* 57(12): 3753-3763.
- [Heegaard, P. E. (2007)]. Evolution of Traffic Patterns in Telecommunication Systems. *Communications and Networking in China, 2007. CHINACOM '07. Second International Conference on*.
- [Horváth, Frigyes, 2004] P. Horváth, I. Frigyes, "Application of the MIMO concept in millimeter-wave broadband wireless access networks", *Int. J. of Wireless Information Networks*, Vol. 11, No. 4, pp.217-225, October 2004. [http-1] <http://www.gigabeam.com>
- [Hossain, M. F., K. S. Munasinghe, et al]. A protooperation-based sleep-wake architecture for next generation green cellular access networks. *Signal Processing and Communication Systems (ICSPCS)*, 2010 4th International Conference on.
- [http-2] <http://www.systemsupportolutions.com/models.htm>
- [ITU-R F.592] Rec. ITU-R F.592-4 Vocabulary of terms for the fixed service. ITU, Geneva, Switzerland, 2008.
- [ITU-R P.1814] Rec. ITU-R P.1814 Prediction methods required for the design of terrestrial free-space optical links. ITU, Geneva, Switzerland, 2008.

- [ITU-R P.837, 2007] ITU-R, Recommendation P.837-5. Characteristics of precipitation for propagation modeling, International Telecommunication Union, Geneva, Switzerland, 2007.
- [Jones, D. (2008)]. "[http://www.lightreading.com/document.asp?doc\\_id=154434](http://www.lightreading.com/document.asp?doc_id=154434)."
- [Karagiannidis 2009] G.K. Karagiannidis & al., "Optical wireless communication with heterodyne detection...", *J. Lightw. Techn.*, Vol. 27, No 20, pp. 4440-4445, Oct. 15, 2009.
- [Kim, I. I. and E. Korevaar (2001)]. Availability of free space optics (FSO) and hybrid FSO/RF systems. Proc. SPIE, Optical Wireless Communications IV, Denver, CO, USA.
- [Korevaar & al. 2003] Korevaar, E. , I. I. Kim, and B. McArthur, "Atmospheric propagation characteristics of highest importance to commercial free space optics," *Proc. of SPIE*, vol. 4976, pp. 1-12, 2003.
- [Kvicera & al., 2008] Kvicera, V., M. Grabner, and O. Fiser, "Visibility and Attenuation Due to Hydrometeors at 850 nm Measured on an 850 m Path," *Proc. of the Sixth International Symposium on Communication Systems, Networks and Digital Signal Processing*, pp. 270-272, 2008.
- [Leitgeb & al., 2004] Leitgeb, E, M. Gebhart, U. Birnbacher, W. Kogler, and P. Schrotter, "High availability of hybrid wireless networks," *Proc. of SPIE*, vol. 5465, pp. 238-249, 2004.
- [Luna & al, 2009] R. Luna, D.K. Borah, H. Tapse, "Behaviour of hybrid optical/RF channels...", Proc. IEEE GLOBECOM 2009, paper # ONS-05/4, Honolulu, HA, 2009 Nov.-Dec.
- [Mahdy, A. and J. S. Deogun (2004)]. Wireless optical communications: a survey. Wireless Communications and Networking Conference, 2004. WCNC. 2004 IEEE.
- [McMillan & al, 1997] R. W. McMillan, R. A. Bohlander, W. J. Baldygo, Jr., "Millimeter-wave atmospheric turbulence", *Int. J. Infrared and Millimeter Waves*, Vol 18, No. 1, pp. 233-258, 1997.
- [Nadeem & al., 2009] Nadeem, F., V. Kvicera, M. S. Awan, E. Leitgeb, S. S. Muhammad, and G. Kandus, "Weather effects on hybrid FSO/RF communication link," *IEEE Journal on Selected Areas in Communications*, vol. 27, pp. 1687-1697, September 2009.
- [NEC (2009)]. Self organizing network: NEC's proposals for next-generation radio network management.
- [Networks, D. (2011)]. SoC-based mobile broadband evolution.
- [Networks, N. S. (2009)]. Self-organizing network (SON): Introducing the Nokia Siemens Networks SON Suite - an efficient, future-proof platform for SON.
- [Piamrat, K., A. Ksentini, et al. (2011)]. "Radio resource management in emerging heterogeneous wireless networks." *Computer Communications* 34(9): 1066-1076.
- [Prokes, 2009,] A. Prokes, "Modeling of atmospheric turbulence effect on terrestrial FSO links", *Radioengineering*, Vol 18, No1, pp. 42-47, April 2009.
- [Research, A. (2010)]. The emergence of compact base stations in the new RAN architecture paradigm.
- [Tipmongkolsilp, O., S. Zaghloul, et al. (2011)]. "The Evolution of Cellular Backhaul Technologies: Current Issues and Future Trends." *Communications Surveys & Tutorials*, IEEE 13(1): 97-113.
- [Tjelta & Breivik, 2009] T. Tjelta, T. O. Breivik, "Measured attenuation data and predictions for a gigabit radio link in the 80 GHz band", Proc. EUCAP-2009, pp. 657-661, Berlin, Germany, Apr. 2009.
- [Tuttlebee, W., S. Fletcher, et al. (2010)]. "Saving the planet - the rationale, realities and research of green radio." *The Journal of the Institute of Telecommunications Professionals* 4(3).
- [Vadgama, S. (2009)]. "Trends in green wireless access." *Fujitsu Sci. Tech. J.* 45(4): 404-408.
- [VCE, M. (2011)]. "<http://www.mobilevce.com/>."
- [Vereecken, W., W. Van Heddeghem, et al]. "Power consumption in telecommunication networks: overview and reduction strategies." *Communications Magazine*, IEEE 49(6): 62-69.
- [WiMAX.com. (2011)]. "<http://www.wimax.com/microwave-backhaul/backhaul-for-wimax-top-8-technical-considerations>."
- [Zhang, W., S. Hranilovic, et al]. (2009)]. "Soft-switching hybrid FSO/RF links using short-length raptor codes: design and implementation." *Selected Areas in Communications*, IEEE Journal on 27(9): 1698-1708.

## 13 THE WEATHER INFLUENCE AND ITS MITIGATION

(Zabih Ghassemlooy, Sujjan Rajbhandari, Wasiu Popoola, Joaquin Perez)

### 13.1 Overview

This chapter analyses the effect of atmospheric turbulence on the different modulation techniques used in FSO. The classical modulation technique used for FSO communications system is on-off keying (OOK). This is primarily because of the simplicity of its design and implementation. However the performance of OOK with a fixed threshold level is not optimal in atmospheric turbulence, as will be shown in the following section. In atmospheric turbulence an optimal performing OOK requires the threshold level to be adaptive in order to counter balance the irradiance fluctuation. On the other hand, pulse position modulation (PPM) with a soft decision decoding does not require an adaptive threshold and is predominantly used for optical communication links because of its enhanced power efficiency compared to the other baseband signalling [Kiasaleh 2005; Razavi and Shapiro 2005; Wilson, Brandt-Pearce et al. 2005; Djordjevic, Vasic et al. 2006a; Hemmati 2006; Sheikh Muhammad, Gappmair et al. 2006]. The PPM modulation technique, however, requires a complex transceiver design due to requirement of slot and symbol synchronisation and suffers from a higher bandwidth requirement. The subcarrier intensity modulation (SIM) on the other hand does not require an adaptive threshold and offers bandwidth efficiency in comparisons to PPM. However, SIM suffers from a high peak-to-average power ratio (PAPR), which translates into poor power efficiency. Choosing a modulation scheme for a particular application therefore entails trade-offs among these listed factors.

### 13.2 On-Off Keying

OOK is the dominant modulation scheme employed in commercial terrestrial FSO communications systems. This is primarily due to its simplicity and resilience to the innate nonlinearities of the laser and the external modulator. OOK can use either non-return-to-zero (NRZ) or return-to-zero (RZ) pulse formats. In NRZ-OOK, the transmission of an optical pulse of peak power  $P_T$  represents a digital symbol '1' and a digital symbol '0' is represented by an empty bit durations. The finite duration of the optical pulse is the same as the symbol or bit duration  $T_b$ . With OOK-RZ, the pulse duration is lower than the bit duration, giving an improvement in power efficiency over NRZ-OOK at the expense of an increased bandwidth requirement.

#### 13.2.1 OOK in a Gaussian Atmospheric Optical Channel

With large signal photoelectron counts, and by taking the detection thermal noise into account, the generated signal current probability distribution can be approximated as the Gaussian distribution. Without any loss of generality, the receiver area may be normalised to unity such that the optical power may be represented by the optical intensity,  $I$ . If  $R$  represents the responsivity of the PIN photodetector, the received signal in an OOK system is therefore given by:

$$i(t) = RI \left[ 1 + \sum_{j=-\infty}^{\infty} d_j g(t - jT_b) \right] + n(t) \quad (13.2-1)$$

where  $n(t) \sim N(0, \sigma^2)$  is the additive white Gaussian noise,  $g(t - jT_b)$  is the pulse shaping function and  $d_j = [-1, 0]$ . At the receiver, the received signal is fed into a threshold detector which compares the received signal with a pre-determined threshold level. A digital symbol '1' is assumed to have been received if the received signal is above the threshold level and '0' otherwise.

The bit error probability in Gaussian channel with a threshold value of  $i_{th}$  is given as:

$$P_{ec} = Q\left(\frac{i_{th}}{\sigma}\right) \quad (13.2-2)$$

where  $Q(x) = 0.5\text{erfc}(x/\sqrt{2})$ .

In the presence of atmospheric turbulence, the threshold level is no longer fixed midway between the signal levels representing symbols '1' and '0'. The marginal probability  $p(i/1)$  is then modified by averaging the conditional pdf of  $i(t)$  over the scintillation statistics. Note that scintillation does not occur when no pulse is transmitted.

$$p(i/1) = \int_0^{\infty} p(i/1, I) p(I) dI \quad (13.2-3)$$

Assuming equiprobable symbol transmission and invoking the maximum a posteriori symbol-by-symbol detection, the likelihood function  $L$ , becomes [Popoola, Ghassemlooy et al. 2008]:

$$L = \int_0^{\infty} \exp\left[\frac{-(i - RI)^2 - i^2}{2\sigma^2}\right] p(I) dI \quad (13.2-4)$$

Fig. 13.2-1 below shows the plot of  $\log(L)$  against the average photocurrent  $i$ , at various levels of scintillation and noise variance of  $10^{-2}$ . The threshold level, as would be expected, is at the point where  $L = 1$  (i.e. when  $\log(L) = 0$ ).

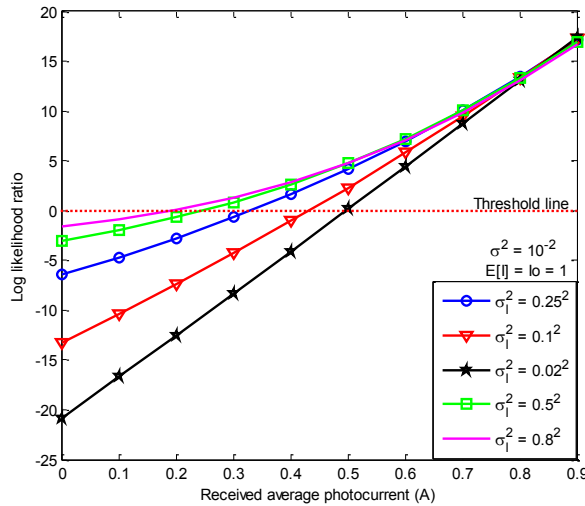


Figure 13.2-1: The likelihood ratio against the received signal for different turbulence levels and noise variance of  $10^{-2}$ .

In Fig. 13.2-2, the BER is plotted against the normalised SNR at various levels of scintillation including when for a fixed threshold value of 0.5 and adaptive threshold level obtained from (13.2-4). This is intended to show the effect of turbulence strength on the amount of SNR required to maintain a given error performance level. With a fixed threshold, the BER reaches a floor at a BER that is greater than  $10^{-4}$ , meaning that a lower BER is not achievable at the specified low scintillation level. From this graph, it can be inferred that atmospheric turbulence: i) causes SNR penalty, for example  $\sim 26$  dB of SNR is needed to achieve a BER of  $10^{-6}$  due to a very weak scintillation of strength  $\sigma_l^2 = 0.25^2$ , this however increases by over 20 dB as the scintillation strength increases to  $\sigma_l^2 = 0.7^2$ ; and ii) implies that adaptive threshold will be required to avoid a BER floor in the system performance.

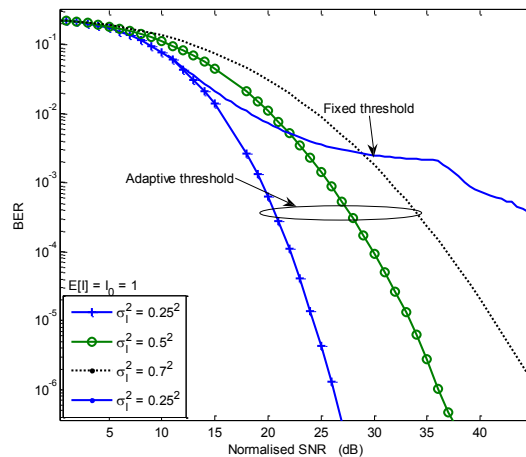


Figure 13.2-2: BER of OOK-FSO with fixed and adaptive threshold at various levels of scintillation,  $\sigma_l = [0.2, 0.5, 0.7]$  and  $I_0 = 1$ .

The above results illustrate that for the OOK modulated FSO system to perform at its best, the receiver will require knowledge of both the fading strength and the noise level. This can be resolved by integrating into the system an intensity estimation network which can

predict the scintillation level based on past events. The implementation of this is not trivial, and as such, commercial FSO designers tend to adopt the fixed threshold approach and include a sufficiently large link margin in the link budget to cater for turbulence induced fading [Willebrand and Ghuman, 2002].

### 13.3 Pulse Position Modulation

PPM is an orthogonal modulation technique where each block of  $\log_2 M$  data bits is mapped to one of  $M$  possible symbols. Each symbol consists of a pulse of constant power  $P_t$ , occupying one slot, along with  $M-1$  empty slots. The position of the pulse corresponds to the decimal value of the  $\log_2 M$  data bits. Hence, the information is encoded by the position of the pulse within the symbol. The slot duration,  $T_{s\_ppm}$ , is related to the bit duration by the following expression:

$$T_{s\_ppm} = \frac{T_b \log_2 M}{M} \quad (13.3-1)$$

The transmitted waveforms for 16-PPM and OOK are shown in Fig. 13.3-1.

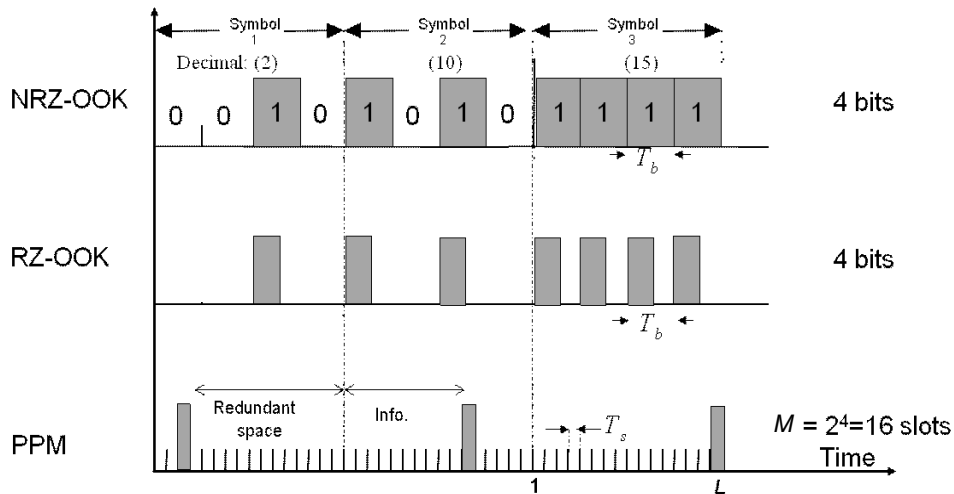


Figure 13.3-1: Time waveforms for 4-bit OOK and 16-PPM.

A PPM receiver will require both slot and symbol synchronisation in order to demodulate the information encoded on the pulse position. Nevertheless, because of its superior power efficiency, PPM is an attractive modulation technique for optical wireless communication systems particularly in deep space laser communication applications [Hemmati, 2007]. Assuming that complete synchronisation is maintained between the transmitter and receiver at all times, the optical receiver detects the transmitted signal by attempting to determine the energy in each possible time slot. It then selects the signal which corresponds to the maximal energy. In direct photodetection, this is equivalent to “counting” the number of released electrons in each  $T_s$  interval. The photo count per PPM slot can be obtained from:

$$K_s = \frac{\eta \lambda P_r T_{s\_ppm}}{hc} \quad (13.3-2)$$

where  $P_r$  is the received optical power during a slot duration. For a moderately high received signal, as is the case in commercial and short range FSO systems, the BER conditioned on  $K_s$  is given by [Gagliardi and Karp, 1995]:

$$P_{ec} = Q \left( \sqrt{\frac{(\bar{G}q)^2 K_s^2}{(\bar{G}q)^2 F(K_s + 2K_{Bg}) + 2\sigma_{th}^2}} \right) \quad (13.3-3)$$

where the parameters are defined as:

$K_{Bg} = \eta\lambda P_{Bg} T_s / hc$	Average photon count per PPM slot due to the background Radiation of power $P_{Bg}$
$\bar{G}$	Average APD gain
$q$	Electronic charge
$F \approx 2 + \zeta\bar{G}$	Noise factor of the APD
$\zeta$	APD ionisation factor
$\sigma_{Th}^2 = (2\kappa T_e q / R_L)(T_{s\_ppm})$	Equivalent thermal noise count within a PPM slot duration [Gagliardi and Karp, 1995]
$R_b = 1/T_b$	Bit rate.
$\kappa$	Boltzmann's constant
$R_L$	Equivalent load resistance

In the presence of log normal atmospheric turbulence, the unconditional BER for a binary PPM modulated FSO obtained by averaging (13.3-3) over the scintillation statistics can be approximated as [Kiasaleh, 2005]:

$$P_e \approx \frac{1}{\sqrt{\pi}} \sum_{i=1}^n w_i Q \left( \frac{\exp(2(\sqrt{2}\sigma_k x_i + m_k))}{F \exp(\sqrt{2}\sigma_k x_i + m_k) + K_n} \right) \quad (13.3-4)$$

where  $[w_i]_{i=1}^n$  and  $[x_i]_{i=1}^n$  are the weight factors and the zeros of an  $n^{\text{th}}$  order Hermite polynomial. These values are contained in Appendix A for a 20<sup>th</sup> order Hermite polynomial.  $m_k$  represents the mean of  $\ln(K_s)$ ,  $K_n = (2\sigma_{Th}^2 / (\bar{G}q)^2) + 2FK_{Bg}$  and  $\sigma_k^2 = \ln(\sigma_N^2 + 1)$ . It is noteworthy that the fluctuation of the mean count,  $K_s$ , is brought about by the atmospheric turbulence and its ensemble average is given by the following [Kiasaleh, 2005]:

$$E[K_s] = \exp\left(\frac{\sigma_k^2}{2} + m_k\right) \quad (13.3-5)$$

For an  $M$ -PPM system, the BER denoted by  $P_e^M$  has an upper bound given by [Kiasaleh, 2005]:

$$P_e^M \leq \frac{M}{2\sqrt{\pi}} \sum_{i=1}^n w_i Q \left( \frac{\exp(2(\sqrt{2}\sigma_k x_i + m_k))}{F \exp(\sqrt{2}\sigma_k x_i + m_k) + K_n} \right) \quad (13.3-6)$$

The BER performance of a binary PPM modulated FSO is shown in Fig. 13.3-2 at different levels of scintillation. The extension of the result is straight forward from (13.3-6) and hence not presented here.

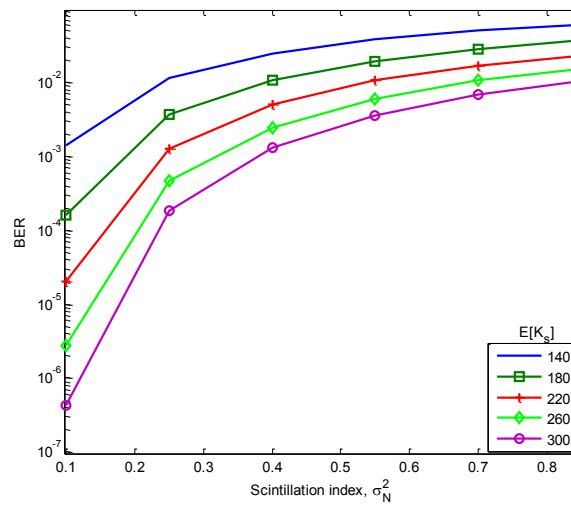


Figure 13.3-2: Binary PPM BER as a function of scintillation index for  $K_{Bg} = 10$ ;  $T_e = 300$  K,  $\zeta = 0.028$ ,  $R_b = 155$  Mbps and  $\bar{g} = 150$ .

As expected, an increase in the atmospheric scintillation results in an increase in the required signal level to achieve a given BER. Increasing the signal strength can be used to minimise the scintillation effect at a low scintillation index, but as turbulence strength increases, it is observed that the BERs all tend towards a high BER asymptotic value.

## 13.4 Subcarrier Intensity Modulation

SIM is a technique borrowed from the very successful multiple carrier radio frequency (RF) communications already deployed in applications such as digital television, local area networks (LANs), asymmetric digital subscriber line (ADSL), 4G communication systems and optical fibre communications [Ohtsuki, 2003; Djordjevic and Vasic, 2006b]. For the seamless integration of FSO systems into present and future networks, which already harbour subcarrier modulated (or multiple carrier) signals, the study of subcarrier modulated FSO is thus imperative. The SIM avoids the need for an adaptive threshold required by optimum performing OOK modulated FSO [Popoola, Ghassemlooy et al. 2007]. However, there is the possibility of signal distortions due to inherent laser non-linearity and signal clipping due to over-modulation. The SIM suffer from high PAPR and several methods have been researched and documented [You and Kahn 2001; Teramoto and Ohtsuki 2003; Teramoto and Ohtsuki 2005] to improve the poor power efficiency of SIM.

### 13.4.1 SIM Generation and Detection

Fig. 13.4-1 illustrates the system block diagram of a SIM-FSO with  $N$  subcarriers. In optical SIM links an RF subcarrier signal  $m(t)$ , pre-modulated with the source data  $d(t)$ , is used to modulate the intensity  $P_T$ , of the optical source - a continuous wave laser diode. The serial-to-parallel converter distributes the incoming data across the  $N$ -subcarriers. Each subcarrier carries a reduced symbol rate but the aggregate must be equal to the symbol rate of  $d(t)$ . Since the subcarrier signal,  $m(t)$ , is sinusoidal, having both positive and negative values,

a DC level  $b_0$  is added to  $m(t)$  before it is used to directly drive the laser diode – to avoid any signal clipping.

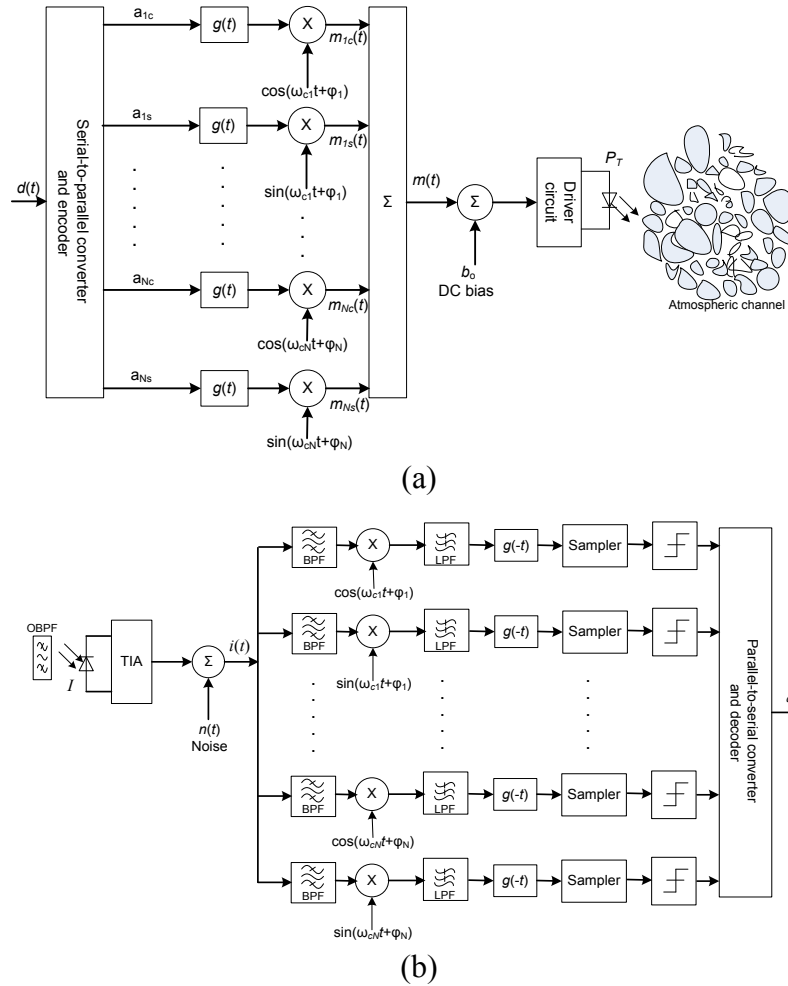


**Figure 13.4-1:** Block diagram of SIM-FSO: (a) transmitter, and (b) receiver. TIA – trans-impedance, OBPF – Optical band pass filter.

The following gives the general expression for  $m(t)$  in the  $N$ -SIM-FSO system:

$$m(t) = \sum_{i=1}^N m_i(t) \tag{13.4-1}$$

During one symbol duration, each RF subcarrier signal is generally represented by:

$$m_i(t) = g(t)a_{ic} \cos(\omega_{ci}t + \varphi_i) + g(t)a_{is} \sin(\omega_{ci}t + \varphi_i) \tag{13.4-2}$$

where  $g(t)$  is the pulse shaping function, and the subcarrier angular frequency and phase are represented by  $[\omega_{ci}, \varphi_i]_{i=1}^N$ . It follows that each subcarrier can be modulated by any standard RF digital/analogue modulation technique, such as QAM,  $M$ -PSK,  $M$ -FSK and  $M$ -ASK. Using direct detection at the receiver, the incoming optical radiation,  $P_R$ , is converted into an electrical signal,  $i(t)$ . This is followed by a standard RF demodulator to recover the transmitted symbol as shown in Fig. 13.4-1(b). By normalising the receiver area to unity and representing the received power by irradiance,  $I$ , the received signal can be modelled as:

$$i(t) = RI[1 + \xi m(t)] + n(t) \tag{13.4-3}$$

where the optical modulation index  $\xi = \left| \frac{m(t)}{i_B - i_{Th}} \right|$ .

The electrical band pass filter (BPF) with a minimum bandwidth of  $2R_b$  performs the following functions: selection of the individual subcarrier for demodulation; reduction of the noise power; and suppression of any slow varying  $RI$  component present in the received signal. For a subcarrier at  $\omega_{ci}$  the received signal is:

$$i(t) = I_{comp} + Q_{comp} \quad (13.4-4)$$

where

$$I_{comp} = RI\xi g(t)a_{ic} \cos(\omega_{ci}t + \varphi_i) + n_I(t) \quad (13.4-5a)$$

$$Q_{comp} = -RI\xi g(t)a_{is} \sin(\omega_{ci}t + \varphi_i) + n_Q(t) \quad (13.4-5a)$$

and  $n_I(t)$  and  $n_Q(t)$  are the independent additive white Gaussian noise (AWGN) with a zero mean and a variance  $\sigma^2$ . The quadrature components  $I_{comp}$  and  $Q_{comp}$  are down converted by the reference signals  $\cos\omega_c t$  and  $\sin\omega_c t$ , respectively, and applied to the standard receiver architecture. The electrical low pass filters, which are part of the standard RF receiver, remove any out of band (unwanted) signals from the down converted signal and then pass it onto the decision circuit. In the case of phase shift keying modulated subcarrier, the decision circuit estimates the phase of the received signal and decides which symbol has been received. By adopting the approach in [Proakis, 2004], the conditional BER expressions can be deduced.

### 13.4.2 Bit Error Probability Analysis of SIM-FSO

In this section the BER analysis is presented in a turbulent atmospheric channel, the turbulence induced irradiance fluctuation considered in this section is based on the log normal model. A single BPSK pre-modulated subcarrier will first be considered and this will be followed by the  $M$ -PSK and then the DPSK modulated subcarrier.

#### 13.4.2.1 BPSK Modulated Subcarrier

In this section a single BPSK pre-modulated subcarrier  $m(t) = g(t)a_c \cos(\omega_c t + \varphi)$ , over a symbol duration, where  $a_c = [-1,1]$  represents the data symbols '0' and '1' is presented. By employing a coherent demodulation at the subcarrier level, the symbol-by-symbol detection is carried out by multiplying the received signal, by a locally generated RF signal of the same frequency  $\omega_c$ , and phase as follows. Without any loss of generality, the subcarrier phase is equated to zero, that is  $\varphi = 0$ . The coherent demodulator output  $i_D(t)$  is then given by:

$$\begin{aligned} i_D(t) &= I_{comp} \times \cos(\omega_c t) \\ &= \frac{R\xi I a_c g(t)}{2} [1 + \cos(2\omega_c t)] + n(t) \cos(\omega_c t) \end{aligned} \quad (13.4-6)$$

Passing  $i_D(t)$  through a low pass filter with a bandwidth of  $1/T$  suppresses the  $\cos(2\omega_c t)$  term without distorting the information bearing signal. This also reduces the noise variance at the output of the coherent demodulator filter to half its value at the input of the demodulator. Equation (13.4-6) therefore reduces to:

$$i_D(t) = \frac{R\xi I a_c g(t)}{2} + n_D(t) \quad (13.4-7)$$

where the additive noise  $n_D(t) \sim N(0, \sigma^2/2)$ . Assuming an equiprobable data transmission such that  $p(0) = p(1) = 1/2$ , the probability of error conditioned on the received irradiance becomes:

$$\begin{aligned} P_{ec} &= p(1)p(e/1) + p(0)p(e/0) \\ &= 0.5[p(e/1) + p(e/0)] \end{aligned} \quad (13.4-8)$$

The marginal probabilities are given by:

$$p(e/1) = \int_{-\infty}^0 \frac{1}{\sqrt{\pi\sigma^2}} \exp\left\{-\frac{(i_D(t) - \mathcal{K})^2}{\sigma^2}\right\} di_D(t) \quad (13.4-9a)$$

$$p(e/0) = \int_0^{\infty} \frac{1}{\sqrt{\pi\sigma^2}} \exp\left\{-\frac{(i_D(t) + \mathcal{K})^2}{\sigma^2}\right\} di_D(t) \quad (13.4-9b)$$

where  $\mathcal{K} = IR\xi/2$  and  $g(t) = 1$  for  $0 \leq t \leq T$  and zero elsewhere. Here both binary symbols '1' and '0' are affected by the irradiance fluctuation since the optical source is on during the transmission of both data symbols '1' and '0'. This is in contrast to the OOK signalling technique where irradiance fluctuation only affects the data symbol '1'. Based on the antipodal nature of (13.4-7), the decision threshold level can hence be fixed at the zero mark. This zero level threshold is irradiance independent and hence not affected by the irradiance fluctuation caused by the atmospheric turbulence. From the foregoing and the apparent symmetry of (13.4-9a), the BER conditioned on the received irradiance can now be written as:

$$\begin{aligned} P_{ec} &= \int_0^{\infty} \frac{1}{\sqrt{\pi\sigma^2}} \exp\left\{-\frac{(i_D(t) + \mathcal{K})^2}{\sigma^2}\right\} di_D(t) \\ &= 0.5 \operatorname{erfc}(\mathcal{K}/\sigma) = Q\left(\frac{\mathcal{K}\sqrt{2}}{\sigma}\right) \end{aligned} \quad (13.4-10)$$

At the input of the subcarrier coherent demodulator, the electrical SNR per bit is given by:

$$\gamma(I) = \frac{(\xi RI)^2 P_m}{\sigma^2} \quad (13.4-11)$$

where  $P_m = \frac{A^2}{2T} \int_0^T g^2(t) dt$ , from which  $\sqrt{\gamma(I)} = \sqrt{2} \mathcal{K}/\sigma$ . Equation (13.4-11) can now be expressed in terms of the SNR at the demodulator input as:

$$P_{ec} = Q(\sqrt{\gamma(I)}) \quad (13.4-12)$$

The unconditional probability  $P_e$ , is obtained by averaging (13.4-12) over the log normal irradiance fluctuation statistics to obtain the following:

$$P_e = \int_0^{\infty} P_{ec} p(I) dI \quad (13.4-13a)$$

$$P_e = \int_0^{\infty} Q(\gamma(I)) \frac{1}{I\sqrt{2\pi\sigma_l^2}} \exp\left\{-\frac{[\ln I/I_0 + \sigma_l^2/2]^2}{2\sigma_l^2}\right\} dI \quad (13.4-13b)$$

A closed form solution of equation (13.4-13a) does not exist and using the numerical integration could result in truncating its upper limit. Also, the presence of the argument of the Q-function at the lower limit of the Q-function integral always poses analytical problems [Simon and Alouini, 2004]. By combining an alternative representation of the Q-function given by (13.4-14) with the Gauss-Hermite quadrature integration approximation of (13.4-15), the analytical difficulty involved solving (13.4-13a) can be circumvented.

$$Q(y) = \frac{1}{\pi} \int_0^{\pi/2} \exp\left(-\frac{y^2}{2\sin^2(\theta)}\right) d\theta, \quad \text{for } y > 0, \quad (13.4-14)$$

$$\int_{-\infty}^{\infty} f(x) \exp(-x^2) dx \cong \sum_{i=1}^n w_i f(x_i) \quad (13.4-15)$$

where  $[w_i]_{i=1}^n$  and  $[x_i]_{i=1}^n$ , are the weight factors and the zeros of an  $n^{\text{th}}$  order Hermite polynomial,  $He_n(x)$  (2009). The degree of accuracy of (13.4-14) depends on the order  $n$  of the Hermite polynomial. By invoking a change of variable,  $y = \frac{\ln(I/I_0) + \sigma_l^2/2}{\sqrt{2}\sigma_l}$  in (13.4-13a) and combining this with (13.4-14) and (13.4-15), the unconditional BER given by (13.4-13a) can be reduced to the following form:

$$P_e \cong \frac{1}{\pi} \int_0^{\pi/2} \frac{1}{\sqrt{\pi}} \sum_{i=1}^n w_i \exp\left(-\frac{K_0 \exp(2K_1[\sqrt{2}\sigma_l x_i - \sigma_l^2/2])}{2\sin^2(\theta)}\right) d\theta \quad (13.4-16)$$

$$P_e \cong \frac{1}{\sqrt{\pi}} \sum_{i=1}^n w_i Q\left(\sqrt{K_0} \exp(K_1[\sqrt{2}\sigma_l x_i - \sigma_l^2/2])\right) \quad (13.4-17)$$

The values of  $K_1$  and  $K_0$  are as given in Table 13.4-1 for different noise limiting conditions.

Table 13.4-1: Values of  $K_1$  and  $K_0$  for different noise limiting conditions

	Noise limiting conditions			
	Quantum limit	Thermal noise	Background noise	Thermal and background noise
$K_0$	$\frac{\xi^2 R I_0 P_m}{2qR_b}$	$\frac{(\xi R I_0)^2 P_m R_L}{4kT_e R_b}$	$\frac{(\xi I_0)^2 R P_m}{2qR_b(I_{sky} + I_{sun})}$	$\frac{(\xi R I_0)^2 P_m}{(\sigma_{Bg}^2 + \sigma_{Th}^2)}$
$K_1$	0.5	1	1	1

In order to keep the optical source (laser) within its linear dynamic range and avoid signal clipping distortion, the condition  $|\xi m(t)| \leq 1$  must always hold. For a given value of  $\xi$ , this places an upper bound on the amplitude of each subcarrier. The BER given by (13.4-17) is plotted against the normalised SNR for different noise limiting conditions in Fig. 13.4-2, based on the simulation parameters given in Table 13.4-2. The figure illustrates clearly that

for an FSO link with a suitable optical BPF and a narrow FOV detector, the system performance is limited by thermal noise. Moreover, under this thermal noise limited condition, the SIM-FSO still requires about additional 30 dB of SNR compared with the theoretical quantum limit.

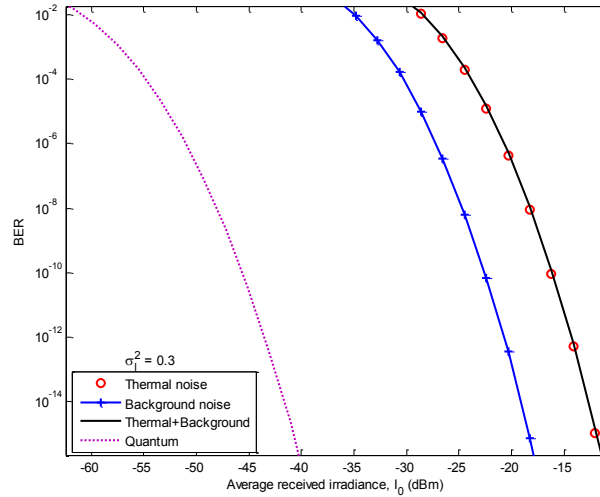


Figure 13.4-2: The BER against the average received irradiance in weak turbulence under different noise limiting conditions for  $R_b = 155$  Mbps and  $\sigma_1^2 = 0.3$ .

Table 13.4-2: Simulation parameters

Parameter	Value
Symbol rate $R_b$	155 Mbps
Spectral radiance of the sky $N(\lambda)$	$10^{-3}$ W/cm <sup>2</sup> μmSr
Spectral radiant emittance of the sun $W(\lambda)$	0.055 W/cm <sup>2</sup> μm
Optical band-pass filter bandwidth $\Delta\lambda$ @ $\lambda = 850$ nm	1 nm
PIN photodetector field of view (FOV)	0.6 rad
Radiation wavelength $\lambda$	850 nm
Number of subcarriers $N$	1
Link range $L$	1 km
Index of refraction structure parameter $C_n^2$	$0.75 \times 10^{-14}$ m <sup>-2/3</sup>
Load resistance $R_L$	50 Ω
PIN photodetector responsivity $\mathfrak{R}$	1
Operating temperature $T_e$	300 K
Optical modulation index $\xi$	1

#### 13.4.2.2 $M$ -ary PSK Modulated Subcarrier

Here the data symbols which comprise of  $\log_2 M$  binary digits are mapped onto one of the  $M$  available phases on each subcarrier signal,  $m(t)$ . Based on the subcarrier coherent demodulation and by following the analytical approach given in [Proakis, 2004], the following conditional BER expressions are obtained:

$$P_{ec} \approx \frac{2}{\log_2 M} Q \left( \sqrt{(\log_2 M) \gamma(I)} \sin(\pi/M) \right) \quad \text{for } M - \text{PSK}, M \geq 4 \quad (13.4-18a)$$

$$P_{ec} = \frac{2(1 - 1/\sqrt{M})}{\log_2 M} Q \left( \sqrt{\frac{3 \log_2 M \gamma(I)}{2(M-1)}} \right) \quad \text{for } M - \text{QAM}, \log_2 M \text{ even} \quad (13.4-18b)$$

The unconditional BER,  $P_e$ , is thus obtained in a similar fashion, by averaging the conditional bit error rate over the atmospheric turbulence statistics. The resulting BER

expression (13.4-19) for  $M$ -PSK has no closed form solution and can only be evaluated numerically.

$$P_e \cong \frac{2}{\log_2 M} \int_0^{\infty} Q\left(\sqrt{\gamma(I)} \log_2 M \sin(\pi/M)\right) p(I) dI \quad (13.4-19)$$

Whenever a subcarrier coherent detection is used, there is always an ambiguity associated with the estimation of the absolute phase of the subcarrier signal [Proakis, 2004]. This poses an implementation challenge for the subcarrier coherent demodulation based systems, this can however be solved by considering a differential phase shift keying (DPSK) based SIM-FSO system.

### 13.4.3 SIM-FSO Performance in Gamma-Gamma and Negative Exponential Atmospheric Channels

To obtain the unconditional BER in a gamma-gamma turbulent atmospheric channel, the irradiance fluctuation statistics in the previous section is replaced appropriately by the gamma-gamma pdf. For a BPSK pre-modulated subcarrier, the unconditional BER now becomes:

$$P_e = \int_0^{\infty} Q(\sqrt{\gamma(I)}) \frac{2(\alpha\beta)^{(\alpha+\beta)/2}}{\Gamma(\alpha)\Gamma(\beta)} I^{\left(\frac{\alpha+\beta}{2}\right)-1} K_{\alpha-\beta}(2\sqrt{\alpha\beta}I) dI \quad (13.4-20)$$

This BER expression can only be evaluated numerically as it does not have a closed form solution. The values of the parameters  $\alpha$  and  $\beta$ , which are used to describe the turbulence strength, are as given in Table 13.4-3.

Table 13.4-3: Fading strength parameters for gamma-gamma turbulence model

Parameter	Turbulence regime		
	Weak	Moderate	Strong
$\sigma_I^2$	0.2	1.6	3.5
$\alpha$	11.6	4.0	4.2
$\beta$	10.1	1.9	1.4

In the limit of strong turbulence, that is, in the saturation regime and beyond, the BER is obtained by replacing the pdf in the conditional BER by the fully developed speckle (negative exponential) pdf discussed in Chapter Three. By applying the alternative representation of  $Q(\cdot)$  given by (13.4-14) the unconditional BER in the fully developed speckle regime is derived as:

$$P_e = \frac{1}{\pi I_0} \int_0^{\pi/2} \int_0^{\infty} \exp\left(-\frac{(\xi RI)^2}{4\sigma^2 \sin^2 \vartheta} - \frac{I}{I_0}\right) dI d\vartheta \quad (13.4-21)$$

The multiple integration involved in (13.4-21) can be conveniently circumvented, and doing this reduces the BER expression  $P_e$ , to the following:

$$P_e = \frac{1}{\pi} \int_0^{\pi/2} \sqrt{\pi \mathcal{K}_0(\vartheta)} \exp(\mathcal{K}_0(\vartheta)) \operatorname{erfc}(\sqrt{\mathcal{K}_0(\vartheta)}) d\vartheta \quad (13.4-22)$$

where  $\mathcal{K}_0(\vartheta) = (\sigma \sin(\vartheta)/\xi R)^2$  and  $\text{erfc}(\cdot)$  is the complementary error function. The following upper bound, given by (13.4-16), is then obtained by maximising the integrand with the substitution of  $\vartheta = \pi/2$  in (13.4-22).

$$P_e \leq \sqrt{\pi \mathcal{K}_0} \exp(\mathcal{K}_0) Q(\sqrt{2\mathcal{K}_0}) \tag{13.4-23}$$

where  $\mathcal{K}_0 = (\sigma / \xi R)^2$ . From these BER expressions, the error performance of the system can be predicted for any given value of SNR and turbulence strength (or link range). The numerical simulations of the BER expressions (13.4-20), (13.4-22) and the upper bound (13.4-23) are shown in Fig. 13.4-3, where the  $P_e$  is plotted against the normalised SNR under different turbulence regimes.

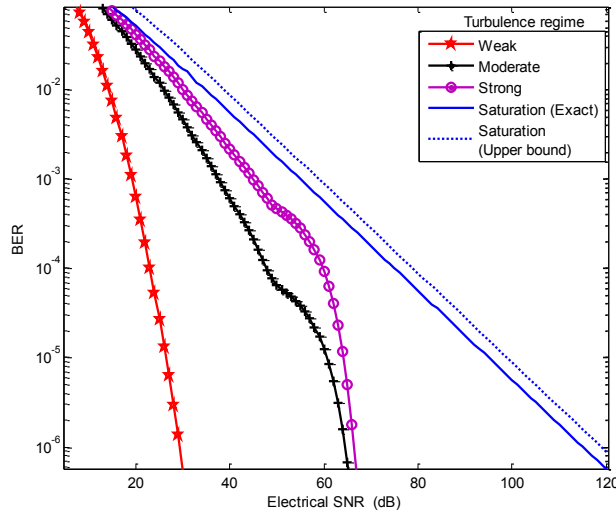


Figure 13.4-3: BER performance against the normalised electrical SNR across all of turbulence regimes based on gamma-gamma and negative exponential modes.

For instance, to achieve a BER of  $10^{-6}$  in a weak atmospheric turbulence, the required SNR is  $\sim 29$  dB and this rises to  $\sim 65$  dB and  $\sim 67$  dB, respectively for moderate and intermediate regimes. While in the saturation regime, a staggering  $\sim 115$  dB (the upper bound value is 4 dB higher) is required to achieve the same level of error performance (i.e. BER of  $10^{-6}$ ). Achieving a BER lower than  $10^{-6}$  in the saturation regime requires a phenomenal increase in SNR as seen in Fig. 13.4-3. It is noteworthy that the normalised SNR is in the electrical domain and it is based on the average received irradiance,  $E[I]$ . Also the ‘kinks’ observed in the curves for strong and moderate turbulence are due to the numerical integration process.

On order to compare the error performance BPSK-SIM with an OOK modulated FSO system of the same average transmitted optical power, the unconditional BER of the OOK-FSO is modified to become:

$$P_e = 0.5 \left[ \int_{i_{th}}^{\infty} \frac{1}{\sqrt{\pi\sigma^2}} \exp(-i^2/\sigma^2) di + \int_0^{\infty} \int_0^{i_{th}} \frac{1}{\sqrt{\pi\sigma^2}} \exp\left[-\frac{(i - 2RI)^2}{\sigma^2}\right] p(I) di dI \right] \tag{13.4-24}$$

In Fig. 13.4-4, the BER performances of the OOK system employing adaptive (optimum) and fixed threshold values of 0.05 and 0.8 are shown alongside that of BPSK-SIM in a weak

turbulent atmospheric fading. Although the optimum OOK is marginally superior to BPSK-SIM under the stated conditions, as it requires 1.6 dB electrical SNR less at a BER of  $10^{-6}$ , it does require an accurate knowledge of both the additive noise and fading levels to achieve this performance. With the threshold fixed at say 0.05, the OOK requires about 7 dB electrical SNR more than BPSK-SIM at a BER of  $10^{-6}$ . Also, the BER performance of OOK with a fixed threshold level exhibits a BER floor as shown in Fig. 13.4-4 for  $i_{th} = 0.8$ . The SIM is therefore recommended in atmospheric turbulence channels as against the fixed threshold OOK currently used in commercial terrestrial FSO systems.

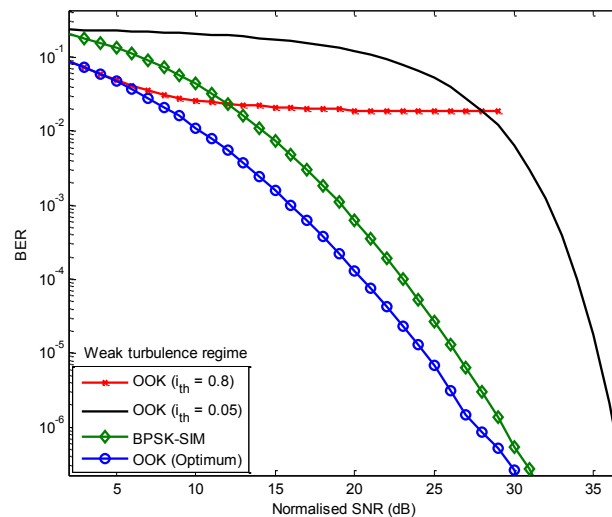


Figure 13.4-4: Error performance of BPSK SIM and OOK with fixed and adaptive threshold based FSO in weak turbulence regime modeled using gamma-gamma distribution.

#### 13.4.4 Comparison of Modulation Schemes

In order to prove the validity of the performance dependency of different modulation schemes under the influence of turbulence, three modulation schemes OOK, PAM and BPSK are studied under the same turbulence level. The  $Q$ -factor against the scintillation index of  $\{0-0.2\}$  for the OOK-NRZ, 4-PAM and BPSK at the same transmitted power level of -1.32 dBm is shown in Fig. 13.4-5(a). It can be observed that the  $Q$ -factor decreases with the increase in turbulence level for both OOK-NRZ and 4-PAM modulation due to random fluctuation of received signal. Notice that the  $Q$ -factor linearly decreases with the logarithmic scale of the scintillation index. However,  $Q$ -factor for BPSK decrease less sharply and offer much improved performance compared to OOK and PAM.

In order to established performance gain for OOK, the normalised  $Q$ -factor against scintillation index is illustrated in Fig. 13.4-5(b). The  $Q$ -factor is normalized using the average  $Q$ -factor of the OOK-NRZ at given scintillation index value. The ratio of  $Q$ -factor for the OOK and PAM does not vary significantly for the range of scintillation index. However, the  $Q$ -factor of the BPSK diverges from the  $Q$ -factor of OOK as the level of turbulence increases and the BPSK offers  $\sim 6.5$  times higher  $Q$ -factor than that of OOK and  $\sim 16$  times higher than that of 4-PAM indicating less severe effect of turbulence. Unlike OOK and PAM, the information is hidden in the phase of the carrier in BPSK and since the turbulence does not affect the phase of carrier significantly, BPSK is less sensitive to the scintillation.

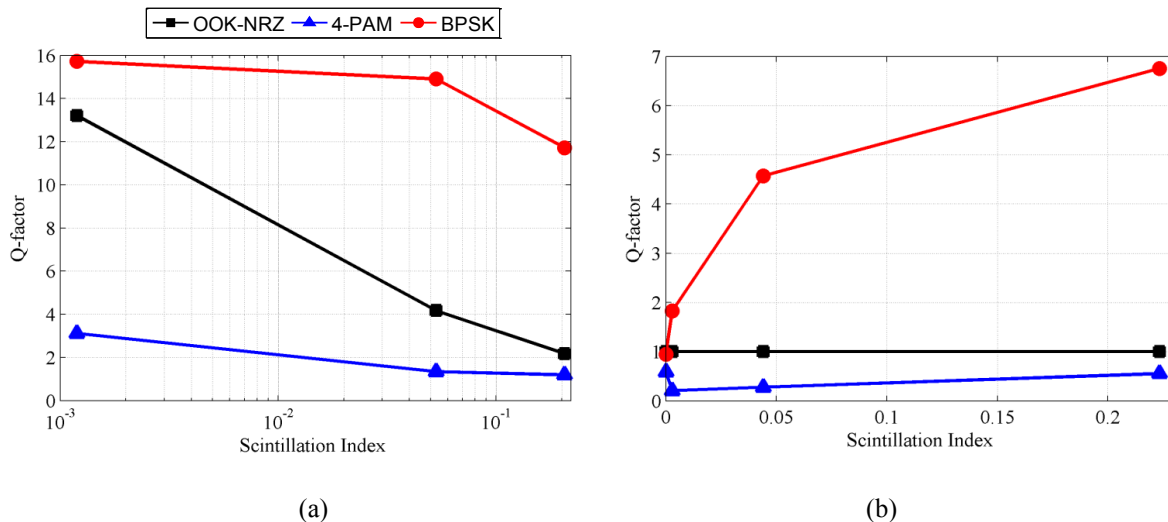


Figure 13.4-5: Measured  $Q$ -factor values against a range of Rytov variance for OOK, 4-PAM and BPSK signalling (a) the absolute scale at 5 Mbit/s, and (b) normalized to the  $Q$ -factor of OOK-NRZ.

### 13.5 Summary

The modulation techniques for FSO have been discussed. The error performance of OOK, PPM and SIM is analysed in the presence of noise and atmospheric turbulence, and the effect of turbulence on the BER highlighted. The shortcoming of the baseband modulation techniques with threshold detection in the presence of turbulence is discussed highlighting the need for adaptive threshold for the optimum. The PPM offers a significant improvement in the performance in the presence of turbulence; however PPM requires the slot and symbol synchronisation. On the other hand, the informations are carried in the phase in SIM offering more resilient to turbulence induced fading. The high error floor observed in the OOK modulation schemes is not observed in SIM.

### 13.6 References

- [Djordjevic and Vasic, 2006a] Djordjevic, I. B., B. Vasic, et al. "Multilevel coding in free-space optical MIMO transmission with  $Q$ -ary PPM over the atmospheric turbulence channel." *IEEE Photonics Technology Letters* **18**(14): 1491-1493, 2006.
- [Djordjevic and Vasic, 2006b] Djordjevic, I. B. and B. Vasic. "100-Gb/s transmission using orthogonal frequency -division multiplexing." *IEEE Photonics Technology Letters* **18**(15): 1576-1578, 2006
- [Gagliardi and Karp, 1995] Gagliardi, R. M. and S. Karp. *Optical Communications*. New York, John Wiley, 1995
- [Hemmati, 2006] Hemmati, H., Ed.. *Deep Space Optical Communications*. Deep space communications and navigation series. California, Wiley-Interscience, 2006.
- [Hemmati, 2007] Hemmati, H. "Interplanetary laser communications." *Optics and Photonics News* **18**(11): 22-27, 2007.
- [Kiasaleh, 2005] Kiasaleh, K. "Performance of APD-based, PPM free-space optical communication systems in atmospheric turbulence." *IEEE Transactions on Communications* **53**(9): 1455-1461, 2005.

- [Ohtsuki, 2003] Ohtsuki, T. "Multiple-subcarrier modulation in optical wireless communications." *IEEE Communications Magazine*: 74-79, 2003.
- [Popoola, Ghaseemlooy et al., 2007] Popoola, W. O., Z. Ghassemlooy, et al. "Free-space optical communication using subcarrier modulation in gamma-gamma atmospheric turbulence." *9th International Conference on Transparent Optical Networks (ICTON '07)* **3**: 156-160, 2007.
- [Popoola, Ghaseemlooy et al., 2008] Popoola, W. O., Z. Ghassemlooy, et al. "Free-space optical communication employing subcarrier modulation and spatial diversity in atmospheric turbulence channel." *IET Optoelectronics* **2**(1): 16-23, 2008.
- [Proakis, 2004] Proakis, J. G. *Digital Communications*. New York, McGraw-Hill, 2004.
- [Razavi and Shapiro, 2005] Razavi, M. and J. H. Shapiro. "Wireless optical communications via diversity reception and optical preamplification." *IEEE Transaction on Communications* **4**(3): 975-983, 2005.
- [Sheikh Muhammad, Gappmair et al., 2006] Sheikh Muhammad, S., W. Gappmair, et al. "PPM channel capacity evaluation for terrestrial FSO links." *International Workshop on Satellite and Space Communications*: 222-226, 2006.
- [Simon and Alouini, 2004] Simon, M. K. and M.-S. Alouini. *Digital Communication Over Fading Channels*. New York, John Wiley & Sons Inc, 2004.
- [Teramoto and Ohtsuki, 2003] Teramoto, S. and T. Ohtsuki . "Multiple-subcarrier optical communication systems with peak reduction carriers". *IEEE Global Telecommunications Conference (GLOBECOM)* **6**: 3274-3278, 2003
- [Teramoto and Ohtsuki, 2005] Teramoto, S. and T. Ohtsuki. "Multiple-subcarrier optical communication systems with subcarrier signal-point sequence." *IEEE Transactions on Communications* **53**(10): 1738-1743, 2005.
- [Willebrand and Ghuman, 2002] Willebrand, H. and B. S. Ghuman. *Free Space Optics: Enabling Optical Connectivity in today's network*. Indianapolis, SAMS publishing, 2002.
- [Wilson, Brandt-Pearce et al., 2005] Wilson, S. G., M. Brandt-Pearce, et al. "Free-space optical MIMO transmission with Q-ary PPM." *IEEE Transactions on Communications* **53**(8): 1402-1412, 2005.
- [You and Kahn, 2001] You, R. and J. M. Kahn. "Average power reduction techniques for multiple-subcarrier intensity-modulated optical signals." *IEEE Transaction on Communications* **49**(12): 2164-2171, 2001.

## 14 DIVERSITY, NETWORKING AND REDUNDANCY

(Wasiu Popoola, Zabih Ghassemlooy, Stanislav Zvanovec)

### 14.1 Overview

As discussed in the previous chapters, there is need to use clever techniques to control the output optical power reaching the detector and therefore compensate for the power fluctuations due to turbulence and other atmospheric phenomena in urban scenario. In order to overcome turbulence induced fades, several techniques have been proposed. These include: spatial transmitter/receiver diversity, adaptive beam forming based on the wave front phase error measurement and the setting of the opposite phase aberration on the beam by a deformable mirror [Hashmi, A., Eftekhari, A., et al. 2008], wavelength diversity [Weerackody, V. and Hammons, A. R., 2006] multiple-beam communication [Anguita, J. A., M. A. Neifeld, et al. , 2007] and novel modulation techniques [Lioumpas, A. S., Karagiannidis, G. K. et al. 2011].

In this chapter, the performance of FSO systems with spatial and time diversities will be discussed. To illustrate the diversity techniques, only the subcarrier intensity modulation (SIM) will be considered. The techniques can however be extended to other modulation techniques. The spatial diversity analysis will be based on the following linear combining techniques: equal gain combining (EGC), maximum ratio combining (MRC) and selection combining (SelC). Inter-symbol interference will not be considered since terrestrial FSO is basically a line-of-sight technology with negligible delay spread.

### 14.2 Receiver Diversity in Log-normal Atmospheric Channels

The idea of spatial diversity is premised on the fact that for a given  $\mathcal{N}$  separated photodetectors, the chance that all the photodetectors will experience deep fade (due to scintillation) simultaneously at any given instant is remote. An important consideration in spatial diversity is the amount of correlation that exists between the signals received by the different photodetectors. Apart from mitigating scintillation, the spatial diversity in an FSO communication link is also advantageous in combating temporary link blockage/outage due to birds or other small object flying cross the link path. It is also a good means of combating misalignment when combined with wide divergence optical sources, thereby circumventing the need for an active tracking. Moreover, it is much easier to provide independent aperture averaging with a multiple aperture system, than in a single aperture where the aperture size has to be far greater than the irradiance spatial coherence distance [Lee, E. J. and Chan, V. W. S. 2004]. In dense fog regime however, an FSO link with spatial diversity offers limited advantage and an alternative configuration such as the hybrid FSO/RF should be considered. In the following analysis, both instances of correlated and uncorrelated received signals will be considered. Since the spatial coherence length of the atmospheric channel only measures a few centimetres, it follows therefore that the photodetectors only need to be separated by a few centimetres to achieve uncorrelated reception. At the receiver, the beam footprint covers the entire field of view (FOV) of all the  $\mathcal{N}$  detectors. The photocurrents  $\{i_i(t)\}_{i=1}^{\mathcal{N}}$ , as shown in Figure 14.2-1, are then linearly combined before being sent to the coherent demodulator that separates the composite signal into its constituent subcarriers and then demodulates each subcarrier. The linear combining techniques considered are: MRC, EGC and SelC.

Scintillation is a random phenomenon that changes with time, thereby making the received irradiance time variant and the coherence time  $\tau_0$ , of the irradiance fluctuation in atmospheric turbulence is known to be in the order of milliseconds [Lee, E. J. and Chan, V. W. S. 2004]. This implies that within a time duration  $t < \tau_0$ , the received signal is constant and time invariant. A typical data symbol duration  $T \ll \tau_0$  ( $T = 1.6$  ns when transmitting at a moderate 625 Mbps symbol rate), it follows therefore, that though the channel is time varying, the received irradiance  $\{I_i\}_{i=1}^N$  is time invariant over one symbol duration.

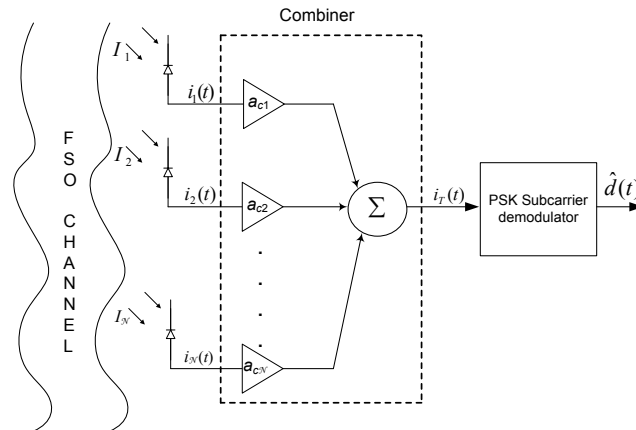


Figure 14.2-1: Block diagram of a spatial diversity receiver with  $N$  detectors

To facilitate a fair comparison between an FSO link with and without spatial diversity, each detector aperture in the  $N$ -detector system is assumed to have an area of  $A_D/N$ , where  $A_D$  is the detector aperture area with no diversity. It follows therefore, that the background radiation noise on each branch with detector diversity is reduced by a factor of  $N$ . Hence, on each branch the additive white Gaussian background noise variance will be  $\sigma^2/N$ . The thermal noise on each photodetector is however not reduced by a factor of  $N$ . The output of the individual detector during a symbol duration is given as:

$$i_i(t) = \frac{R}{N} I_i (1 + \sum_{j=1}^N A_j g(t) \cos(\omega_{c_j} + \theta_j)) + n(t); i = 1, 2 \dots N, \quad (14.2-1)$$

The combiner shown in Figure 14.2-1 scales the signal from each photodetector by a gain factor,  $\{a_{ci}\}_{i=1}^N$ , before adding them together. Since the photodetectors are required to be a few centimetres apart, and the link range a few kilometres, the difference in the propagation delay across the receiver array becomes negligible. The combiner's output thus become:

$$i_T(t) = \sum_{i=1}^N a_{ci} i_i(t), \quad (14.2-2)$$

### 14.2.1 Maximum Ratio Combining (MRC)

In the MRC linear combiner, the gain factor  $\{a_{ci}\}_{i=1}^N$  is proportional to the received irradiance. The weighted signals are then co-phased and summed coherently to obtain the combiner's output current given by (14.2-2). Without any interference, the MRC is optimal regardless of the fading statistics. This, according to [Simon, M. K. and Alouin, M.-S., 2004], is because it results in a maximum-likelihood receiver structure. On the other hand, MRC requires the knowledge of the individual received irradiance and phase on each branch, making it unsuitable for non-coherent demodulated subcarriers, such as the DPSK-SIM.

By substituting (14.2-1) into (14.2-2) and suppressing the DC components via filtering, the MRC combiner output becomes:

$$i_{MRC}(t) = \sum_{i=1}^N \left[ \frac{Ra_{ci}}{\mathcal{N}} I_i \sum_{j=1}^N A_j g(t) \cos(\omega_{cj}t + \theta_j) \right] + a_{ci}n_i(t) \quad (14.2-3)$$

The signal demodulation and the consequently extraction of the transmitted data is done separately for each subcarrier; as such, the photocurrent at a particular subcarrier frequency  $\omega_c$  is given by:

$$i_{MRC}(t) = \sum_{i=1}^N \left[ \frac{Ra_{ci}}{\mathcal{N}} I_i A g(t) \cos(\omega_c t + \theta) \right] + a_{ci}n_i(t) \quad (14.2-4)$$

Since the coherence time of the turbulent atmospheric  $\tau_0 \gg T$ , the branch irradiance  $I_i$  is therefore time invariant over a period  $T$ . This leads to the following expression for the signal power  $S_p$ , at the subcarrier frequency of interest:

$$\begin{aligned} S_p &= \left( \sum_{i=1}^N a_{ci} I_i \right)^2 \frac{1}{T} \int_0^T \left[ \frac{R A g(t) \cos(\omega_c t + \theta)}{\mathcal{N}} \right]^2 dt \\ &= \left( \frac{RA}{\mathcal{N}\sqrt{2}} \right)^2 \left( \sum_{i=1}^N a_{ci} I_i \right)^2 \end{aligned} \quad (14.2-5)$$

The overall noise is Gaussian, with a zero mean and a variance  $\sigma_{MRC}^2 = \sum_{i=1}^N a_{ci}^2 \sigma_i^2 = \sigma_{sc}^2 \sum_{i=1}^N a_{ci}^2$ . The electrical SNR at the demodulator input conditioned on the received irradiance is thus derived as:

$$\gamma_{MRC}(\vec{I}) = \left( \frac{RA}{\mathcal{N}\sqrt{2}} \sum_{i=1}^N a_{ci} I_i \right)^2 / \sigma_{MRC}^2 \quad (14.2-6)$$

Applying Cauchy inequality [Gradshteyn, I. S. and Ryzhik, I. M., 1994],  $(\sum_{i=1}^N a_{ci} I_i)^2 \leq (\sum_{i=1}^N a_{ci}^2)(\sum_{i=1}^N I_i^2)$ , to (14.2-6) results in the following expression for the combiner's output SNR:

$$\gamma_{MRC}(\vec{I}) \leq \frac{\left( \frac{RA}{\mathcal{N}\sqrt{2}} \right)^2 (\sum_{i=1}^N a_{ci}^2 \sigma_{sc}^2) (\sum_{i=1}^N I_i^2 / \sigma_{sc}^2)}{(\sum_{i=1}^N a_{ci}^2 \sigma_{sc}^2)} \quad (14.2-7)$$

The left hand side of the Cauchy inequality is apparently equal to the right hand side when  $a_{ci} \equiv I_i$ . For a background noise limited FSO link, the noise variance on each branch is proportional to the pupil receiver aperture area,  $A_D/\mathcal{N}$  and  $\sigma_{sc}^2 = \sigma^2/\mathcal{N}$ . It should be noted that in arriving at (14.2-7), the intermodulation distortion due to the inherent nonlinearity of the optical source has not been considered. For an ideal optical source with a modulation index of one, the subcarrier amplitude is constrained by the condition  $A < 1/\mathcal{N}$ . The optimum electrical SNR for each subcarrier frequency  $\omega_c$  now becomes:

$$\gamma_{MRC}(\vec{I}) = \left( \frac{RA}{\sqrt{2\mathcal{N}}} \right)^2 \left( \sum_{i=1}^{\mathcal{N}} I_i^2 / \sigma^2 \right) = \sum_{i=1}^{\mathcal{N}} \gamma_i(I_i) \quad (14.2-8)$$

where  $\gamma_i(I_i) = \frac{(RAI_i)^2}{2\mathcal{N}\sigma^2}$  is the conditional SNR on each diversity branch. The average SNR,  $\tilde{\gamma}_{MRC}$ , obtained by averaging (14.2-8) over the scintillation statistics is given as:

$$\tilde{\gamma}_{MRC} = \int \gamma_{MRC}(\vec{I}) p(\vec{I}) d\vec{I} \quad (14.2-9)$$

where  $p(\vec{I})$  is the joint pdf of scintillation, given by  $p(\vec{I}) = \prod_{i=1}^{\mathcal{N}} p(I_i)$  for  $\mathcal{N}$  photodetectors receiving uncorrelated signals. Similarly, for a BPSK pre-modulated subcarrier, the unconditional BER for the subcarrier at frequency  $\omega_c$  obtained by averaging the conditional error rate over the statistics of the intensity fluctuation across all branches is given by:

$$P_{e(MRC)} = \int_0^{\infty} Q\left(\sqrt{\gamma_{MRC}(\vec{I})}\right) p(\vec{I}) d\vec{I} \quad (14.2-10)$$

Solving (14.2-10) involves  $(\mathcal{N} + 1)$  fold integrations if the classical definition of the Q-function is used, but by using the alternative form of the Q-function and the Gauss-Hermite quadrature integration, this can be simplified to the form below:

$$P_{e(MRC)} = \frac{1}{\pi} \int_0^{\pi/2} [S(\theta)]^{\mathcal{N}} d\theta \quad (14.2-11)$$

where  $S(\theta) \approx \frac{1}{\sqrt{\pi}} \sum_{j=1}^{\mathcal{N}} w_j \exp\left(-\frac{K_0^2}{2 \sin^2 \theta} \exp[2(x_j \sqrt{2} \sigma_l - \sigma_l^2/2)]\right)$  and  $K_0 = \Re I_0 A / \sqrt{2\mathcal{N}} \sigma$ . With  $\mathcal{N} = 1$ , expression (14.2-11) expectedly reduces the BER with no diversity.

### 14.2.2 Equal Gain Combining (EGC)

In implementing the EGC spatial diversity technique, the irradiance estimate on each branch is not required but an estimate of the phase of all subcarrier signals on each branch is still very much needed. The EGC combiner samples the photocurrents  $\{i_i(t)\}_{i=1}^{\mathcal{N}}$  and sums them coherently with equal weights  $\{a_{ci}\}_{i=1}^{\mathcal{N}} = 1$ , to produce the decision statistics [Komiya, T., Kobayashi, K. et al. 2011]. With the DC component suppressed via filtering, the photocurrent at the output of the EGC combiner is given by:

$$i_{EGC}(t) = \sum_{i=1}^{\mathcal{N}} \left[ \frac{R}{\mathcal{N}} I_i \sum_{j=1}^{\mathcal{N}} A_j g(t) \cos(\omega_{c_j} t + \theta_j) \right] + n_i(t) \quad (14.2-12)$$

The conditional SNR at the output of the EGC combiner obtained is thus obtained as:

$$\gamma_{EGC}(\bar{I}) = \left( \frac{RA}{\sqrt{2\mathcal{N}}\sigma} \right)^2 \left( \sum_{i=1}^{\mathcal{N}} I_i \right)^2 < \left( \frac{\Re A}{\sqrt{2\mathcal{N}}} \right)^2 \left( \sum_{i=1}^{\mathcal{N}} \frac{I_i^2}{\sigma^2} \right) \quad (14.2-13)$$

From the foregoing, it is clear that  $\gamma_{EGC}(\bar{I}) < \gamma_{MRC}(\bar{I})$ . Since the noise variance is proportional to the individual receiver aperture area  $\sigma_{EGC}^2 = \sum_{i=1}^{\mathcal{N}} \sigma_i^2 = \sum_{i=1}^{\mathcal{N}} \sigma^2 / \mathcal{N} = \sigma^2$ .

For a log normal distributed scintillation, the sum of moderate number of irradiances is known to be another log normal variable [Mitchell, R. L, 1968; Lee, E. J. and. Chan, V. W. S. 2004]. That is, the sum of  $\mathcal{N}$  independent irradiance  $Z = \sum_{i=1}^{\mathcal{N}} I_i = \exp(\mathcal{U})$ , where  $\mathcal{U}$  is normally distributed with mean  $\mu_{\mathcal{U}}$  and variance  $\sigma_{\mathcal{U}}^2$ . Equation (14.2-14) below gives the pdf of  $Z$  while its first and second moments are given by (14.2-15a). The application of central limit is not appropriate here because the number of photodetectors  $\mathcal{N}$  is too small to justify its use.

$$P(Z) = \frac{1}{\sqrt{2\pi}\sigma_{\mathcal{U}}} \frac{1}{Z} \exp\left(-\frac{(\ln Z - \mu_{\mathcal{U}})^2}{2\sigma_{\mathcal{U}}^2}\right) \quad (14.2-14)$$

$$\mu_{\mathcal{U}} = \ln(\mathcal{N}) - \frac{1}{2} \ln\left(1 + \frac{\exp(\sigma_{\mathcal{U}}^2) - 1}{\mathcal{N}}\right) \quad (14.2-15a)$$

$$\sigma_{\mathcal{U}}^2 = \ln\left(1 + \frac{\exp(\sigma_{\mathcal{U}}^2) - 1}{\mathcal{N}}\right) \quad (14.2-15a)$$

The average SNR and the unconditional BER for a BPSK pre-modulated subcarrier are then given by (14.2-16) and (14.2-17) respectively:

$$\tilde{\gamma}_{EGC} = \int_0^{\infty} \gamma_{EGC}(Z) p(Z) dZ \quad (14.2-16)$$

$$\begin{aligned} P_{e(EGC)} &= \int_0^{\infty} Q\left(\sqrt{\gamma_{EGC}(Z)}\right) p(Z) dZ \\ &= \int_0^{\infty} \frac{1}{\pi} \int_0^{\pi/2} \exp\left(-\frac{K_1^2}{2 \sin^2(\theta)} Z^2\right) p(Z) d\theta dZ \end{aligned} \quad (14.2-17)$$

$$= \frac{1}{\sqrt{\pi}} \sum_{i=1}^n w_i Q(K_1 \exp[x_i \sqrt{2} \sigma_u + \mu_u]),$$

where  $K_1 = RI_0A/\sqrt{2} \mathcal{N} \sigma$ ,  $w_i$  and  $x_i$  remain as the weights and roots of the Gauss-Hermite function. With one photodetector, (14.2-17) gives the same result as for the case with no diversity.

### 14.2.3 Selection Combining (SelC)

Both MRC and EGC spatial diversity techniques discussed thus far require the irradiance level and/or the subcarrier signals phase estimates, also a separate receiver chain is needed for each diversity branch thereby adding to the overall complexity of the receiver. The SelC linear combiner on the other hand samples the entire received signal through the multiple branches and selects the branch with the highest SNR or irradiance level, provided the photodetectors receive same dose of background radiation. The output is equal to the signal on only one of the branches and not the coherent sum of the individual photocurrents as is the case in MRC and EGC. This makes SelC suitable for differentially modulated, non-coherent demodulated subcarrier signals. In addition, the SelC is of reduced complexity compared to the MRC and EGC and its conditional SNR is given by:

$$\gamma_{selc}(I) = \frac{R^2 A^2 I_{max}^2}{2 \mathcal{N} \sigma^2} \quad (14.2-18)$$

where  $I_{max} = \max(I_1, I_2, \dots, I_{\mathcal{N}})$ . The pdf of the received irradiance,  $p(I_{max})$ , given by (14.2-19), is obtained by first determining its cumulative density function (cdf) and then differentiating.

$$p(I_{max}) = \frac{2^{1-\mathcal{N}} \mathcal{N} \exp(-y^2)}{I \sigma_l \sqrt{2\pi}} [1 + \operatorname{erf}(y)]^{\mathcal{N}-1} \quad (14.2-19)$$

where  $y = \frac{\ln(I/I_0) + \sigma_l^2/2}{\sqrt{2}\sigma_l}$ . The average SNR and the unconditional BER, for a BPSK pre-modulated subcarrier in a turbulent atmospheric channel, are given by:

$$\tilde{\gamma}_{selc} = \int_0^{\infty} \frac{R^2 A^2 I_{max}^2}{2 \mathcal{N} \sigma^2} p(I_{max}) dI_{max} \quad (14.2-20)$$

$$P_{e(selc)} = \frac{2^{1-\mathcal{N}} \mathcal{N}}{\sqrt{\pi}} \sum_{i=1}^n w_i [1 + \operatorname{erf}(x_i)]^{\mathcal{N}-1} Q(K_0 \exp[x_i \sigma_l \sqrt{2} - \sigma_l^2/2]) \quad (14.2-21)$$

where  $K_0 = RI_0A/\sqrt{2\mathcal{N}} \sigma$ . For a binary DPSK pre-modulated SIM, the unconditional bit error obtained using the Gauss-Hermite quadrature integration approach is derived as:

$$\begin{aligned}
P_{e(\text{SelC})} &= \int_0^{\infty} \frac{1}{2} \exp\left(-\frac{\gamma_{\text{SelC}}(I)}{2}\right) p(I_{\text{max}}) dI \\
&\cong \frac{\mathcal{N}}{2^{\mathcal{N}} \sqrt{\pi}} \sum_{i=1}^{\mathcal{N}} w_i [1 + \text{erf}(x_i)]^{\mathcal{N}-1} \exp(-K_2^2 \exp(2x_i \sigma_i \sqrt{2} - \sigma_i^2))
\end{aligned} \tag{14.2-22}$$

where  $K_2 = RI_0 A / 2\sigma \sqrt{\mathcal{N}}$ .

The SelC diversity schemes may not be best for high speed FSO links. This is because SelC is characterised by the high processing load owing to repetitive branch monitoring and switching occurrences, thus resulting in augmented implementation complexities. To reduce the high processing load (thus the complexity) *switched combining* diversity, switch-and-stay combining (SSC) and switch-and-examine combining (SEC) diversity schemes are introduced. In SSC, once the existing received SNR drops below a certain threshold level the combiner switches to the next branch, regardless of SNR for the new branch even if it is less than the original branch [Komiyama, T., Kobayashi, K. et al. 2011]. In SSC and SEC diversity schemes there is no need for continual monitoring of all receiving signals, thus leading to a much simplified receiver design compared to SelC, but at the cost of inferior performance [Kaushal, H., Kumar, V. et al. , 2011].

### 14.3 Transmitter Diversity in a Log-normal Atmospheric Channel

In this section, the error performance of a SIM-FSO with a multiple optical transmitter and a single photodetector is discussed. The sources are assumed sufficiently spaced so that the photodetector receives uncorrelated optical radiations. To ensure a fair comparison and to maintain a constant power requirement, it is assumed that the power available for a single-transmitter system is equally shared among  $\mathcal{M}$ -laser transmitters. This requirement is similar to that specified in the preceding section. As such, the irradiance from each optical source is reduced by a factor of  $\mathcal{M}$  compared to a single transmitter system. An alternative approach will be for each source in the array to transmit the same power as in a single transmitter system, in this instance, the power requirement is increased by a factor of  $\mathcal{M}$ . Based on the former, the received signal is obtained as:

$$i(t) = \sum_{i=1}^{\mathcal{M}} \left[ \frac{R}{\mathcal{M}} I_i \sum_{j=1}^{\mathcal{N}} A_j g(t) \cos(\omega_{c_j} t + \theta_j) \right] + n(t) \tag{14.3-1}$$

Since the optical sources in the array are only separated by few centimetres, the phase shift experienced by the received irradiance due to the path difference is therefore negligible. The SNR on each subcarrier, conditioned on the received irradiance is derived as:

$$\gamma_{MISO}(\vec{I}) = \left( \frac{RA}{\sqrt{2}\mathcal{M}\sigma} \right)^2 \left( \sum_{i=1}^{\mathcal{M}} I_i \right)^2 \quad (14.3-2)$$

From the obvious similarity between (14.2-13) and (14.3-2), it can then be concluded that the unconditional BER for a SIMO system is the same as that of single source with the EGC combined multiple photodetectors.

#### 14.4 Transmitter-Receiver Diversity in a Log-normal Atmospheric Channel

In consistency with the earlier assumptions, the total transmitted power is equal to the transmitted power when a single optical source is used with the same bit rate. In addition, the combined aperture area of the  $\mathcal{N}$  photodetectors is the same as the no spatial diversity case. Moreover, the  $\mathcal{M}$  optical sources and the  $\mathcal{N}$  photodetectors are assumed well-spaced to avoid any correlation in the received signals. First, the received signals are combined using the EGC, and from the preceding section, a MISO system with  $\mathcal{M}$  laser sources is said to be identical to an EGC combined SIMO with  $\mathcal{M}$  photodetectors, these combined lead to the following as the conditional SNR of the SIM-FSO in MIMO configuration:

$$\gamma_{MIMO}(\vec{I}) = \left( \frac{RA}{\sqrt{2}\mathcal{M}\mathcal{N}\sigma} \right)^2 \left( \sum_{i=1}^{\mathcal{N}} \sum_{j=1}^{\mathcal{M}} I_{ij} \right)^2 = \left( \frac{RA}{\sqrt{2}\mathcal{M}\mathcal{N}\sigma} \right)^2 \left( \sum_{i=1}^{\mathcal{M}\mathcal{N}} I_i \right)^2 \quad (14.4-1)$$

This expression is the same as that of an EGC combiner with a total of  $\mathcal{M}\mathcal{N}$  photodetectors. Hence, the unconditional BER is obtained by replacing  $\mathcal{N}$  in (14.2-17) by  $\mathcal{M}\mathcal{N}$ . If however, the received signals are combined using the MRC linear combining scheme, the conditional SNR on each receiver branch will be:

$$\gamma_i(I_i) = \left( \frac{RA}{\sqrt{2}\mathcal{N}\mathcal{M}\sigma} \sum_{j=1}^{\mathcal{M}} I_{ij} \right)^2 \quad (14.4-2)$$

Considering the fact that the sum of independent lognormal random variables is another log-normal distribution [Mitchell, R. L, 1968], the unconditional BER becomes:

$$P_e = \frac{1}{\pi} \int_0^{\pi/2} [S(\theta)]^{\mathcal{N}} d\theta \quad (14.4-3)$$

where  $S(\theta) \approx \frac{1}{\sqrt{\pi}} \sum_{j=1}^{\mathcal{N}} w_j \exp\left(-\frac{K_2^2}{2 \sin^2 \theta} \exp[2(x_j \sqrt{2}\sigma_u + \mu_u)]\right)$  and  $K_2 = RI_0A/\sqrt{2}\mathcal{N}\mathcal{M}\sigma$ , while  $\sigma_u^2$  and  $\mu_u$  are as previously defined by (14.2-15a) with  $\mathcal{N}$  replaced by  $\mathcal{M}$ .

### 14.5 Results and Discussions of SIM-FSO with Spatial Diversity in a Log-normal Atmospheric Channel

In order to analyse the results obtained so far, a 20<sup>th</sup> order Hermite polynomial is assumed while the log irradiance variance is assumed to vary between 0.2<sup>2</sup> and unity, (i.e.  $0.2^2 \leq \sigma_l^2 \leq 1$ ). By plotting the BER expressions against the normalised SNR =  $(R\xi E[I])^2/\sigma^2$ , the link margin  $m_{\mathcal{N},\sigma_l}$ , defined as  $\frac{SNR \text{ with no diversity}}{SNR \text{ with } \mathcal{N} \text{ photodetectors}}$  at a BER of  $10^{-6}$  and turbulence strength  $\sigma_l^2$ , is obtained. In

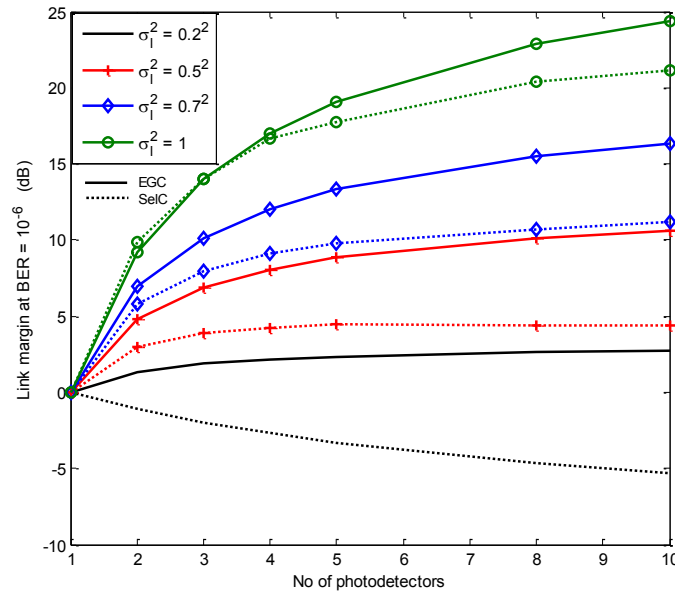


Figure 14.5-1: BPSK-SIM link margin with EGC and SelC against number of photodetectors for various turbulence levels and a BER of  $10^{-6}$ .

In both situations, the use of SelC in weak turbulence results in negative link margins. For instance, Figure 14.5-2 shows that for  $\sigma_l < 0.4$ , SelC spatial diversity results in between -2 dB and -7 dB link margin for  $2 \leq \mathcal{N} \leq 10$ , similarly in Figure 14.5-1, it results in a margin of up to -5 dB at  $\sigma_l = 0.2$ . The negative link margin experienced with SelC can be attributed to the fact that at a very low turbulence level, the effect of reducing the received intensity by a factor of  $\mathcal{N}$  on each branch is dominant over the turbulence induced intensity fluctuation.

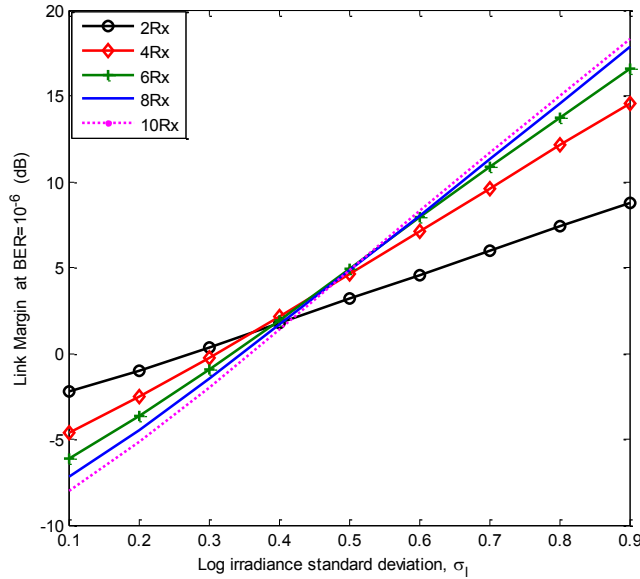


Figure 14.5-2: DPSK-SIM with SelC spatial diversity link margin against turbulence strength for  $\mathcal{N} = [2, 4, 6, 8, 10]$ .

However, as the turbulence level increases beyond  $\sigma_l = 0.4$ , SelC spatial diversity starts to yield a positive link margin; producing up to 9 dB link margin with two photodetectors in a DPSK pre-modulated SIM link. And for  $\sigma_l > 0.2$  in Figure 14.5-1, SelC proves worthwhile with positive link margins but the gains are still lower than that obtainable from EGC by about ~1 to ~6 dB depending on the number of photodetectors used. Based on the foregoing, SelC spatial diversity will not be recommended for use on short link FSO experiencing weak irradiance fluctuation.

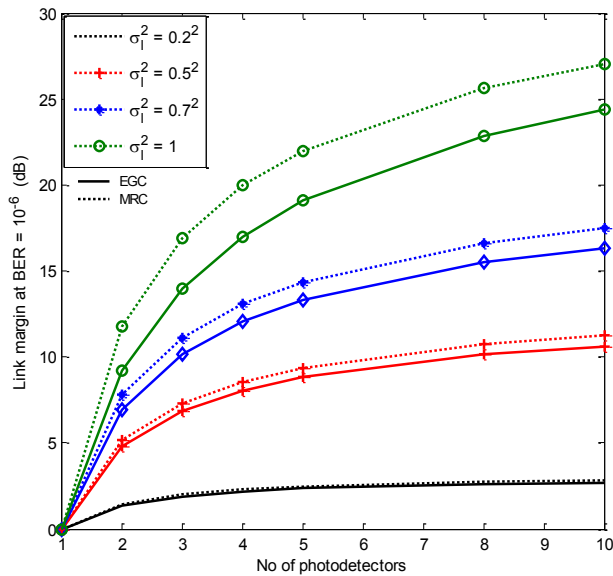


Figure 14.5-3: BPSK-SIM diversity link margin with EGC and MRC against number of photodetectors for various turbulence levels and a BER of 10<sup>-6</sup>.

The performance of EGC and MRC linear combiners is compared in Figure 14.5-3, this figure shows very clearly, that the link margin obtainable using the EGC is between 0 and ~2 dB (depending on the turbulence severity) lower than using the complex MRC.

Using two photodetectors with optimal MRC in atmospheric turbulence with  $0.2^2 \leq \sigma_l^2 \leq 1$ , has the potential to reduce the SNR required to achieve a BER of  $10^{-6}$  by between  $\sim 2$  and  $\sim 12$  dB. With up to four independent photodetectors however, the theoretical link margin for the MRC combiner increases to  $\sim 20$  dB as shown in Figure 14.5-3. Another inference from this figure is that the spatial diversity gain (link margin) becomes more pronounced as scintillation increases; using two detectors with MRC at turbulence level,  $\sigma_l = 0.2$  results in a link margin which is  $\sim 10$  dB lower than at  $\sigma_l = 1$ .

Also for  $\mathcal{N} \geq 4$ , the marginal link margin per unit detector ( $m_{\mathcal{N},\sigma_l} - m_{\mathcal{N}-1,\sigma_l}$ ) reduces drastically as the graphs begin to flatten out. For instance, increasing  $\mathcal{N}$  from 4 to 10 with MRC across the turbulence levels  $0.2^2 \leq \sigma_l^2 \leq 1$  only results in a meagre increase of between 0 and  $\sim 6$  dB link margins, while increasing  $\mathcal{N}$  from 1 to 4 over the same turbulence range results in between  $\sim 3$  and  $\sim 22$  dB diversity gains.

Furthermore in Figure 14.5-4, the plot of (14.5-17) against the normalised SNR is shown at a turbulence level  $\sigma_l^2 = 0.3$  for different values of  $\mathcal{N}$  and  $\mathcal{M}$ . It can be inferred from the plot that at a BER of  $10^{-6}$ , using a  $2 \times 2$  MIMO requires  $\sim 0.4$  dB of SNR more than employing a  $1 \times 4$ -MIMO configuration. However, spacing four photodetectors to ensure that the received signals are uncorrelated is far more demanding and cumbersome than spacing two photodetectors. Also, to achieve a BER of  $10^{-6}$ , the use of  $4 \times 4$ -MIMO system requires about  $\sim 4$  dB and 1 dB less SNR compared with using a lone source with 4 and 8 photodetectors, respectively.

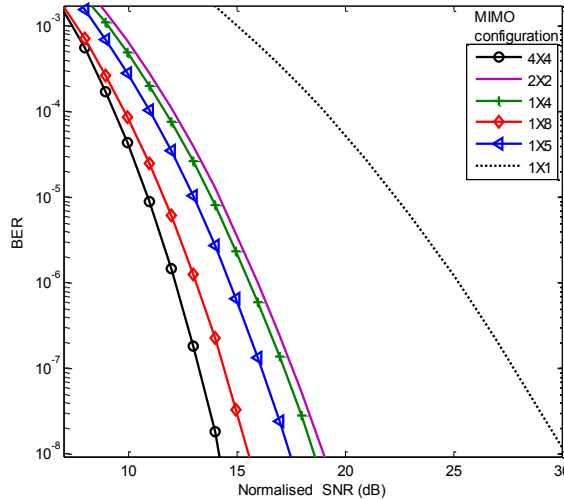


Figure 14.5-4: Error performance of BPSK-SIM with MIMO configuration in turbulent atmospheric channel for  $\sigma_l^2 = 0.3$ .

## 14.6 Terrestrial Free Space Optical Links with Subcarrier Time Diversity

In the previous sections, the use of spatial diversity to lessen the effect of atmospheric turbulence has been discussed. And as highlighted in the spatial diversity results, the best gains are achieved when the detectors are physically separated by a distance greater than the turbulence coherence length. The channel coherence length depends on the turbulence strength and is typically in the order of centimetres. Similarly, the use of aperture averaging

requires the receiver aperture to be larger than the turbulence coherence length. This does not only make the system bulky, it is cumbersome and not always feasible. The use of the turbo product code (TPC), as the channel coding scheme, with interleaving have shown that to offer good resistance to burst errors and no error floor due to the channel fading in FSO links [Ohteru, S. and Takachio, N., 1999].

This section will be looking at the subcarrier time delay diversity (STDD) as an alternative or complementary means of mitigating the channel fading in SIM-FSO links. The conventional use of multiple subcarriers is to increase throughput/capacity via subcarrier multiplexing. But in this scheme, different subcarriers at different frequencies are used to transmit the delayed copies of the original data. The proposed subcarrier STDD scheme has an advantage of simplicity and low cost to achieve a reasonable diversity gain compared to schemes such as adaptive optics or forward error correction. Moreover, the reduction in throughput associated with the temporal diversity can be compensated for through subcarrier multiplexing.

#### 14.6.1 Error Performance with STDD

In the STDD scheme, delayed copies of the data are re-transmitted on different subcarriers as shown in Figure 14.6-1. The STDD scheme relies solely on the statistical temporal variation of the atmospheric turbulence induced fading. Apart from re-transmitting the delayed version of the original data on different subcarriers, other viable options include using different wavelengths or polarisations for the retransmission. Details of how these two other options are done can be found in [Trisno, S., Smolyaninov, I. I., et al., 2004; Trisno, S., Smolyaninov, I. I., et al., 2005; Kwok, C. H., Penty, R.V. et al., 2008]. Time delay diversity schemes have the advantage of simplicity and low cost to achieve a reasonable diversity gain compared to schemes such as adaptive optics or forward error correction [Trisno, S., Smolyaninov, I. I., et al., 2004; Trisno, S., Smolyaninov, I. I., et al., 2005]. These gains are however at a cost of retransmission latency and data rate reduction. The system under consideration must therefore be able to trade low error rate for high latency.

According to the Taylor frozen turbulence hypothesis [Trisno, S., Smolyaninov, I. I., et al., 2005], turbulent eddies responsible for the fading are frozen in space and only move across the beam path by the transverse component of the wind. Thus from the knowledge of the average transverse wind speed, the spatial statistics of turbulence can be translated into temporal statistics. From this transformation, the temporal covariance function of the irradiance fluctuations can be obtained as outline in [Kwok, C. H., Penty, R.V. et al., 2008]. The temporal covariance is useful in determining the correlation time  $\tau_c$ . For weak turbulence,  $\tau_c$  has been experimentally measured to vary between 3 ms and 15 ms [Kwok, C. H., Penty, R.V. et al., 2008]. This suggests the sort of values required for  $\tau$  in order for the TDD systems to be efficient in fading channels. In the analysis we assume the following:  $\tau \geq \tau_c$ , and the minimum required buffer size  $R_b\tau$  is set prior to transmission. To illustrate the performance with the proposed STDD, we consider a BPSK-subcarrier intensity modulated system with a single data carrying subcarrier and  $U$ -STDD paths. During a symbol duration, the data carrying signal  $m(t)$  is given by:

$$m(t) = \sum_{i=1}^{U+1} d(t - (i - 1)\tau) \cos(\omega_i t + \varphi_i) \tag{14.6-1}$$

where  $d(\cdot) \in [-1, 1]$ . The standard RF coherent demodulator employed extracts the reference carrier needed to down convert the received signal to base band. The sum of the demodulator outputs is then fed into the decision circuit as illustrated in Figure 14.6-1. From this the electrical SNR per bit can then be easily derived as:

$$\gamma(\bar{I}) = \frac{(R\xi)^2 P_m}{\sigma^2} \left( \sum_{i=1}^{U+1} I_i \right)^2 \tag{14.6-2}$$

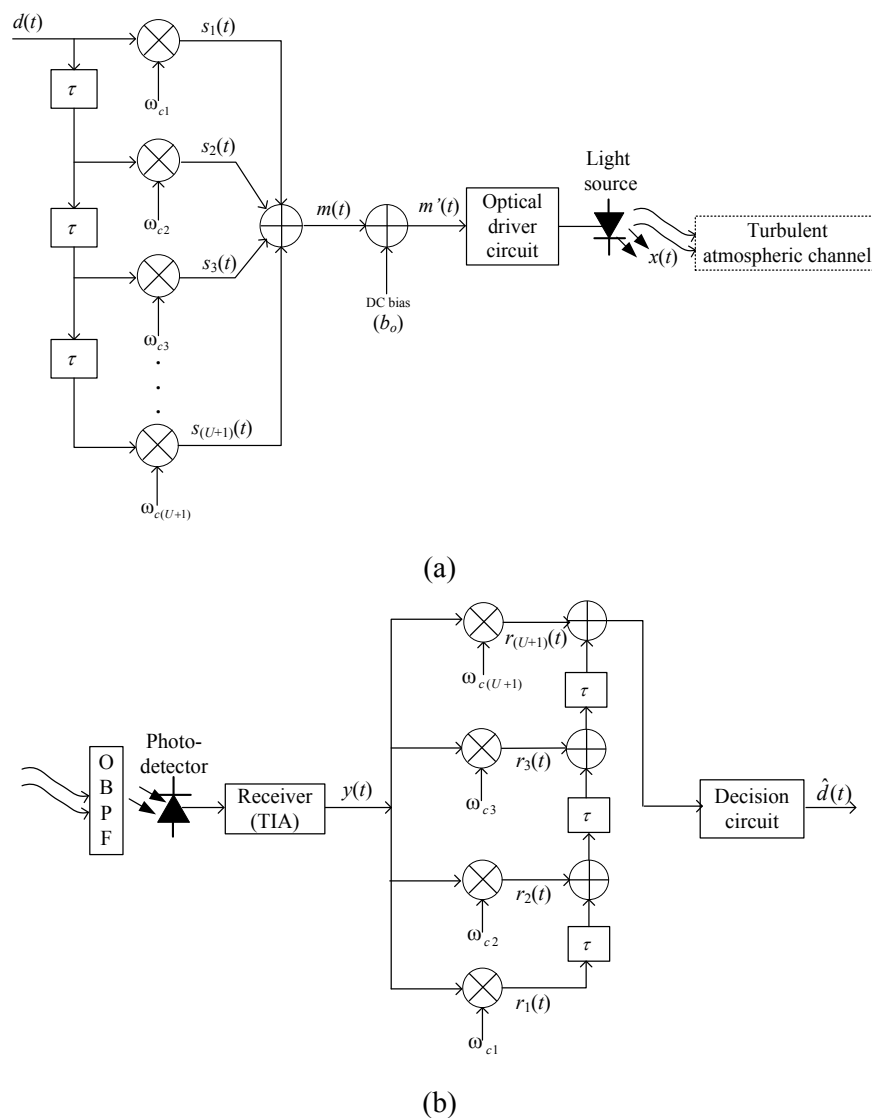


Figure 14.6-1: The subcarrier STDD block diagram: (a) transmitter, and (b) receiver

TIA-trans-impedance amplifier; OBPF-optical bandpass filter.

The noise variance is given by  $\sigma^2 = \sigma_{Bg}^2 + (U + 1)\sigma_{Th}^2$ , since there are now  $(U+1)$  demodulation paths associated with every photodetector. It should be noted that with the

addition of  $U$ -STDD paths,  $\xi = 1/(U + 1)A$  becomes the minimum modulation depth needed to avoid any clipping distortions.

#### 14.6.1.1 Error Performance of Short Range Links

To evaluate the BER with the subcarrier STDD in a log normal turbulence channel, expression (14.6-2) is substituted and  $p(\bar{I})$  replaced with the probability density function (pdf) of the sum of  $(U+1)$  independent but identical log normal variables. Although the sum of independent log normal variables does not have a closed form [Nadeem, F., Kvicera, V. et al., 2009], it is often approximated as another log normal variable [Mitchell, R. L, 1968]. There are several approaches to make this approximation, a survey and comparison of these approaches can be found in [Matera, F. and Settembre, M., 2000]. In this work, we will use the moment-matching approach (otherwise called the Wilkinson's method) to make the approximation. This approach is chosen because it is simple, straight forward and has also been reported [Ambrosio, L. A., M. Zamboni-Rached, et al., 2011] to work well for small values of  $\sigma_l^2$  as is the case here. We now make the approximation that the  $\sum_{i=1}^{U+1} I_i \equiv Z$ , where  $Z$  is a log normal variable described as  $Z = \exp(v)$  and  $v$  is Gaussian. The following are the approximate values of the mean and variance of  $v$  obtained by matching the first and second moments of  $\sum_{i=1}^{U+1} I_i$  to that of  $Z$ ; see [Ambrosio, L. A., M. Zamboni-Rached, et al., 2011] for detailed proof.

$$\mu_v = \ln(U + 1) - \frac{1}{2} \ln \left( 1 + \frac{\exp(\sigma_l^2) - 1}{U + 1} \right) \quad (14.6-3a)$$

$$\sigma_v^2 = \ln \left( 1 + \frac{\exp(\sigma_l^2) - 1}{U + 1} \right) \quad (14.6-3b)$$

The resulting BER expression is then simplified using the Gauss Hermite approximation. The unconditional BER for the BSPK-SIM link with  $U$ -STDD thus becomes:

$$P_e = \frac{1}{\sqrt{\pi}} \sum_{i=1}^n w_i Q \left( \sqrt{K'_0} \exp(x_i \sqrt{2} \sigma_v + \mu_v) \right) \quad (14.6-4)$$

where  $K'_0 = \frac{(R\xi I_0)^2 P_m}{\sigma_{B_g}^2 + (U+1)\sigma_{T_h}^2}$ . The penalty due to the turbulence fading at a given BER with and without STDD can therefore be obtained from this equation.

#### 14.6.1.2 Long Range Links

For longer range FSO links ( $>1$  km), the procedure for obtaining the error rate expression is similar to that of the short range link above except that  $p(\bar{I})$  now becomes the pdf of the sum of independent negative exponential variables. This pdf is tractable and is easily derived as [Osche, G. R., 2002]:

$$p(\bar{I} = Z) = \frac{I_0^{-(U+1)} Z^U \exp(-Z/I_0)}{\Gamma(U+1)} \quad (14.6-5)$$

where  $\Gamma(\cdot)$  is the gamma function. The resulting BER expression given by (14.6-6), which is obtained (14.6-2) and (14.6-5), does not have a closed form solution. As a result, the BER will have to be evaluated numerically.

$$P_e = \frac{I_0^{-(U+1)}}{\pi\Gamma(U+1)} \int_0^{\pi/2} \int_0^{\infty} Z^U \exp(-K'_1(\theta)Z^2 - Z/I_0) dZ d\theta \quad (14.6-6)$$

where  $K'_1(\theta) = (R\xi)^2 P_m / 2\sigma^2 \sin^2 \theta$  .  $K_1(\theta) = (RA)^2 / 4N^3 \sigma^2 \sin^2(\theta)$

From (14.6-6) it is observed that within the  $(0 - \pi/2)$  limit of integration, the function  $\sin^2 \theta$  is monotonically increasing and an upper bound of (14.6-6) can then be obtained by maximising the integrand with  $\theta = \pi/2$  to obtain:

$$P_e \leq \frac{1}{2\sqrt{(2K_1)^{U+1}}} \exp\left(\frac{\sigma^2}{4(R\xi)^2 P_m}\right) D_{-(U+1)}(1/\sqrt{2K_1}) \quad (14.6-7)$$

where  $K_1 = (RA)^2 / 4N^3 \sigma^2 D_\rho$  is the parabolic cylinder function whose definition is available in [Gradshteyn, I. S. and Ryzhik, I. M., 1994].

The results presented in this section are based on the simulation parameters of Table 14.6-1 and the BPSK-SIM scheme. Unless otherwise stated the background, thermal noise and scintillation are considered as the system limiting factors.

#### 14.6.1.3 Short Range Link

From the combination of (14.2-7), (14.2-12) and (14.6-4), we obtain Figure 14.6-1 which shows the FSO link's BER with and without STDD at different values of normalised SNR,  $\bar{\gamma} = \frac{(RI_0)^2 P_m}{\sigma^2}$  . This plot shows  $\bar{\gamma}$  to be decreasing as the number of temporal diversity paths increases. To determine the optimum number of diversity paths required, we present in Table 16.2 the following parameters: diversity gain (difference between  $\bar{\gamma}$  with and without STDD), fading penalties (difference between  $\bar{\gamma}$  in fading channel and under no fading) and the effective data rates. This table explicitly shows that at  $\sigma_1^2 = 0.3$ , 1-STDD has the highest STDD gain per additional path of ~6.9 dB and the least reduction in data rate. It is interesting to note that the gain per unit path decreases as more paths are added. This makes sense because for a given peak optical power, the modulation index has to be reduced as more paths are added in order to keep the laser within its dynamic range. These findings appear to be independent of how the STDD scheme is implemented. A similar conclusion was previously reported when the delayed data was transmitted on different polarizations/wavelengths [Trisno, S., Smolyaninov, I. I., et al., 2005; Kwok, C. H., Penty, R.V. et al., 2008]. Hence, single re-transmission (1-STDD) will be suggested to mitigate channel fading for short range links.

Table 14.6-1: Simulation parameters

Parameters	Values
Symbol rate $R_b$	155 - 625 Mbps
Spectral radiance of the sky $N(\lambda)$	$10^{-3}$ W/cm <sup>2</sup> μmSr
Spectral radiant emittance of the sun $W(\lambda)$	0.055 W/cm <sup>2</sup> μm
Optical band-pass filter bandwidth $\Delta\lambda$ @ $\lambda = 850$ nm	1 nm
PIN photodetector field of view	0.6 radian
Radiation wavelength $\lambda$	850 nm
Link range $L$	1 km
Index of refraction structure parameter $C_n^2$	$0.25 \times 10^{-14}$ - $2.45 \times 10^{-14}$ m <sup>-2/3</sup>
Load resistance $R_L$	50 Ω
PIN photodetector responsivity $R$	1
Optical band-pass filter transmissivity	90%
Equivalent temperature, $T_e$	300 K

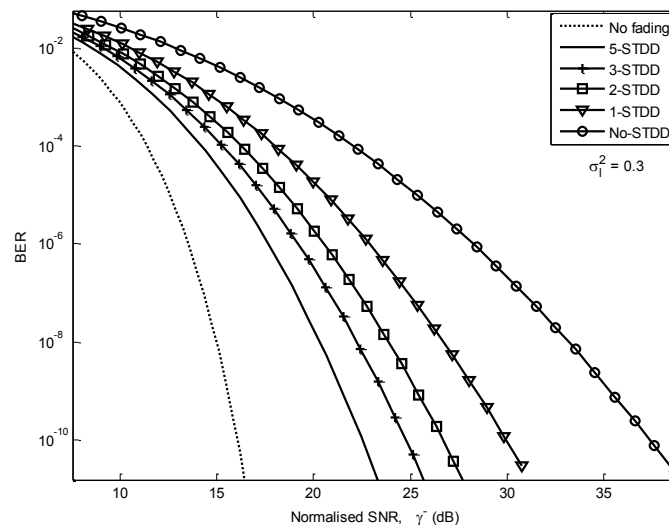


Figure 14.6-1: The BER against  $\bar{\gamma}$  with and without STDD

at 155 Mbps,  $\sigma_f^2 = 0.3$ ,  $C_n = 0.75 \times 10^{-14} \text{ m}^{-2/3}$

Using (16.31) with  $\xi = 1/(U + 1)A$ , it is shown in Figure 14.6-2 that the average received irradiance and indeed the diversity gain both increase as the fading strength increases. However, the fading penalties and diversity gains are independent of the data rate. For instance, at  $\sigma_f^2 = 0.1$  the estimated gains and fading penalties with 1-STDD stood at 0.36 dB and ~4.2 dB for  $R_b = 155$  and 625 Mbps, respectively. For stronger fading condition with  $\sigma_f^2 = 0.5$ , these values increase to 3 dB and ~11 dB, respectively.

Table 14.6-2 Fading penalty and STDD gain at

$BER = 10^{-9}$ ,  $R_b = 155$  Mbps,  $\sigma_f^2 = 0.3$ , and  $\xi = 1/(U + 1)A$

	0- STDD	1-STDD	2-STDD	3-STDD	5-STDD
$\bar{\gamma}$ (dB) (no fading: 15.56 dB)	35.32	28.41	25.34	23.54	21.48
Fading penalty (dB)	19.76	12.85	9.78	7.98	5.92
Diversity gain (dB)	0	6.91	9.89	11.78	13.84
(gain / unit path)	(0)	(6.91)	(4.99)	(3.93)	(2.77)
Effective data rate (Mbps)	$R_b$	$0.5R_b$	$0.33R_b$	$0.25R_b$	$0.17R_b$

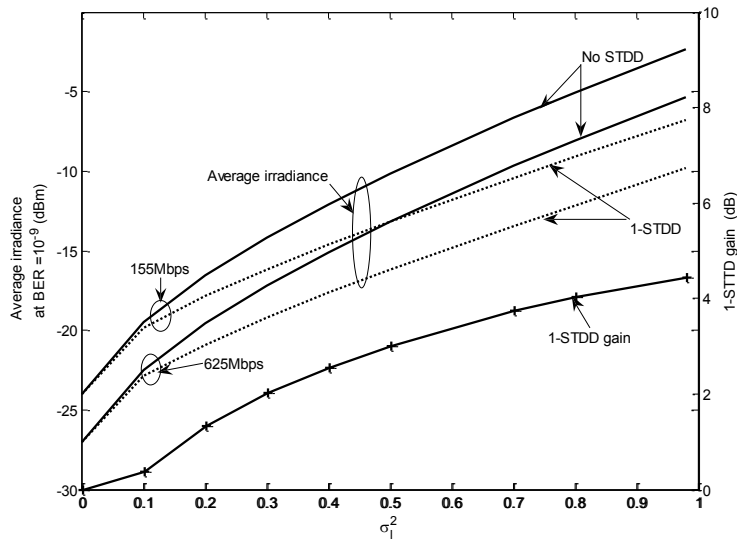


Figure 14.6-2: The average received irradiance at a BER of  $10^{-9}$ ,  $R_b$  (Mbps) = [155, 625] and 1-STDD gain for different strengths of turbulence.

14.6.1.4 Long Range Link

The performance of the link in the negative exponential turbulence channel is depicted in Figure 14.6-3. From the figure it is quite clear that achieving a low error rate communication in a long range FSO link is almost impossible without any diversity technique. To achieve a moderate BER of  $10^{-6}$  requires a huge  $\bar{\gamma}$  of 112 dB at the receiver if no diversity technique is implemented. And this translates into  $\sim 97$  dB fading penalty. The implication of this high fading penalty is that at least one fading mitigation technique has to be used in order to establish the link. However with 1-, 2- and 3-STDD the required  $\bar{\gamma}$  values are estimated to be 62 dB, 43.6 dB and 35.8 dB, respectively. These gains, (reduction in  $\bar{\gamma}$  with STDD) are achieved at the price of reduced  $R_b$  by a factor of 2, 3 and 4 in that order. The STDD technique can therefore be used for the long range FSO to achieve a low BER communication.

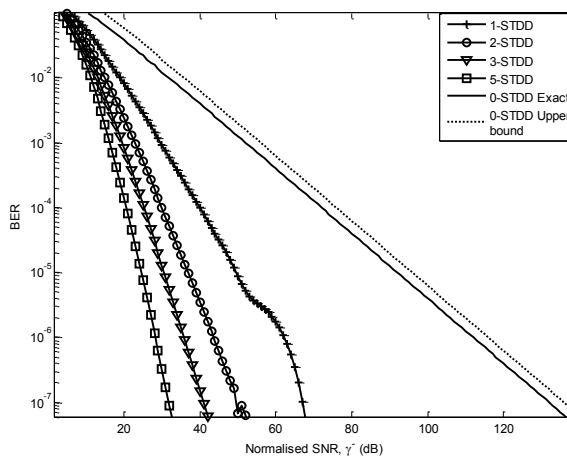


Figure 14.6-3: Link BER performance against the normalised SNR with the subcarrier STDD in the negative exponential turbulence induced fading channel.

## 14.7 Analysis of route diversity of FSO links influenced by rain

In order to obtain precise fading statistics, the rain database from a four year period 2002-2005 was utilized including 250 km x 250 km rain scans from Czech meteoradars (rain rate distributions with 1 km grid resolution and 1 minute time steps). Since we tried to focus on elevated links, HAP flying at 20 km altitudes were considered. Two evaluation methods were tested based on simulation results: the first appropriated for alone elevated systems following terrestrial approaches of two joint transmitting techniques and the second utilizing a combination of millimeter (transmitting frequency of 48 GHz was assumed - the frequency allocated worldwide to HAP systems [ITU-R, 2000] and Free Space Optical system. The comparison of complementary cumulative distribution functions of rain attenuation for the a single HAP to user link at 48 GHz (ground distance 3 km) and, newly, for two branch diversity links at the same frequency, where a user is able to connect to two HAPs, can be seen in Figure 14.7-1. In the latter case, one of the two diversity links was identical to the standalone link and the second was angularly separated by 180 degrees with the land distance of 4.5 km.

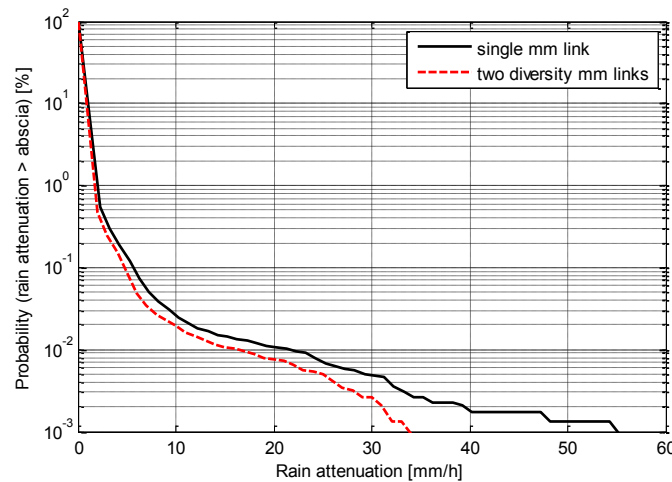


Figure 14.7-1: CDFs of rain attenuation for a single link and two-branch diversity HAP links at 48 GHz with the angular separation of 180 degrees and main and diversity ground link distance 3 and 4.5 km

For the case of the same scenario, but with optical links, resulted statistics are depicted in Figure 14.7-2. As it can be distinguished, both systems can in similar way compensate rain attenuation in term of diversity gain. In next step of our analyses, performance of single FSO link was tested for different elevation angles. See Figure 14.7-3, where complementary cumulative distribution functions of single FSO link are demonstrated for elevations of 90 degrees, 60 degrees and 45 degrees. Consequently, statistics of elevated single FSO links were compared to rain attenuations of when the links between the same user and HAP used both parallel transmitted FSO and millimeter waves. Table 14.7-1 presents some of determined values of diversity gains when combined links is employed compare to the single FSO. As it can be seen there is evident increase of diversity gain with decrease of elevation towards the Earth.

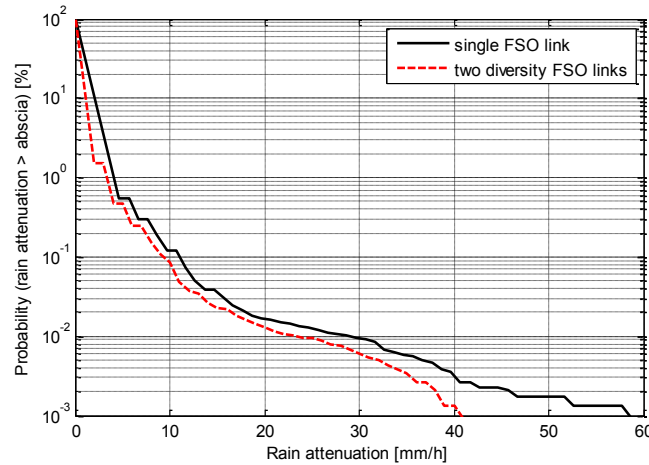


Figure 14.7-2: CDFs of rain attenuation for a single link and two-branch diversity HAP links at FSO wavelengths with the angular separation of 180 degrees and main and diversity ground link distance 3 and 4.5 km

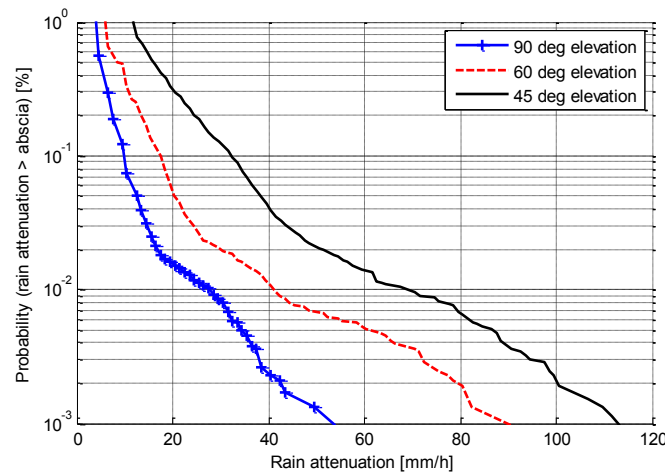


Figure 14.7-3: CDFs of different elevated single FSO links influenced by rain

Table 14.7-1: Diversity Gains in dB for Particular Elevation and Availability of Parallel MM and FSO HAP Link Compare to Single FSO Link

Availability	Elevation 90 deg	Elevation 60deg	Elevation 45 deg
99%	2.15	3.35	6.56
99.9%	4.38	6.58	11.81
99.99%	6.30	6.75	13.05

Regarding whole system performance the main focus of analyzes was to derive corresponding relations among rain event parameters and the availability of optical systems independently on the particular deployment of optical nodes and spatial distribution of users. In the case of a rainstorm with considerably high rain rates the network was capable of combating undesirable rain attenuation by route diversity - by setting proper angular separations, outage improvement probability within network can be increased by 11.4% (from 13.6 up to 25.2%). This is very interesting indicator especially for the Czech Republic where higher percentage of rain storms with smaller rain spatial parameter occurs.

To introduce an example of results from an analysis, a five-day sequence of rain occurring in May 2002 with a specific center situated above Prague, in the Czech Republic, was selected. In Figure 14.7-4 one can see the evolution of maximum rain rates (non-rainy periods and periods with a maximum rain rate of less than 3 mm/h were omitted) at the top and the evolution of rain spatial features as described by the rain spatial parameter at the bottom.

The time dependence of the outage improvement probability - the percentage of terminal stations with a successfully established diversity link out of the total number of terminal stations receiving a level of power input from the nearest base station that falls below the threshold – of the virtual FSO network as derived for rainfall from Figure 14.7-4 is depicted in Figure 14.7-5. The difference between the values obtained for particular rain rate distributions by network and derived using the rain spatial parameter is in this case less than 2%.

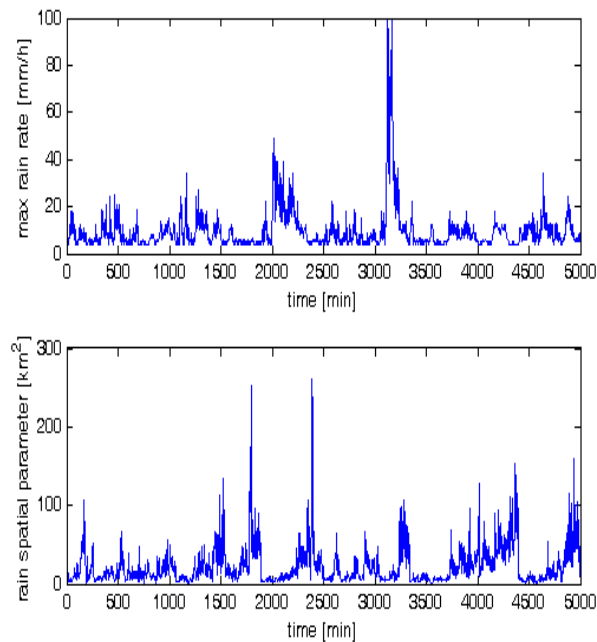


Figure 14.7-4: Time dependences of a maximum rain rate (upper) and the rainfall spatial parameter (bottom) for rainy minutes

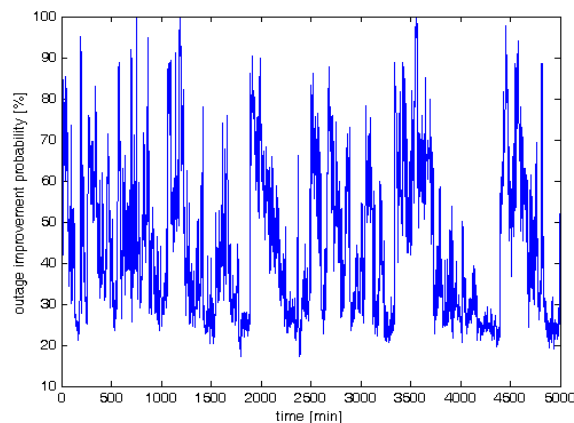


Figure 14.7-5: Time dependence of the outage improvement probability

Example of comparison of outage improvement probability dependence on angular separations between diversity links and main to diversity link length ratio for microwave system working at the frequency of 48 GHz and optical system is then shown in Figure 14.7-6.

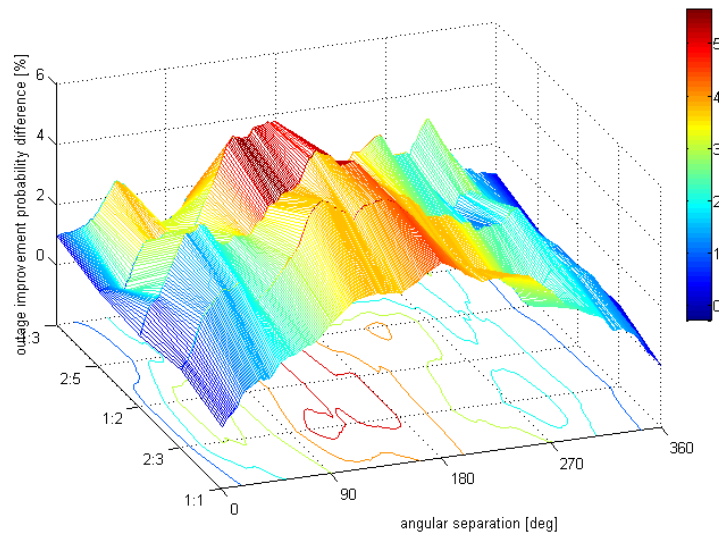


Figure 14.7-6: Example of comparison outage improvement probability [%] of microwave and optical networks

As it can be seen in case of optical network higher outage improvements probabilities – varying between 1.6 and 5.3% - can be reached compare to RF network. Especially the dependence of the parameter  $a$  [Zvanovec, S. and Pechac, P. 2006] for higher rain intensities has rapid slope than in case of 48 GHz. Outage improvements have proved to have an exponential dependence on rain spatial parameter. In order to check derived statistics, we are planning analyses with rain distributions valid for other climatic areas.

## 14.8 Outdoor measurements of diversity links

Experimental measuring network was set up in the university campus of the Czech Technical University in Prague (CTU). The network consists of three FSO links and comprises a star topology network. Parameters of particular optical links are characterized in terms of lengths, wavelengths and positions of transceivers characterized in Table 14.8-1.

Table 14.8-1: Parameters of used FSO links

	Link A	Link B	Link C
Type	WaveBridge 500	LightPointe Strata G	MRV Telescope 700
Length (m)	120	450	390
Wavelength (nm)	800 - 900	850	830 - 860
Optical Source	LED	LD	LD
Divergence (mrad)	17.5	2.0	3.5
Max Data Rate (Mbps)	155	1250	155
1. point of the link	CTU Campus	CTUCampus	CTU Campus
2. point of the link	CTU Campus	ORLIK Dormitory	BUBENEC Dormitory

Arrangement of the network and sensors is then depicted in Figure 14.8-1. Weather conditions are observed by two meteorological stations collecting air temperature and humidity, atmospheric pressure, wind velocity and amount of precipitations. In order to

investigating of influence of buildings on FSO link, set of thermal sensors was installed between at first quarter of the link A. In the next step, the measuring network will be extended to a mesh topology. New FSO link will be added and it will enclose links B and C.

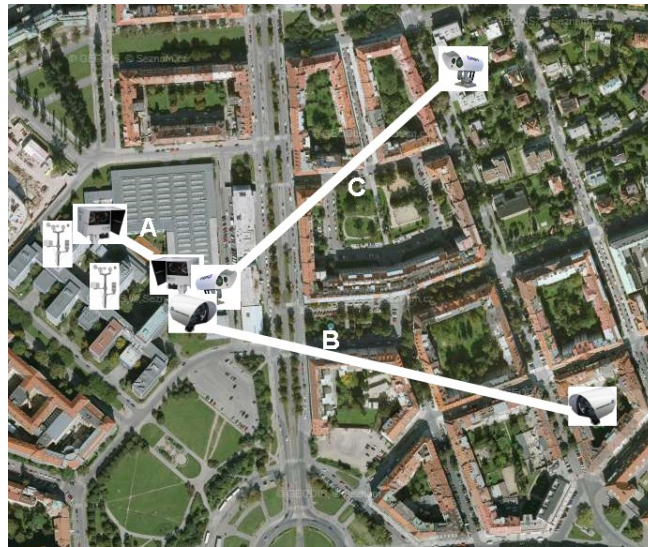


Figure 14.8-1: Measuring network and sensors arrangement

Data from two FSO links A and B as a part of a star topology network were analyzed in order to investigate diversity statistics. In order to obtain these results, cumulative distribution functions (CDF) were analyzed and compared. All above mentioned propagation impairments were dealt and recalculated especially with their spatial properties. Because of different length of the links, the diversity gain was recalculated to 1 km long propagation path.

Table 14.8-2 gives the diversity gain of two FSO links derived from measured statistics during April to May 2011. Availability of single links A and B was enumerated at first. In next step it was distinguished improvement of such statistics when the second link was added. As can be seen diversity gains up to 8 dB can be yielded. This contribution can introduce very perspective possibility especially within dense FSO networks during drops of particular network segments (links) due to the harsh atmospheric conditions.

Table 14.8-2: Diversity Gain Derived from Statistics of Two Adjacent FSO Links

Availability (%)	Diversity Gain (dB) Link A	Diversity Gain (dB) Link B	Availability (%)	Diversity Gain (dB) Link A	Diversity Gain (dB) Link B
99.00	0.75	5.27	99.975	1.05	7.02
99.25	0.81	5.42	99.990	1.07	7.49
99.50	0.85	5.74	99.9925	1.10	7.60
99.75	0.89	6.03	99.9950	1.17	7.74
99.90	0.94	6.39	99.9975	1.23	8.02
99.925	1.01	6.67	99.9990	1.27	8.36
99.950	1.04	6.79			

For analysis we used statistics measured by 450 m long link B between CTU building and Orlik dormitory. The free space link consisting of a four-beam free space optical communication system FlightStrata G by LightPointe (1.25 Gbps of full-duplex, VCSEL at 850 nm, 2.0 mrad divergence). The FSO link B is equipped with a backup RF link Mikrotik RB600A with miniPCI cards working at the frequency of 5 GHz with data rates up to 54

Mbps. Deployment of both transceivers at the roof of Orlik dormitory is depicted in Figure 14.8-2.

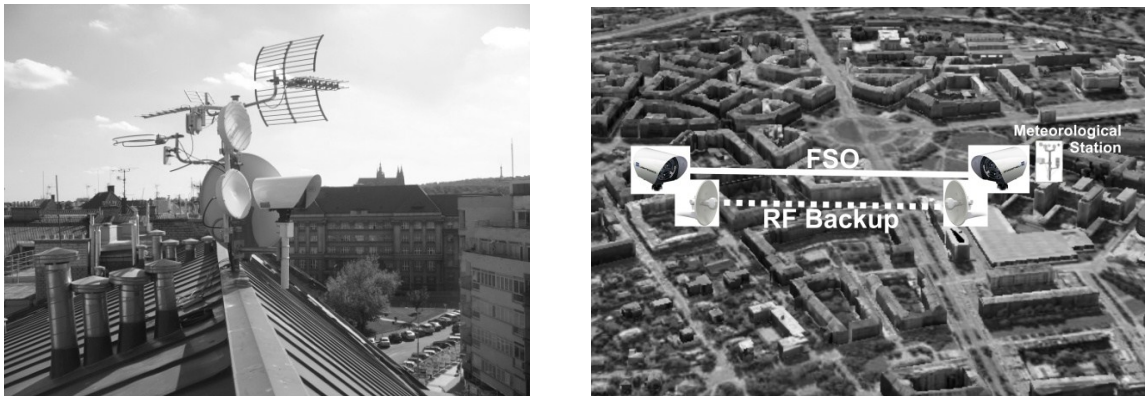


Figure 14.8-2: a) FSO/RF transmitting site at the Orlik dormitory; b) experimental campaign arrangement for RF/FSO

The RF part includes 17 dBi gain antennas, maximal output power is set to 23 dBm, horizontal polarization is used. The values of the received optical power of these two links are acquired by using SNMP protocol and stored in the computer in a second time interval. Weather conditions are observed by two meteorological stations placed on the roof of the faculty. The first station collects value of the temperature, atmospheric pressure, relative humidity, velocity and direction of wind and amount of precipitation within the time interval of one minute. The second station allows observation of the temperature, relative humidity and amount of precipitation. Hybrid link and meteorological stations deployment is shown in Figure 14.8-2b.

Example of relative attenuation variations of the FSO link B with adjacent RF link measured is depicted in Figure 14.8-3. Sample data shown in the figure was collected from 30<sup>th</sup> October to 9<sup>th</sup> December 2011. It can be seen that the FSO link is much more sensitive to meteorological changes and its attenuation reaches higher values. The other advantage of the radio link over FSO technology is its relatively higher dynamic range. The maximum power on the output of the RF link is approximately 23 dBm and the sensitivity of the receiver varies between -70 to -90 dBm with respect to required data rates.

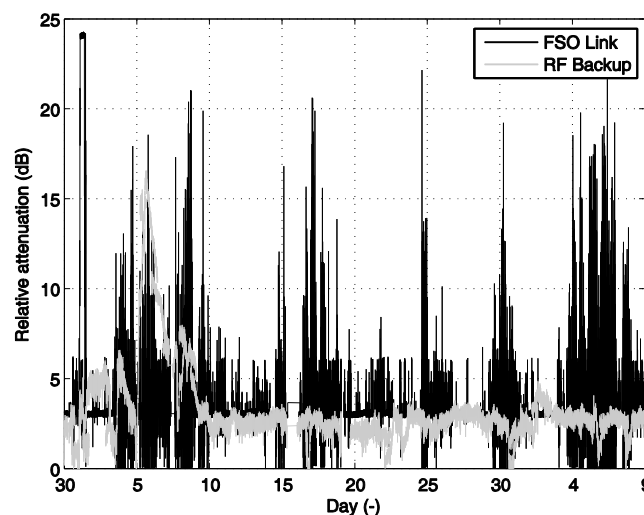


Figure 14.8-3: Received optical power of the link B and RF backup link measured from 30<sup>th</sup> October to 9<sup>th</sup> December.

The cumulative distribution function (CDF) of attenuation relative to fade margin is depicted in Figure 14.8-4. The solid black line stands for the FSO link and the gray line for RF link. The dashed line corresponds to the minimal loss observed in the case of joint receiving statistics.

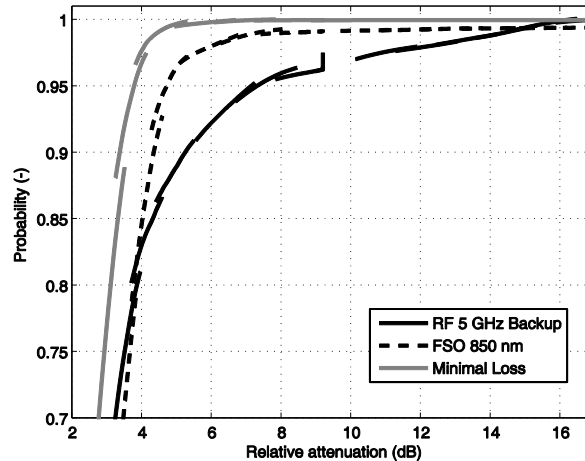


Figure 14.8-4: CDF the FSO and RF link attenuation compared to minimal loss of both links

As it can be seen from Figure 14.8-4, CDF of joint hybrid RF/FSO link tends to be almost parallel to CDF of FSO in case of lower availabilities, but starts to diverge with availabilities higher than 99.7%. This can be illustrated on derived diversity gains in Table 14.8-3.

Table 14.8-3. Diversity gain of the hybrid RF/FSO link

Availability [%]	Diversity gain [Strickland, B. R., Lavan, M. J. et al., 1999]
70.0	0.70
80.0	0.73
90.0	0.82
99.0	3.20
99.9	17.2

The availability of the alone FSO link was 99.57 % within one month interval. Outages were typically observed during foggy days. Contrary to parallel analyzed data in real scenario we implemented the outage criterion for reconfiguration of the connection –when the connection fails, the traffic is redirected to the RF link. Once the FSO link B is available, it immediately used to again transmit data. Additional increasing of the availability can be reached by reconfiguration of the network when the received optical power drops to less than a certain threshold (prior to the link outage). In the case of joining 5 GHz backup link usage in this scenario, the availability reached 100 %, i.e. fades of RF/FSO link had not exceeded fade margin.

## 14.9 Summary

In this chapter the error performance and outage probability of a SIM-FSO system employing spatial and temporal diversity to combat the channel fading have been discussed. Subcarrier intensity modulation with PSK is considered in the chapter though the technique can

easily be applied to other modulation techniques. The log-normal, gamma-gamma and negative exponential atmospheric turbulence models are investigated the error performance is derived for the three different linear combining techniques. It has also been illustrated that a multiple transmitter-single photodetector system is in effect a single transmitter-multiple photodetector configuration employing EGC linear combining, and that a reasonable number of independent photodetectors to mitigate scintillation without overwhelming complexity can be put at between two and four. The subcarrier TDD as an alternative technique for ameliorating the channel fading has equally been introduced and its error performance analysed. Retransmitting the delayed copy of the information just once is however found to be the optimum with a gain of up to 4.5 dB in weak atmospheric turbulence. Expectedly, the TDD gain was shown to be proportional to the fading strength but independent of the data rate. In the second part of the chapter, diversity for FSO links influenced by rain and fog is discussed. The hybrid RF/FSO link diversity is considered and it is observed that outage improvement probability dependence on angular separations between diversity links.

## 14.10 References

- [Ambrosio, L. A., M. Zamboni-Rached, et al., 2011] Ambrosio, L. A., M. Zamboni-Rached, et al. "Overcoming Diffraction in FSO Systems Using (GRIN) Axicons for Approximating the Longitudinal Intensity Profiles." *Journal of Lightwave Technology* 29(17): 2527-2532, 2011.
- [Anguita, J. A., M. A. Neifeld, et al. , 2007] Anguita, J. A., M. A. Neifeld, et al. "Spatial correlation and irradiance statistics in a multiple-beam terrestrial free-space optical communication link." *Applied Optics* 46(26): 6561-6571, 2007.
- [Gradshteyn, I. S. and Ryzhik, I. M., 1994] Gradshteyn, I. S. and I. M. Ryzhik, *Table of integrals, series, and products*. London, Academic Press, Inc. 1994
- [Hashmi, A., Eftekhari, A., et al. 2008] Hashmi, A., Eftekhari, A. et al. "Analysis of optimal Adaptive Optics system for Hybrid RF-wireless optical communication for maximum efficiency and reliability." 4th International Conference on Emerging (ICET): 62-67, 2008.
- [Kaushal, H., Kumar, V. et al. , 2011] Kaushal, H., V. Kumar, et al., "Experimental Study on Beam Wander Under Varying Atmospheric Turbulence Conditions." *IEEE Photonics Technology Letters* 23(22): 1691-1693, 2011.
- [Komiya, T., Kobayashi, K. et al. 2011] Komiya, T., K. Kobayashi, et al.. "Study of visible light communication system using RGB LED lights" *Proceedings of SICE Annual Conference (SICE)*, 2011.
- [Kwok, C. H., Pentty, R.V. et al., 2008]. Kwok, C. H., Pentty, R.V. et al "Link reliability improvement for optical wireless communication systems with temporal domain diversity reception." *IEEE Photonics Technology Letters* 20(9): 700-702, 2008.
- [Lee, E. J. and Chan, V. W. S. 2004] Lee, E. J. and V. W. S. Chan "Optical communications over the clear turbulent atmospheric channel using diversity." *IEEE Journal on Selected Areas in Communications* 22(9): 1896-1906, 2004.

- [Lioumpas, A. S., Karagiannidis, G. K. et al. 2011] Lioumpas, A. S., G. K. Karagiannidis, et al.. "Adaptive Subcarrier PSK Intensity Modulation in Free Space Optical Systems." IEEE Transactions on Communications 59(5): 1368-1377, 2011.
- [Matera, F. and Settembre, M., 2000] Matera, F. and M. Settembre. "Role of Q-factor and of time jitter in the performance evaluation of optically amplified transmission systems." Selected Topics in Quantum Electronics, IEEE Journal of 6(2): 308-316, 2000.
- [Mitchell, R. L, 1968] Mitchell, R. L.. "Permanence of the log-normal distribution." Journal of the Optical Society of America 58(9): 1267-1272, 1968.
- [Nadeem, F., Kvicera, V. et al., 2009] Nadeem, F., V. Kvicera, et al. "Weather effects on hybrid FSO/RF communication link." IEEE Journal on Selected Areas in Communications 27(9): 1687-1697, 2009.
- [Ohteru, S. and Takachio, N., 1999] Ohteru, S. and N. Takachio. "Optical signal quality monitor using direct Q-factor measurement." IEEE Photonics Technology Letters 11(10): 1307-1309, 1999.
- [Osche, G. R., 2002] Osche, G. R. Optical Detection Theory for Laser Applications, Wiley-Interscience, 2002.
- [ITU-R, 2000] Recommendation ITU-R Rec F.1500. Preferred Characteristics of Systems in the Fixed Service Using High-Altitude Platform Stations operating in the Bands 47.2-47.5 GHz an 47.9-48.2 GHz., 2000.
- [Simon, M. K. and Alouini, M.-S., 2004] Simon, M. K. and M.-S. Alouini. Digital Communication Over Fading Channels. New York, John Wiley & Sons Inc, 2004.
- [Strickland, B. R., M. J. Lavan, et al., 1999] Strickland, B. R., M. J. Lavan, et al., "Effects of fog on the bit-error rate of a free space laser communication system", Journal of applied optics, 38(3),1999, 424-431.
- [Trisno, S., Smolyaninov, I. I., et al., 2004] Trisno, S., I. I. Smolyaninov, et al. "Delayed diversity for fade resistance in optical wireless communications through turbulent media." Proceedings of SPIE 5596: 385-394, 2004.
- [Trisno, S., Smolyaninov, I. I., et al., 2005] Trisno, S., I. I. Smolyaninov, et al. "Characterization of time delayed diversity to mitigate fading in atmospheric turbulence channels." Proceeding of SPIE 5892: 589215.589211-589215.589210, 2005.
- [Weerackody, V. and Hammons, A. R., 2006] Weerackody, V. and A. R. Hammons. "Wavelength Correlation in Free Space Optical Communication Systems". IEEE Military Communications Conference, 2006.
- [Zvanovec, S. and Pechac, P. 2006] Zvanovec, S. and P. Pechac. "Rain Spatial Classification for Availability Studies of Point-to-Multipoint Systems." IEEE Transactions on Antennas and Propagation 54: 3789-3796, 2006.

## 15 CONCLUSIONS

(Joaquin Perez Soler, Erich Leitgeb, Zabih Ghassemlooy, Gorazd Kandus)

The COST Action IC0802 Working Group 3 (WG3) has developed an intensive activity on FSO measurement campaigns as reflected in this report. In order to assess them correctly we have defined the most relevant atmospheric parameters to measure, in chapter 2 (considering the FSO link attenuation point of view). We considered the fog as the worst phenomenon which attenuates the optical signal in the order of hundreds dB per km. Then, rain is causing lower attenuation of the order of tens dB per km. On the other hand, wind as well as atmospheric turbulence play lower role in the attenuation of optical wireless links.

The measurement campaigns were installed in different outdoor locations of our partners, Nice, Graz, Milano, Prague, Mileksova, Budapest, Rome and Canada. Results are presented in chapters 3 to 9. On the other hand, a complete test bed has been developed under laboratory conditions in Northumbria University, Newcastle, to test and analyse relevant atmospheric parameters, as mentioned in chapters 10 and 11. These measurement campaigns have been supported by the study of different solutions to mitigate and improve the FSO systems under adverse atmospheric conditions. Regarding these studies, chapters 12 to 14 include relevant analysis of RF/FSO hybrid systems, new modulation schemes, diversity and networking techniques in order to improve the FSO communication systems.

### 15.1 Final results

The main contribution from each chapter in this final report can be summarised in three main topics, namely international outdoor FSO measurements campaigns, indoor modelling and laboratory reliable test-bed for FSO and design and analysis of FSO improvements under new system models regarding transceiver, channel modelling and signal formatting.

The outdoor FSO campaign has proved the high international cooperation level, reached by WG3. From European partners with a solid and recognized background on weather metrology, to important atmospheric physics experts around the world, from Canada to Pakistan. This provides one of the main outcomes of this WG3, which is the formation of links and actions between the partners in order to build an international database of experts and provide a common framework of measurements of outdoor FSO systems under different atmospheric scenarios, mainly fog. This common international knowledge becomes the first successful attempt providing a valuable asset that will help to improve the research in the FSO communications field. We could compare this step with the public RF experiments resulting in database of meteorological stations and satellite stations that started 50 years ago and helped to boost and understand the RF technology and its application to communications.

From the viewpoint of results it is clear that the complexity of WG3 tasks is focused on the provision of common theory in order to develop and analyse the experimental results from very different outdoor locations, from sea level to high mountain meteorological stations. Each experiment has provided a valuable analysis and understanding of the FSO reliability under different atmospheric conditions.

In the Graz and Nice experiments the FSO systems were evaluated under maritime and continental fog conditions. For the continental fog in Graz the stability and low variance of this event indicate that with appropriate power margins high data rates could be reached

without using coding and diversity techniques. On the other hand under maritime fog conditions due to its fast and high variability, the use of diversity, coding techniques and hybrid solutions could help to improve these FSO systems.

In Milano the measurement results of FSO links indicate under fog conditions that it is necessary for usual optical communications wavelengths to know local long term variation of the atmospheric events in order to enhance the proposed theoretical model and improve the performance of FSO systems.

The Prague FSO-set-ups have shown that physical parameters of main atmospheric events could help in real time variation to estimate the lightwave attenuation and improve the performance of the FSO systems. At Milesovka, the intensive measurement campaign has delivered very interesting results showing that energy of the wind and sonic temperature are well correlated with FSO attenuation due to atmospheric turbulence.

On the other hand the Budapest measurement set-ups have introduced the concept of liquid water content as a basis for FSO link attenuation measurements in fog conditions. The result indicates a great correlation between this parameter for FSO and microwave link attenuation.

The extensive measurement campaign deployed in Rome has provided very interesting correlation between radiative transfer theory and multiple scattering effects along the FSO path. The observations in Canada have provided a broad database of urban FSO link system measurements under great range of atmospheric events. These measurements were correlated with previous channel estimations of weather parameters and with both statistics, providing a broader understanding of the FSO outdoor channel statistics.

The common characteristics of all these outdoor measurement campaigns are the long-time observation, because the experiments have been realised during periods from 1 year to 6 years.

Next objective of the WG3 action was to understand and start the generation of new real model for FSO link and system, based on this database. In order to ensure the reliability of this theories and findings a test-bed campaign has been developed based on indoor and controlled FSO environments.

For the fog events, Northumbria University (UK) has developed an intensive and extensive test-bed based on atmospheric indoor chamber that replicates outdoor atmospheric events under controlled laboratory environment. The results of this campaign have led to a proposal of a new wavelength dependent model for the atmospheric fog and smoke (also smog), which is valid for the visible – NIR range. Measurements over the visibility range of 1 km calibrated for outdoor FSO links using the Kim model are validating the laboratory-based empirical model.

Regarding the influence of turbulence on FSO systems, this laboratory test-bed has provided interesting results that support outdoor FSO measurements in order to characterize the atmospheric channel.

Following these results from outdoor measurements, data analysis, test-beds and initial new models for FSO channel estimation, the study of how to improve the performance of FSO system is the final goal of WG3. The study of hybrid system for FSO to overcome link unavailability at any weather condition has been carried out. The main finding indicates that it

is necessary to implement redundancy concepts for FSO networks jointly with Hybrid RF/FSO links to minimize the impact of the hydrometeors, fog and turbulence on the link availability. Here arises the concept of Metrozone networks applicable to FSO Hybrid networks that will reduce the power consumption, increase their capacity and the performance of the overall FSO network.

Moreover, some work has been done in WG3 also on the analysis and design of efficient signal formats that allows the improvement of FSO systems performance at any weather condition. In this case the main analysis is focused on the FSO system performance under turbulence effects using PPM, OOK and in special SIM modulation formats. Following an extensive discussion about spatial and temporal diversity techniques used to combat channel fading and improve the FSO systems in terms of error performance and outage probability was reported.

The extensive work led by WG3 on outdoor FSO systems has brought interesting results regarding the new model approach for FSO link attenuation under fog conditions and the use of Hybrid links and MIMO at FSO networks, what improves the link availability.

## **15.2 Future work and open tasks**

The results obtained and summarized by WG3 imply open questions that should be solved in the near future. First of all it is necessary to complete the initial outdoor FSO channel model to cover at least the 90% of the locations using the extensive new measurements database available from IC0802 WG3 and regarding not just fog attenuation but also all other atmospheric events. Then it will be very interesting to provide an analytical framework of how to analyse drop size distribution and its relevant parameters, based on weather measurements in order to characterize fog and improve the reliability of FSO systems. And finally, it would be helpful to open this database to new measurement campaigns including more specialists in atmospheric turbulences.

We would like to remark that these future objectives have been partially included in the COST Action IC1101 OpticWise but not all of them. This allows the provision of well-connected, related group of experts on outdoor FSO links that forms a great networking grid to be used in future projects and consultations internationally from the first time in Europe.

A lot of work in modelling is still to be done, because WG3 has started the investigation of models by some early verifications and updates. Compared to the RF-technology in optical free space wave propagation we have a delay of 50 years that must be considered for all future activities. We tried to show the complexity of our different sites of experiments to find a well suited scenario for all Free Space Optics measurements for the future.

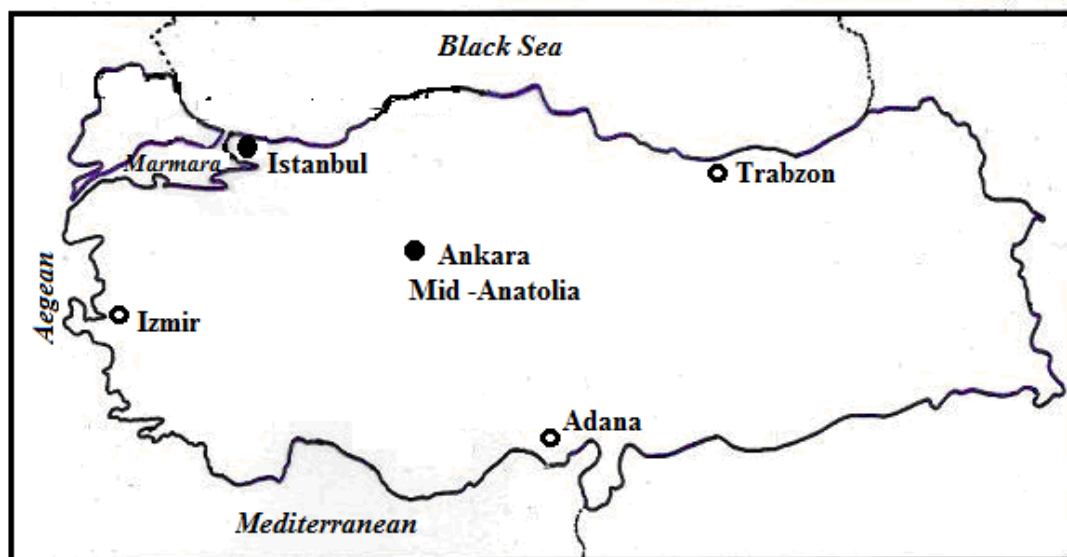
For realistic FSO-systems, redundancy, site diversity and hybrid links are one answer to counteract the atmospheric conditions. But in future we will also implement new technologies like higher order modulation and coding schemes, adaptive optics, automatic gain control and MIMO-systems. To investigate those technologies it is important to generate a model for the FSO-channel suited for 90% of locations and cases (including different climate environments and various weather conditions). In future we will carry out further measurements to analyse drop size distribution (and all relevant particle parameters) in fog. The final model should also include all possible parameters for turbulence conditions. Further closer co-operation with the turbulence specialists would improve the work and the quality of results.

## INITIAL RESULTS OF RESEARCH ON THE CONSTRUCTION OF A COUNTRYWIDE OPTICAL WIRELESS AVAILABILITY MAP, TURKEY

Faruk Ozek, Prof

Mrs Filiz Sari, Dr

*Ankara University*



A map of Turkey, indicating the regional centers considered for  
optical wireless availability estimation

<b>Region Center</b>	<b>Weather Conditions</b>	<b>Present/Potential Users</b>
Marmara Istanbul *	Mostly Favourable	University Commerce Industry
Mid-Anatolia Ankara *	Mostly Favourable	University Industry
Aegean İzmir	Favourable	University Commerce
Mediterranean Adana	Very Favourable	University Industry
Black Sea Trabzon	Fair	University

\* Research completed

## MATERIALS AND METHOD

**Material** : Historical airport visibility data

<http://www.wunderground.com>

**Statistics** : Cumulative distribution function, CDF

**Application** : Enterprise class systems, 99% availability criterion

### *GENERAL PROCEDURE*

#### *AND THE SEQUENCE OF COMPUTATIONS*

**First** : Elimination of the airport visibility data for favourable months, then consideration of the *unfavourable* months, alone

**Computations** : Attenuation : atmospheric, geometrical, scintillation, etc.

Link margin

CDF fitting of airport visibility data

Availability

Link range

**Basic reference:** A. Prokes, V. Skorpil, "Estimation of free space optics systems availability based on meteorological visibility," *IEEE LATINCOM'09*, pp. 1 – 4, September 2009.

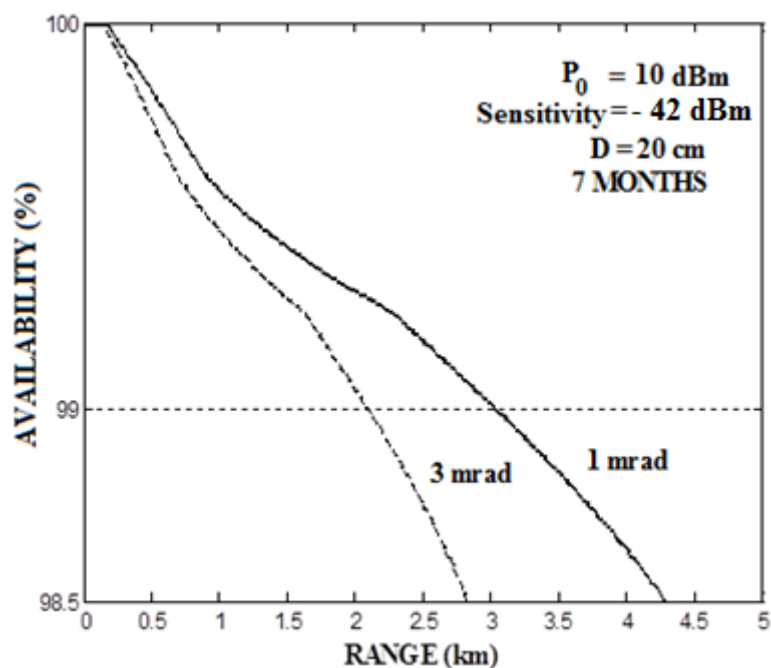
## INITIAL RESULTS 1. CITY OF ISTANBUL, MARMARA

*Most of the operational optical wireless systems located.*

MONTHS	OBSERVATIONS $V \leq 4$ km
August	0
September	5
<b>OCTOBER</b>	<b>37</b>
<b>NOVEMBER</b>	<b>158</b>
<b>DECEMBER</b>	<b>85</b>
<b>JANUARY</b>	<b>128</b>
<b>FEBRUARY</b>	<b>114</b>
<b>MARCH</b>	<b>33</b>
<b>APRIL</b>	<b>19</b>
May	4
June	8
July	3

Airport data: 2007 – 10

*Unfavourable Months: October to April, inclusively (7 Months)*



Losses due to mispointing, optical components and scintillation are almost constant and therefore can be taken as  $-3$  dB,  $-9$  dB and  $-5$  dB, respectively.

### Publications

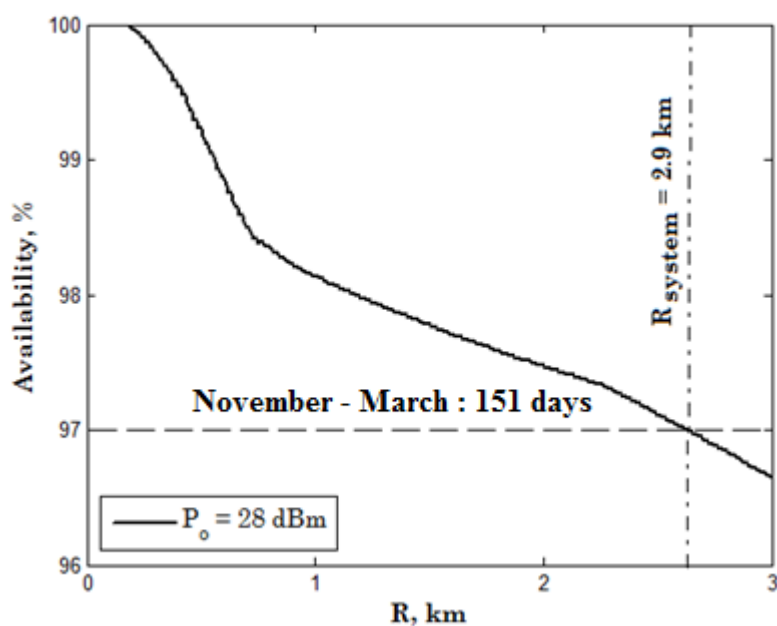
1. F. Sari and F. Ozek, "Optical Wireless Communications: Link Availability Prediction for the City of Istanbul" 11<sup>th</sup> International Conference on Telecommunications (ConTEL 2011), pp. 207- 209, 15-17 June 2011.
2. F. Sari, "Link Margin and availability analysis for coast-to-ship optical wireless applications", The Mediterranean Journal of Electronics and Communications, Vol. 7, No. 2, pp. 211 – 215, 2011.

## INITIAL RESULTS 2. CITY OF ANKARA, mid – ANATOLIA

*There are at least two systems operational.*

MONTHS	OBSERVATIONS $V \leq 4$ km
August	0
September	0
October	13
<b>NOVEMBER</b>	<b>97</b>
<b>DECEMBER</b>	<b>206</b>
<b>JANUARY</b>	<b>167</b>
<b>FEBRUARY</b>	<b>67</b>
<b>MARCH</b>	<b>62</b>
April	9
May	9
June	3
July	0

*Unfavourable months: November to March, inclusively*



*Annual cut – off 4.5 days  $\cong$  99 % availability*

Computed with reference to Ankara University optical wireless system parameters

$P_o$  : adaptable laser power = 28 dBm max, 1550 nm

Beam divergence : 2.8 mrad

Receiver lens (D) : 20 cm dia

**Publication** : Prepared for submission (for detailed information)

# WG3 of IC0802



**COST IC0802:** Propagation tools and data for integrated Telecommunication, Navigation and Earth Observation systems

## WG3: Channel modelling for free-space optical systems and airborne terminals

*Erich Leitgeb / Gorazd Kandus*

Kick-Off: 5 organisations

Now at MCM8 / WG3 Meeting at DLR: 15 partners



## Discussing the WG3 Results

It addresses:

- Scientific activities  
(meetings, STSMs, Workshops, Conferences, Tr. Schools)
- Final Report

### 1) RESULTS VS OBJECTIVES

### 2) MAIN RESULTS FROM THE ACTION

Innovative knowledge

Scientific results

Socio-economic impact (e.g. radio regulations ITU)

Spin-off of new National, EU and other International activities

### 3) INTERDISCIPLINARITY

### 4) NEW COST NETWORKING

New members joining the WG

Total number of participants involved in the action

Key Early Stage Researchers and Junior Engineers

Researchers from non-COST countries





# WG3 Results

It addresses:

➤ **Scientific activities**

(meetings, STSMs, Workshops (WS), Conferences, Training Schools); 4 STSM's in WG3, additional STSMs with additional resources (from participating institutions or special funds); add. WS together with other organisations (BONE FP7 project, CSNDSP, EuCAP and ConTEL conferences)

➤ **Final Report**

## 1) RESULTS VS OBJECTIVES

WG3 focused on FSO Channel modelling. A relatively new area of R&D (about 10 years)

- 1) Establishment of a coordinated set of experimental optical links and laboratories and definition of common measurement procedures (10 in EU, CA, PK)
- 2) A common theoretical framework (made models and definitions) on FSO propagation has been established
- 3) Data-base of sites and experts was Input to WG1 of COST IC1101, delivered in Autumn (WG1 chair of IC1101 Carlo Capsoni), planned also as data-base for EurAAP



# Final Report WG3

- Work mainly concentrated on Outdoor FSO (diff. to IC1101) and mainly on fog evaluation and measurements
- Co-operations
- Compared to RF experimental sites (50 years delay)
- Not a finished new model, we started with updating and verifying
- Future activity in IC1101 and new projects
- Complexity of the work of WG3, theory available, measurements done on different sites (different climates and set-ups and monitoring, data collecting), data analysis and verification; Special value of each experiment and topic and focus

# WG3 Results

It addresses:

➤ **Scientific activities**

(meetings, STSMs, Workshops, Conferences, Tr. Schools); 4 STSM's in WG3, additional STSMs with additional resources (from participating institutions or special funds); add. WS together with other organisations (BONE FP7 project, CSNDSP, EuCAP and ConTEL conferences)

➤ **Final Report**

## 1) RESULTS VS OBJECTIVES

WG3 focused on FSO Channel modelling. A relatively new area of R&D (about 10 years)

- 1) Establishment of a coordinated set of experimental optical links and laboratories and definition of common measurement procedures (10 in EU, CA, PK)
- 2) A common theoretical framework (made models and definitions) on FSO propagation has been established
- 3) Data-base of sites and experts was Input to WG1 of COST IC1101, delivered in Autumn (WG1 chair of IC1101 Carlo Capsoni), planned also as data-base for EurAAP



# WG3 Main Results

It addresses:

➤ **Scientific activities**  
(meetings, STSMs, Workshops, Conferences, Tr. Schools)

➤ **Final Report**

## 2) MAIN RESULTS FROM THE WG

**Innovative knowledge on experimental techniques** generated by collaboration and exchange between different research groups (10 active R&D groups).

**Network of Labs and Groups is an Asset** (a building block) for future development of channel models for FSO. Input to WG1 of IC1101, proposed for ITU-R, EurAAP

**Scientific results** visible in a high number of scientific publication: only reviewed conferences, IEEE Transactions on Communications, Photonics, Journal on Selected Areas in Com., Int.l Journal on Satellite Communications, Electronic letters, IET, OSA

**Socio-economic impact** (e.g. radio regulations ITU)

Link with Industry (e.g. Siemens GE, see MCM2, France Telecom exp. site)

FP7 BONE, IC1101,

Italian Ministry of Industry,

National Czech COST project,

ESA Activity on Optical Feeder links TU Graz/JR 2010



# WG3 Main Results

## 3) **INTERDISCIPLINARITY**

RF and Optical Communications systems (visible also in the final report)  
Atmospheric Physics  
Statistical Theory  
Atmospheric Remote Sensing

## 4) **NEW COST NETWORKING**

New members joining the WG

at KO 5: TU Graz, JSI, BME-HU, POLIMI, Northumbria Univ.

At MCM8: 15:

IAP, Univ. La Sapienza, Brno Univ. Techn., Univ. Pardubice, CTU, CMI,  
McMaster (CA), FAST Lahore (PK), Glasgow Caledonia (UK),  
Ozyegin Univ. (TU)

Total number of participants involved in the action

Key Early Stage Researchers and Junior Engineers: About 30 ESRs: UK 7, AT 5, SL  
2, CZ 6, IT 2, HU 3, PK 2, CA 2

Researchers from non-COST countries: CA, PK

4 STSMs plus about 10 missions (supported by Universities/ Erasmus)



# NEW COST NETWORKING

## **New members joining the WG**

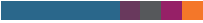
at Kick-Off: 5; TU Graz, JSI, BME-HU, POLIMI, Northumbria Univ.

at MCM8: 15; IAP, Univ. La Sapienza, Brno Univ. Techn., Univ.  
Pardubice, CTU, CMI, McMaster (CA), FAST Lahore (PK), Glasgow  
Caledonia (UK), Ozyegin Univ. (TU)

Total number of participants involved in the action

**Publications:** Joint !! Usual 5 Journal contributions and around 20  
reviewed conference contributions / year





## WG3: Final work

- To complete the Final Report; well shaped version until November 2012 (DLR-Meeting), finished end of the year
- Further joint publications (visible in the Annual Report: Joint publications 7/2011 – 6/2012: ~10 OWC at CSNDSP 2012, ~8 at EuCAP 2012, ~5 at NOC 2012, ~5 Journal publications, further joint work and publications
- Further Inputs to ITU-R; IC1101 etc.



## Special thanks!!!!!!

- to all participants of WG3!!!!!!!!!!!!
- to **Chair** of COST IC0802 (Co-Chair, Grant-Holder and IC0802 secretary)
- to **COST office in Brussels**